Control of Spin Relaxation in Disordered Quantum Wells and Nanowires

DISSERTATION

Zur Erlangung des

DOKTORGRADES DER NATURWISSENSCHAFTEN (DR. RER. NAT.)

der Fakultät für Physik der Universität Regensburg

vorgelegt von

Michael Dieter Kammermeier

aus

Regensburg

im Jahr 2018

Das Promotionsgesuch wurde eingereicht am 23.04.2018.
Die Arbeit wurde angeleitet von Prof. Dr. John Schliemann.

Prüfungsausschuss:	Vorsitzender:	Prof. Dr. Dominique Bougeard
	1. Gutachter:	Prof. Dr. John Schliemann
	2. Gutachter:	Prof. Dr. Thomas Schäpers (FZ Jülich)
	weiterer Prüfer:	Prof. Dr. Klaus Richter

Termin des Promotionskolloquiums: 18.09.2018.

Dedicated to my parents Michaela and Karl
and my sisters Anne and Laura.

"Not only is the universe stranger than we think, it is stranger than we can think."
— Werner Heisenberg.

Abstract

A central theme in semiconductor spintronics is the control of spin-polarized charge carriers. In order to utilize the spin for information processing, a long spin lifetime is essential. In this thesis, we address this issue for important types of semiconductor systems: disordered quantum wells and nanowires. Typically, the most prominent process that limits the spin lifetime in inversion-asymmetric systems is the D'yakonov-Perel' mechanism. It results from the random spin precessions due to the combined effect of impurity scattering and spin-orbit coupling. One very convenient experimental tool to gather information about the spin-relaxation properties, as well as transport parameters, are magnetoconductance measurements of the weak (anti)localization. In particular, the latter is mainly determined by the spin lifetime of the long-lived spin states.

After giving a comprehensive introduction of the underlying theoretical fundamentals, we identify spin-preserving symmetries in quantum wells of zinc-blende structure. First, we focus on electron systems and prove that persistent spin states can be found due to the interplay of Rashba and Dresselhaus spin-orbit coupling if at least two growth-direction Miller indices agree in modulus. Additionally, a general closed-form expression for the weak (anti)localization is provided to enable an experimental verification. Secondly, we show that also in [001]-oriented hole systems such symmetries can be realized if in addition uniaxial shear strain is present.

Semiconductor nanowires can have very distinct mesoscopic characteristics. We concentrate on three important kinds of nanowires with diffusive transport channels: (i) tubular zinc-blende nanowires as well as cylindrical (ii) zinc-blende and (iii) wurtzite nanowires. In each of these cases, the impact of a gate-induced Rashba effect is taken into account which allows an external manipulation of the spin relaxation. Employing a Cooperon-based approach, we theoretically analyze the spin-relaxation features, identify the long-lived spin states, and compute the weak (anti)localization correction. The obtained expressions for both types of zinc-blende nanowires are fitted to the experimental data of magnetoconductance measurements of InAs nanowires. We find good agreement between theory and experiment and extract reasonable transport parameters. Regarding the spin relaxation, in contrast to the cylindrical counterpart, the tubular zinc-blende nanowires exhibit a growth-direction dependence. In the cylindrical channels, the spin relaxation is sensitive to the wire diameter and suppressed in narrow wires due to boundary-induced motional narrowing. The suppression is particularly pronounced in wurtzite nanowires as the relaxation due to the intrinsic linear-in-momentum spin-orbit terms becomes ineffective. Yet, the corresponding long-lived spin states possess a complex helical spin texture which is difficult to realize. This can yield very dissimilar values for the spin lifetimes when extracted from distinct experiments. We explicitly demonstrate the arising discrepancies for optical and magnetotransport measurements.

Related Publications

A major part of the present thesis also appears in the following publications:

[1] F. Dirnberger, **M. Kammermeier**, J. König, M. Forsch, P. E. Faria Junior, T. Campos, J. Fabian, J. Schliemann, C. Schüller, T. Korn, P. Wenk, D. Bougeard,
Ultralong Spin Lifetimes in One-Dimensional Semiconductor Nanowires,
to be published,

[2] **M. Kammermeier**, P. Wenk, F. Dirnberger, D. Bougeard, and J. Schliemann,
Spin Relaxation in Wurtzite Nanowires,
Phys. Rev. B **98**, 035407 (2018),

[3] **M. Kammermeier**, P. Wenk, J. Schliemann, S. Heedt, T. Gerster, and Th. Schäpers,
Magnetoconductance Correction in Zinc-Blende Semiconductor Nanowires with Spin-Orbit Coupling,
Phys. Rev. B **96**, 235302 (2017),

[4] **M. Kammermeier**, P. Wenk, and J. Schliemann,
Control of Spin Helix Symmetry in Semiconductor Quantum Wells by Crystal Orientation,
Phys. Rev. Lett. **117**, 236801 (2016),
(selected for the front cover of issue 23, vol. 117)

[5] **M. Kammermeier**, P. Wenk, J. Schliemann, S. Heedt, and Th. Schäpers,
Weak (Anti-)Localization in Tubular Semiconductor Nanowires with Spin-Orbit Coupling,
Phys. Rev. B **93**, 205306 (2016),
(Editor's Suggestion)

[6] P. Wenk, **M. Kammermeier**, and J. Schliemann,
Conserved Spin Quantity in Strained Hole Systems with Rashba and Dresselhaus Spin-Orbit Coupling,
Phys. Rev. B **93**, 115312 (2016),

[7] T. Dollinger, **M. Kammermeier**, A. Scholz, P. Wenk, J. Schliemann, K. Richter and R. Winkler,
Signatures of Spin-Preserving Symmetries in Two-Dimensional Hole Gases, Phys. Rev. B. **90** 115306 (2014).

Also, due to their relevance, revised sections of my Master thesis, Ref. [8], on *Strained Hole Systems with Rashba and Dresselhaus Spin-Orbit Coupling*, submitted in 2014 at the University of Regensburg, were adopted.

Contributed Presentations

The related research results have been presented in form of oral or poster contributions at the following conferences, workshops, Winterschools, and journal clubs.

2018:

- DPG Meeting in Berlin, Germany, *Talk.* [3]
- International Winterschool in Mauterndorf, Austria, *Poster.* [3]

2017:

- Journal Club at CNyN in Ensenada, Mexico, *Talk.* [4]
- SPIE X in San Diego, USA, *Poster.* [4]
- International Workshop on 1D Systems in Regensburg, Germany, *Poster.*[4, 5]
- International Workshop on Collective Spin Transport in Natal, Brazil, *Poster.* [4]
- DPG Meeting in Dresden, Germany, *Poster.* [4]
- NTSD Workshop in Sao Carlos, Brazil, *Talk* & *Poster.* [4]

2016:

- International Workshop on Emergent Relativistic Effects in Regensburg, Germany, *Talk* & *Poster.* [4–6]
- PASPS 9 in Kobe, Japan, *Poster.* [5]
- ICPS in Beijing, China, *Poster.* [5] (★ Best-Poster-Award Winner)
- DPG Meeting in Regensburg, Germany, *Poster.* [5]
- International Winterschool in Mauterndorf, Austria, *Poster.* [5]

2015:

- Journal Club at CNyN in Ensenada, Mexico, *Talk.* [6, 7]
- Gordon Research Seminar and Conference in Hong Kong, China, *Talk* & *Poster.* [6, 7]
- DPG Meeting in Berlin, Germany, *Talk.* [6, 7]

Contents

List of Symbols

Throughout this thesis we frequently use the following notations and abbreviations.

Notations

$\mathbf{A}$	magnetic field induced vector potential
$\mathbf{A}_s$	spin-orbit induced vector potential
$\mathbf{B}$	magnetic field
$\hat{\mathcal{C}}/\hat{H}_{\mathcal{C}}$	Cooperon/Cooperon Hamiltonian
ΔG	(magneto)conductance correction
$\Delta\sigma$	weak (anti)localization correction
D_e	diffusion constant
$e > 0$	electron charge
$\boldsymbol{\mathcal{E}}$	electric field
ϵ_{ij}	strain tensor components
$E_F/v_F/k_F$	Fermi energy/velocity/wave vector
$\mathcal{G}$	Green's function in the first Born approximation
$\mathcal{H}$	Hamiltonian
$\mathbf{J}$	vector of total-angular-momentum-$\frac{3}{2}$ matrices
l_e/τ_e	elastic mean free path/scattering time
l_ϕ/τ_ϕ	dephasing length/time
l_s/τ_s	spin-relaxation length/time
l_B/τ_B	magnetic dephasing length/time
L_{so}	spin precession length
m_0	bare electron mass
m^*	effective electron mass
$\boldsymbol{\Omega}$	spin-orbit field

$\mathcal{R}$	rotation operator
$\mathbf{S}$	vector of spin-1 matrices
$\boldsymbol{\sigma}$	vector of Pauli matrices
$[A, B] = AB - BA$	commutator
$\{A, B\} = AB + BA$	anti-commutator
$\{A, B\}_{(s)} = \frac{1}{2}(AB + BA)$	symmetrized anti-commutator

Abbreviations

1BA	first Born approximation
1D/2D/3D	one/two/three-dimensional
2DEG/2DHG	two-dimensional electron/hole gas
BIA	bulk inversion asymmetry
c.p.	cyclic permutation
DP	D'yakonov-Perel'
EY	Elliott-Yafet
GMR	giant magnetoresistance
HH/LH	heavy/light hole
MOSFET	metal-oxide-semiconductor field-effect transistor
SIA	structure inversion asymmetry
SOC	spin-orbit coupling
SOF	spin-orbit field
WL/WAL	weak localization/antilocalization

Introduction

Although electrons carry charge and spin, in the history of information technology both properties have been employed separately. While classical data storage uses the manifestation of spins as the magnetization of ferromagnets, data processing employs the transport of charges in response to applied electric fields.

This individual focus started to fade in the late 80th with the discovery of the *giant magnetoresistance* (GMR) by Grünberg and Fert who were jointly awarded the Nobel Prize in 2007. This effect is based on the influence of magnetic materials on charge currents and is used in the *spin-valve device*. Here a non-magnetic layer is sandwiched between two magnetic layers of either parallel or antiparallel magnetization. In one magnetic layer, the magnetization is pinned while in the other one it can be rotated by an applied magnetic field. An antiparallel configuration of the two magnetizations yields a significantly larger resistance than the parallel one. This makes it possible to detect tiny magnetic fields even at room temperature with high sensitivity and allows to read-out data stored in great density. As a result, the spin-valve GMR along with other successive devices based on the same principles have triggered a large increase in memory capacity and processing speed and are by now indispensable in state-of-the-art hard disc drives. Yet, the GMR is only a paradigmatic example to demonstrate how the combined utilization of charge and spin can largely impact the modern information world. In fact, a rapidly growing field of research and technology has emerged, which is today well known as *spintronics*.

While spintronic devices based on magnetic materials have already found its place in the modern data storage industry, spin-dependent data processing devices are yet to be developed. In this context, the most important component is the field-effect transistor, which is predominantly built from semiconductor materials. Today's computer processors host millions of transistors. This number follows the trend of an exponentially increasing transistor density on integrated circuits, which was observed already in 1965 by Moore [9]. The continuing miniaturization allowed us to steadily enhance the functionality and processing speed of computer chips without significantly increasing the power dissipation. However, at some point the down-scaling naturally comes to an end. A practical reason is that the channel length between source and drain becomes so short that quantum tunneling makes it possible to transport charge carriers despite a potential barrier. The arising *off-state leakage current* leads to static power consumption and makes it hard to distinguish between an on-state and off-state (or 1 and 0 in binary language) of the transistor [10–12]. Hence, it becomes apparent that in order to obtain further improvements in functionality or performance, alternative device concepts

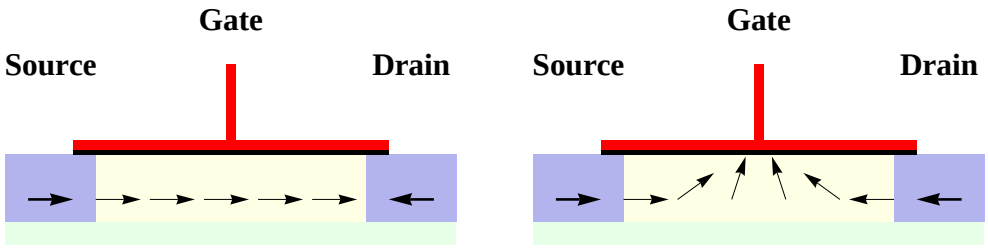

(a) $V_G = 0$ (OFF) **(b)** $V_G \neq 0$ (ON)

Fig. 1: *Datta-Das spin field-effect transistor.* (a) Off-state: The injected spins do not precess and are antiparallel to the spin orientation in the drain: The transistor is locked. (b) On-state: The spins precess in a way that they are parallel to the spin orientation in the drain: The transistor is conducting.

are needed which do not rely on classical physical laws. One of the ideas is to develop a device that operates on a more fundamental level, using the spin degree of freedom. In contrast to conventional electronics, we do not manipulate charge currents but the currents of spin-polarized electrons.

A prominent and inspiring example for such a prototypical device is the spin field-effect transistor as proposed by Datta and Das in 1990 [13]. Its functional principle is illustrated in Fig. 1. The source and drain are modeled by ferromagnets (blue regions) which have a certain fixed antiparallel magnetization. Due to the magnetization, the source injects carriers of a well-defined spin polarization into a gated region (yellow), which is assumed to be a ballistic n-doped semiconductor channel. For a vanishing gate voltage, the spin orientation of the electrons remains unchanged while they are transported through the channel. Since the spin orientation is antiparallel to the magnetization in the drain, the transmission is suppressed and the transistor is locked (cf. Fig. 1a). The conducting state can be realized by applying a gate voltage. As a consequence of *Rashba spin-orbit coupling*, the electron spins precess in the gated region about an angle that is controlled by the gate voltage. If the final spin polarization at the drain is parallel to its magnetization, the electrons can pass through the drain and the transistor is conducting (cf. Fig. 1b).

For practical applications above device yields several conceptual problems and its realization has so far not been too successful although a few working examples have been presented [14, 15]. Aside from the obstacle of inefficient spin injection due to the conductance mismatch at the ferromagnet-semiconductor interface [16], one major issue is that the spin in solids is not a good quantum number. Ironically, the key mechanism that allows for an all-electric manipulation of the spin orientation, the spin-orbit coupling, at the same time constitutes the primary source of spin relaxation. Since a realistic semiconductor is rarely free of impurities, the disorder scattering in combination with spin precession due to spin-orbit coupling causes an efficient spin relaxation process called D'yakonov-Perel' mechanism [17].

Advantageously, this effect is sensitive to the properties of the system, such as the device geometry and dimensionality, the strength and structure of the spin-orbit coupling, as well as the initial spin polarization texture. Hence, there exist several ways to manipulate the spin relaxation or even suppress it. To identify such scenarios in semiconductor quantum wells and nanowires constitutes a central theme of this thesis.

One possibility to overcome this issue is to find special parameter configurations which yield spin-preserving symmetries. These symmetries allow for long-lived or even persistent spin states which remain intact in the presence of spin-independent disorder. In a structurally confined two-dimensional electron gas (2DEG) such persistent solutions have been predicted by Schliemann *et al.* in 2003 [18]. The necessary ingredient is a crystal orientation along the [001]-direction of the zinc-blende lattice and a certain ratio between the linear-in-momentum Dresselhaus and Rashba spin-orbit coupling coefficients. As a consequence, the spin of the electrons traversing the system undergoes a well-defined rotation which is independent of the propagated path but solely determined by the initial and final position. The controlled spin rotation opens the possibility to build a spin transistor whose functionality is not only restricted to the ballistic case. This phenomenon is known today as *persistent spin helix* [19] and its existence has been unambiguously confirmed in numerous experiments by means of optical and transport measurements [20–24]. The latter exploit the impact of spin-orbit coupling on the weak (anti)localization correction to the conductivity. Other systems that are known to host persistent spin states comprise rolled-up as well as [110] and [111]-oriented 2DEGs [25]. Aside from that, spin-preserving symmetries in two-dimensional hole gases (2DHGs) were also predicted but with the requirement for rather unusual bandstructure parameters [7, 26]. In this thesis, we determine the necessary conditions for such symmetries in zinc-blende 2DEGs of arbitrary crystal orientation and derive analytic expressions for the weak (anti)localization correction to support experimental probing. In particular, it is shown that at least two growth-direction Miller indices have to agree in modulus and the Rashba and Dresselhaus coefficients must be appropriately tuned. Moreover, it is demonstrated that persistent spin states can be also found in [001]-oriented zinc-blende 2DHGs for realistic parameter configurations if a uniaxial shear strain is present.

Modern techniques enable the fabrication of semiconductor devices at the nanoscale. At this size, the dephasing length can become comparable to the system size and the effects of coherent quantum mechanics become important. And yet, at the same time, these systems are often too large and complex for a pure microscopic description. In this so-called mesoscopic regime, quantum effects are often combined with statistical and classical features [27]. Here, the quantum interference correction to the Drude conductivity, the weak (anti)localization, is a prime example. The properties of a mesoscopic system crucially depend on the relation of the characteristic length scales, such as the system size, the Fermi wavelength, the dephasing length, the elastic mean free path, and - for spin-related phenomena - the spin precession length. Nanowires are typical objects that fall into that mesoscopic range.

Semiconductor nanowires are very popular within the nanoscience community as they form the cornerstone for several fundamental discoveries [28–31] and represent a key element of future electronic and spintronic devices [32–40]. To support this technical progress, a sound knowledge and reliable control of the system's transport parameters, the spin-orbit coupling, and the spin relaxation are essential. Low-field magnetoconductance measurements of the weak (anti)localization provide convenient access to the desired information [41–50]. Since the weak (anti)localization characteristics are primarily determined by the spin-relaxation minima, they are particularly suited to determine the lifetime of the long-lived spin states. The method requires experimental data fitting with the appropriate theoretical model, which depends on the mesoscopic details of the system. Yet, this becomes problematic since the huge degree of freedom in the device preparation process allows to manipulate many of the nanowire properties over a wide range. More precisely, one is able to effectively control the size, morphology, potential landscape, carrier and impurity concentration, or even crystal structure [51–60]. The great diversity makes it difficult to build up a general suitable theoretical description of the weak (anti)localization correction. In fact, a variety of theoretical models is needed to appropriately characterize the differing nanowires.

In the diffusive regime, where the elastic mean free path is much smaller than the system size, the weak (anti)localization was analyzed by Kettemann for planar quantum wires with a zinc-blende lattice [61]. In accordance with other studies [21, 62–67], it is shown that the D'yakonov-Perel' spin-relaxation process suffers a considerable slowdown for certain spin polarizations in narrow wires of widths much smaller than the spin precession length. This results from motional narrowing due to spin-conserving scattering at the boundaries and becomes relevant as soon as the wire width is shorter than the dephasing length. Complimentary to this, the present thesis covers an important class of diffusive semiconductor nanowires with spin-orbit coupling. Analytical expressions are derived for the magnetoconductance correction due to weak (anti)localization and the D'yakonov-Perel' spin-relaxation rates. Depending on the type of surface states, the doping, or the appropriate bandgap engineering in core/shell nanowires, the electrons form either a tubular or cylindrical conductive channel [55, 59, 68]. We develop theoretical models for zinc-blende systems accounting for both situations and employ them to fit experimental data of magnetoconductance measurements. The comparison with experiment shows good agreement and delivers reasonable transport parameters. In the last chapter, we provide an analogous model for wurtzite nanowires with a cylindrical diffusive channel. With regard to spin-relaxation properties, we observe that the tubular zinc-blende nanowires exhibit a growth-direction dependence opposed to the cylindrical counterpart. Similar to the planar quantum wires, the finite wire diameter yields a suppression of the spin relaxation in the cylindrical systems. The impact of the boundary is particularly pronounced in wurtzite due to the presence of linear-in-momentum spin-orbit terms. As a consequence, the intrinsic spin relaxation can be significantly reduced in comparison to the bulk system. At the same time, the corresponding long-lived spin states assume a complex helical spin texture which is sensitive to the system parameters and difficult to realize. This

yields severe challenges for the experimental characterization of the intrinsic spin relaxation in these systems.

This thesis is falls into three parts:

- **Part I: Theoretical Foundation**
  In the first part, we introduce the relevant theoretical fundamentals. We discuss the bandstructure in zinc-blende and diamond-type semiconductors with a particular focus on the spin-orbit effects. Also, the most important spin-relaxation phenomena are briefly described. At last, we give a detailed derivation of the weak (anti)localization correction which is based on linear response theory and Green's function techniques.

- **Part II: Persistent Spin Textures in Quantum Wells**
  In the second part, we focus on the identification of system configurations which yield spin-preserving symmetries. The investigated objects comprise electrons and holes in two-dimensional zinc-blende quantum wells with Rashba and Dresselhaus spin-orbit coupling. In case of holes, the ramifications of strain are also considered.

- **Part III: Spin Relaxation and Conductivity in Nanowires**
  In the last part, we perform a detailed study of the spin-relaxation properties and the weak (anti)localization correction to the conductivity in semiconductor nanowires. We cover diffusive tubular zinc-blende systems and diffusive cylindrical transport channels with an underlying zinc-blende or wurtzite lattice.

Part I

Theoretical Foundation

CHAPTER 1

Band Structure of Semiconductors

1.1 The Origin of Spin-Orbit Coupling

In contrast to traditional electronics, spintronics exploits the spin degree of freedom of the electron in addition to its charge. The essential effect, which allows an effective control of the spin, is the spin-orbit coupling (SOC). For this reason, it is quite illuminating to recall its origins.

It can be traced back to the Lorentz-invariant formulation of quantum mechanics. Here, electrons and positrons with spin-1/2 are simultaneously described by the *Dirac equation*, which can be written in the stationary case as

$$(c\,\boldsymbol{\alpha}\cdot\mathbf{p}+\beta\,m_0c^2+V\,\mathbb{1}_{4\times4})\,|\psi\rangle=E\,|\psi\rangle\,, \tag{1.1}$$

where

$$\boldsymbol{\alpha}=\begin{pmatrix}0&\boldsymbol{\sigma}\\ \boldsymbol{\sigma}&0\end{pmatrix},\ \beta=\begin{pmatrix}\mathbb{1}_{2\times2}&0\\ 0&-\mathbb{1}_{2\times2},\end{pmatrix},$$

$\mathbf{p}$ denotes the kinetic momentum, m_0 the bare electron mass, c the speed of light in vacuum, $\boldsymbol{\sigma}$ the vector of Pauli matrices, E the energy, and $|\psi\rangle$ the four-component spinor. The potential V is considered in this context as purely electrostatic as we are interested in the interaction with atomic potentials, i.e., $V=V(\mathbf{r})$. We further include electromagnetic interactions by substituting $\mathbf{p}\to\mathbf{p}_c+e\mathbf{A}$ with the canonical momentum $\mathbf{p}_c=-i\hbar\nabla$. The above matrix representation assumes the basis order $\{|A\uparrow\rangle,|A\downarrow\rangle,|B\uparrow\rangle,|B\downarrow\rangle\}$, where A labels the electrons, B the positrons and the arrow the spin z-component. It becomes obvious, that the mixing of the different spin species occurs only due to the coupling of electrons and positrons. In the following, we apply Löwdin perturbation theory (cf. App. 1.A) to derive an effective Hamiltonian $\widetilde{\mathcal{H}}_A$ for the electrons that perturbatively includes the spin mixing.

At rest, the electron and positron branches are separated by the energy gap $\Delta=2m_0c^2$. In the non-relativistic limit, this gap largely exceeds the kinetic energy and we may decompose the Dirac Hamiltonian as

$$\mathcal{H}^0=\beta\,m_0c^2, \tag{1.2}$$
$$\mathcal{H}'=c\,\boldsymbol{\alpha}\cdot\mathbf{p}+V\,\mathbb{1}_{4\times4}, \tag{1.3}$$

where $\mathcal{H}'$ constitutes a small perturbation to $\mathcal{H}^0$. Since $\mathcal{H}^0$ is diagonal in the given basis, the effective Hamiltonian $\widetilde{\mathcal{H}}_A$ for the electrons yields in third-order Löwdin perturbation theory, according to Eqs. (1.A.3)-(1.A.6),

$$\widetilde{\mathcal{H}}_A = \mathcal{H}_A^{(0)} + \mathcal{H}_A^{(1)} + \mathcal{H}_A^{(2)} + \mathcal{H}_A^{(3)}, \tag{1.4}$$

with

$$\mathcal{H}_A^{(0)} = m_0 c^2 \, \mathbb{1}_{2\times 2}, \tag{1.5}$$

$$\mathcal{H}_A^{(1)} = V \, \mathbb{1}_{2\times 2}, \tag{1.6}$$

$$\mathcal{H}_A^{(2)} = \frac{\mathbf{p}^2}{2m_0} \, \mathbb{1}_{2\times 2} + \frac{e\hbar}{2m_0} \boldsymbol{\sigma} \cdot \mathbf{B}, \tag{1.7}$$

$$\mathcal{H}_A^{(3)} = \frac{e\hbar^2}{8m^2c^2} \nabla \cdot \boldsymbol{\mathcal{E}} \, \mathbb{1}_{2\times 2} - \frac{e\hbar}{4m^2c^2} \boldsymbol{\sigma} \cdot (\mathbf{p} \times \boldsymbol{\mathcal{E}}), \tag{1.8}$$

where $\mathbf{B} = \nabla \times \mathbf{A}$ is the magnetic field associated with the vector potential $\mathbf{A}$ and $\boldsymbol{\mathcal{E}} = \frac{1}{e}\nabla V$ the internal electric field.

Including terms up to second-order gives rise to the *Pauli equation*,[1] which extents the (non-relativistic) Schrödinger equation by taking into account the interaction of the electron spin with an external electromagnetic field [69]. Responsible for this coupling is the second term in $\mathcal{H}_A^{(2)}$, which is denoted as *Zeeman term*. It underlines the close relation of the electron spin $\boldsymbol{S}$ and the magnetic moment $\boldsymbol{\mu}$, which becomes obvious through the substitution $\boldsymbol{\mu} = -g\mu_B \boldsymbol{S}/\hbar$ and $\mathbf{S} = \frac{\hbar}{2}\boldsymbol{\sigma}$, where $\mu_B = \frac{e\hbar}{2m_0}$ is the Bohr magneton and $g \approx 2$ the electron g-factor. It is common practice to rewrite the SOC term as Zeeman term with an effective momentum-dependent magnetic field $\mathbf{B}_{\text{eff}}$ and a modified effective g-factor. Third-order relativistic corrections include the Darwin term and the SOC term, the first and second term in $\mathcal{H}_A^{(3)}$, respectively. These two terms reflect the non-commutativity of $\mathbf{p}$ and V, that is, $[\mathbf{p}, V] = -ie\hbar\boldsymbol{\mathcal{E}}$ [70]. The Darwin term is related to the *Zitterbewegung* of the relativistic electron and is relevant in the fine structure of s-type atomic orbitals [71]. Our major interest concerns the second term in $\mathcal{H}_A^{(3)}$, which represents the SOC and will be labeled by $\mathcal{H}_{\text{so}}$ hereafter. For convenience, we will frequently rewrite it in terms of a *spin-orbit field* (SOF) $\boldsymbol{\Omega}(\mathbf{k})$ with $\mathbf{k} = \mathbf{p}/\hbar$, that is,

$$\mathcal{H}_{\text{so}} = \boldsymbol{\Omega}(\mathbf{k}) \cdot \boldsymbol{\sigma}. \tag{1.9}$$

As previously mentioned, we are interested in the influence of atomic potentials, which means, in general, an average Coulomb field of the nuclei and the other electrons. For an approximately radial symmetric electrostatic potential $V(r) = -e\phi(r)$ and the according electric field $\boldsymbol{\mathcal{E}} = -(d\phi/dr)\,\mathbf{e}_r$, the SOC can be rewritten in terms of the orbital angular momentum $\mathbf{L}$ as

$$\mathcal{H}_{\text{so}} = -\frac{e\hbar}{4m_0^2c^2} \boldsymbol{\sigma} \cdot (\mathbf{p} \times \boldsymbol{\mathcal{E}})$$

[1] The rest energy is usually excluded.

$$
\begin{aligned}
&= -\frac{e\hbar}{4m_0^2c^2}\left(\frac{1}{r}\frac{d\phi}{dr}\right)\boldsymbol{\sigma}\cdot(\mathbf{r}\times\mathbf{p}) \\
&= \lambda\,\mathbf{S}\cdot\mathbf{L}, \qquad (1.10)
\end{aligned}
$$

with $\lambda = -\frac{e}{2m_0^2c^2}\frac{1}{r}\frac{d\phi}{dr}$. In this form, the coupling of the spin to the orbital angular momentum becomes obvious. Notably, the above expression can also be derived in classical relativistic electrodynamics by taking into account the Thomas precession [72].

Summarizing, we see that the intrinsic degree of freedom, the spin, emerges from the non-relativistic approximation to the Lorentz-invariant description of fermions in quantum mechanics. The resulting SOC Hamiltonian $\mathcal{H}_{\text{so}}$ is essential for describing the electronic band structure in a solid, which will be the task of the following section.

1.2 $\mathbf{k}\cdot\mathbf{p}$ Method and the Envelope Function Approximation

Beyond question, the most important material class for building data processing devices is the semiconductor. The fundamental property that distinguishes semiconductors from other materials is the small energy gap between conduction and valence band (typically $< 3\,\text{eV}$), which opens vast possibilities for external manipulation. A prime example of this is the transistor, which allows switching between a conducting and an insulation state by applying a gate voltage. Therefore, it is of central importance to have a sophisticated understanding of its unique band structure, which will be investigated in the following.

Several different methods have been developed to model the band structure in a semiconductor, such as the free electron model, the pseudopotential method, tight-binding or LCAO (Linear Combination of Atomic Orbitals) approach, or the $\mathbf{k}\cdot\mathbf{p}$ method. Each of these computation techniques involves approximations that tend to emphasize some aspect of the electronic properties while at the same time de-emphasizing others [73]. Most suitable for our purpose will be the $\mathbf{k}\cdot\mathbf{p}$ method and its generalization the Envelope Function Approximation (EFA). This method can deal with distinct geometries of quantum structures and perturbations such as magnetic fields, strain, and internal or external potentials. It provides a comprehensive analytical description of the band dispersion in the vicinity of a given $\mathbf{k}_0$-point in the Brillouin zone and pictures subtleties like non-parabolicity, spin splitting, and coupling between heavy and light hole-like states [70]. The obtained analytical expressions are related to optical matrix elements and energy gaps, which can be directly extracted from experiments. Usually, the expansion point $\mathbf{k}_0$ corresponds to a high-symmetry point in the Brillouin zone, which allows taking advantage of symmetry properties of the crystal lattice. Thereby, the number of contributing input parameters can be significantly reduced [16]. The physics of semiconductors is predominantly determined by the states close to the band extrema. In direct bandgap semiconductors, which are important for spintronics, such as GaAs, InAs,

or InSb, the valence band maximum, and the conduction band minimum are located at the Γ-point, i.e., $\mathbf{k}_0 = 0$, which is, therefore, the relevant symmetry point to determine many properties of the materials [74].

The Schrödinger equation for Bloch electrons in the microscopic lattice-periodic potential $V_0(\mathbf{r})$ in absence of any fields forms the basis of both the $\mathbf{k}\cdot\mathbf{p}$ theory and the EFA. For the Bloch functions $\Psi_{\nu\mathbf{k}}(\mathbf{r}) = e^{i\mathbf{k}\cdot\mathbf{r}}\, u_{\nu\mathbf{k}}(\mathbf{r})$, it reads as

$$\left[\frac{p^2}{2m_0} + V_0(\mathbf{r})\right] \Psi_{\nu\mathbf{k}}(\mathbf{r}) = E_\nu(\mathbf{k})\, \Psi_{\nu\mathbf{k}}(\mathbf{r}), \tag{1.11}$$

where $u_{\nu\mathbf{k}}(\mathbf{r}) = \langle \mathbf{r}|\nu\mathbf{k}\rangle$ is the lattice-periodic part, $\mathbf{k}$ the wave vector, ν the band index, and m_0 the free electron mass. The principle idea now consists of expanding the lattice periodic part $|\nu\mathbf{k}\rangle$ in terms of known band edge functions $\{|\nu\mathbf{k}_0\rangle\}$, which constitute a complete orthonormal basis. In the following, we give a brief description of the EFA formalism, which is more general than the $\mathbf{k}\cdot\mathbf{p}$ approach as it also accounts for spatial dependent fields. A consideration of these fields is, for instance, essential to explain the Rashba spin splitting in inversion-asymmetric quantum wells, an effect that is of central importance in this work.

From here on, let us consider a semiconductor crystal lattice in the presence of electric and magnetic fields that modulate slowly in comparison with the lattice constant. As shown in the previous section, the Schrödinger equation with relativistic corrections (disregarding the Darwin term and the rest energy) reads as

$$\left(\frac{\mathbf{p}^2}{2m_0} + V(\mathbf{r}) - \frac{\hbar}{4m_0^2c^2}\boldsymbol{\sigma}\cdot(\mathbf{p}\times\nabla V(\mathbf{r})) + \mu_B\boldsymbol{\sigma}\cdot\mathbf{B}\right)\Psi(\mathbf{r}) = E\,\Psi(\mathbf{r}), \tag{1.12}$$

where $\mathbf{p} = -i\hbar\nabla + e\mathbf{A}(\mathbf{r})$ denotes the *kinetic* momentum and $\mathbf{B} = \nabla\times\mathbf{A}(\mathbf{r})$ the magnetic field with the according vector potential $\mathbf{A}(\mathbf{r})$. The potential $V = V_0 + V_1$ is composed of the lattice-periodic potential $V_0(\mathbf{r})$ and an additional potential $V_1(\mathbf{r})$, which typically results from built-in or external electric fields as well as step-like potentials[2] due to the position-dependent band edges in heterostructures. Since the strong Coulomb potential V_0 in the vicinity of the atomic core region largely exceeds V_1, we can drop the latter in the SOC term. As mentioned above, we expand the wave functions in terms of band edge functions including the spin degree of freedom $|\sigma'\rangle$, that is,

$$\Psi(\mathbf{r}) = \sum_{\nu',\sigma'} \phi_{\nu',\sigma'}(\mathbf{r}) u_{\nu'0}(\mathbf{r})\,|\sigma'\rangle\,, \tag{1.13}$$

where we set $\mathbf{k}_0 = 0$. The expansion coefficients $\phi_{\nu',\sigma'}(\mathbf{r})$ comprise the slowly varying spatial dependence of V_1 and $\mathbf{A}$ and are called *envelope functions*. By way of illustration, we sketch a wave function $\Psi(\mathbf{r})$ in Fig. 1.1, which might appear in a

[2] The inclusion of step-like potentials appears here to be a violation of the requirement for a slowly modulating potential. Yet, the excellent agreement of the theoretical predictions with the experimental results justifies the application of EFA also in such scenarios [74].

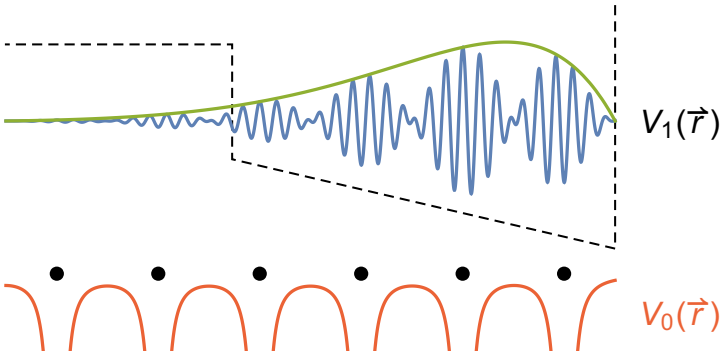

Fig. 1.1: Illustration of a possible wave function obtained in EFA. The green line depicts the slowly varying envelope function, whereas the blue line shows the full wave function including the quickly oscillating lattice-periodic part. The black dots represent the atomic cores with the corresponding potential V_0 (red). The black dashed line depicts the potential V_1, which could occur in a similar way in a heterostructure.

similar fashion in a heterostructure. Substituting the Ansatz above into Eq. (1.12), multiplying $\langle\sigma|\, u^*_{\nu' 0}(\mathbf{r})$ from the left, and integrating over one lattice unit cell, where we may treat V_1, $\mathbf{A}$, and $\phi_{\nu',\sigma'}$ as constants due to their negligible spatial modulation in contrast to $u_{\nu' 0}$, we obtain

$$\sum_{\nu',\sigma'} \Bigg\{ \left[E_{\nu'}(0) + \frac{\mathbf{p}^2}{2m_0} + V_1(\mathbf{r}) \right] \delta_{\nu\nu'}\delta_{\sigma\sigma'} + \frac{\mathbf{p}}{m_0}\cdot\mathbf{P}^{\nu\nu'}_{\sigma\sigma'} + \Delta^{\nu\nu'}_{\sigma\sigma'} + \mu_B \boldsymbol{\sigma}_{\sigma\sigma'}\cdot\mathbf{B} \Bigg\} \phi_{\nu',\sigma'}(\mathbf{r}) = E\,\phi_{\nu,\sigma}(\mathbf{r}), \tag{1.14}$$

where $\boldsymbol{\sigma}_{\sigma\sigma'} = \langle\sigma|\boldsymbol{\sigma}|\sigma'\rangle$ and

$$\mathbf{P}^{\nu\nu'}_{\sigma\sigma'} = \langle\nu\sigma|\mathbf{p}_c + \frac{\hbar}{4m_0^2c^2}\,(\boldsymbol{\sigma}\times\nabla V_0(\mathbf{r}))|\nu'\sigma'\rangle\,, \tag{1.15}$$

$$\Delta^{\nu\nu'}_{\sigma\sigma'} = \frac{\hbar}{4m_0^2c^2}\,\langle\nu\sigma|\mathbf{p}_c\cdot(\boldsymbol{\sigma}\times\nabla V_0(\mathbf{r}))|\nu'\sigma'\rangle\,, \tag{1.16}$$

with $|\nu'\sigma'\rangle := |\nu'\mathbf{0}\rangle\otimes|\sigma'\rangle$, the canonical momentum $\mathbf{p}_c = -i\hbar\nabla$,and the Kronecker symbol δ_{ij} [70]. Obviously, both matrix elements $\mathbf{P}^{\nu\nu'}_{\sigma\sigma'}$ and $\Delta^{\nu\nu'}_{\sigma\sigma'}$ lead to a coupling of the band edge states. In most cases, though, the momentum contribution in $\mathbf{P}^{\nu\nu'}_{\sigma\sigma'}$ is much larger than the term due to SOC and we can set $\mathbf{P}^{\nu\nu'}_{\sigma\sigma'} = \mathbf{P}_{\nu\nu'}\delta_{\sigma\sigma'}$. The SOC matrix elements $\Delta^{\nu\nu'}_{\sigma\sigma'}$ lift the degeneracy even at the band edge. For instance, at the Γ-point the valence band of a diamond or zinc-blende semiconductor is sixfold degenerate without SOC and otherwise fourfold degenerate (including spin).

In absence of V_1 and $\mathbf{A}$, the spatial dependence of the envelope functions is simply given by plane waves, i.e., $\phi_{\nu',\sigma'}(\mathbf{r}) \propto \exp(i\mathbf{k}\cdot\mathbf{r})$. Noting this, we can derive an equation analogous to Eq. (1.14), where the momentum operator $\mathbf{p}$ is replaced by the plane wave vector $\mathbf{k}$ and which describes the $\mathbf{k}\cdot\mathbf{p}$ Hamiltonian. Remarkably,

in the chosen representation both the EFA and the $\mathbf{k}\cdot\mathbf{p}$ Hamiltonian matrix are characterized by the momentum and SOC matrix elements $\mathbf{P}^{\nu\nu'}_{\sigma\sigma'}$, $\Delta^{\nu\nu'}_{\sigma\sigma'}$, as well as the band edge energy gaps $E_{\nu'}(0)$. Advantageously, from symmetry analysis, it turns out that many of the matrix elements vanish [74]. The remaining parameters are, in practice, considered as purely phenomenological and directly extracted from experimental data.

In principle, Eq. (1.14) constitutes an infinite dimensional eigenvalue problem. However, as it was first noticed by Kane [75], the essential physical features are already captured within a few consecutive bands, below and above the fundamental band gap. The finite-dimensional Hamiltonian can then be further reduced by means of Löwdin perturbation theory (cf. App. 1.A). In second order, the momentum matrix elements lead to a significant correction to the free electron mass, the effective mass. Similar as in the derivation of the SOC Hamiltonian from the Dirac equation in the previous section, the non-commutativity of the momentum and position operator yields further considerable consequences. In particular, the momentum components in presence of a magnetic field do not commute, i.e., $\mathbf{p}\times\mathbf{p} = -ie\hbar\mathbf{B}$, and produce thereby additional magnetic field contributions, which can be condensed in an effective g-factor. In general, both effective mass and effective g-factor become tensorial quantities. More important for our purpose is the non-commutativity of the momentum operator and the slowly-varying potential $V_1(\mathbf{r})$, i.e., $[\mathbf{p}, V_1(\mathbf{r})] = -ie\hbar\boldsymbol{\mathcal{E}}_1(\mathbf{r})$ with $\boldsymbol{\mathcal{E}}_1(\mathbf{r}) = \frac{1}{e}\nabla V_1(\mathbf{r})$. Together with the SOC matrix elements $\Delta^{\nu\nu'}_{\sigma\sigma'}$, it gives rise to the Rashba SOC in the bulk [70]. From this, it becomes clear that the $\mathbf{k}\cdot\mathbf{p}$ method is insufficient to describe the Rashba SOC since the non-commuting quantities do not appear. We will discuss the appearance of the Rashba effect in more detail in the subsequent section, Sec. 1.4.3.

To develop a more elaborate understanding, we introduce, hereafter, an important paradigmatic model Hamiltonian, which works in such a reduced Hilbert space, the *Extended Kane Model*. In accordance with our primary interest in this thesis, it focuses on the important class of diamond and zinc-blende type semiconductors. Yet, other important lattice types, such as the wurtzite lattice, can be treated analogously [76]. Also, since magnetic field effects in this work play a limited role, we will disregard them in the following sections. Due to the close similarity between the $\mathbf{k}\cdot\mathbf{p}$ and the EFA Hamiltonian, we follow the common practice and replace the wave vector in the $\mathbf{k}\cdot\mathbf{p}$ formulation by an operator whenever spatial-dependent potentials V_1 are present [70].

1.3 Extended Kane Model

The symmetry at the band extrema takes a crucial role in setting up an appropriate model. Elemental semiconductors such as Si or Ge typically have a diamond lattice, whose unit cell is a face centered cubic (fcc) with two basis atoms (cf. Fig. 1.2a). In the reciprocal space, which plays a key role in the analysis of periodical structures, this fcc structure becomes a body centered cubic (bcc) [77]. Its first Brillouin zone is displayed in Fig. 1.10a. Compound III-V semiconductors, such as GaAs,

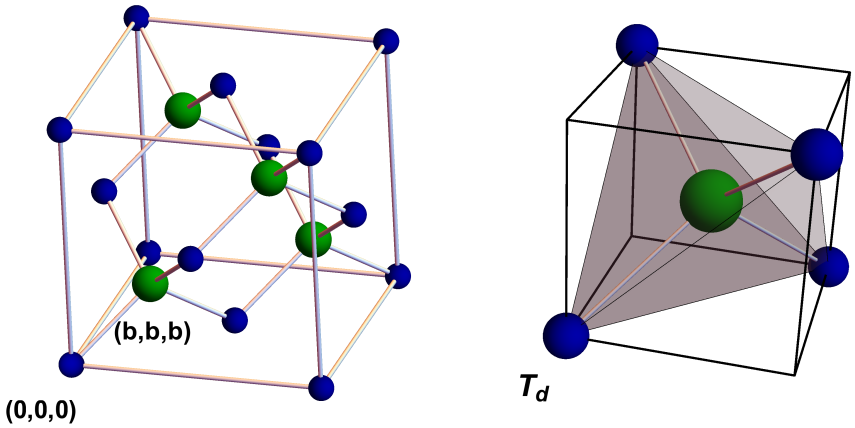

(a) **(b)**

Fig. 1.2: The graphic (a) displays the diamond structure of the cubic (fcc) lattice with two basis atoms located at $(0,0,0)$ and (b,b,b), where $b = 1/4\,a$ and a is the side length of the cube. These basis atoms are identical for diamond and distinct for zinc-blende. Figure (b) pictures the tetrahedral symmetry of the zinc-blende structure.

crystallize in zinc-blende structure, which differs from the diamond structure by having two distinct basis atoms [77]. Semiconductors with a diamond lattice belong to the point group O_h of the cube, whereas zinc-blende structure has symmetry of point group T_d of the tetrahedron, which has lower symmetry than the cube [78]. To obtain O_h from T_d, one needs to add inversion symmetry, labeled by the group element C_i, that is, $O_h = T_d \otimes C_i$ [70]. Since the point group of the cube is a subgroup of the group R of arbitrary rotations, one can generally split the Hamiltonian of a zinc-blende crystal into [70]

$$\mathcal{H} = \mathcal{H}_{\text{sphere}} + \mathcal{H}_{\text{cube}} + \mathcal{H}_{\text{tetrahedron}}. \tag{1.17}$$

Here, $\mathcal{H}_{\text{sphere}}$, $\mathcal{H}_{\text{cube}}$, and $\mathcal{H}_{\text{tetrahedron}}$ denote the spherical, cubic, and tetrahedral symmetric parts of the Hamiltonian $\mathcal{H}$ which transform according to R, O_h, and T_d, respectively. In spherical approximation $\mathcal{H} \approx \mathcal{H}_{\text{sphere}}$ the eigenstates of the Hamiltonian are eigenstates of the total angular momentum $\mathbf{J}^2$ and its z-component J_z or, correspondingly, the orbital angular momentum if SOC is absent. It describes well the energy spacing at the Γ-point. The other terms, $\mathcal{H}_{\text{cube}}$ and $\mathcal{H}_{\text{tetrahedron}}$, cause only small corrections [78]. The absence of the center of inversion in tetrahedral crystals leads to additional terms in the Hamiltonian, called Dresselhaus terms, that give rise to a momentum-dependent spin splitting. As the SOC usually constitutes a small perturbation, it is common to classify the bands according to the orbital wave functions in atomic physics (s, p, d-orbitals, etc.).

The Kane model describes the band structure in the vicinity of the Γ-point for diamond or zinc-blende type semiconductor materials. In the original version

of Kane, the topmost bonding p-like valence band edge states ($|X\rangle, |Y\rangle, |Z\rangle$) and the lowest s-like ($|S\rangle$) anti-bonding conduction band edge states were taken into account [75]. The extended Kane model also includes the p-like ($|X'\rangle, |Y'\rangle, |Z'\rangle$) anti-bonding conduction band edge states [79]. Couplings to other (remote) bands are incorporated by second-order perturbation theory (cf. App. 1.A) [70]. In most materials the p-like conduction band lies higher in energy than the s-like band. Yet, for some diamond semiconductors, such as Si, the order is reversed [74]. In absence of SOC, the corresponding states can be expressed in terms of orbital momentum eigenstates $|l, m_l\rangle$, with the orbital and magnetic quantum numbers, l and m_l, respectively. The quantization axis is commonly aligned with the [001] crystal axis. Using the standard phase convention of real-valued band edge states, we find the relations

$$|0,0\rangle = |S\rangle, \tag{1.18}$$
$$|1,1\rangle = -(|X\rangle + i|Y\rangle)/\sqrt{2}, \tag{1.19}$$
$$|1,0\rangle = |Z\rangle, \tag{1.20}$$
$$|1,-1\rangle = (|X\rangle - i|Y\rangle)/\sqrt{2}, \tag{1.21}$$

and equivalently for ($|X'\rangle, |Y'\rangle, |Z'\rangle$) [73].

However, if SOC is included the eigenbasis of $\mathbf{J}^2$, where $\mathbf{J}$ is the total angular momentum, is more suitable. More precisely, the SOC is most significant in the vicinity of the atomic cores, where the lattice potential V_0 is approximately spherically symmetric. Using this simplification, we can rewrite $\mathcal{H}_{so}$ as (cf. Sec. 1.1)

$$\mathcal{H}_{so} = \lambda\, \mathbf{S}\cdot\mathbf{L} \tag{1.22}$$
$$= \frac{\lambda}{2}(\mathbf{J}^2 - \mathbf{L}^2 - \mathbf{S}^2), \tag{1.23}$$

and treat λ as a phenomenological parameter [74]. Note that an eigenstate of $\mathbf{J}^2$ is simultaneously an eigenstate of $\mathbf{L}^2$, $\mathbf{S}^2$, J_z, L_z, and S_z with the corresponding quantum numbers j, l, s, m_j, m_l, and m_s, respectively. A mutual eigenstate is given by $|l, s, j, m_j\rangle$. Since $s = 1/2$ and the orbital angular momentum quantum number l determines the band, s-like ($l = 0$) or p-like ($l = 1$), it is common practice to label the basis vectors by specifying the band and the quantum numbers j and m_j [74]. These basis vectors are then expanded in terms of the band edge states $|j, m_j\rangle$ times spin eigenstates $|\sigma\rangle$, $\sigma \in \{\pm\}$, as

$$|1/2, \pm 1/2\rangle_c = |S\rangle \otimes |\pm\rangle, \tag{1.24}$$

for the Γ_{6c},

$$|3/2, \pm 3/2\rangle_{c/v} = \mp \frac{1}{\sqrt{2}}(|X\rangle \pm i|Y\rangle) \otimes |\pm\rangle, \tag{1.25}$$
$$|3/2, \pm 1/2\rangle_{c/v} = \frac{1}{\sqrt{6}}[2|Z\rangle \otimes |\pm\rangle + (\mp|X\rangle - i|Y\rangle) \otimes |\mp\rangle], \tag{1.26}$$

for the $\Gamma_{8c/8v}$, and

$$|1/2, \pm 1/2\rangle_{c/v} = -\frac{1}{\sqrt{3}}[\pm|Z\rangle \otimes |\pm\rangle + (|X\rangle \pm i\,|Y\rangle) \otimes |\mp\rangle], \tag{1.27}$$

for the $\Gamma_{7c/7v}$ conduction (c) and valence (v) bands [70, 73, 78]. Here, we used the conventional group theoretical notation. It classifies the bands according to the irreducible representations of the symmetry group of the crystal, which characterizes the transformation properties of the wave functions at the Γ-point [74]. By means of this basis, the resulting 14×14 Hamiltonian falls into blocks

$$\mathcal{H}_{14\times 14} = \begin{pmatrix} \mathcal{H}_{8c8c} & \mathcal{H}_{8c7c} & \mathcal{H}_{8c6c} & \mathcal{H}_{8c8v} & \mathcal{H}_{8c7v} \\ \mathcal{H}_{7c8c} & \mathcal{H}_{7c7c} & \mathcal{H}_{7c6c} & \mathcal{H}_{7c8v} & \mathcal{H}_{7c7v} \\ \mathcal{H}_{6c8c} & \mathcal{H}_{6c7c} & \mathcal{H}_{6c6c} & \mathcal{H}_{6c8v} & \mathcal{H}_{6c7v} \\ \mathcal{H}_{8v8c} & \mathcal{H}_{8v7c} & \mathcal{H}_{8v6c} & \mathcal{H}_{8v8v} & \mathcal{H}_{8v7v} \\ \mathcal{H}_{7v8c} & \mathcal{H}_{7v7c} & \mathcal{H}_{7v6c} & \mathcal{H}_{7v8v} & \mathcal{H}_{7v7v} \end{pmatrix}, \tag{1.28}$$

where each block represents one of the considered bands or the coupling between them [80]. Owing to symmetry, most of the momentum and SOC matrix elements, Eqs. (1.15) and (1.16), vanish. The remaining matrix elements are given by

$$P = \frac{\hbar}{m_0}\langle S|p_x|X\rangle\,, \tag{1.29}$$

$$P' = \frac{\hbar}{m_0}\langle S|p_x|X'\rangle\,, \tag{1.30}$$

$$Q = \frac{\hbar}{m_0}\langle X|p_y|Z'\rangle\,, \tag{1.31}$$

$$\Delta_0 = -\frac{3i\hbar}{4m_0^2c^2}\langle X|\,[(\nabla V_0)\times \mathbf{p}]_y\,|Z\rangle\,, \tag{1.32}$$

$$\Delta_0' = -\frac{3i\hbar}{4m_0^2c^2}\langle X'|\,[(\nabla V_0)\times \mathbf{p}]_y\,|Z'\rangle\,, \tag{1.33}$$

$$\Delta^- = -\frac{3i\hbar}{4m_0^2c^2}\langle X|\,[(\nabla V_0)\times \mathbf{p}]_y\,|Z'\rangle\,, \tag{1.34}$$

where P, Q, Δ_0 and Δ_0' are real and P' and Δ^- are purely imaginary [70].

In Fig. 1.3, the bulk band structure in the extended Kane model and the impact of the involved parameters is illustrated. While the matrix elements Δ_0 and Δ_0' only contain intraband coupling due to SOC, the elements P, P', Q, and Δ^- mix the distinct bands with each other. The SOC lifts the six-fold degeneracy of the p-like bands and splits them into two-fold degenerate bands with the total angular momentum $j = 3/2$ and four-fold degenerate bands with $j = 1/2$. The emerging gaps, Δ_0 for the valence band and Δ_0' for the higher conduction band, are called *spin-orbit gaps*. The Γ_{7v} valence band for $j = 1/2$ is frequently referred to as *split-off band*. Responsible for the distinct curvature within the Γ_8 bands are the

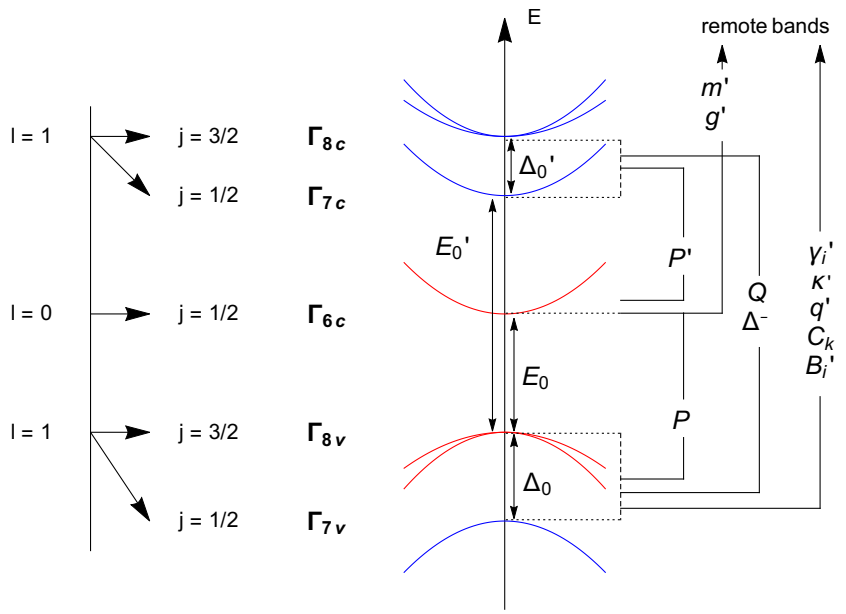

Fig. 1.3: Sketch of the band structure and the involved parameters at the Γ-point described by the extended Kane model. Values for the parameters are given in App. 1.C. The Γ_{6c} and the Γ_{8v} bands (red), are of particular interest in the subsequent part of this thesis.

momentum matrix elements P, P', and Q. Regarding Γ_{8v}, these arising bands are commonly distinguished as *heavy hole* (HH) and *light hole* (LH) band due to their different effective masses. Additional parameters occur, i.e., $\gamma_i', m', g', \kappa', q', C_k$, and B_i' ($i \in \{1, 2, 3\}$), that take into account contributions from the coupling to remote bands, which are not included in the model and are determined empirically. The prime indicates that these band parameters are *reduced*, which will be explained below. The γ_i' are called reduced *Luttinger parameters* and are crucial for the dispersion of HH and LH states. m' and g' are the reduced effective mass and g-factor. The parameters κ and q describe magnetic interactions. Furthermore, there are very small terms in the valence band with the prefactor C_k, that are linear in k. This prefactor is mainly produced by bilinear second-order perturbation terms, consisting of $\mathbf{k} \cdot \mathbf{p}$ and SOC interactions with remote Γ_3-like intermediate states [70, 81]. The factors B_i' occur only in the matrix elements between the valence and lowest conduction band, e.g., in $\mathcal{H}_{6c7v}$ and $\mathcal{H}_{6c8v}$. In diamond lattices the factors C_k, B_i', P', and Δ^- vanish as they are a result of the bulk inversion asymmetry. These factors produce a momentum-dependent spin splitting as will be discussed in Sec. 1.4.2. The full extended Kane Hamiltonian can be found in Refs. [70, 80, 82].

Besides the extended Kane model, there are a number of lower dimensional models that are frequently used, such as the 6×6 (8×8) Kane model, which takes into account the lowest conduction band Γ_{6c}, the Γ_{8v} (and the Γ_{7v}) valence

band.[3] The 4×4 Luttinger Hamiltonian includes the Γ_{8v} valence band and the 6×6 Luttinger Hamiltonian additionally the split-off band. All these models are formulated consistently, that is, couplings to other bands of the higher dimensional counterparts are included by second-order perturbation theory to $\mathcal{O}(k^3)$. Yet, the terms cubic in k are treated separately, in general, since they lead to spin splitting and are due to the lack of the inversion center only non-vanishing for zinc-blende lattices. As a consequence, each model yields the same dispersion up to $\mathcal{O}(k^2)$ for diamond and $\mathcal{O}(k^3)$ for zinc-blende structure, respectively. To this end, *reduced band parameters* m', g', γ_i', κ', q', and B_i' are introduced, where the second-order corrections must be subtracted depending on the dimension of the considered $\mathbf{k} \cdot \mathbf{p}$ model [70, 80]. Notably, the reduction takes into account the bulk band structure. In Ref. [8], it was shown that the correct reduction is problematic in case of a multisubband system when spatial confinement is present.

Hereafter, we investigate the Γ_{6c} conduction band and the Γ_{8v} valence band (cf. Fig. 1.3), which are mainly relevant for spintronics. Effective Hamiltonians can be obtained by Löwdin perturbation theory from the extended Kane model. We pay particular attention to the spin splitting as a consequence of inversion-symmetry breaking.

1.4 Effective Electron and Hole Hamiltonian

The physics in a semiconductor is governed by states near the fundamental band gap that separates conduction and valence band. These states are occupied by free carriers that are made available through doping and/or thermal, optical, or electrical excitations.[4] Starting from the extended Kane model, introduced in the previous section, we can derive an effective model Hamiltonian, which characterizes the dispersion in the lowest conduction band and the topmost valence band in the bulk, Γ_{6c} and Γ_{8v} (cf. Fig. 1.3), respectively. Following the standard procedure, using group theoretical methods, the obtained expressions are sorted in terms of invariants [73, 83, 84]. The expansion coefficients are functions of the band parameters of the extended Kane model. This leads to a rescaling of the mass of electrons as well as heavy and light holes. If the inversion symmetry is broken, additional terms arise that mix the different spin states. The relevant SOC terms are identified in Secs. 1.4.2 and 1.4.3.

The approach is formally analogous to the perturbative study of relativistic electrons (cf. Chap. 1.1). In both situations the small expansion coefficients depend essentially on the fundamental energy gap. Yet, comparing the energy scales, it becomes obvious that the impact in the semiconductor is far more dramatic. While the electron and positron branches are separated by their rest energy $2m_0c^2 \approx 1\,\mathrm{MeV}$, the band gap in a semiconductor E_0 is merely of the order of $1\,\mathrm{eV}$. From this follows that relativistic effects in a semiconductor play a considerable role.

[3] The explicit form of the 6×6 Kane model is given in the appendix (Tab. 1.2).

[4] Optically excited carriers usually form an electron-hole pair, called *exciton*. Depending on the physical situations, it can be justified to treat electrons or holes individually.

1.4.1 Centrosymmetric Crystals

Considering a crystal with a center of inversion, the effective Hamiltonian describing the bulk electrons of Γ_{6c} conduction band is written as

$$\mathcal{H}_{6c6c} = \frac{\hbar^2 k^2}{2m^*} \mathbb{1}_{2\times 2} \tag{1.35}$$

with the effective electron mass m^*, which is related to the reduced effective electron m' mass via [70]

$$\frac{1}{m^*} = \frac{1}{m'} + \frac{2P^2}{3\hbar^2}\left(\frac{2}{E_0} + \frac{1}{E_0 + \Delta_0}\right), \tag{1.36}$$

up to second order in Löwdin perturbation theory. If couplings to remote bands are neglected, the reduced mass coincides with the free electron mass m_0 [75]. It turns out that the momentum parameter P is of comparable size for the different materials. Thus, the effective mass is primarily determined by the size of the fundamental energy gap E_0. For most materials, it is 1-2 orders of magnitude smaller than the free electron mass. While the Hamiltonian yields a spherical symmetric dispersion for the electrons, this does not apply for the holes in the Γ_{8v} valence band.

Analogously, the bulk Hamiltonian for the fourfold degenerate Γ_{8v} valence band of a diamond lattice is derived in second-order Löwdin perturbation theory. This model was first proposed by J. M. Luttinger and is, therefore, named *Luttinger Hamiltonian* [85]. Choosing $\hat{x} \parallel [100]$, $\hat{y} \parallel [010]$, and $\hat{z} \parallel [001]$, it reads as

$$\begin{aligned}\mathcal{H}_{8v8v} = -\frac{\hbar^2}{2m_0}\Big\{&\gamma_1 \mathbf{k}^2 - 2\gamma_2\left[\left(J_x^2 - \frac{1}{3}J^2\right)k_x^2 + \text{c.p.}\right] \\ &- 4\gamma_3\left[\{J_x, J_y\}_{(s)}\{k_x, k_{,y}\}_{(s)} + \text{c.p.}\right]\Big\},\end{aligned} \tag{1.37}$$

where c.p. stands for cyclic permutation of the preceding indices and $\{A, B\}_{(s)} = (AB+BA)/2$ is the symmetrized anti-commutator, following the notation of Ref. [70]. The total angular momentum matrices J_i ($i \in \{x, y, z\}$) for $j = 3/2$ are listed in App. 1.B. The Hamiltonian refers to the terms $\mathcal{H}_{\text{sphere}} + \mathcal{H}_{\text{cube}}$ in Eq. (1.17) and since the sphere is a subgroup of the cube, it has cubic symmetry. This symmetry is reflected in the altered band curvature, called *band warping*, of the Fermi contours, which is depicted in Fig. 1.4. The band warping is proportional to the difference between γ_3 and γ_2 since the dispersion along [100], [110] and [111] is found as

$$E_{\text{LH/HH}}^{[100]} = -\frac{\hbar^2}{2m_0}\left(\gamma_1 \pm 2\gamma_2\right) k_{[100]}^2, \tag{1.38}$$

$$E_{\text{LH/HH}}^{[110]} = -\frac{\hbar^2}{2m_0}\left(\gamma_1 \pm \sqrt{\gamma_2^2 + 3\gamma_3^2}\right) k_{[110]}^2, \tag{1.39}$$

$$E_{\text{LH/HH}}^{[111]} = -\frac{\hbar^2}{2m_0}\left(\gamma_1 \pm 2\gamma_3\right) k_{[111]}^2, \tag{1.40}$$

where the upper sign corresponds to LH and the lower to HH states. Hence, in *spherical* (in three dimensions) or so-called *axial approximation* (in two dimensions) the Luttinger Hamiltonian is often simplified by setting $\gamma_2 = \gamma_3 = \tilde{\gamma} := (2\gamma_2 + 3\gamma_3)/5$, which corresponds to, $\mathcal{H}_{8v8v} \approx \mathcal{H}_{\text{sphere}}$ [86]. The above equations are particularly useful for determining the Luttinger parameters experimentally [82]. In accordance with the effective mass for electrons, the Luttinger parameters follow the relations [70, 80]

$$\gamma_1 = \gamma_1' + \frac{2m_0}{3\hbar^2}\left(\frac{P^2}{E_0} + \frac{Q^2}{E_0' + \Delta_0'} + \frac{Q^2}{E_0'}\right), \tag{1.41}$$

$$\gamma_2 = \gamma_2' + \frac{m_0}{3\hbar^2}\left(\frac{P^2}{E_0} - \frac{Q^2}{E_0'}\right), \tag{1.42}$$

$$\gamma_3 = \gamma_3' + \frac{m_0}{3\hbar^2}\left(\frac{P^2}{E_0} + \frac{Q^2}{E_0'}\right). \tag{1.43}$$

The reduced Luttinger parameters in absence of remote band contributions yield $\gamma_1' = -1$ and $\gamma_2' = \gamma_3' = 0$ [73, 80]. Remarkably, within this approximation, we obtain

$$\gamma_3 - \gamma_2 = \frac{2m_0 Q^2}{3\hbar^2 E_0'}. \tag{1.44}$$

Since $P > Q$ and $P, Q \in \mathbb{R}$, we find the generic relations $\gamma_3 > \gamma_2$ and $\gamma_2 \wedge \gamma_3 > 0$. This observation is in agreement with the experimental results (cf. Tab. 1.17 or Ref. [87]) and will become important in Chap. 5 when searching for realistic parameter configurations, that allow for a conserved spin quantity in two-dimensional hole systems.

The following two subsections are devoted to the effect of spin splitting due to inversion asymmetry, which is the essential ingredient for controlling the spin rotation and, at the same time, the source of the D'yakonov-Perel' spin relaxation mechanism.

1.4.2 Bulk Inversion Asymmetry

As stated by *Kramers' Theorem*, double spin-degeneracy for spin-1/2 particles is a direct consequence of the mutual interplay between time and space inversion symmetry [88]. Both symmetry operations reverse the wave vector $\mathbf{k} \to -\mathbf{k}$, while the time inversion also flips the spin [74]:

$$\left.\begin{array}{ll} \text{time-reversal symmetry} & \Rightarrow\ E_\uparrow(\mathbf{k}) = E_\downarrow(-\mathbf{k}) \\ \text{space reversal symmetry} & \Rightarrow\ E_\uparrow(\mathbf{k}) = E_\uparrow(-\mathbf{k}) \end{array}\right\} \Rightarrow\ E_\uparrow(\mathbf{k}) = E_\downarrow(\mathbf{k}).$$

Therefore, the single-particle energies are only degenerate if both symmetries are fulfilled. The first symmetry can be broken by the application of an external magnetic field $\mathbf{B}$, which leads to the Zeeman spin splitting. The spatial inversion symmetry depends on the material and is satisfied for semiconductors with diamond

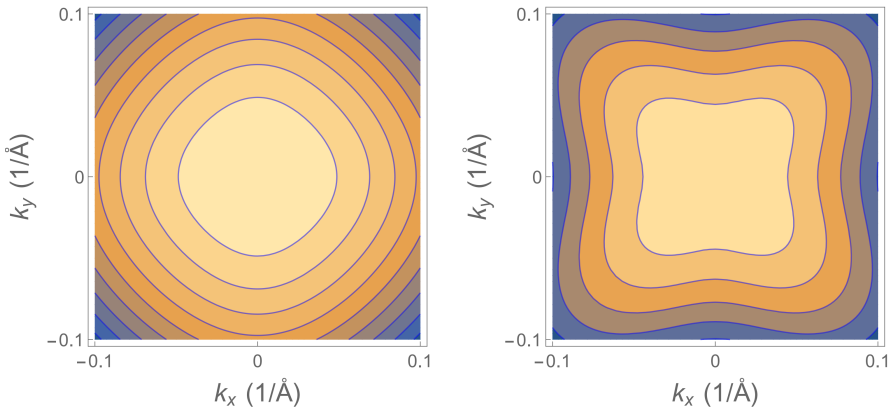

(a) Heavy Hole (b) Light Hole

Fig. 1.4: Equal-energy contours of the Γ_{8v} valence bands of GaAs at $k_z = 0$ in order to emphasize the band warping. The innermost contours correspond to the energy (a) $E = -20\,\text{meV}$ and (b) $E = -100\,\text{meV}$. Band parameters are taken from Ref. [70]

structure. In a zinc-blende crystal, however, there is no center of inversion due to the two distinct basis atoms. Commonly it is said that these crystals possess *bulk inversion asymmetry* (BIA). As a consequence, the double spin-degeneracy is lifted in zinc-blende crystals even for $\mathbf{B} = 0$.

Regarding the extended Kane model, the non-vanishing parameters P', Δ^-, B_i', and C_k are a result of the BIA. In Fig. 1.5 the BIA spin splitting in the extended Kane model is shown for GaAs along different crystallographic axes. For symmetry reasons, there is no BIA spin splitting along $\mathbf{k} \parallel [100]$ and $\mathbf{k} \parallel [111]$. If a smaller model is used, the BIA contribution is included by means of third-order perturbation theory to $\mathcal{O}(k^3)$ [70]. The resulting terms $\mathcal{H}^{\text{BIA}}$ are known as *Dresselhaus* SOC [89] and correspond to the correction $\mathcal{H}_{\text{tetrahedron}}$ in Eq. (1.17). For the Γ_{6c} conduction band and the Γ_{8v} valence band, one finds [70]

$$\mathcal{H}^{\text{BIA}}_{6c6c} = b^{6c6c}_{41}(\{k_x, k_y^2 - k_z^2\}_{(s)}\sigma_x + \text{c.p.}), \tag{1.45}$$

$$\begin{aligned}\mathcal{H}^{\text{BIA}}_{8v8v} = {} & \frac{2}{\sqrt{3}} C_k (k_x \{J_x, J_y^2 - J_z^2\}_{(s)} + \text{c.p.}) \\ & + b^{8v8v}_{41}(\{k_x, k_y^2 - k_z^2\}_{(s)} J_x + \text{c.p.}) \\ & + b^{8v8v}_{42}(\{k_x, k_y^2 - k_z^2\}_{(s)} J_x^3 + \text{c.p.}) \\ & + b^{8v8v}_{51}(\{k_x, k_y^2 - k_z^2\}_{(s)} \{J_x, J_y^2 - J_z^2\}_{(s)} + \text{c.p.}) \\ & + b^{8v8v}_{52}(k_x^3 \{J_x, J_y^2 - J_z^2\}_{(s)} + \text{c.p.}).\end{aligned} \tag{1.46}$$

It includes a k-linear term proportional to C_k, which is very small for realistic materials [70, 81] and therefore often ignored [7, 90–92]. Values for the SOC coef-

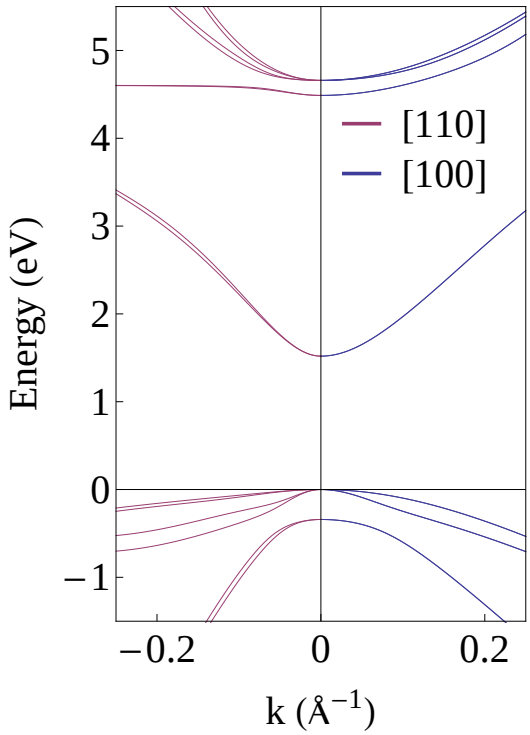

Fig. 1.5: Bulk dispersion in the extended Kane Model for GaAs and different crystallographic directions using the band parameters from Ref. [70]. There is no BIA spin splitting along [100].

ficients are listed in Tab. 1.18. Aside from that, all corrections are cubic in k and each prefactor is proportional to the product $PP'Q$.[5] As a consequence, the BIA spin splitting has the same order of magnitude for electrons as for holes. Since holes typically have larger effective masses, the SOC becomes more important for holes, though [70].

An exemplary comparison of the cubic contributions in the valence band in App. 5.A.1 shows that in a bulk system the term proportional to b_{41}^{8v8v} is the most relevant one. It should nevertheless be noted that there are discrepancies in the perturbative determination of the coefficients b_i^{8v8v} as outlined in App. 5.A.1. More importantly, due to quantum confinement, strain, or interface effects, the relative importance of the respective contribution can alter significantly. We will address this subject in more detail in Chap. 5.

1.4.3 Structure Inversion Asymmetry

As it was first observed by Bychkov and Rashba [93, 94], an alternative path to lifted spin-degeneracy lies in the introduction of *structure inversion asymmetry* (SIA). This can be achieved by an asymmetric potential due to, e.g., heterointerfaces or electrical gating. Therefore, it provides an external control, which makes it particularly attractive for applications in spintronics.

The most rudimentary model, that allows studying the impact of a potential of

[5] In the lower dimensional Kane models, which exclude the Γ_{7c} conduction band, the parameters B_i' take over the role of P' and Δ^-.

this sort, considers a linear potential of the form

$$V_1(\mathbf{r}) = e\boldsymbol{\mathcal{E}} \cdot \mathbf{r}, \tag{1.47}$$

where $\boldsymbol{\mathcal{E}}$ denotes the electric field. Including this expression in the Hamiltonian of the extended Kane model, we can compute the corrections to the $\mathcal{H}_{6c6c}$ and $\mathcal{H}_{8v8v}$ blocks by means of Löwdin perturbation theory. Analogously to the perturbative study of the electron branch in the Dirac Hamiltonian (cf. Chapt. 1.1), we obtain in third order additional terms due to the non-commutativity of the momentum and position operators. The resulting expressions are called *Rashba* SOC and read as [70]

$$\mathcal{H}_{6c6c}^{\mathrm{SIA}} = r_{41}^{6c6c}[(k_y\mathcal{E}_z - k_z\mathcal{E}_y)\sigma_x + \text{c.p.}], \tag{1.48}$$

$$\begin{aligned}\mathcal{H}_{8v8v}^{\mathrm{SIA}} = {} & r_{41}^{8v8v}[(k_y\mathcal{E}_z - k_z\mathcal{E}_y)J_x + \text{c.p.}] \\ & + r_{42}^{8v8v}[(k_y\mathcal{E}_z - k_z\mathcal{E}_y)J_x^3 + \text{c.p.}] \\ & + r_{51}^{8v8v}[\mathcal{E}_x\{J_y, J_z\}_{(s)} + \text{c.p.}] \\ & + r_{52}^{8v8v}[(k_y\mathcal{E}_z + k_z\mathcal{E}_y)\{J_x, J_y^2 - J_z^2\}_{(s)} + \text{c.p.}].\end{aligned} \tag{1.49}$$

Comparing empirical values for the coefficients of the valence band invariants (cf. Tab. 1.19), we find that r_{41}^{8v8v} is clearly dominating. The underlying reason for this is that r_{41}^{8v8v} (as same as r_{41}^{6c6c}) is mainly defined through the coupling of the Γ_{8v} to the adjacent Γ_{6c} band, whereas the remaining terms require the coupling to the further distant Γ_{8c} and Γ_{7c} conduction bands [70]. The Rashba Hamiltonian of the conduction band as well as the leading invariant in the valence band have axial symmetry, where the symmetry axis is given by the orientation of the electric field. Both terms have a strong resemblance with the SOC Hamiltonian for the relativistic electrons (cf. Eq. (1.8)), which becomes obvious when rewriting $\mathcal{H}_{6c6c}^{\mathrm{SIA}} = r_{41}^{6c6c}\boldsymbol{\sigma} \cdot (\mathbf{k} \times \boldsymbol{\mathcal{E}})$ and $\mathcal{H}_{8v8v}^{\mathrm{SIA}} \approx r_{41}^{8v8v}\mathbf{J} \cdot (\mathbf{k} \times \boldsymbol{\mathcal{E}})$. Their impact on the band dispersion is depicted in Fig. 1.6.

The Rashba SOC in the conduction band lies the foundation for the prominent device concept of the *Datta-Das spin field-effect transistor* (cf. Fig. 1) [13]. It is based on the spin precession due to Rashba SOC of conduction electrons in a ballistic semiconductor. The spin-rotation angle is externally controlled by a gate-induced electric field. Assuming an electric field $\boldsymbol{\mathcal{E}} = (0, 0, \mathcal{E}_z)^\top$, we can rewrite the Rashba Hamiltonian in terms of a SOF, i.e., $\mathcal{H}_{6c6c}^{\mathrm{SIA}} = \boldsymbol{\Omega}(\mathbf{k}) \cdot \boldsymbol{\sigma}$, where $\boldsymbol{\Omega}(\mathbf{k}) = \alpha_{\mathrm{R}}(k_y, -k_x, 0)$ with $\alpha_{\mathrm{R}} = r_{41}^{6c6c}\mathcal{E}_z$. The spin orientation of the corresponding eigenstates is (anti)parallel to the SOF, which is shown in Fig. 1.6(a). For the sake of simplicity, we focus now on the propagation along the x-axis, i.e., $k_y = k_z = 0$ and $k = |k_x|$. The energy dispersion for a periodic boundary condition is given by

$$E_\pm(k_x) = \frac{\hbar^2 k^2}{2m^*} \pm \alpha_{\mathrm{R}} k, \tag{1.50}$$

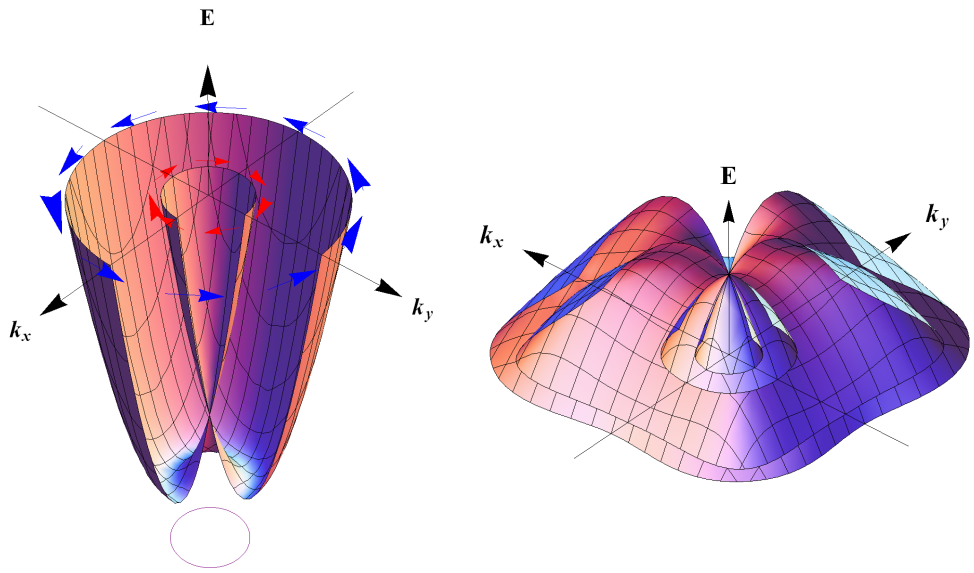

(a) Γ_{6c} conduction band **(b)** Γ_{8v} valence band

Fig. 1.6: Dispersion in presence of Rashba SOC for $k_z = 0$ and $\boldsymbol{\mathcal{E}} = (0, 0, \mathcal{E}_z)^\top$. Vectors in (a) represent the spin orientation of the eigenstates.

with the according eigenstates

$$\psi_\pm(x) = \frac{e^{ikx}}{\sqrt{2}} \begin{pmatrix} 1 \\ \mp i \end{pmatrix}. \tag{1.51}$$

We consider an electron being injected at $x = 0$ with the spin pointing along the z-direction, i.e., $\psi(0) = (1, 0)^\top = (\psi_+(0) + \psi_-(0))/\sqrt{2}$, and the given Fermi energy $E_F = \hbar^2 k_F^2/(2m^*)$. The corresponding state at position x has the form

$$\psi(x) = \frac{1}{2}\left[e^{ik_- x} \begin{pmatrix} 1 \\ i \end{pmatrix} + e^{ik_+ x} \begin{pmatrix} 1 \\ -i \end{pmatrix} \right], \tag{1.52}$$

where $k_\pm = \sqrt{k_F^2 + (\delta k/2)^2} \mp \delta k/2$ and $\delta k = 2m^* \alpha_\mathrm{R}/\hbar^2$. As a consequence, the spin expectation value becomes position dependent as $\langle \mathbf{S}(x) \rangle = \frac{\hbar}{2} \langle \boldsymbol{\sigma}(x) \rangle$, where

$$\langle \boldsymbol{\sigma}(x) \rangle = (-\sin(\delta k\, x), 0, \cos(\delta k\, x))^\top. \tag{1.53}$$

As pictured in Fig. 1.7, the injected spin rotates in real space about the axis, that is given by the SOF. A full precession cycle is completed after the distance $L_{so} = 2\pi/\delta k = \pi\hbar^2/(m^* \alpha_\mathrm{R})$, which is called *(ballistic) spin precession length*.[6] It can be externally manipulated by the strength of the electric field $\mathcal{E}_z$, which in

[6] It has to be distinguished from the spin precession length in a diffusive system. In case of a persistent spin helix symmetry both lengths coincide [4].

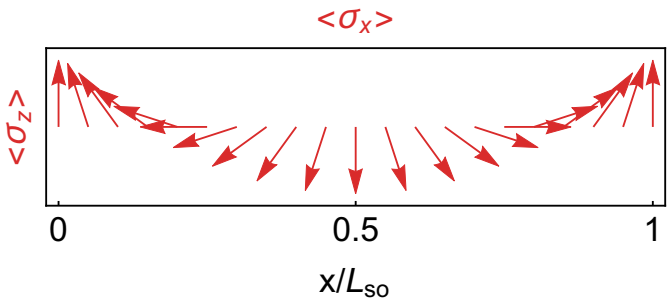

Fig. 1.7: Spin precession due to Rashba SOC. The spin, that is injected at $x = 0$, performs a full precession cycle after the length $L_{so} = \pi\hbar^2/(m^*\alpha_{\mathrm{R}})$.

turn is accessible via the gate voltage. A key issue with this device concept lies in the precondition of a *ballistic* semiconductor. In reality, these materials are barely free of disorder which induces scattering processes and thereby causes spin relaxation (cf. Chap. 2). As a result, the spin information may be lost over a short distance or time. However, since the spin relaxation often strongly depends on the device geometry as well as strength and structure of the SOC, there exist many possibilities to control it. These properties will be investigated in the main parts of this thesis, Parts II and III.

So far, we have only discussed the impact of structure inversion asymmetry in the bulk. In practice, these asymmetries often originate from the combination of distinct semiconductor materials in layered structures. Owing to the differences in the fundamental bandgap and lattice constants, new effects emerge that have significant consequences on the band structure and the SOC. We address these features in the following.

1.4.4 Quantum Confinement

Since the finite size of a real solid does not seem to have influence in the bulk properties, a bulk crystal is modeled by the use of periodic boundary conditions. However, if we scale it down to the size of a nanostructure device, the energy level spacing gets close to the thermal energy and produces observable effects and thus can no more be ignored [95].

A standard example is the two-dimensional electron or hole gas (2DEG or 2DHG), which is fundamental for the invention of the MOSFET,[7] a device that constitutes one of the most important advances in semiconductor history [96]. A 2DEG can be formed by combining an n-doped AlGaAs and an undoped GaAs layer as illustrated in Fig. 1.8. Both materials have a different band gap and the Fermi energy of the n-AlGaAs is closer to the conduction band due to doping. As soon as the layers are brought into contact, the electrons detach from the donor atoms and move to the GaAs leaving behind the positively charged donors. The space charge

[7] *metal-oxide-semiconductor field-effect transistor*

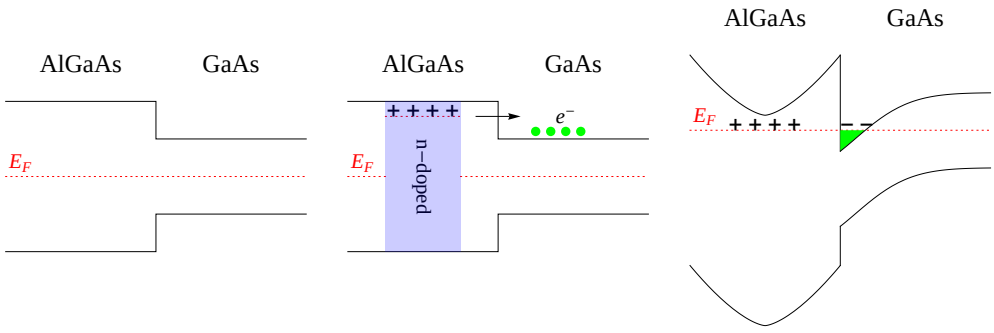

(a) Heterostructure without doping

(b) n-doped AlGaAs before relaxation

(c) Resulting band structure

Fig. 1.8: Fig. (a) shows a heterostructure with different sized energy gaps and aligned Fermi energy in the middle of the gap. (b) An n-type doping in the AlGaAs layer near the interface raises the Fermi energy locally. The donators ionize as the electrons move to the lower energy level in GaAs. (c) The Fermi energies equilibrate and the bending of the band structure forms a triangular quantum well at the interface.

induces an electric field and a bending of the energy bands. A thin triangular shaped quantum well is formed at the interface, where the conduction band edge is now below the Fermi energy. The confinement splits the bands into an infinite set of subbands that are separated in energy. If only the lowest subband is populated, the system is called *two-dimensional* (2D) because the degree of freedom in the direction of confinement is suppressed. In a similar way, it is possible to generate an analogous situation for holes being the majority carriers.

One useful feature of these 2D gases is the achievable high carrier density without a significant loss of mobility. In a semiconductor the inclusion of donor or acceptor atoms increase the carrier concentration. However, at the same time the impurity concentration rises, which limits the mobility through a higher scattering rate. In the 2D gases, the dopants are spatially separated and do not hinder the carrier motion. This doping technique is called *remote* or *modulation doping* [97].

More relevant for our purpose is the impact of the quantum confinement on the band structure and, in particular, the SOC. Without loss of generality, we consider a spatial confinement potential V_1 in z-direction, i.e., $V_1(\mathbf{r}) = V_1(z)$. Since the wave vector $\mathbf{k}_\parallel = (k_x, k_y, 0)^\top$ in the x-y-plane is a good quantum number, we can write the envelope function, Eq. (1.13), as

$$\psi_{n,\sigma}(\mathbf{r}) = \frac{e^{i\mathbf{k}_\parallel \cdot \mathbf{r}_\parallel}}{2\pi} \chi_n(z) \left|\sigma\right\rangle , \tag{1.54}$$

where $n \in \mathbb{N}^+$ denotes the subband index and we focus, for simplicity, only on a single (decoupled) bulk band. The functions $\chi_n(z)$ are the quantum well eigenfunctions, that obey the boundary conditions of the potential V_1. In order to obtain

analytical expressions, it is often convenient to consider the simple case of a *square well potential* (cf. Fig. 1.9(a)) of length L, i.e.,

$$V_1(z) = \begin{cases} 0 & \text{for } z \in [0, L]\,, \\ \infty & \text{otherwise.} \end{cases} \tag{1.55}$$

The normalized eigenfunctions in position space are given by

$$\chi_n(z) = \langle z|n\rangle = \sqrt{\frac{2}{L}} \sin\left(\frac{\pi\, n}{L} z\right). \tag{1.56}$$

The asymmetry of the confinement potential can be modeled by an additional potential $V_2 = e\mathcal{E}_z z$ (cf. Eq. (1.47)), which is treated as a perturbative correction to V_1.[8] Representing the Hamiltonian $\mathcal{H}$ in this basis leads to the matrix elements of the k_z and z operators

$$\langle n|z|l\rangle = \begin{cases} \frac{L}{2} & \text{for } n = l, \\ \frac{4nlL\left((-1)^{l+n}-1\right)}{\pi^2\left(l^2-n^2\right)^2} & \text{otherwise,} \end{cases} \tag{1.57}$$

$$\langle n|k_z|l\rangle = \frac{2inl\left((-1)^{l+n}-1\right)}{L\left(n^2-l^2\right)}(1-\delta_{nl}), \tag{1.58}$$

$$\langle n|k_z^2|l\rangle = \left(\frac{\pi n}{L}\right)^2 \delta_{nl}. \tag{1.59}$$

Advantageously, many matrix elements vanish due to the even and odd symmetry of the basis functions. Notice that the Dresselhaus SOC involves also terms that are cubic in k (cf. Sec. 1.4.2). Due to the projection $\propto \langle n|k_z^2|n\rangle$ the terms $\propto k_x k_z^2$ and $\propto k_y k_z^2$ will lead to a k-linear spin splitting weighted by the width of the quantum well. In 2DEGs this enables a formation of persistent spin textures (cf. Chap. 4). Notably, due to the discontinuity of the square well potential, the k-cubic terms normal to the quantum well, k_z^3, result in non-Hermitian matrix elements. This problem can be solved by a regularization procedure as shown in Ref. [98].

It is common practice to project the effective bulk Hamiltonian on the lowest eigenstate, $n = 1$, and use this as a definition for the effective 2D system, i.e., $\mathcal{H}_{2D} := \langle 1|\mathcal{H}|1\rangle$. This procedure, however, turns out to be insufficient to describe the SOC in the 2D hole system precisely [6]. Instead, we can make use of the lifted fourfold degeneracy of the heavy and light hole states in the Γ_{8v} valence band due to the subband splitting. Similar as in the derivation of the bulk BIA and SIA contributions, we can then decouple the topmost valence subband by Löwdin perturbation theory and obtain the relevant effective SOC terms. In Chap. 5, we perform this calculation for a strained 2DHG grown along the [001] crystal axis. The impact of the confinement potential is strongly influenced by its orientation

[8] It would seem more appropriate to alternatively use an infinite triangular potential where the according eigenfunctions are Airy functions (cf. Fig. 1.9(b)). Yet, these eigenfunctions lack the even and odd symmetry of the square well eigenfunctions. As a result, many additional matrix elements appear, which are small but finite and therefore inconvenient for an analytical study.

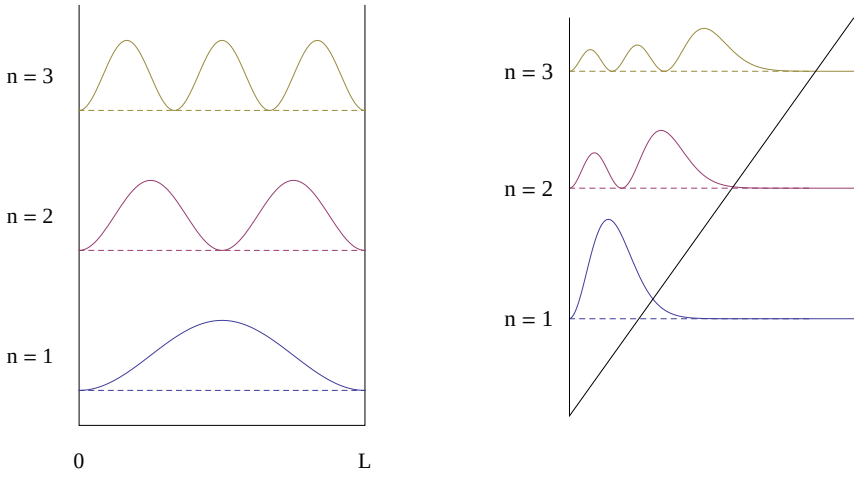

(a) Square well potential **(b)** Triangular quantum well

Fig. 1.9: Probability density $|\chi_n(z)|^2$ for different (infinitely high) confinement potentials.

with respect to the crystal axes. In the following section, we extend this approach to arbitrary growth directions of the quantum well.

Last, we point out that the idealized picture of an infinitely large square well potential restricts to the wave function to one section, which corresponds to a certain material layer. In reality, the wave function also penetrates the adjacent layers, which have a different bandgap and therefore distinct band parameters. We can take into account the inhomogeneity of the layered system by introducing position-dependent parameters [74]. This treatment causes a rescaling of the effective mass and the SOC coefficients and certain contributions can become significant that appear small in the simplified approach of an infinite square well [90, 92, 99, 100]. Since the resulting invariants for the SOC are symmetry-allowed, we can assume that the expressions from both approaches are only distinct in the coefficients. As we are mainly interested in the structure of the SOC terms, the simplified approach is preferable. Also, we will disregard SOC contributions that could arise from the inversion asymmetric bonding of the interface atoms [101]. These terms can become important if the quantum well and barrier do not share a common atom [102].

1.4.5 Quantum Wells of General Crystal Orientation

So far we have chosen a coordinate system $\mathcal{K}$, in which the basis vectors correspond to the $\langle 100 \rangle$ crystal axes. Accordingly, the wave vectors, i.e., $k_x \parallel [100]$, $k_y \parallel [010]$, and $k_z \parallel [001]$ point towards the high-symmetry points X of the Brillouin zone (cf. Fig. 1.10a). However, it is often convenient to use another coordinate system $\mathcal{K}'$ where one axis, here $\hat{\boldsymbol{z}}'$, is parallel to a different crystal direction, e.g., corresponding

to the quantum well orientation. The transformation can be performed by means of the rotation operator $\mathcal{R}$, which relates a vector $\mathbf{v}$ of the old system $\mathcal{K}$ to a vector $\mathbf{v}'$ of the new system $\mathcal{K}'$ as

$$\mathbf{v} = \mathcal{R}\,\mathbf{v}'. \tag{1.60}$$

Analogously, a tensor $\boldsymbol{\mu}$, e.g., the strain tensor as introduced in Sec. 1.5, in the basis of the old coordinate system is replaced by

$$\boldsymbol{\mu} = \mathcal{R}\,\boldsymbol{\mu}'\,\mathcal{R}^{\top}, \tag{1.61}$$

where $\boldsymbol{\mu}'$ corresponds to the new coordinate system $\mathcal{K}'$. The rotation operator $\mathcal{R}$ is given by

$$\mathcal{R}(\theta,\phi) = \begin{pmatrix} \cos(\phi)\cos(\theta) & -\sin(\phi) & \cos(\phi)\sin(\theta) \\ \sin(\phi)\cos(\theta) & \cos(\phi) & \sin(\phi)\sin(\theta) \\ -\sin(\theta) & 0 & \cos(\theta) \end{pmatrix}, \tag{1.62}$$

where θ denotes the polar and ϕ the azimuth angle of the former coordinate system $\mathcal{K}$. Fig. 1.10b illustrates how the z'-axis of the new system is related to z-axis of the old system. The full rotation consists of two subsequent rotations, where the first rotation is about the y-axis and the second about the z-axis with the respective angles ϕ and θ. Notably, an additional rotation about the new z'-axis can be applied to choose the alignment of the $\hat{\boldsymbol{x}}'$ and $\hat{\boldsymbol{y}}'$ basis vectors with the crystal axes of the new system as desired.

A different approach has been used by D'yakonov *et al.* to describe the SOC of a 2DEG with arbitrary growth direction [103, 104]. In this method, the original coordinate system $\mathcal{K}$ is not rotated. Instead, a unit vector $\mathbf{n}$ normal to the plane of the 2D system is defined (cf. Fig. 1.10b) and the wave vector $\mathbf{k}$ is separated into $\mathbf{k} = \mathbf{q}^{\parallel} + \mathbf{q}^{\perp}$. Here, the vector $\mathbf{q}^{\parallel}$ lies in the plane of the 2D system, i.e., $\mathbf{q}^{\parallel}\cdot\mathbf{n} = 0$, whereas the vector $\mathbf{q}^{\perp}$ points into the growth direction, i.e., $\mathbf{q}^{\perp} = \mathbf{n}\cdot(\mathbf{k}\cdot\mathbf{n})$. Projecting on the lowest subband in an infinitely deep quantum square well of width L that is oriented along $\mathbf{n}$, we find according to Sec. 1.4.4 that $\langle q^{\perp}\rangle = \langle (q^{\perp})^3\rangle = 0$ and $\langle (q^{\perp})^2\rangle = (\pi/L)^2$. This yields the relations for arbitrary products of the general wave vectors $\mathbf{k}$ up to third order as

$$\langle k_i\rangle = q_i^{\parallel}, \tag{1.63}$$

$$\langle k_i k_j\rangle = q_i^{\parallel} q_j^{\parallel} + n_i n_j \left(\frac{\pi}{L}\right)^2, \tag{1.64}$$

$$\langle k_i k_j k_k\rangle = q_i^{\parallel} q_j^{\parallel} q_k^{\parallel} + \left(\frac{\pi}{L}\right)^2 \left[n_i n_j q_k^{\parallel} + \text{c.p.}\right]. \tag{1.65}$$

Notably, the correspondence of the in-plane vector components $q_i^{\parallel}$ with the crystal axes is not unique. In Chap. 4, we apply this method to identify general conditions for persistent spin states in 2DEGs of arbitrary orientation in the crystal.

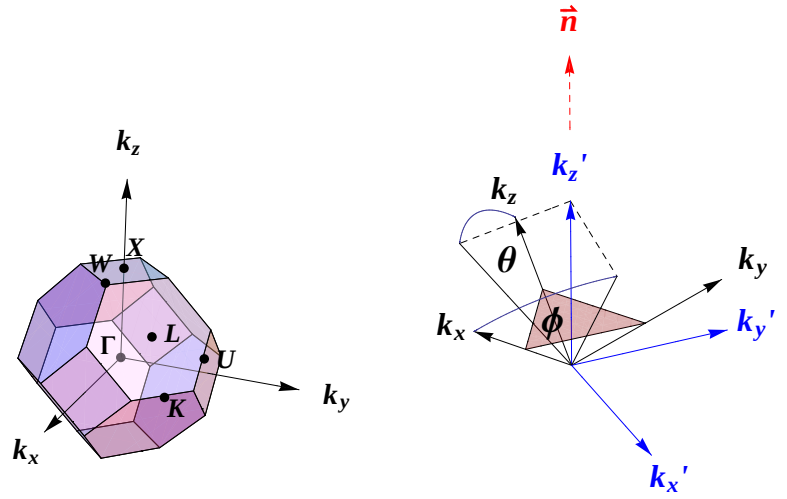

Fig. 1.10: (a) The orientation of the axes in the coordinate system $\mathcal{K}$ with respect to the symmetry points in reciprocal space. (b) The relation between the z-axes of the coordinate systems $\mathcal{K}$ and $\mathcal{K}'$. In the new system $\mathcal{K}'$, k_z' is parallel to the normal vector $\mathbf{n}$ of the 2D system, that is depicted by the red plane.

1.5 Strain Effects

Even though the concept of strain is old in semiconductor physics, its large-scale implementation in logic-device technology is relatively new [96]. After many years, the diminishing of the size of MOSFETs has come to a standstill due to increasing *off-state channel leakage* [11, 12]. Yet, in presence of strain further performance enhancements were discovered [105]. As an additive feature, it was first introduced into Si MOSFETs by Intel in 2002 and is now adopted in nearly all logic, communication, and consumer technologies [106].

Strain induces a broad range of important effects on the semiconductor band structure. It can alter the interatomic distance and reduce the crystal symmetry, which strongly affects bandgap energies, band warping, effective mass, and the SOC [106]. In a semiconductor, strain results from phonon-induced lattice vibrations, lattice-mismatch in epitaxially grown heterostructures, and externally applied stress [106]. We will focus on the latter two sources that are often found in semiconductors and technologically most important. They typically induce uniaxial or biaxial stress (cf. Figs. 1.11 and 1.12). In Chap. 5, we find that uniaxial strain is the key component for increasing the spin lifetime in [001]-oriented 2DHGs.

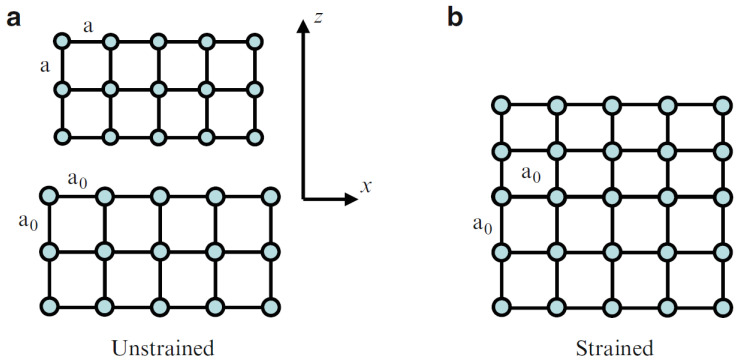

Fig. 1.11: Illustration of biaxial stress (strain) in an epitaxially grown heterostructure. (a) Material layers have a different lattice constant before growth. (b) After pseudomorphic film growth, the lattice constant of the top layer conforms to that of the bottom layer and is under biaxial stress (strain). Taken from Ref. [96].

1.5.1 Relation between Strain and Stress

In a crystal, strain is defined as the relative lattice displacement due to deformation. Focusing on a cubic crystal, the lattice vectors r_i' of the deformed crystal are related to the undeformed vectors r_i via [84]

$$r_i' = \sum_j (\delta_{ij} + \epsilon_{ij})\, r_j, \tag{1.66}$$

where $\boldsymbol{\epsilon}$ denotes the symmetric 3×3 strain tensor. In this definition, negative (positive) strain tensor components refer to compressive (tensile) strain. The tensor is commonly decomposed into three contributions

$$\boldsymbol{\epsilon} = \boldsymbol{\epsilon}_{\mathrm{H}} + \boldsymbol{\epsilon}_{\mathrm{S1}} + \boldsymbol{\epsilon}_{\mathrm{S2}}, \tag{1.67}$$

with

$$\boldsymbol{\epsilon}_{\mathrm{H}} = \frac{1}{3}(\epsilon_{xx} + \epsilon_{yy} + \epsilon_{zz})\, \mathbb{1}_{3\times 3}, \tag{1.68}$$

$$\boldsymbol{\epsilon}_{\mathrm{S1}} = \frac{1}{3} \begin{pmatrix} 2\epsilon_{xx} - (\epsilon_{yy} + \epsilon_{zz}) & 0 & 0 \\ 0 & 2\epsilon_{yy} - (\epsilon_{zz} + \epsilon_{xx}) & 0 \\ 0 & 0 & 2\epsilon_{zz} - (\epsilon_{xx} + \epsilon_{yy}) \end{pmatrix}, \tag{1.69}$$

$$\boldsymbol{\epsilon}_{\mathrm{S2}} = \begin{pmatrix} 0 & \epsilon_{xy} & \epsilon_{xz} \\ \epsilon_{yx} & 0 & \epsilon_{yz} \\ \epsilon_{zx} & \epsilon_{zy} & 0 \end{pmatrix}, \tag{1.70}$$

where $\boldsymbol{\epsilon}_{\mathrm{H}}$ corresponds to *hydrostatic strain* and $\boldsymbol{\epsilon}_{\mathrm{S1}}$ as well as $\boldsymbol{\epsilon}_{\mathrm{S2}}$ to *shear strain* [106]. Hydrostatic strain only alters the volume of the crystal, which becomes

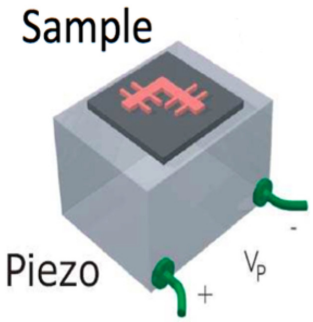

Fig. 1.12: Externally applied stress by means of a Piezo crystal. An external voltage deforms the Piezo crystal along with the sample on top of it. Transferred from Ref. [26].

apparent from the unit volume $\mathcal{V}'$ of the deformed cell that reads

$$\mathcal{V}' = \hat{\mathbf{x}}' \cdot (\hat{\mathbf{y}}' \times \hat{\mathbf{z}}') = 1 + \sum_i \epsilon_{ii}, \tag{1.71}$$

with the deformed unit vectors $\hat{\mathbf{x}}'$, $\hat{\mathbf{y}}'$, and $\hat{\mathbf{z}}'$. Since it does not reduce the symmetry it has no effect on lifting the band degeneracies. However, it changes the distance between the atoms which affects the bandgap. Shear strain, in turn, has additional consequences as it reduces the symmetry of the crystal. An important result is the lifted degeneracy of the heavy and light holes at the Γ-point. The diagonal shear strain tensor $\boldsymbol{\epsilon}_{\mathrm{S1}}$ refers to a change in length along the three $\langle 100 \rangle$ axes and the off-diagonal shear strain tensor $\boldsymbol{\epsilon}_{\mathrm{S2}}$ to a change along the $\langle 110 \rangle$ or $\langle 111 \rangle$ axes. Therefore, in case of an arbitrary non-vanishing $\boldsymbol{\epsilon}_{\mathrm{S1}}$, the shape of the cube becomes *orthorhombic* and for an arbitrary non-vanishing $\boldsymbol{\epsilon}_{\mathrm{S2}}$ it becomes *triclinic* [96].

Strain can be a response of an externally or internally induced force and is thus related to the symmetric 3×3 *stress* tensor $\boldsymbol{\tau}$. Its components τ_{kl} represent a force that is applied to the surfaces of an infinitesimal cube, which is illustrated in Fig. 1.13. Both are linearly dependent via the elastic stiffness constants C_{ijkl} or its inverse, the compliance tensor S_{ijkl}:

$$\epsilon_{ij} = \sum_{kl} S_{ijkl} \tau_{kl}, \tag{1.72}$$

where the components of C_{ijkl} and S_{ijkl} are material-specific parameters. Considering a cubic crystal and making use of the symmetry of the stress and strain tensors, the compliance tensor reduces to a 6×6 matrix. In the basis $\{\widehat{xx}, \widehat{yy}, \widehat{zz}, \widehat{xy}, \widehat{yz}, \widehat{xz}\}$ it takes the simple form

$$(S_{ij}) = \begin{pmatrix} S_{11} & S_{12} & S_{12} & 0 & 0 & 0 \\ S_{12} & S_{12} & S_{11} & 0 & 0 & 0 \\ S_{12} & S_{12} & S_{11} & 0 & 0 & 0 \\ 0 & 0 & 0 & S_{44} & 0 & 0 \\ 0 & 0 & 0 & 0 & S_{44} & 0 \\ 0 & 0 & 0 & 0 & 0 & S_{44} \end{pmatrix}, \tag{1.73}$$

where one uses the following symmetry properties:

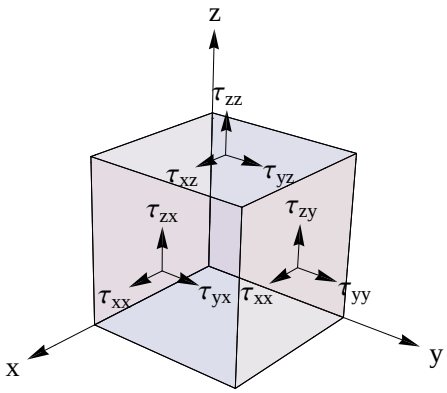

Fig. 1.13: Stress tensor components τ_{kl} acting on the surfaces of the infinitesimal cube.

- The compliance tensor must be symmetric.
- For cubic crystals the axes $\hat{x}$, $\hat{y}$ and $\hat{z}$ are equivalent, i.e., $S_{11} = S_{22} = S_{33}$.
- Shear stress cannot lead to normal strain, e.g., $S_{14} = 0$.
- Shear stress along one axis cannot cause shear stress along another axis, e.g., $S_{45} = 0$.
- Normal stress along one axis affects the other two normal axes in the same way, e.g., $S_{12} = S_{13}$.

The same holds for the elastic stiffness constants, that is, the 6×6 matrix (C_{ij}) has equivalent form. We will utilize this relation for two cases that frequently appear in semiconductors and are most important in Chap. 5.

Biaxial Stress

In pseudomorphically grown semiconductor heterostructures, layers of different materials are combined. Since these materials, in general, possess a different lattice constant, the lattice structure of the top layer accommodates the lattice structure of the bottom layer. Considering a [001]-grown semiconductor, the top layer suffers a biaxial stress along the [100] and [010] axes, i.e., $\tau_{xx} = \tau_{yy} = T$ and $\tau_{ij} = 0$ otherwise. The sign of T depends on the kind of the applied stress: $T < 0$ for *compressive* and $T > 0$ for *tensile* stress in compliance with the definition of strain. According to Eq. (1.72), we obtain the biaxial strain tensor components

$$\epsilon_{xx} = \epsilon_{yy} = (S_{11} + S_{12})\, T, \tag{1.74}$$

$$\epsilon_{zz} = 2 S_{12} T, \tag{1.75}$$

where an extra strain component ϵ_{zz} appears that is in general distinct from the others. A comparison with Eq. (1.67) reveals the symmetry change from cubic to tetragonal [96]. The case of biaxial tensile stress is displayed for a tetrahedral crystal in Figs. 1.14a and 1.14b.

Uniaxial Stress

Process-introduced or externally applied [110] uniaxial stress yields a reduction of the crystal symmetry that are even more significant. This causes additional valence band mixing and warping, which together with Rashba and Dresselhaus SOC leads to spin-preserving symmetries (cf. Chap. 5).

We consider a coordinate system where the x-axis corresponds to the [110] direction. Applying [110] uniaxial stress yields only one non-vanishing stress tensor component $\tau'_{xx} = T$. By means of Eq. (1.61), we can transform the stress tensor into the common coordinate system, where the x-axis corresponds to the [100]-axis, that is, $\mathcal{R}(\theta = 0, \phi = \pi/4)$. This way, we find the [110] uniaxial stress tensor

$$\boldsymbol{\tau} = T/2 \begin{pmatrix} 1 & 1 & 0 \\ 1 & 1 & 0 \\ 0 & 0 & 0 \end{pmatrix}. \tag{1.76}$$

By substituting $\boldsymbol{\tau}$ into Eq. (1.72), we obtain the non-vanishing strain tensor components:

$$\epsilon_{xx} = \epsilon_{yy} = \frac{S_{11} + S_{12}}{2} T, \tag{1.77}$$

$$\epsilon_{xy} = \frac{S_{44}}{2} T, \tag{1.78}$$

$$\epsilon_{zz} = S_{12} T. \tag{1.79}$$

In contrast to biaxial strain, the second type of shear strain is also involved and the cube will become *orthorhombic* [96]. We illustrate the situation for both compressive and tensile stress in the Figs. 1.14c, 1.14d, and 1.14e. Notably, by means of [111] uniaxial strain a zinc-blende lattice can be transformed into a *wurtzite* lattice [76].

1.5.2 Strain in $\mathbf{k} \cdot \mathbf{p}$ Theory

Hereafter, we shortly demonstrate how strain effects are included within the $\mathbf{k} \cdot \mathbf{p}$ framework and the *Bir-Pikus Strain Hamiltonian* is constructed following Refs. [70, 84, 96]. Naturally, one is tempted to describe the changes in a crystal due to strain as a perturbation. However, this encounters the following difficulties: First, the strain-induced potential differences can be large even for a small strain. Second, the presence of strain changes the periodicity of the crystal. The latter point has the consequence that a perturbative expansion of the wave function of the strained lattice in terms of the wave function of an unstrained lattice is not practical. The reason is that in both situations the lattice periodic parts of the Bloch functions $u_{\nu\mathbf{k}}(\mathbf{r})$ have distinct periodicity. In order to avoid these issues, Bir and Pikus introduced "deformed" coordinates $\mathbf{r}'$, which are expressed in terms of the undeformed coordinates $\mathbf{r}$ (cf. Eq. (1.66)). In this case, both the potential V_0 of the undeformed

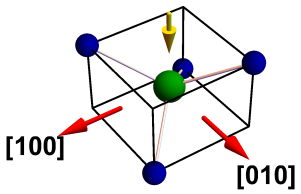

(a) Biaxial tensile stress.

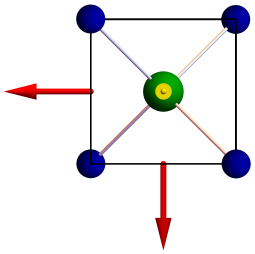

(b) Biaxial tensile stress (top view).

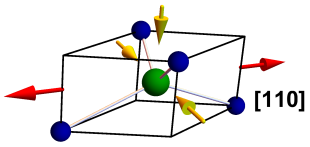

(c) Uniaxial tensile stress.

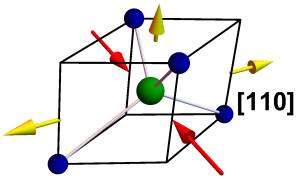

(d) Uniaxial compressive stress.

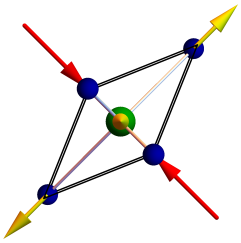

(e) Uniaxial compressive stress (top view)

Fig. 1.14: Deformation of a T_d crystal due to biaxial stress in the [100]-[010] plane in (a) and (b). The deformation due to [110] uniaxial stress is shown in (c), (d) and (e). The red arrows indicate the externally applied stress, the yellow arrows the induced *additional* deformation.

lattice and the potential V of the deformed lattice have the same periodicity [96]. In accordance with the definition in Eq. (1.66), the components of the momentum $\mathbf{p}$ read as

$$p_i' = \sum_j \left(\delta_{ij} - \epsilon_{ij}\right) p_j. \tag{1.80}$$

Restricting to linear terms in ϵ_{ij}, we can write the deformed potential $V(\mathbf{r}')$ as [96]

$$V(\mathbf{r}') \approx V_0(\mathbf{r}) + \sum_{ij} V_{ij}(\mathbf{r})\epsilon_{ij}, \tag{1.81}$$

where

$$V_{ij} = \frac{\partial V}{\partial \epsilon_{ij}} = \lim_{\epsilon \to 0} \frac{V\left[\left(\mathbb{1}_{3\times 3} + \boldsymbol{\epsilon}\right)\mathbf{r}\right] - V_0(\mathbf{r})}{\epsilon_{ij}}. \tag{1.82}$$

Using these expressions, the $\mathbf{k}\cdot\mathbf{p}$ Hamiltonian of the deformed system can be derived, which involves new fundamental matrix elements [96]

$$\mathcal{V}^{ij}_{\sigma\sigma'\nu\nu'} = \langle \nu\sigma | V_{ij} - \frac{p_i p_j}{m_0} | \nu'\sigma' \rangle \,. \tag{1.83}$$

Eq. (1.85), Ref. [26]	Ref. [70]	Refs. [84, 106], [96][a], [73][b]
a_v	$D_d - \frac{5}{6}D_u$	$a_v + \frac{5}{4}b$
b	$\frac{2}{3}D_u$	$-b$
d	$\frac{2}{3}D'_u$	$-d/\sqrt{3}$

Tab. 1.1: Relations between different conventions for the deformation potentials for the Γ_{8v} valence band.

[a] The sign of a_v has to be inverted.
[b] The sign of b and d has to be inverted.

These quantities are related to the *deformation potentials*. The strain-induced modifications are collected in the Bir-Pikus strain Hamiltonian $\mathcal{H}^\epsilon$ and are sorted by means of the theory of invariants. For the Γ_{6c} conduction and the Γ_{8v} valence bands, the Hamiltonian reads as [26, 84]

$$\mathcal{H}^\epsilon_{6c6c} = \sum_i a_c\, \epsilon_{ii}\, \mathbb{1}_{2\times 2}, \tag{1.84}$$

$$\mathcal{H}^\epsilon_{8v8v} = \sum_i \left(a_v\, \epsilon_{ii} \mathbb{1}_{4\times 4} + b\, \epsilon_{ii}\, J_i^2 + d \sum_{j,\, j\neq i} \epsilon_{ij}\, \{J_i, J_j\}_{(s)} \right), \tag{1.85}$$

where a_c, a_v, b, and d denote the deformation potentials.[9] Notably, there are distinct conventions for the deformation potentials and also the signs of the strain tensor components. We defined Eq. (1.84) consistently with Refs. [96, 106] and Eq. (1.85) with Ref. [26]. Thus, the potentials b and d are positive whereas a_v can be positive or negative. In Tab. 1.1, we list the relations to some definitions that appear in the literature.

It becomes obvious that the holes are much more sensitive to strain than the electrons. While the strain shifts the conduction band as a whole since only hydrostatic strain is present, the impact on the valence band is more complicated. Due to a reduction of symmetry, the degeneracy at the Γ-point can be removed. Also, it induces additional couplings between HH and LH states, which significantly affects the band warping and the SOC. In Chap. 5, we demonstrate that by use of [110] uniaxial strain the SOC can be altered such that it gives rise to a conserved spin quantity in a [001]-grown 2DHG.

[9] Notably, the equations above are defined for band structure around the Γ point. In Si and Ge the conduction band minima is not located at $k = 0$. As a consequence, more deformation potentials are needed to properly describe the effect of strain in non-direct semiconductors [106].

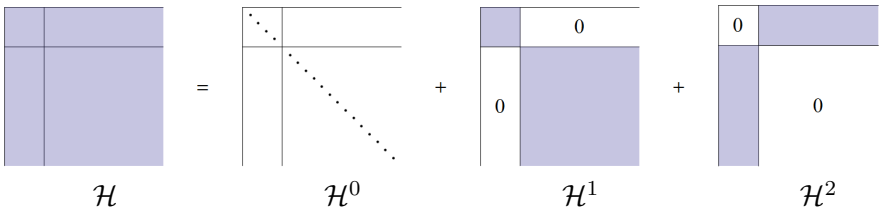

Fig. 1.15: Partition of $\mathcal{H}$. The grey areas indicate arbitrary populated matrix blocks.

Appendix 1.A: Löwdin Perturbation Theory

Quasi-degenerate perturbation theory, also called *Löwdin partitioning* or *Löwdin perturbation theory*, is a powerful tool for the perturbative study of time-independent multiband Hamiltonians [107, 108]. This technique allows to derive effective models that describe subspaces of the full Hamiltonian without losing the information that originates from the coupling to the other subspaces. An advantage of this method is that, in comparison with conventional perturbation theory, we do not need to distinguish between degenerate or non-degenerate perturbation theory [70]. Thus, it is perfectly suitable for $\mathbf{k}\cdot\mathbf{p}$ multiband Hamiltonians where the bands often contain degeneracies and the inter(sub)band coupling is the key element for SOC effects [6, 70, 74, 109]. Although this method is by now well-established, we shortly resume the derivation as described in great detail in Refs. [70, 84].

Consider a given Hamiltonian $\mathcal{H}$ that can be expressed as a sum of a Hamiltonian $\mathcal{H}^0$ with known eigenvalues E_n and eigenfunctions $|\psi_n\rangle$ and $\mathcal{H}'$, which is treated as a perturbation. This Hamiltonian can be rewritten in the form

$$\mathcal{H} = \mathcal{H}^0 + \mathcal{H}' = \mathcal{H}^0 + \mathcal{H}^1 + \mathcal{H}^2, \tag{1.A.1}$$

where the decomposition is illustrated in Fig. 1.15. Under the condition that the eigenfunctions can be separated into weakly coupled subsets A and B (cf. Fig. 1.16), we can apply an appropriate unitary transformation e^{-S} such that the transformed Hamiltonian $\widetilde{\mathcal{H}}$ becomes block-diagonal, i.e., $\widetilde{\mathcal{H}} = e^{-S}\mathcal{H}e^{S}$.

In accordance with Refs. [70, 84], we define the indices m, m', m'' corresponding to the states in set A, the indices l, l', l'' to the states in set B and the matrix elements between them as $\mathcal{H}'_{ij} = \langle\psi_i|\mathcal{H}'|\psi_j\rangle$. Using these definitions and realizing that operator S must be block off-diagonal like $\mathcal{H}^2$ (see Fig. 1.15) and anti-Hermitian, i.e., $S = -S^\dagger$, one finds equations for the successive approximations to $\mathcal{H}'$:

$$\widetilde{\mathcal{H}} = \mathcal{H}^{(0)} + \mathcal{H}^{(1)} + \mathcal{H}^{(2)} + \mathcal{H}^{(3)} + ..., \tag{1.A.2}$$

where

$$\mathcal{H}^{(0)}_{mm'} = \mathcal{H}^0_{mm'}\,, \tag{1.A.3}$$

$$\mathcal{H}^{(1)}_{mm'} = \mathcal{H}'_{mm'}\,, \tag{1.A.4}$$

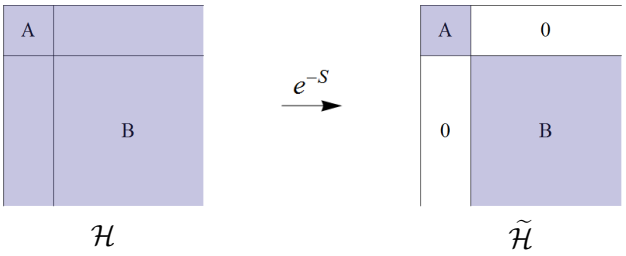

Fig. 1.16: Unitary transformation to remove the off-diagonal elements of $\mathcal{H}$.

$$\mathcal{H}^{(2)}_{mm'} = \frac{1}{2}\sum_{l} \mathcal{H}'_{ml}\mathcal{H}'_{lm'}\left[\frac{1}{E_m - E_l} + \frac{1}{E_{m'} - E_l}\right], \tag{1.A.5}$$

$$\begin{aligned}\mathcal{H}^{(3)}_{mm'} = &-\frac{1}{2}\sum_{l,m''}\left[\frac{\mathcal{H}'_{ml}\mathcal{H}'_{lm''}\mathcal{H}'_{m''m'}}{(E_{m'} - E_l)(E_{m''} - E_l)} + \frac{\mathcal{H}'_{mm''}\mathcal{H}'_{m''l}\mathcal{H}'_{lm'}}{(E_m - E_l)(E_{m''} - E_l)}\right] \\ &+ \frac{1}{2}\sum_{l,l'} \mathcal{H}'_{ml}\mathcal{H}'_{ll'}\mathcal{H}'_{l'm'}\times \\ &\times\left[\frac{1}{(E_m - E_l)(E_m - E_{l'})} + \frac{1}{(E_{m'} - E_l)(E_{m'} - E_{l'})}\right],\end{aligned} \tag{1.A.6}$$

$$\ldots = \ldots$$

Note that these equations remain valid if the matrix elements of $\mathcal{H}$ include operators. What type of operator is still present in the final expression of $\widetilde{\mathcal{H}}$ strictly depends on the eigenfunctions of $\mathcal{H}_0$, though. Moreover, each of the subsets A and B may be degenerate but it is crucial that the subsets are chosen to be separated in energy, i.e., $E_m \neq E_l$.

As an introductory example, we apply this theory to derive the Pauli SOC from the Dirac Hamiltonian in Sec. 1.1. Later, in Sec. 5 we use this method to compute an effective Hamiltonian for the lowest subband in a strained 2DHG and identify conserved spin quantities.

Appendix 1.B: Spin and Total Angular Momentum Matrices

In this appendix, we display the explicit form of the total angular momentum matrices J_i for $j = 3/2$ and the Pauli matrices σ_i. These matrices are contained in the definitions of the Luttinger Hamiltonian in Eq. (1.37) as well as the Dresselhaus and Rashba spin-orbit coupling corrections in Eqs. (1.45), (1.46), (1.48) and (1.49) through their expansion by the theory of invariants. Here, we chose the commonly used order of the total angular momentum eigenbasis as

$$\{|j, m_j\rangle\} = \{|3/2, +3/2\rangle, |1/2, +1/2\rangle, |1/2, -1/2\rangle, |3/2, -3/2\rangle\}. \tag{1.B.7}$$

$$J_x = \tfrac{1}{2}\begin{pmatrix} 0 & \sqrt{3} & 0 & 0 \\ \sqrt{3} & 0 & 2 & 0 \\ 0 & 2 & 0 & \sqrt{3} \\ 0 & 0 & \sqrt{3} & 0 \end{pmatrix}, \qquad J_y = \tfrac{i}{2}\begin{pmatrix} 0 & -\sqrt{3} & 0 & 0 \\ \sqrt{3} & 0 & -2 & 0 \\ 0 & 2 & 0 & -\sqrt{3} \\ 0 & 0 & \sqrt{3} & 0 \end{pmatrix},$$

$$J_z = \tfrac{1}{2}\begin{pmatrix} 3 & 0 & 0 & 0 \\ 0 & 1 & 0 & 0 \\ 0 & 0 & -1 & 0 \\ 0 & 0 & 0 & -3 \end{pmatrix}, \qquad \mathbb{1}_{4\times 4} = \begin{pmatrix} 1 & 0 & 0 & 0 \\ 0 & 1 & 0 & 0 \\ 0 & 0 & 1 & 0 \\ 0 & 0 & 0 & 1 \end{pmatrix}, \tag{1.B.8}$$

$$\sigma_x = \begin{pmatrix} 0 & 1 \\ 1 & 0 \end{pmatrix}, \qquad \sigma_y = \begin{pmatrix} 0 & -i \\ i & 0 \end{pmatrix}, \qquad \sigma_z = \begin{pmatrix} 1 & 0 \\ 0 & -1 \end{pmatrix}, \qquad \mathbb{1}_{2\times 2} = \begin{pmatrix} 1 & 0 \\ 0 & 1 \end{pmatrix}. \tag{1.B.9}$$

Appendix 1.C: Parameters and Spin-Orbit Coupling Coefficients

Here, we provide a list of band structure parameters and spin-orbit coupling coefficient for different III-V semiconductors, that are used for numerical calculations in this book. All tables are transferred from Ref. [70].

		GaAs	AlAs	InSb	InAs	AlSb
E_0	(eV)	1.519	3.13	0.237	0.418	2.384
E_0'	(eV)	4.488	4.540	3.160	4.390	3.5
Δ_0	(eV)	0.341	0.300	0.810	0.380	0.673
Δ_0'	(eV)	0.171	0.150	0.330	0.240	0.3
Δ^-	(eV)	$-0.050\,\mathrm{i}$				
P	(eV Å)	10.493	8.97	9.641	9.197	8.463
P'	(eV Å)	$4.780\,\mathrm{i}$	$4.780\,\mathrm{i}$	$6.325\,\mathrm{i}$	$0.873\,\mathrm{i}$	
Q	(eV Å)	8.165	8.165	8.130	8.331	
C_k	(eV Å)	-0.0034	0.002	-0.0082	-0.0112	0.006
$m^\star$	(m_0)	0.0665	0.150	0.0139	0.0229	0.120
$g^\star$		-0.44	1.52	-51.56	-14.9	0.843
γ_1		6.85	3.25	37.10	20.40	4.15
γ_2		2.10	0.65	16.50	8.30	1.01
γ_3		2.90	1.21	17.70	9.10	1.71
κ		1.20		15.60	7.60	0.31
q		0.01		0.39	0.39	0.07

Tab. 1.17: Band structure parameters [70].

	GaAs	AlAs	InAs	InSb	CdTe	ZnSe
b_{41}^{6c6c}	27.58	18.53	27.18	760.1	43.88	14.29
C_k	−0.0034	0.0020	−0.0112	−0.0082	−0.0234	−0.0138
b_{41}^{8v8v}	−81.93	−33.51	−50.18	−934.8	−76.93	−62.33
b_{42}^{8v8v}	1.47	0.526	1.26	41.73	1.668	0.375
b_{51}^{8v8v}	0.49	0.175	0.42	13.91	0.556	0.125
b_{52}^{8v8v}	−0.98	−0.35	−0.84	−27.82	−1.11	−0.250
b_{41}^{7v7v}	−58.71	−27.27	−22.31	−146.8	−38.44	−50.71
b_{41}^{8v7v}	−101.9	−44.30	−51.29	−709.5	−82.46	−83.86
b_{51}^{8v7v}	−1.255 i	−0.474 i	−0.910 i	−23.92 i	−1.215 i	−0.335 i
B_{8v}^{+}	−21.32	−34.81	−3.393	−32.20	−22.41	−32.05
B_{8v}^{-}	−0.5175	−1.468	−0.09511	−1.662	−0.6347	−0.2704
B_{7v}	−20.24	−32.84	−3.178	−27.77	−20.47	−31.15

Tab. 1.18: Dresselhaus (BIA) bulk coefficients for various semiconductors (all in eVÅ^3, except for C_k, which is in eVÅ, and B_i, which is in eVÅ^2) [70].

	GaAs	AlAs	InAs	InSb	CdTe	ZnSe
r_{41}^{6c6c}	5.206	−0.243	117.1	523.0	6.930	1.057
r_{41}^{8v8v}	−14.62	−1.501	−159.9	−548.5	−10.79	−4.099
r_{42}^{8v8v}	−0.106	−0.0906	−0.162	−0.530	−0.0836	−0.0193
r_{51}^{8v8v}	0.00418			0.0362		
r_{52}^{8v8v}	−0.00005			−0.0013		
r_{41}^{7v7v}	−9.720	−1.387	−43.35	−27.07	−4.124	−3.097
r_{31}^{8v7v}	−3.87 i	−0.255 i	−87.7 i	−392.0 i	−5.16 i	−0.788 i
r_{41}^{8v7v}	−18.45	−2.336	−152.7	−432.6	−11.34	−5.433
r_{51}^{8v7v}	−0.00807			−0.0967		
r_{52}^{8v7v}	−8.15 i	−0.864 i	−175.9 i	−785.9 i	−10.84 i	−1.753 i

Tab. 1.19: Rashba (SIA) bulk coefficients for various semiconductors (all in eÅ^2, except for r_{51}^{8v8v} and r_{51}^{8v7v}, which are in eÅ) [70].

Appendix 1.D: 6 × 6 Kane Model

We tabulate the full 6×6 Kane Hamiltonian in this appendix taken from Refs. [70, 80]. We used the definitions

$$\begin{aligned} k^2 &= k_x^2 + k_y^2 + k_z^2, \\ k_\parallel^2 &= k_x^2 + k_y^2, \\ k_\pm &= k_x \pm i k_y, \\ K &= k_x^2 - k_y^2. \end{aligned}$$

The reduced parameters are

$$\begin{aligned} \frac{1}{m'} &= \frac{1}{m^*} - \frac{4P^2}{\hbar^2 E_0}, \\ \gamma_1' &= \gamma_1 - \frac{2m_0 P^2}{3\hbar^2 E_0}, \\ \gamma_2' &= \gamma_2 - \frac{m_0 P^2}{3\hbar^2 E_0}, \\ \gamma_3' &= \gamma_3 - \frac{m_0 P^2}{3\hbar^2 E_0}. \end{aligned}$$

Note that in case of zinc-blende structure, the BIA spin splitting is explicitly taken into account solely by the factors B_i and C_k. Further BIA corrections are not necessary.

$\left\vert\frac{1}{2},\frac{1}{2}\right\rangle_c$	$\left\vert\frac{1}{2},-\frac{1}{2}\right\rangle_c$	$\left\vert\frac{3}{2},\frac{3}{2}\right\rangle_v$	$\left\vert\frac{3}{2},\frac{1}{2}\right\rangle_v$	$\left\vert\frac{1}{2},-\frac{1}{2}\right\rangle_v$	$\left\vert\frac{3}{2},-\frac{3}{2}\right\rangle_v$
$\frac{\hbar^2k^2}{2m'}+E_0$	0	$\frac{1}{\sqrt{2}}B_{8v}^{+}k_{-}k_z-\frac{1}{\sqrt{2}}Pk_{+}$	$\frac{1}{\sqrt{6}}B_{8v}^{-}K+i\sqrt{\frac{2}{3}}B_{8v}^{+}k_xk_y+\sqrt{\frac{2}{3}}Pk_z$	$\frac{1}{\sqrt{6}}B_{8v}^{+}k_{+}k_z+\frac{1}{\sqrt{6}}Pk_{-}$	$\frac{1}{3\sqrt{2}}B_{8v}^{-}\left(k_{\parallel}^2-2k_z^2\right)$
0	$\frac{\hbar^2k^2}{2m'}+E_0$	$-\frac{1}{3\sqrt{2}}B_{8v}^{-}\left(k_{\parallel}^2-2k_z^2\right)$	$\frac{1}{\sqrt{6}}B_{8v}^{+}k_{-}k_z-\frac{1}{\sqrt{6}}Pk_{+}$	$-\frac{1}{\sqrt{6}}B_{8v}^{-}K+i\sqrt{\frac{2}{3}}B_{8v}^{+}k_xk_y+\sqrt{\frac{2}{3}}Pk_z$	$\frac{1}{\sqrt{2}}B_{8v}^{+}k_{+}k_z+\frac{1}{\sqrt{2}}Pk_{-}$
$\frac{1}{\sqrt{2}}B_{8v}^{+}k_{+}k_z-\frac{1}{\sqrt{2}}Pk_{-}$	$-\frac{1}{3\sqrt{2}}B_{8v}^{-}\left(k_{\parallel}^2-2k_z^2\right)$	$-\frac{\hbar^2}{2m_0}\left(\gamma_1'+\gamma_2'\right)k_{\parallel}^2-\frac{\hbar^2}{2m_0}\left(\gamma_1'-2\gamma_2'\right)k_z^2$	$\frac{\sqrt{3}\hbar^2}{m_0}\gamma_3'k_{-}k_z-\frac{1}{2}C_kk_{+}$	$\frac{\sqrt{3}\hbar^2}{2m_0}\gamma_2'K-\frac{i\sqrt{3}\hbar^2}{m_0}\gamma_3'k_xk_y+C_kk_z$	$-\frac{\sqrt{3}}{2}C_kk_{-}$
$\frac{1}{\sqrt{6}}B_{8v}^{-}K-i\sqrt{\frac{2}{3}}B_{8v}^{+}k_xk_y+\sqrt{\frac{2}{3}}Pk_z$	$\frac{1}{\sqrt{6}}B_{8v}^{+}k_{+}k_z-\frac{1}{\sqrt{6}}Pk_{-}$	$\frac{\sqrt{3}\hbar^2}{m_0}\gamma_3'k_{+}k_z-\frac{1}{2}C_kk_{-}$	$-\frac{\hbar^2}{2m_0}\left(\gamma_1'-\gamma_2'\right)k_{\parallel}^2-\frac{\hbar^2}{2m_0}\left(\gamma_1'+2\gamma_2'\right)k_z^2$	$\frac{\sqrt{3}}{2}C_kk_{+}$	$\frac{\sqrt{3}\hbar^2}{2m_0}\gamma_2'K-\frac{i\sqrt{3}\hbar^2}{m_0}\gamma_3'k_xk_y-C_kk_z$
$\frac{1}{\sqrt{6}}B_{8v}^{+}k_{-}k_z+\frac{1}{\sqrt{6}}Pk_{+}$	$-\frac{1}{\sqrt{6}}B_{8v}^{-}K-i\sqrt{\frac{2}{3}}B_{8v}^{+}k_xk_y+\sqrt{\frac{2}{3}}Pk_z$	$\frac{\sqrt{3}\hbar^2}{2m_0}\gamma_2'K+\frac{i\sqrt{3}\hbar^2}{m_0}\gamma_3'k_xk_y+C_kk_z$	$\frac{\sqrt{3}}{2}C_kk_{-}$	$-\frac{\hbar^2}{2m_0}\left(\gamma_1'-\gamma_2'\right)k_{\parallel}^2-\frac{\hbar^2}{2m_0}\left(\gamma_1'+2\gamma_2'\right)k_z^2$	$-\frac{\sqrt{3}\hbar^2}{m_0}\gamma_3'k_{-}k_z-\frac{1}{2}C_kk_{+}$
$\frac{1}{3\sqrt{2}}B_{8v}^{-}\left(k_{\parallel}^2-2k_z^2\right)$	$\frac{1}{\sqrt{2}}B_{8v}^{+}k_{-}k_z+\frac{1}{\sqrt{2}}Pk_{+}$	$-\frac{\sqrt{3}}{2}C_kk_{+}$	$\frac{\sqrt{3}\hbar^2}{2m_0}\gamma_2'K+\frac{i\sqrt{3}\hbar^2}{m_0}\gamma_3'k_xk_y-C_kk_z$	$-\frac{\sqrt{3}\hbar^2}{m_0}\gamma_3'k_{+}k_z-\frac{1}{2}C_kk_{-}$	$-\frac{\hbar^2}{2m_0}\left(\gamma_1'+\gamma_2'\right)k_{\parallel}^2-\frac{\hbar^2}{2m_0}\left(\gamma_1'-2\gamma_2'\right)k_z^2$

Tab. 1.2: 6×6 Kane model [70, 80].

CHAPTER 2

Types of Spin-Relaxation Processes

The SOC in semiconductors allows the external manipulation of spin, which makes it essential for spintronics. However, at the same time this effect is linked to spin-relaxation processes since the spin is not a good quantum number anymore. These processes lead to a spin equilibration of an injected spin density after a certain characteristic time or distance, which is denoted as spin lifetime τ_s or spin-relaxation length l_s, respectively. As the loss of spin information represents a key issue for the realization of spin-based devices, the following chapter is devoted to provide a short overview of the most relevant spin-relaxation mechanisms. While most mechanisms occur simultaneously, the spin-relaxation process discovered by D'yakonov and Perel' is often considered predominant and the central topic in this thesis.

Originally, the study of spin relaxation is rooted in the investigation of the nuclear spin dynamics. As the nuclear spins do not move freely in space, there is no coupling to an orbital motion and the spin relaxation is normally much weaker [110]. Their decay is traditionally defined by means of the *Bloch-Torrey equations*, which describes the magnetization dynamics in a magnetic field with a homogeneous static component $\mathbf{B}_0$, and an oscillating component $\mathbf{B}_1(t)$ perpendicular to it [111, 112]. Consequently, two spin lifetimes T_1 and T_2 are defined, which are denoted as *spin-relaxation time* and *spin dephasing time* and refer to the decay time of the longitudinal and transversal magnetization with respect to $\mathbf{B}_0$, respectively [104]. In this thesis, we do not need to discriminate between the two terms since magnetic field effects are considered small (causing only the necessary phase breaking in the study of magnetoconductance) [104]. Also, in order to account for anisotropic systems, we treat the spin-relaxation rate τ_s^{-1} as a tensorial quantity.

2.1 D'yakonov-Perel' Mechanism

The D'yakonov-Perel' (DP) spin relaxation [17] plays a significant role in diffusive semiconductor structures which lack inversion symmetry. As discussed in Sec. 1.4, the latter results in a Rashba or Dresselhaus SOC Hamiltonian $\mathcal{H}_{\text{so}}$ and gives rise to an intrinsic Zeeman-like spin splitting, which can be interpreted as an effective magnetic field called SOF $\mathbf{\Omega}$, i.e., $\mathcal{H}_{\text{so}} = \mathbf{\Omega} \cdot \boldsymbol{\sigma}$. The SOF induces a precession of the electron or hole spins, where the precession axis and frequency are determined

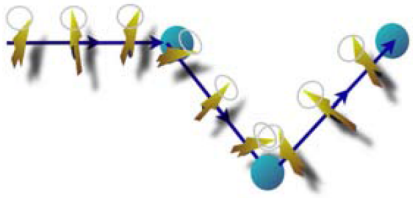

Fig. 2.1: The presence of a SOF in combination with impurity scattering leads to a randomization of the spin precession which causes D'yakonov-Perel' spin relaxation. Taken from Ref. [116].

by the orientation and magnitude of $\mathbf{\Omega}$. Yet, the SOF is in general not uniform since it depends on the wave vector of the carriers, i.e., $\mathbf{\Omega} = \mathbf{\Omega}(\mathbf{k})$. The presence of disorder leads to scattering, which randomly changes the momentum direction and therewith the precession axis and frequency. However, we need to distinguish two different regimes depending on the relative weight of the SOC-induced average spin precession length L_{so} and the mean free path l_e. We focus on scattering events in the following that are elastic, uncorrelated, and spin-independent.

(i) In the weak scattering regime, i.e., $L_{so} \leq l_e$, the spins precess a full cycle or more before they are scattered. Here, the spin polarization decays initially due to the anisotropy of $\mathbf{\Omega}(\mathbf{k})$. The corresponding spin-relaxation rate τ_s^{-1} can be estimated as $\tau_s^{-1} \approx \sqrt{\langle \Omega^2 \rangle}$, where $\langle . \rangle$ denotes the average over the Fermi surface [101]. In the second stage, the spin information is irreversibly lost after the time τ_e when the randomizing scattering takes place [104, 113]. Notably, this decay is in general not exponential [104, 114, 115].

(ii) In most cases, the system is found in the strong scattering regime, i.e., $L_{so} \geq l_e$, which is commonly known as the DP regime [101]. Here, the spins perform only slight rotations about the SOF before it is scattered. As illustrated in Fig. 2.1, a process occurs which is very similar to a random walk of the spin and leads to spin relaxation [74]. The physics behind this mechanism is *motional narrowing*. Between the uncorrelated scattering events, the spin precesses in a small angle $\delta\phi = \Omega\tau_e/\hbar$ about a random field $\mathbf{\Omega}$. For times t much larger than the scattering time τ_e, i.e., $t = N\tau_e$ with $N \in \mathbb{N}$ and $N \gg 1$, the total spin phase increment ϕ follows a random walk and is, thus, given by the standard deviation, which yields $\phi = \delta\phi\sqrt{N}$ [74]. Defining the spin-relaxation time τ_s as the time at which the total spin phase increment becomes $\phi \approx 1$, we find the relation [74, 101, 104]

$$\frac{1}{\tau_s} = \langle \Omega^2 \rangle \, \tau_e/\hbar^2. \tag{2.1}$$

A salient feature of the motional narrowing effect is the reduction of spin relaxation due to momentum scattering as $\tau_s^{-1} \propto \tau_e$. The original derivation of D'yakonov and Perel' in the regime (ii), which is based on solving the kinetic rate equation for the spin-dependent density matrix, yields a more precise expression for the spin-relaxation rate [17, 104]. In fact, it provides a spin-relaxation tensor $\left(1/\hat{\tau}_s^{(0)}\right)_{ij}$ with $i, j \in \{x, y, z\}$ that describes the polarization-dependent decay of a spin den-

sity which is homogeneously excited in real space. Assuming isotropic scattering, it reads as [17, 117, 118]

$$\left(1/\hat{\tau}_s^{(0)}\right)_{ij} = \frac{4\tau_e}{\hbar^2}(\langle \mathbf{\Omega}^2 \rangle \, \delta_{ij} - \langle \Omega_i \Omega_j \rangle). \tag{2.2}$$

A further extension is given by the *spin diffusion equation*, which determines the temporal and spatial evolution of a local spin density $\mathbf{s}(\mathbf{r}, t)$. Selecting the Fourier representation with small wave vectors $\mathbf{k}$, $\mathbf{q}$, and frequencies ω, leads to the equation for the spin density

$$\mathbf{s}(\mathbf{q}, \omega) = \int \mathrm{d}^d r \int \mathrm{d}t \, e^{-i(\mathbf{q}\cdot\mathbf{r} - \omega t)} \, \mathbf{s}(\mathbf{r}, t), \tag{2.3}$$

that is [64, 67, 119],

$$0 = \left(D_e q^2 - i\omega + 1/\hat{\tau}_s^{(0)}\right) \mathbf{s}(\mathbf{q}, \omega) + \frac{4i\tau_e}{m^*} \langle (\mathbf{q} \cdot \mathbf{k}) \, \mathbf{\Omega} \rangle \times \mathbf{s}(\mathbf{q}, \omega), \tag{2.4}$$

where $D_e = v_F^2 \tau_e / d$ is the diffusion constant in d dimensions and v_F the Fermi velocity. For $\mathbf{q} = 0$, the spin density $\mathbf{s}(\mathbf{r})$ is homogeneous in real space and we recover the situation described by the DP tensor. In contrast to the regime (i), the decay of the total average spin polarization $\boldsymbol{\mathcal{S}}(t) = \int \mathrm{d}^d r \, \mathbf{s}(\mathbf{r}, \mathbf{t})$ in the regime (ii) is exponential. Depending on the initial spin density distribution, locally distinct behavior can be observed as shown in Ref. [120] or Sec. 8.2.2.

Throughout the main parts of this work, Parts II and III, we will focus on the DP spin-relaxation process in the regime (ii). Alternatively to the spin diffusion equation, we mostly follow a Cooperon-based approach, which has the advantage of the simultaneous determination of the quantum correction to the conductivity (cf. Chap. 3). The latter can be studied in magnetoconductance measurements and provides experimental access to the information on spin relaxation and SOC. We determine circumstances in which the DP spin relaxation is suppressed or even absent. For instance, finite-size effects can cause an additional boundary-induced motional narrowing effect, which prolongates the spin lifetime. Also, for certain parameter configurations, the SOF gains a special symmetry, that leads to spin conservation as will be briefly explained in the following.

Spin-Preserving Symmetries

For the realization of spintronic devices, it is crucial to find circumstances in which spin states do not relax, which are called *spin-preserving symmetries*. For non-vanishing SOC and spin-independent disorder, this can be generally fulfilled if the corresponding SOF $\mathbf{\Omega}(\mathbf{k})$ is collinear in k-space. In such a scenario, we can identify a conserved spin quantity Σ, that commutes with the Hamiltonian $\mathcal{H}$, i.e., $[\mathcal{H}, \Sigma] = 0$. This yields persistent solutions for the spin diffusion equation, exhibiting either a homogeneous or a helical spin texture in real space. For k-linear SOC, this special symmetry is characterized by circular Fermi contours $\varepsilon_\pm$, shifted by a constant wave vector $\mathbf{Q}$, i.e., $\varepsilon_-(\mathbf{k}) = \varepsilon_+(\mathbf{k} + \mathbf{Q})$. As a consequence,

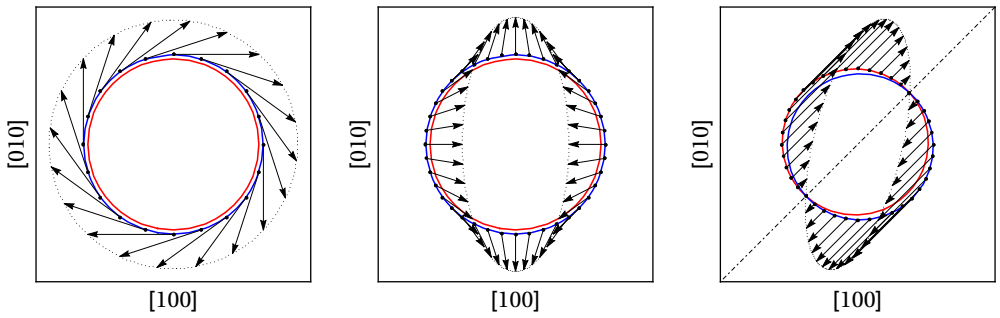

(a) $\boldsymbol{\Omega}_{\mathrm{R}}$ (b) $\boldsymbol{\Omega}_{\mathrm{D}}^{[001]}$ (c) $\boldsymbol{\Omega}_{\mathrm{R}} + \boldsymbol{\Omega}_{\mathrm{D}}^{[001]}|_{\alpha=\beta}$

Fig. 2.2: Rashba (a) and k-linear Dresselhaus (b) SOF $\boldsymbol{\Omega}$ in k-space for a 2DEG grown along [001]. The blue and red circles depict the Fermi contours of the different spin species. For $\alpha = \beta$ the total SOF becomes collinear which allows for persistent spin states.

the spin of electrons traversing the system undergoes a well-defined rotation about the constant direction of the SOF, which is independent of the propagated path, but solely determined by the initial and final position [18], a phenomenon known by now as the *persistent spin helix* [19]. In 2D electron and hole systems due to the interplay of Rashba SOC, Dresselhaus SOC, strain, or curvature effects spin-preserving symmetries can be realized [4, 6, 7, 18, 19, 26, 121]. We study this special feature in 2D electron and hole systems in detail in Part II.

As an introductory example, we shall focus on a 2DEG with Rashba and linear Dresselhaus SOC in the strong scattering regime. Choosing a quantum square well oriented along the [001]-axis and an electric field $\boldsymbol{\mathcal{E}}$ parallel to the growth direction, i.e. $\boldsymbol{\mathcal{E}} = \mathcal{E}_z \hat{\boldsymbol{z}}$, the respective SOF $\boldsymbol{\Omega}(\mathbf{k})$ can be derived by projecting on the lowest subband. Following the definitions of Sec. 1.4, the SOF can be decomposed as $\boldsymbol{\Omega} = \boldsymbol{\Omega}_{\mathrm{R}} + \boldsymbol{\Omega}_{\mathrm{D}}$, where $\boldsymbol{\Omega}_{\mathrm{R}}$ corresponds to the Rashba field and $\boldsymbol{\Omega}_{\mathrm{D}}^{[001]}$ to the Dresselhaus field. Together it yields

$$\boldsymbol{\Omega}(\mathbf{k}) = \begin{pmatrix} \alpha k_y - \beta k_x \\ \beta k_y - \alpha k_x \\ 0 \end{pmatrix}, \tag{2.5}$$

where $\alpha = r_{41}^{6c6c} \mathcal{E}_z$ and $\beta = b_{41}^{6c6c} \langle k_z^2 \rangle$. The SOC in this system permits two special cases corresponding to $\alpha = \pm\beta$, which imply $\boldsymbol{\Omega}(\mathbf{k}) = \alpha(k_y \mp k_x)(1, \pm 1, 0)^\top$, respectively. Hence, the SOF has a uniaxial orientation in k-space and the quantity $\Sigma = \sigma_x \pm \sigma_y$ is conserved for $\alpha = \pm\beta$. Selecting $\alpha = \beta$, we present the Rashba and Dresselhaus SOFs in k-space as well as the combination of both in Fig. 2.2. Accordingly, we can identify two distinct persistent spin textures by means of the spin diffusion equation, Eq. (2.4), that are,

$$\mathbf{s}_{\mathrm{hom}}(\mathbf{r}, t) \propto (1, 1, 0)^\top, \tag{2.6}$$

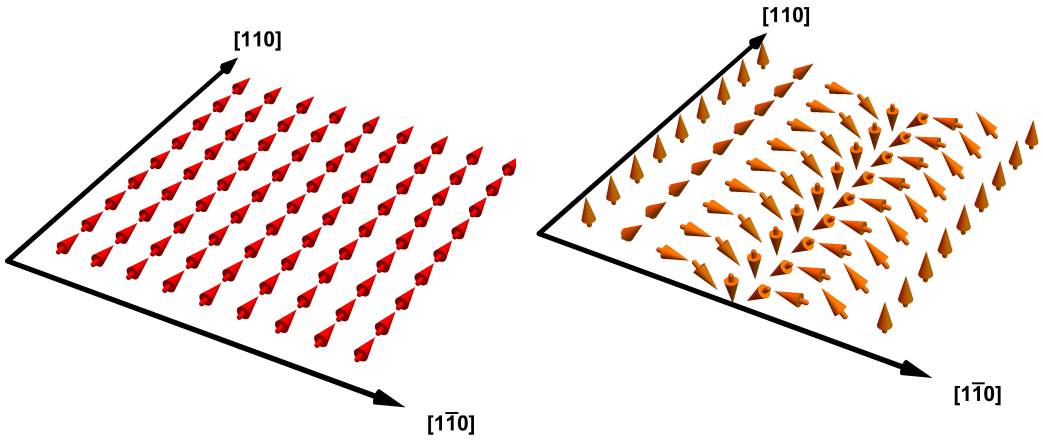

(a) $\mathbf{s}_{\mathrm{hom}}$ **(b)** $\mathbf{s}_{\mathrm{psh}}$

Fig. 2.3: Persistent spin textures in real space for in a 2DEG grown along [001] with equally tuned Rashba and linear Dresselhaus SOC coefficients, i.e., $\alpha = \beta$. (a) Homogeneous spin texture. (b) Persistent spin helix.

$$\begin{aligned}\mathbf{s}_{\mathrm{psh}}(\mathbf{r},t) \propto (0,0,1)^{\top}\cos(Q_{so}(x-y)) \\ + (1,-1,0)^{\top}\sin(Q_{so}(x-y))/\sqrt{2},\end{aligned} \tag{2.7}$$

where $Q_{so} = 4m^*\beta/\hbar^2$. While the first solution is homogeneous in real space with spins oriented parallel to the SOF axis, the second performs a precession about the SOF axis and represents the *persistent spin helix* (PSH). The characteristic wave-like real space pattern of the PSH has been visualized in experiment by means of time-resolved optical Kerr rotation measurements [23]. As the PSH is robust against disorder, it constitutes a candidate for the realization of a spin transistor that also works in a non-ballistic regime, in contrast to the Datta-Das spin field-effect transistor (cf. Fig. 1 and Sec. 1.4.3). Here, the spin precession length of the PSH $L_{so} = 2\pi/Q_{so}$ can be modulated by a simultaneous tuning of the Rashba and Dresselhaus coefficients as shown in Ref. [122]. Notably, in this system the DP spin relaxation is not entirely absent due to the presence of cubic Dresselhaus terms. Furthermore, the spin lifetime can be limited by other relaxation processes as discussed hereafter.

Last but not least, it is to mention that this special symmetry yields also a significant impact on other effects. Some remarkable examples are the cancellation of plasmon damping [123], the vanishing of interband optical absorption and Zitterbewegung [124, 125], and the crossover from weak localization to weak antilocalization [24]. The latter phenomena is introduced in Chap. 3 and constitutes a major theme in this thesis.

2.2 Elliott-Yafet Mechanism

Since in presence of SOC the spin is not a good quantum number, an eigenstate is in general an admixture of spin-up and spin-down components, which depends on the carrier momentum. For simplicity, we consider a bulk semiconductor with a center of inversion. Focusing on a single band, the spin-degenerate eigenstates can

be written as [74, 104, 126, 127]

$$\Psi_{\mathbf{k}\uparrow}(\mathbf{r}) = \Big[a_{\mathbf{k}}(\mathbf{r})\,|+\rangle + b_{\mathbf{k}}(\mathbf{r})\,|-\rangle\Big]e^{i\mathbf{k}\cdot\mathbf{r}}, \tag{2.8}$$

$$\Psi_{\mathbf{k}\downarrow}(\mathbf{r}) = \Big[a^*_{-\mathbf{k}}(\mathbf{r})\,|-\rangle - b^*_{-\mathbf{k}}(\mathbf{r})\,|+\rangle\Big]e^{i\mathbf{k}\cdot\mathbf{r}}, \tag{2.9}$$

with the lattice-periodic coefficients $a_{\mathbf{k}}(\mathbf{r})$ and $b_{\mathbf{k}}(\mathbf{r})$. The ratio of $|b_{\mathbf{k}}|/|a_{\mathbf{k}}| \approx L_{\mathbf{k}}/\Delta E$ depends typically on the strength of the SOC matrix elements $L_{\mathbf{k}}$ between the near-lying bands in comparison to the corresponding band separation ΔE (cf. Sec. 1.2) [104, 127]. If the SOC is weak, we can select the eigenstates such that $|a_{\mathbf{k}}| \approx 1$ and $|b_{\mathbf{k}}| \ll 1$, and we may refer to the states $\Psi_{\mathbf{k},\uparrow}$ and $\Psi_{\mathbf{k},\downarrow}$ as spin-up ($|+\rangle$) and spin-down ($|-\rangle$) states, respectively. However, as it was first noted by Elliott and Yafet (EY) the finite coefficient $b_{\mathbf{k}}$ gives rise to a small probability of flipping the spin in case of momentum scattering [128, 129]. Within first-order perturbation theory, the transition rate $\Gamma_{\mathbf{k},\sigma\to\mathbf{k}',\sigma'}$ can be evaluated by means of Fermi's golden rule. Noting that the spin-flip transition rate $\Gamma_{\mathbf{k},\uparrow\to\mathbf{k}',\downarrow}$ corresponds to the EY spin-relaxation rate τ_s^{-1} and the non-spin-flip transition rate $\Gamma_{\mathbf{k},\uparrow\to\mathbf{k}',\uparrow}$ to momentum scattering rate τ_e^{-1}, we can estimate [104, 126, 127]

$$\frac{\tau_e}{\tau_s} \approx \frac{|\,\langle\Psi_{\mathbf{k}\uparrow}|\hat{V}|\Psi_{\mathbf{k}'\downarrow}\rangle\,|^2}{|\,\langle\Psi_{\mathbf{k}\uparrow}|\hat{V}|\Psi_{\mathbf{k}'\uparrow}\rangle\,|^2} \sim \frac{\langle L^2_{\mathbf{k}}\rangle}{\Delta^2}. \tag{2.10}$$

In the last step, a spin-independent impurity potential $\hat{V}$ is considered, that varies slowly on the scale of a unit cell, and $\langle L^2_{\mathbf{k}}\rangle$ is averaged over the Fermi surface [104, 126, 127].

In particular, the EY spin-relaxation rate for the conduction electrons in a III-V semiconductor was found as [130]

$$\frac{1}{\tau_s} \sim \left(\frac{\Delta_0}{E_0+\Delta_0}\right)^2\left(\frac{E_F}{E_0}\right)^2\frac{1}{\tau_e}, \tag{2.11}$$

where E_F denotes the Fermi energy and E_0 and Δ_0 the band parameters as defined in Sec. 1.3. The EY mechanism is, thus, important for small gap semiconductors with large SOC and high electron densities. It becomes particularly relevant in solids with a center of inversion, where the DP mechanism is absent. An important property of the EY mechanism is the scaling $\tau_s \propto \tau_e$, which is opposed to $\tau_s \propto \tau_e^{-1}$ as found in the DP theory. Therefore, in presence of both mechanisms the experimental investigation of the dependence of τ_s on the electron mobility μ allows to identify the responsible mechanism [16]. Another way to distinguish the two mechanisms is the dissimilar temperature dependence [104].

2.3 Bir-Aronov-Pikus Mechanism

As proposed by Bir, Aronov, and Pikus (BAP), in p-doped semiconductors another spin-relaxation process becomes relevant [131]. Optically excited electron spins in

such a system decay due to the exchange interaction with holes [126]. In this mechanism, electrons with spin-up and holes with spin-down scatter at each other and simultaneously exchange their spins [74]. The scattering process itself does not lead to spin relaxation as it preserves the total spin. However, since the spin-mixing in the valence band is very large as a result of the heavy and light hole coupling, the hole spins relax very quickly by virtue of the EY or DP mechanism [74]. Therefore, this mechanism is important in systems with large hole concentrations and strong hole spin-mixing. It can be distinguished from the EY and DP mechanism through its density and temperature dependence [104].

2.4 Hyperfine Interaction

The exchange interaction between the electron and nuclear spins is another source of spin relaxation. The magnetic moment of the nucleus causes a local Zeeman-field, also called *Overhauser field*, which acts on the electron spin and can cause spin-flips [74, 101, 132]. Since the spins of the lattice nuclei are normally in a disordered state, the nuclei only provide a random effective magnetic field [113]. Thus, this mechanism is ineffective in metallic systems with itinerant electrons since the interaction is motionally narrowed [104]. It is also less important for holes than for electrons as the p-like wave functions have a reduced probability density near the nuclei. Yet, if electrons are confined on quantum dots or bound to donors, this effect can become significant [74, 104].

CHAPTER 3

Quantum Transport Corrections

In the previous chapter, we have seen that scattering processes in combination with spin precession due to SOC in a semiconductor lead to DP spin relaxation. At the same time, the disorder scattering is also the main source for the finite conductivity in metallic systems. Thus, it turns out that the impact of spin relaxation becomes also manifest in the quantum correction to the conductivity, which is called *weak (anti)localization*. Advantageously, this offers the possibility to investigate the spin-relaxation properties and the underlying mechanism, the SOC, experimentally by means of transport measurements. As a particularly attractive feature, it does not require any initial spin polarization and the results are not obscured by excitonic effects in contrast to optical measurements. Yet, the extracted spin lifetime in the magnetoconductance study always refers to long-lived spin states which often exhibit a complex inhomogeneous spin texture in real space. Since the measurement itself does not yield any information about this texture, an in-depth understanding of the linkage between intrinsic spin dynamics and conductivity is an essential prerequisite. To capture this effect theoretically, the SOC needs to be included in the diagrammatic description of quantum transport in disordered conductors.

3.1 Kubo Formula for the Conductivity

The electrical conductivity is described in the classical limit by the *Drude model* and in the semiclassical limit by the *Boltzmann equation*. However, in order to obtain the weak (anti)localization correction a more comprehensive picture is necessary. The quantum mechanical approach is based on the *linear response theory*. It states that the response of a physical observable to a weak external perturbation is in lowest order proportional to the perturbation. Therefore, the proportionality constant contains all the relevant information.

3.1.1 Linear Response Theory

We consider a general Hamiltonian $\mathcal{H}'(t) = \mathcal{H} + V(t)$, where $\mathcal{H}$ represents an time-independent many-body system in thermodynamic equilibrium with the corresponding density matrix $\hat{\rho}$. The quantum system $\mathcal{H}$ interacts with a time-dependent external field $F(t)$ that couples to the operator $\hat{B}$ and, thereby, gives rise to the per-

turbative contribution $V(t) = \hat{B}F(t)$. The resulting non-equilibrium state causes a relative change of the thermal average of an observable $\langle\hat{A}(t)\rangle$ since $\hat{\rho} \to \hat{\rho}'(t)$, that is, $\Delta\hat{A} = \langle\hat{A}(t)\rangle - \langle\hat{A}\rangle_0$, where $\langle\hat{A}\rangle_0 = \mathrm{Tr}(\hat{\rho}\hat{A})$ is the expectation value in absence of the perturbation. To linear order in the perturbation $V(t)$ it yields [133]

$$\Delta\hat{A} = -\frac{i}{\hbar}\int_{-\infty}^{\infty} \mathrm{d}t'\,\theta(t-t')\,\langle[\hat{A}^D(t), \hat{B}^D(t')]\rangle_0\,F(t'), \tag{3.1}$$

where the perturbation is switched on at $t \to -\infty$ and the superscript D indicates that the operators are to be considered in the Dirac picture. This result is known as *Kubo formula*. Notably, within this approximation the non-equilibrium characteristics of the system are fully determined by its unperturbed equilibrium state.

3.1.2 Electrical Conductivity Tensor

Now, let us specify to a disordered system with N electrons, which is represented by the many-body Hamiltonian $\mathcal{H}$. The system is perturbed by a time-dependent electric field $\boldsymbol{\mathcal{E}}(t) = \boldsymbol{\mathcal{E}}_0 \exp[-i(\omega + i\eta)t]$ with frequency ω. Due to an infinitesimally small positive value $\eta \in \mathbb{R}^+$ the field vanishes at times $t \to -\infty$. The field couples to the operator of the electric dipole moment $\mathbf{P}$, i.e., $\mathbf{P} = -e\sum_{i=1}^{N}\mathbf{r}_i$, which gives rise to the perturbation $V(t) = -\mathbf{P}\cdot\boldsymbol{\mathcal{E}}(t)$ [133]. The electric field induces a finite current density $\mathbf{j}$, where the complex conductivity tensor $\sigma_{\mu,\nu}$ represents the linear response coefficient. Consequently, the change of the current density $\Delta\mathbf{j}$ is given by

$$\Delta j_\mu(t) = \frac{i}{\hbar}\sum_\nu \int_{-\infty}^{\infty} \mathrm{d}t'\,\theta(t-t')\,\langle[j_\mu^D(t), P_\nu^D(t')]\rangle_0\,\mathcal{E}_\nu(t'). \tag{3.2}$$

Since the current density is related to the dipole moment via $\mathbf{j} = \dot{\mathbf{P}}/\mathcal{V}$, where $\mathcal{V}$ denotes the volume of the sample, we can rewrite this expression as

$$\Delta j_\mu(t) = \sum_\nu \sigma_{\mu,\nu}\,\mathcal{E}_\nu(t), \tag{3.3}$$

where the conductivity tensor is expressed in terms of a current-current correlation function as

$$\sigma_{\mu,\nu}(\omega) = \mathcal{V}\int_0^\infty \mathrm{d}t'\,e^{i(\omega+i\eta)t'}\int_0^\beta \mathrm{d}\lambda\,\langle j_\mu^D(t'+i\hbar\lambda)j_\nu^D(0)\rangle_0\,. \tag{3.4}$$

Here, we used the fact that the correlation function depends only on the time difference, i.e., $\langle\hat{A}(t)\hat{B}(t')\rangle = \langle\hat{A}(t-t')\hat{B}(0)\rangle = \langle\hat{A}(0)\hat{B}(t'-t)\rangle$, and we employed the *Kubo identity*

$$\frac{i}{\hbar}[\hat{A},\hat{\rho}] = \hat{\rho}\int_0^\beta \mathrm{d}\lambda\,\dot{\hat{A}}(t - i\lambda\hbar), \tag{3.5}$$

where $\hat{\rho} = \exp(-\beta\mathcal{H})/Z$ is the equilibrium density matrix in the canonical ensemble and $Z = \mathrm{Tr}[\exp(-\beta\mathcal{H})]$ the equilibrium partition function. In the following,

we assume that the operator $\mathcal{H}$ is diagonal in a single-particle basis $\{|i\rangle\}$, i.e., $\mathcal{H} = \sum_i \epsilon_i c_i^\dagger c_i$ with the single-particle energies ϵ_i and the fermionic creation (annihilation) operators $c_i^\dagger(c_i)$. We emphasize that since the Hamiltonian $\mathcal{H}$ is not translation-invariant due to disorder, the single-particle basis $\{|i\rangle\}$ is *not* the Bloch basis $\{|\mathbf{k}\rangle\}$ [134]. Expressing the current density operators in second quantization, i.e., $\mathbf{j} = \frac{e}{m^*\mathcal{V}} \sum_{m,n} \langle m|\mathbf{p}|n\rangle\, c_m^\dagger c_n$, yields in the Schrödinger picture

$$\langle j_\mu^D(t' + i\hbar\lambda) j_\nu^D(0)\rangle_0 = \frac{e^2}{m^{*2}\mathcal{V}^2} \sum_{m,n,j,l} e^{\frac{i}{\hbar}(\epsilon_m - \epsilon_n)t'} \langle m|p_\mu|n\rangle \langle j|p_\nu|l\rangle \operatorname{Tr}(\hat{\rho}_0 c_m^\dagger c_n c_j^\dagger c_l), \tag{3.6}$$

which can be further simplified by means of *Wick's theorem* that implies the identity [135]

$$\operatorname{Tr}(\hat{\rho}_0 c_m^\dagger c_n c_j^\dagger c_l) = \delta_{m,l}\delta_{n,j} f(\epsilon_m)(1 - f(\epsilon_n)), \tag{3.7}$$

with the *Fermi-Dirac distribution* $f(\epsilon)$. Evaluating both integrals, the frequency-dependent complex conductivity tensor is expressed in terms of single-particle states as [135, 136]

$$\sigma_{\mu,\nu}(\omega) = \frac{i\hbar e^2}{\mathcal{V} m^{*2}} \sum_{j,l} \frac{\langle j|p_\mu|l\rangle \langle l|p_\nu|j\rangle}{\hbar\omega + \epsilon_l - \epsilon_j + i\eta} \frac{f(\epsilon_j) - f(\epsilon_l)}{\epsilon_l - \epsilon_j}. \tag{3.8}$$

The real part of $\sigma_{\mu,\nu}$ gives the dissipative contribution, the imaginary part leads to persistent currents.

3.1.3 Longitudinal Static Conductivity

Relevant for our purpose is the real part of the longitudinal conductivity tensor in the zero-frequency (DC) limit. Selecting without loss of generality $\nu = \mu = x$, the real part of Eq. (3.8) takes the form

$$\operatorname{Re}\sigma_{x,x}(\omega) = \frac{2\pi\hbar}{\mathcal{V}} \frac{e^2}{m^{*2}} \sum_{j,l} |\langle j|p_x|l\rangle|^2 \frac{f(\epsilon_j) - f(\epsilon_l)}{\epsilon_l - \epsilon_j} \delta(\hbar\omega + \epsilon_l - \epsilon_j), \tag{3.9}$$

where we included now an additional factor 2 accounting for both spin channels and set $\eta \to 0$. We can further simplify in the DC-limit using the relations

$$\lim_{\omega\to 0} \frac{f(\epsilon_j) - f(\epsilon_l)}{\epsilon_l - \epsilon_j} \delta(\hbar\omega + \epsilon_l - \epsilon_j) = \int_{-\infty}^{\infty} \mathrm{d}E \left(-\frac{\partial f(E)}{\partial E}\right) \delta(E - \epsilon_j)\delta(E - \epsilon_l). \tag{3.10}$$

Employing this identity yields the *Kubo-Greenwood formula*[1] for the longitudinal DC-conductivity [137]. We can write it representation-free as a trace, which reads at temperature $T = 0$ as [134, 136]

$$\operatorname{Re}\sigma_{x,x}(0) = \frac{2\pi\hbar}{\mathcal{V}} \frac{e^2}{m^{*2}} \operatorname{Tr}\left[p_x \delta(E_F - \mathcal{H}) p_x \delta(E_F - \mathcal{H})\right], \tag{3.11}$$

[1] Other closely related expressions are frequently also termed as *Kubo-Greenwood formula*. [134]

with the single-particle Hamiltonian $\mathcal{H}$ and the Fermi energy E_F .

In the present form, the conductivity depends on the spatial arrangement of the disorder potentials. As the disorder potentials are randomly positioned, different probed samples should exhibit individual characteristics for the macroscopic conductance. In the same way, the conductance of a single sample is very sensitve to modifications of external parameters, e.g., the electron density, which are called *(universal) conductance fluctuations* [136]. These features, however, only occur if the dephasing (phase-coherence) length l_ϕ is larger than the system size. In the contrary case, the system can be imagined as being composed of a large number of individual, each phase-coherent, subsystems. As a result, the measured conductance constitutes an incoherent ensemble average over all subsystems and the conductance fluctuations disappear. This important phenomenon is commonly named *self-averaging* [138]. The temperature and magnetic field dependence of the universal conductance fluctuations are a useful feature for gathering information about the dephasing length in experiment [78]. Remarkably, it turns out that many of the features of the randomly disordered conductors are independent of the details of the system. For instance, the leading quantum corrections to the conductivity are not affected by self-averaging if the mean free path l_e is much smaller than the dephasing length l_ϕ. We may use this important fact and perform a disorder (impurity) average $\langle . \rangle_{\text{imp}}$ over all possible impurity configurations of the disorder potential in Eq. (3.11). The average restores the translational invariance and we can employ the Bloch representation.

3.2 Diagrammatics in Disordered Systems

In order to study electron-impurity scattering in disordered conductors, we briefly introduce the diagrammatic perturbation theory. It is based on the Green's function formalism for non-interacting particles described by the single-particle Schrödinger equation. To investigate the propagation in a random potential, we make use of Feynman diagrams, which constitute a representation of perturbation theory to infinite order. These diagrams are then sorted by their magnitude in the case of weak disorder. Performing an average over all impurity configurations, we recover the Drude and Boltzmann result for the longitudinal static conductivity. Additionally, the small but crucial weak (anti)localization correction due to quantum interference is identified.

3.2.1 Green's Functions and the Dyson Equation

We consider a time-independent Hamiltonian $\mathcal{H} = \mathcal{H}_0 + V$, which is composed of a kinetic term $\mathcal{H}_0$ (later also including SOC) and a static spin-independent disorder potential V. The Schrödinger equation that describes the single-particle dynamics reads as

$$i\hbar \frac{\partial}{\partial t} \psi(\mathbf{r}, t) = \mathcal{H}\, \psi(\mathbf{r}, t). \tag{3.12}$$

We define the *full*[2] Green's function $G(\mathbf{r}, t, \mathbf{r}', t')$ as solution to the differetial equation [139]

$$\left[i\hbar\frac{\partial}{\partial t} - \mathcal{H}\right] G(\mathbf{r}, t, \mathbf{r}', t') = 0. \tag{3.13}$$

The Green's function is also called propagator since it allows to construct the wave function $\psi(\mathbf{r}, t)$ at an arbitrary space-time coordinate from a given reference state $\psi(\mathbf{r}', t')$ as [138]

$$\psi(\mathbf{r}, t) = \int \mathrm{d}^d r'\, G(\mathbf{r}, t, \mathbf{r}', t')\psi(\mathbf{r}', t'), \tag{3.14}$$

where we identify $G(\mathbf{r}, t, \mathbf{r}', t') = \langle \mathbf{r}|\hat{G}(t, t')|\mathbf{r}'\rangle$ with the Green operator $\hat{G}(t - t') = e^{-\frac{i}{\hbar}\mathcal{H}(t-t')}$. Following standard convention, we can distinguish the propagation forward and backward in time by defining the retarded (R) and advanced (A) Green operators as $\hat{G}^{R/A}(t - t') = \mp i\theta[\pm(t - t')]\,\hat{G}(t - t')$, respectively. In Fourier representation, the retarded and advanced Green's functions $G^{R/A}(\mathbf{k}, \mathbf{k}', E)$ take the form [136]

$$G^{R/A}(\mathbf{k}, \mathbf{k}', E) = \left\langle \mathbf{k} \middle| \frac{1}{E - \mathcal{H} \pm i\eta} \middle| \mathbf{k}' \right\rangle, \tag{3.15}$$

with the respective Green operators in the energy domain $\hat{G}^{R/A}(E) = (E - \mathcal{H} \pm i\eta)^{-1}$ and an infinitesimally small positive real value η. Using the Dirac identity $(x \pm i\eta)^{-1} = \mathcal{P}(x^{-1}) \mp i\pi\delta(x)$, where $\mathcal{P}$ denotes the Cauchy principal value, we find the general relation to the density of states (per spin)[3] $\nu(E)$ as

$$\begin{aligned}\nu(E) &= \mathrm{Tr}\,[\delta(E - \mathcal{H})] \\ &= \frac{1}{2\pi i}\mathrm{Tr}[\hat{G}^A(E) - \hat{G}^R(E)] = \mp\frac{1}{\pi}\mathrm{Im}\,\mathrm{Tr}(\hat{G}^{R/A}).\end{aligned} \tag{3.16}$$

Accordingly, we can define the *free* Green's functions $G_0^{R/A}(\mathbf{k}, \mathbf{k}', E)$ which are associated with the impurity-free Hamiltonian $\mathcal{H}_0$ and read

$$G_0^{R/A}(\mathbf{k}, \mathbf{k}', E) = \left\langle \mathbf{k} \middle| \frac{1}{E - \mathcal{H}_0 \pm i\eta} \middle| \mathbf{k}' \right\rangle, \tag{3.17}$$

Notice that owing to the translational-invariance of $\mathcal{H}_0$ the relations $G_0^{R/A}(\mathbf{k}, \mathbf{k}') = G_0^{R/A}(\mathbf{k})\delta(\mathbf{k} - \mathbf{k}')$ as well as in real space $G_0^{R/A}(\mathbf{r}, \mathbf{r}') = G_0^{R/A}(\mathbf{r} - \mathbf{r}')$ hold true.

As we are interested in a perturbative treatment of the impurity potential, it is useful to express the full Green's functions in terms of free Green's functions and impurity potentials. This gives rise to an iterative equation, called *Dyson equation*, which reads in spatial representation as [139]

$$G(\mathbf{r}, \mathbf{r}', E) = G_0(\mathbf{r}, \mathbf{r}', E) + \int \mathrm{d}^d R_1\, G_0(\mathbf{r}, \mathbf{R}_1, E)V(\mathbf{R}_1)G(\mathbf{R}_1, \mathbf{r}', E), \tag{3.18}$$

[2] Synonymous expressions for the *full* Green's function, that are sometimes found in literature, are *dressed* or *renormalized* Green's function [139].

[3] Notice that a factor 2 accounting for two-fold spin-degeneracy was included in Sec. 3.1.3.

or equivalently in k-space

$$G(\mathbf{k},\mathbf{k}',E) = G_0(\mathbf{k},E)\delta_{\mathbf{k},\mathbf{k}'} + G_0(\mathbf{k},E)\sum_{\mathbf{q}}\langle\mathbf{k}|V|\mathbf{q}\rangle\, G(\mathbf{q},\mathbf{k}',E), \tag{3.19}$$

where we suppressed the R/A superscript. The full propagator contains all possible ways to connect $|\mathbf{r}\rangle$ and $|\mathbf{r}'\rangle$ (or $|\mathbf{k}\rangle$ and $|\mathbf{k}'\rangle$ in k-space) in presence of a given disorder potential. We can represent this diagrammatically as

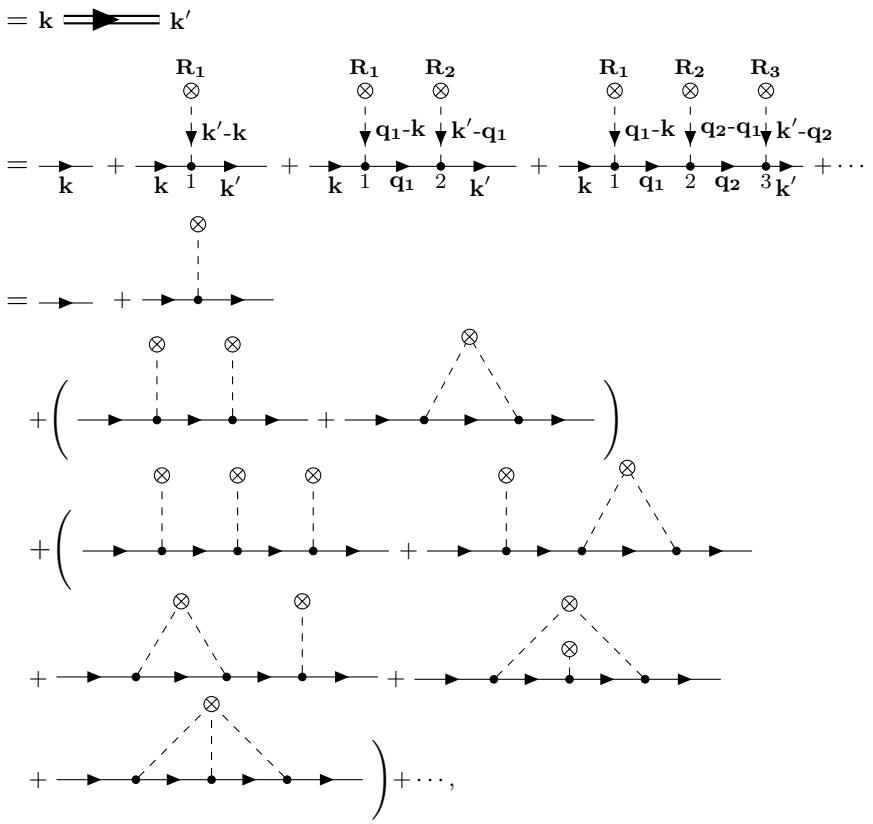

where the full retarded propagator is depicted as double fermion line propagating from $\mathbf{k}$ and $\mathbf{k}'$. It can be expanded as a sum of free propagations (single fermion lines) that are interrupted by scattering incidents, which are depict by the vertices ($\bullet$) and related to the scattering centers ($\otimes$) at the positions $\mathbf{R}_{1,2,3...}$ via the impurity lines (dashed lines). At each impurity, the fermion is elastically scattered, changing randomly the momentum direction $\mathbf{q}_{1,2,3...}$ between two vertices. After the last equality sign, it is shown that the diagrams can be sorted by their order n in the potential V, which corresponds to the number of vertices or scattering events. Double scattering at the same impurity will constitute particularly important contribution. The according advanced Green's function is obtained by reversing the arrows in the fermion lines.

3.2.2 Impurity-Averaged Propagator

Since the particular disorder configurations are usually unknown and the arising observable effects are canceled by the self-averaging (for systems much larger than the dephasing length), we shall only be interested in the impurity-averaged propagator $\langle G \rangle_{\text{imp}}$. To this end, we specify the disorder potential $V(\mathbf{r})$ to be continuous and random. The zero-energy is chosen such that the potential vanishes on average, i.e., $\langle V(\mathbf{r}) \rangle_{\text{imp}} = 0$. Also, we presuppose translational invariance for the correlation function, which we define as $\langle V(\mathbf{r}) V(\mathbf{r}') \rangle_{\text{imp}} = C(\mathbf{r} - \mathbf{r}')$. Later on, we will further simplify to short-range scatterers, which implies that $C(\mathbf{r} - \mathbf{r}') = C\delta(\mathbf{r} - \mathbf{r}')$.[4] The corresponding model for the disorder potential is then called *white noise model* [136].

Using these definitions, the impurity-averaged propagator $\langle G \rangle_{\text{imp}}$ takes a much simpler form. First of all, the translational invariance is recovered, i.e.,

$$\langle G(\mathbf{k}, \mathbf{k}') \rangle_{\text{imp}} = \langle G(\mathbf{k}) \rangle_{\text{imp}} \, \delta(\mathbf{k} - \mathbf{k}'), \tag{3.20}$$

where we suppress from now on the argument E since the elastic scattering preserves the energy. Secondly, all odd-order terms in V drop out of the infinite sum and Eq. (3.18) becomes [136]

$$\langle G(\mathbf{k}) \rangle_{\text{imp}} = G_0(\mathbf{k}) + \frac{1}{\mathcal{V}} \sum_{\mathbf{q}} C(\mathbf{k} - \mathbf{q}) G_0(\mathbf{k}) G_0(\mathbf{q}) G_0(\mathbf{k}) + \cdots . \tag{3.21}$$

with $C(\mathbf{q}') = \int \mathrm{d}^d r \, e^{-i\mathbf{q}' \cdot \mathbf{x}} C(\mathbf{x})$, or diagrammatically

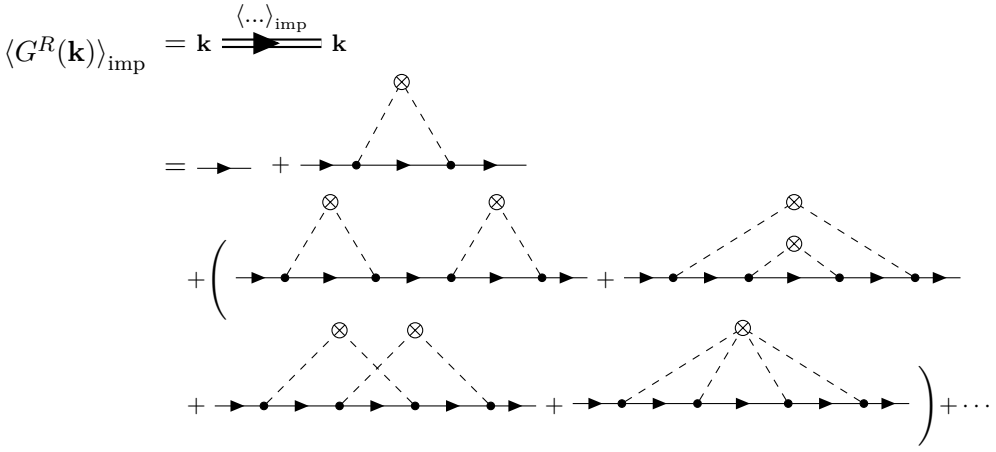

We can distinguish two different types of diagrams: reducible and irreducible diagrams. The reducible diagrams may be separated into irreducible ones without cutting the impurity lines. For instance, the first diagram with four vertices is

[4] Notice that the constant C has the dimension of energy squared times volume.

factorized into a product of the diagram with two vertices. As a consequence, we can rewrite the equation above as a Dyson equation

$$\langle G(\mathbf{k})\rangle_{\text{imp}} = G_0(\mathbf{k}) + G_0(\mathbf{k})\Sigma(\mathbf{k})\,\langle G(\mathbf{k})\rangle_{\text{imp}}\,, \tag{3.22}$$

where $\Sigma(\mathbf{k})$ is called the *self-energy* and contains all irreducible diagrams (without the free propagator before and after the first and the last vertex, respectively). Thus, we can express the full impurity-averaged Green's function in terms of the self-energy as [136]

$$\langle G(\mathbf{k})\rangle_{\text{imp}}^{R/A} = \frac{1}{E - E(\mathbf{k}) - \Sigma^{R/A}(\mathbf{k})}, \tag{3.23}$$

where $\mathcal{H}_0\,|\mathbf{k}\rangle = E(\mathbf{k})\,|\mathbf{k}\rangle$. A remarkable feature of the self-energy is that it can be well approximated by a finite number of (the most significant) diagrams. The Dyson equation nonetheless ensures that certain diagrams are included in the Green's function to *infinite* order.

In the following, we focus on the limit of weak disorder, meaning that the Fermi energy is much larger than the energy associated with the mean free scattering time, i.e., $E_F \gg \hbar/\tau_e$ or equivalently $k_F l_e \gg 1$.[5] A quantitative comparison of the irreducible diagrams reveals that the diagrams without crossed impurity lines and no more than double scattering at the same impurity are dominant. Using this so-called *Born approximation* (BA), the Green's function reads as

$$G_{\text{BA}}^{R/A} = \left\langle G^{R/A}\left(\mathbf{k}, \Sigma_{\text{BA}}^{R/A}\right)\right\rangle_{\text{imp}}, \tag{3.24}$$

with

$$\Sigma_{\text{BA}}^{R/A}(\mathbf{k}) = \frac{1}{\mathcal{V}}\sum_{\mathbf{q}} C(\mathbf{k}-\mathbf{q})G_{\text{BA}}^{R/A}(\mathbf{q}), \tag{3.25}$$

or diagrammatically

$\Sigma_{\text{BA}}^{R}(\mathbf{k}) =$ 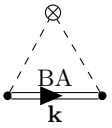

.

The computation of the self-energy is still a delicate issue as it includes an infinite number of terms. A first estimate can be obtained by inserting the free Green's function into Eq. (3.25), which is known as *first Born approximation* (1BA) and will be used hereafter. The real part of the self-energy only causes an unimportant energy shift and shall be disregarded. The imaginary part, on the other hand, moves the poles of $G_{\text{1BA}}^{R/A}$ away from the real axis and gives the momentum states a finite lifetime. Hence, we can write

$$\mathcal{G}^{R/A}(\mathbf{k}) := G_{\text{1BA}}^{R/A}(\mathbf{k}) = \frac{1}{E - E(\mathbf{k}) \pm i\frac{\hbar}{2\tau_e(\mathbf{k})}}, \tag{3.26}$$

[5] The elastic scattering rate τ_e^{-1} can be estimated via Fermi's golden rule which coincides with our definition via the first Born approximation for the self-energy in Eq. (3.27).

where the elastic scattering time τ_e is defined through

$$\frac{\hbar}{2\tau_e} := -\operatorname{Im}\Sigma^R_{\mathrm{1BA}}(\mathbf{k}, G^R_0), \tag{3.27}$$

which yields

$$\frac{\hbar}{\tau_e} = \frac{2\pi}{\mathcal{V}}\sum_{\mathbf{q}} C(\mathbf{k}-\mathbf{q})\delta(E - E(\mathbf{q})). \tag{3.28}$$

Since both $\mathbf{q}$ and $\mathbf{k}$ are fixed at the same energy for elastic scattering, we can replace

$$\sum_{\mathbf{k}} \to \int \frac{\mathrm{d}\Omega_d}{\Omega_d}\int_0^\infty \mathrm{d}E'\,\nu_0(E'), \tag{3.29}$$

where $\Omega_d = 2\sqrt[d]{\pi}/\Gamma\left(d/2\right)$ denotes the d-dimensional solid angle with Euler's Gamma function Γ and $\nu_0(E)$ the free density of states, associated with $\mathcal{H}_0$. Thus, Eq. (3.28) simplifies to

$$\frac{\hbar}{\tau_e} = \frac{2\pi}{\mathcal{V}}\nu_0(E)\left\langle C(E, \hat{\mathbf{k}}-\hat{\mathbf{q}})\right\rangle, \tag{3.30}$$

where $\langle ...\rangle$ represents the angular average over the relative orientation of the unit vectors $\hat{\mathbf{k}}$ and $\hat{\mathbf{q}}$. Therefore, the elastic scattering time is independent of the wave vector orientation. Notably, the identical result is obtained by applying *Fermi's golden rule* [136]. In the limit of short-range scatterers, above expression becomes

$$\frac{\hbar}{\tau_e} = 2\pi C\nu_0(E)/\mathcal{V}. \tag{3.31}$$

The finite lifetime induces a broadening of the δ-distribution in the density of states $\nu(E)$, Eq. (3.16). As a consequence, the energy of a particle with wave vector $\mathbf{k}$ can differ by an amount of $\hbar/(2\tau_e)$ [138].

3.3 Conductivity for Weak Disorder

Hereafter, we employ the framework derived in the previous section to compute the impurity-averaged longitudinal static conductivity in the weak disorder limit. First, we express Eq. (3.11) in terms of the full Green's functions and perform an average over all impurity configurations, which gives

$$\begin{aligned}\operatorname{Re}\sigma_{x,x}(0) = \frac{\hbar^3 e^2}{2\pi\mathcal{V}m^{*2}}\sum_{\mathbf{k},\mathbf{k}'} k_x k'_x \Big\langle &\langle\mathbf{k}|\hat{G}^A(E_F) - \hat{G}^R(E_F)|\mathbf{k}'\rangle \\ &\times \langle\mathbf{k}'|\hat{G}^R(E_F) - \hat{G}^A(E_F)|\mathbf{k}\rangle\Big\rangle_{\mathrm{imp}} \\ = \frac{\hbar^3 e^2}{2\pi\mathcal{V}m^{*2}}\sum_{\mathbf{k},\mathbf{k}'} k_x k'_x \Big\langle &2G^R(\mathbf{k},\mathbf{k}')G^A(\mathbf{k}',\mathbf{k}) - G^R(\mathbf{k},\mathbf{k}')G^R(\mathbf{k}',\mathbf{k})\end{aligned}$$

$$-G^A(\mathbf{k},\mathbf{k}')G^A(\mathbf{k}',\mathbf{k})\Big\rangle_{\text{imp}}\,, \tag{3.32}$$

where we suppressed the argument E_F in the Green's functions. Apparently, the equation above contains the impurity-averaged products $\langle G^R G^A\rangle_{\text{imp}}$, $\langle G^R G^R\rangle_{\text{imp}}$, and $\langle G^A G^A\rangle_{\text{imp}}$. It can be shown that the latter two products are of higher order in $(k_F l_e)^{-1}$ than $\langle G^R G^A\rangle_{\text{imp}}$ and can be disregarded in the limit of weak disorder [136]. Hence, we are left with the term

$$\operatorname{Re}\sigma_{x,x}(0) = \frac{\hbar^3 e^2}{\pi \mathcal{V} m^{*2}} \sum_{\mathbf{k},\mathbf{k}'} k_x k_x' \left\langle G^R(\mathbf{k},\mathbf{k}')G^A(\mathbf{k}',\mathbf{k})\right\rangle_{\text{imp}}\,, \tag{3.33}$$

which will be investigated in the following in first Born approximation.

Due to the occurence of the product $\langle G^R G^A\rangle_{\text{imp}}$, one has, in principle, to consider all possible diagrams that connect both fermion lines via impurity scattering, which are denoted as *vertex corrections* [138]. We diagrammatically represent them by the green box Λ between ingoing and outgoing retarded and advanced full propagators (in 1BA), i.e.,

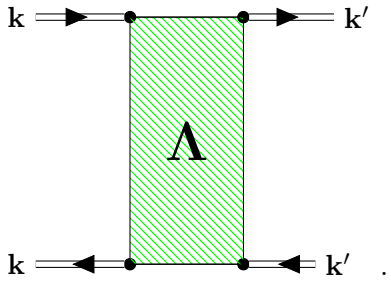

Yet, particle conservation demands that including certain diagrams for the self-energy implies that the corresponding diagrams must also appear in the vertex corrections. This follows from a general relation, called *Ward identity*, which is based on the continuity equation [138]. In practice, this requirement may be relaxed to some extent if the additional inclusion or neglection of certain diagrams does not seriously violate the particle conservation law.

3.3.1 Drude-Boltzmann Conductivity

In the crudest approximation, we perform an individual impurity-average for each of the Green's functions, i.e.,

$$\sigma_0 := \frac{\hbar^3 e^2}{\pi \mathcal{V} m^{*2}} \sum_{\mathbf{k},\mathbf{k}'} k_x k_x' \left\langle G^R(\mathbf{k},\mathbf{k}')\right\rangle_{\text{imp}} \left\langle G^A(\mathbf{k}',\mathbf{k})\right\rangle_{\text{imp}}\,, \tag{3.34}$$

which yields in d dimensions using 1BA

$$\sigma_0 = \frac{\hbar^3 e^2}{\pi \mathcal{V} m^{*2}} \sum_{\mathbf{k}} k_x^2 |\mathcal{G}^R(\mathbf{k})|^2$$

$$
\begin{aligned}
&= \frac{\hbar^3 e^2}{\pi \mathcal{V} m^{*2}} \sum_{\mathbf{k}} \frac{k^2}{d} \frac{1}{(E_F - E(\mathbf{k}))^2 + \left(\frac{\hbar}{2\tau_e}\right)^2} \\
&\approx \frac{e^2 \tau_e}{m^*} \frac{2\Omega_d k_F^d}{(2\pi)^d d} \\
&= \frac{e^2 \tau_e}{m^*} n, \qquad (3.35)
\end{aligned}
$$

where the Fermi wave vector k_F is related to the d-dimensional electron density n as

$$
k_F = \begin{cases} \frac{\pi}{2} n & \text{for } d = 1, \\ \sqrt{2\pi n} & \text{for } d = 2, \\ (3\pi^2 n)^{1/3} & \text{for } d = 3. \end{cases} \qquad (3.36)
$$

Here, we approximated the Lorentzian as $\delta(x) = \lim_{\eta \to 0} \frac{1}{\pi} \frac{\eta}{x^2 + \eta^2}$, which is justified for weak disorder. The above result is identical with the pure classical result, that was found by Drude [140, 141].

Going beyond the approximation of Eq. (3.34), we notice that the 1BA approximation for the self-energy requires to take into account all *ladder diagrams* Λ_D for the vertex corrections, which are depicted as

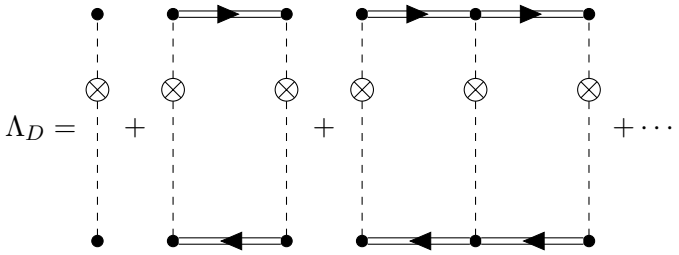

and called *Diffuson corrections*. However, it turns out that for isotropic scattering these diagrams do not contribute to the conductivity. In the case of non-isotropic scattering we recover the semi-classical Boltzmann result. It coincides with the classical Drude conductivity upon the appearance of the *transport time* τ_{tr} instead of the mean elastic scattering time, i.e., $\sigma_0 = e^2 n \tau_{\mathrm{tr}} / m^*$. The transport time is related to the elastic scattering time, Eq. (3.29), as [136]

$$
\frac{\hbar}{\tau_{\mathrm{tr}}(\mathbf{k})} = \frac{2\pi}{\mathcal{V}} \nu_0(E_F) \left\langle C(E_F, \hat{\mathbf{k}} - \hat{\mathbf{q}})(1 - \hat{\mathbf{k}} \cdot \hat{\mathbf{q}}) \right\rangle . \qquad (3.37)
$$

This correction expresses the fact that small-angle scattering does barely diminish the current [139].

In the subsequent study of the weak (anti)localization correction, we focus only on the simple case of isotropic scattering. Nevertheless, it can be shown that the obtained results are also valid for anisotropic collisions if the current operator is renormalized [136]. This is achieved by replacing in Eq. (3.33) one of the wave vectors, e.g., k_x by $k_x \tau_{\mathrm{tr}} / \tau_e$, or equivalently the diffusion constant $D_e \to D_e \tau_{\mathrm{tr}} / \tau_e$.

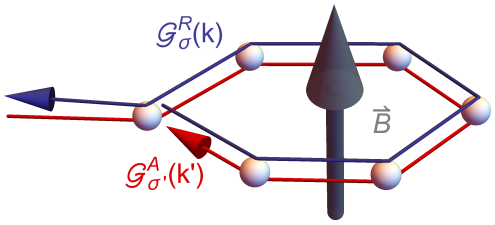

Fig. 3.1: Quantum interference between pairs of electron waves, that are counter-propagating in a closed loops, gives rise to weak (anti)localization. This effect is sensitive to magnetic fields **B** perpendicular to the enclosed area since it breaks the time-reversal symmetry and destroys the constructive (destructive) interference.

3.3.2 Weak (Anti)Localization

So far, we were able to reproduce the formulas for the electrical conductivity also found by the (semi)classical approach. For the vertex correction, only the ladder diagrams were included in which the impurity lines do not cross. There exists another special class of diagrams, which represent interference processes that also survive the self-averaging. In these diagrams, the impurity lines cross a maximum number of times, which corresponds to a situation where two electron waves scatter at the same set of impurities in reversed order. In the case that the electron trajectories form a closed loop and the incident and final waves are antiparallel, the quantum interference between the counter-propagating paths causes a conductivity correction (cf. Fig. 3.1). The maximally crossed diagrams Λ_C, diagrammatically depicted as

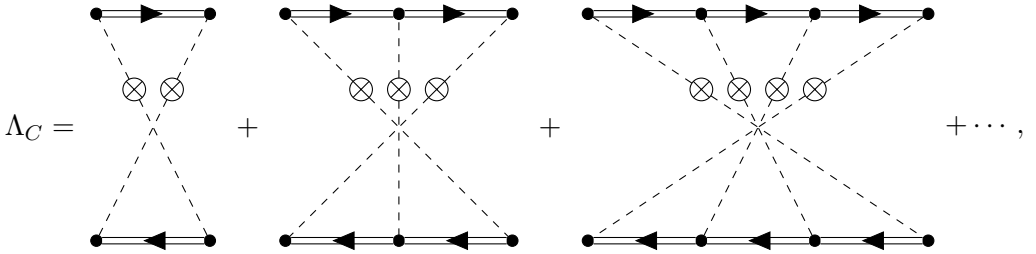

were not included in the first Born approximation and are smaller by a factor $(k_F l_e)^{-1}$ [139]. Nevertheless, they give rise to the leading quantum correction to the conductivity $\Delta\sigma$ called *weak localization* (WL) or *weak antilocalization* (WAL) if $\Delta\sigma < 0$ or $\Delta\sigma > 0$, respectively. As mentioned earlier, taking into account these vertex corrections, we should also include the according diagrams in the self-energy. However, for weak disorder, the resulting violation of particle conservation is insignificant and can be safely ignored [138].

In order to solve this problem, we can make use of the time-reversal symmetry and unwind the lower fermion line. As a result, we are effectively dealing with a diagram, which is analogous to the ladder diagram but with both fermion lines running in the same direction. The respective series of diagrams is represented by

the yellow box as

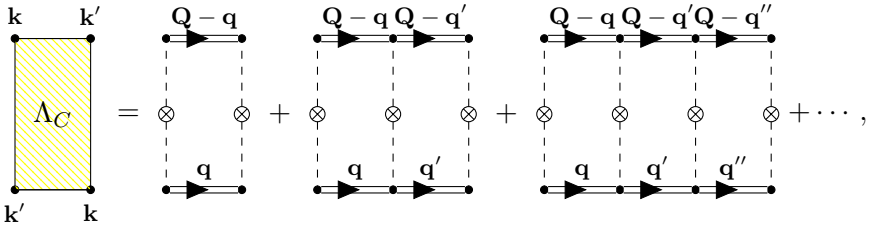

with $\mathbf{Q} = \mathbf{k}+\mathbf{k}'$. It can be rewritten as a Dyson-like equation, called *Bethe-Salpeter equation* [136], as

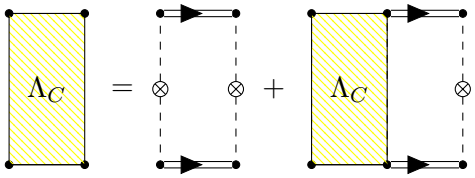

which yields for short-range scatterers the solution

$$\Lambda_C(\mathbf{Q}) = \frac{C}{\mathcal{V}} \frac{I(\mathbf{Q})}{1 - I(\mathbf{Q})}, \tag{3.38}$$

where $C = \mathcal{V}\hbar/(2\pi\nu_0(E_F)\tau_e)$ (cf. Eq. (3.31)) and we introduced the auxiliary function

$$I(\mathbf{Q}) = \frac{C}{\mathcal{V}} \sum_{\mathbf{q}} \mathcal{G}^R(\mathbf{Q}-\mathbf{q})\mathcal{G}^A(\mathbf{q}), \tag{3.39}$$

or diagrammatically

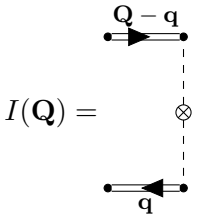

where we used $\mathcal{G}^A(\mathbf{q}) = \mathcal{G}^A(-\mathbf{q})$ due to time-reversal symmetry. Thus, the quantum conductivity correction takes the form

$$\Delta\sigma = \frac{\hbar^3 e^2}{\pi \mathcal{V} m^{*2}} \sum_{\mathbf{k},\mathbf{Q}} k_x(Q_x - k_x)\mathcal{G}^R(\mathbf{k})\mathcal{G}^A(\mathbf{k})\Lambda_C(\mathbf{Q})\mathcal{G}^R(\mathbf{Q}-\mathbf{k})\mathcal{G}^A(\mathbf{Q}-\mathbf{k}), \tag{3.40}$$

where we replaced $\mathbf{k}' = \mathbf{Q}-\mathbf{k}$. Apparently, the main contribution of $\Lambda_C(\mathbf{Q})$ results from the pole, where $I(\mathbf{Q}) \approx 1$. Noticing that $I(0) = 1$, it becomes evident that the conductivity correction is primarily determined by small wave vectors $\mathbf{Q} \approx \mathbf{0}$.

This situation corresponds to backscattering since $\mathbf{k} \approx -\mathbf{k}'$. In this limit, we may approximate Eq. (3.40) as

$$\begin{aligned}\Delta\sigma = & -\frac{\hbar^3 e^2}{\pi \mathcal{V} m^{*2}} \sum_{\mathbf{k},\mathbf{Q}} k_x^2 \mathcal{G}^R(\mathbf{k}) \mathcal{G}^A(\mathbf{k}) \Lambda_C(\mathbf{Q}) \mathcal{G}^R(-\mathbf{k}) \mathcal{G}^A(-\mathbf{k}) \\ \approx & -\frac{\hbar^4 e^2 C}{\pi \mathcal{V}^2 m^{*2} \tau_e} \sum_{\mathbf{Q}} \hat{\mathcal{C}}(\mathbf{Q}) \sum_{\mathbf{k}} \frac{k^2}{d} |\mathcal{G}^R(\mathbf{k})|^4 \\ \approx & -2 \times \frac{2e^2}{h} \frac{\hbar D_e}{\mathcal{V}} \sum_{\mathbf{Q}} \hat{\mathcal{C}}(\mathbf{Q}), \end{aligned} \tag{3.41}$$

with the *Cooperon* propagator

$$\hat{\mathcal{C}}(\mathbf{Q}) = \frac{\tau_e}{\hbar} \left[1 - I(\mathbf{Q})\right]^{-1}. \tag{3.42}$$

and the diffusion constant $D_e = v_F^2 \tau_e / d$. For weak disorder, it is usually expanded in terms of small $\mathbf{Q}$. Approximating the auxiliary function in this limit (cf. App. 3.A), the Cooperon simplifies to

$$\hat{\mathcal{C}}(\mathbf{Q}) = \frac{\tau_e}{\hbar} \left[1 - \int \frac{\mathrm{d}\Omega_d}{\Omega_d} \frac{1}{1 - i\tau_e \hat{\Sigma}(\mathbf{Q})/\hbar}\right]^{-1}, \tag{3.43}$$

where $\hat{\Sigma}(\mathbf{Q}) = \mathcal{H}_0(\mathbf{Q} - \mathbf{k}_F) - \mathcal{H}_0(\mathbf{k}_F)$ and the averaging is performed over all angles of $\mathbf{k}_F$. In real space, the Cooperon $\hat{\mathcal{C}}(\mathbf{r}, \mathbf{r})$ can be interpreted as the quantum interference contribution to the probability of return [136]. For a spin-independent system, the correction Eq. (3.41) reduces the conductivity and is therefore known as WL. The Cooperon is the central object to determine its characteristics. Occurring divergences in the $\mathbf{Q}$-summation in $\Delta\sigma$ can be removed due to finite dephasing and elastic scattering times.

In practice, the quantum conductivity correction is studied in dependence of a magnetic field $\mathbf{B} = \nabla \times \mathbf{A}$ perpendicular to the studied sample. The field breaks the time-reversal symmetry and suppresses the phase-coherence as the electron wave function gains an Aharonov-Bohm phase. The magnetic field effects can be included perturbatively by minimal coupling [5], i.e., $\mathbf{Q} \to \mathbf{Q} + 2e\mathbf{A}/\hbar$, or by means of a magnetic phase-shift rate [4, 61, 67, 142]. Alternatively, the magnetic fields can be treated non-perturbatively using the Landau representation [143–146]. In this work, we focus only on small magnetic fields, where the Landau basis is not suitable.

The Impact of Spin-Orbit Coupling

So far, we have ignored spin-orbit effects. In presence of SOC, we have to explicitly perform the trace over spin states (cf. Eq. (3.11)) and Eq. (3.41) is modified to [143]

$$\Delta\sigma = -\frac{2e^2}{h} \frac{\hbar D_e}{\mathcal{V}} \sum_{\mathbf{Q}} \sum_{s_1, s_2 \in \{\pm\}} \langle s_1, s_2 | \hat{\mathcal{C}}(\mathbf{Q}) | s_2, s_1 \rangle. \tag{3.44}$$

where the term $\hat{\Sigma}(\mathbf{Q}) = \mathcal{H}_0(\mathbf{Q} - \mathbf{k}_F, \boldsymbol{\sigma}) - \mathcal{H}_0(\mathbf{k}_F, \boldsymbol{\sigma}')$ in the expression for the Cooperon, Eq. (3.43), includes now SOC. Note the reversed order of the spin indices in the ket $|s_2, s_1\rangle$, which results from twisting of the lower fermion line in Λ_C. The scattering process above describes interference of two electrons with the wave vectors $\mathbf{k}$ and $\mathbf{k}'$ and spins $\boldsymbol{\sigma}$ and $\boldsymbol{\sigma}'$, respectively. Since we are, thus, effectively dealing with a spin-1 system, it is practical to transform the above equation into singlet-triplet representation (cf. Apps. 3.B and 3.C). As the singlet and triplet sectors are decoupled, the conductivity correction becomes[6]

$$\Delta\sigma = \frac{2e^2}{h}\frac{\hbar D_e}{\mathcal{V}}\mathrm{Re}\left(\sum_{\mathbf{Q}}\sum_{s,m_s}\chi_s \langle s, m_s|\hat{\mathcal{C}}(\mathbf{Q})|s, m_s\rangle\right). \tag{3.45}$$

The states $|s, m_s\rangle$ represent the singlet-triplet basis of the system with two electrons, that is, $s \in \{0, 1\}$ is the total spin quantum number and $m_s \in \{0, \pm 1\}$ the corresponding magnetic quantum number. The prefactor χ_s, which is defined as $\chi_0 = 1$ and $\chi_1 = -1$, reveals the distinct relative contribution of the singlet and triplet states. Since without SOC the states are degenerate, each state contributes equally and we recover Eq. (3.41). However, in presence of SOC the degeneracy is lifted and the relative weight of the triplet terms can be suppressed as a result of spin relaxation, which leads to a positive correction to the conductivity, called WAL. This effect was first pointed out for 2D systems in the seminal paper of Hikami *et al.* [143], who took into account the EY spin-relaxation mechanism (cf. Sec. 2.2). Later, in the pioneering works of Iordanskii *et al.* [144], Pikus *et al.* [145], and Knap *et al.* [146] an analogous theory was developed and applied, accounting for the DP mechanism (cf. Sec. 2.1). The latter is often more relevant and its investigation is the main subject of this thesis. Iordanskii *et al.* [144] took into account Dresselhaus SOC of a [001]-oriented 2DEG. Later, Pikus *et al.* [145] included also Rashba SOC and showed that both contributions to the conductivity correction are not additive, which was afterwards experimentally confirmed in the paper of Knap *et al.* [146] In fact, Pikus *et al.* [145] demonstrated that in absence of the k-cubic Dresselhaus terms and equally tuned Rashba and linear Dresselhaus coefficients, the resulting conductivity correction is equivalent to the case without spin-orbit coupling. However, it took a few more years to realize that this non-additivity also applies to the spin-relaxation rates and the reappearance of the WL features can be a signature of spin-preserving symmetries (cf. Sec. 2.1). Additional ramifications on the conductivity (and therewith the DP spin relaxation) due to finite-size effects were first studied by Kettemann [61].

We can understand this mechanism by noting that a constructive interference after a closed loop demands an alignment of the initial and final spin state. In a system with SOC this requirement is commonly *not* fulfilled, as the spin-orbit field in combination with disorder scattering generates random spin rotations. Therefore, the experimental study of the quantum conductivity correction provides access to the information about spin relaxation. A special situation occurs if the SOC

[6] In order to avoid unphysical small imaginary terms, which may arise as consequence of certain approximations, we restore the real part this general definition.

Hamiltonian exhibits spin-preserving symmetries. In this case, the spin precession is independent of the propagated path and the total rotation vanishes for each closed loop [18]. As a consequence, the suppression of the DP spin relaxation leads at the same time to a (re-)occurrence of WL. This allows for a direct identification of spin-preserving symmetries in transport experiments.

Finally, it shall be mentioned that there exists a unitary transformation between the spin diffusion equation, Eq. (2.4), and the Cooperon [67]. The according basis transformation that relates the components of the spin density $\mathbf{s}$ to the triplet components $|1, m_s\rangle$ of the Cooperon is given in the App. 3.D. Therefore, the physics described by the spin diffusion equation are fully contained in the Cooperon formalism. Since the latter simultaneously enables the determination of the conductivity correction, it is often the preferable approach. In the Part III, we will employ the Cooperon-approach to study the DP spin relaxation but often also refer to the spin diffusion equation.

Appendix 3.A: Auxiliary Function

The auxiliary function $I(\mathbf{Q})$ in Eq. (3.39) is evaluated at zero temperatures for small Cooperon wave vectors $\mathbf{Q}$. In the weak disorder limit, i.e., $E_F\tau_e/\hbar \gg 1$, we may approximate

$$\begin{aligned} I(\boldsymbol{Q}) &= \frac{\hbar}{2\pi\nu_0\tau_e}\sum_{\mathbf{q}}\mathcal{G}^R(\mathbf{q})\mathcal{G}^A(\mathbf{Q}-\mathbf{q}) \\ &\approx \frac{\hbar}{2\pi\nu_0\tau_e}\sum_{\mathbf{q}}\frac{1}{\hat{\Sigma}+\frac{i\hbar}{\tau_e}}\frac{\frac{i\hbar}{\tau_e}}{(E_F-\mathcal{H}_0(\mathbf{q}))^2+\frac{\hbar^2}{4\tau_e^2}} \\ &\approx \frac{1}{\nu_0}\sum_{\mathbf{q}}\frac{1}{1-i\tau_e\hat{\Sigma}/\hbar}\,\delta(E_F-\mathcal{H}_0(\mathbf{q})) \\ &\approx \int\frac{\mathrm{d}\Omega_d}{\Omega_d}\frac{1}{1-i\tau_e\hat{\Sigma}/\hbar}\bigg|_{\mathbf{q}=\mathbf{k}_F}, \end{aligned} \tag{3.A.1}$$

where $\hat{\Sigma} = \mathcal{H}(\mathbf{Q}-\mathbf{k}_F) - \mathcal{H}(\mathbf{k}_F)$.

Appendix 3.B: Singlet-Triplet Representation

The $|s_1, s_2\rangle$ basis of the spin z-components of the two electrons with $s_i \in \{+,-\}$, labeled by $(\pm)$, can be transformed into the singlet-triplet representation $|s, m_s\rangle$ with the spin quantum number $s \in \{0,1\}$ and the according magnetic quantum number $m_s \in \{0, \pm 1\}$ by the relations

$$|0,0\rangle = \frac{1}{\sqrt{2}}(|+,-\rangle - |-,+\rangle), \tag{3.B.2}$$

$$|1,0\rangle = \frac{1}{\sqrt{2}}(|+,-\rangle + |-,+\rangle), \tag{3.B.3}$$

$$|1,\pm 1\rangle = |\pm,\pm\rangle\,. \tag{3.B.4}$$

This yields the unitary transformation matrix

$$U = \frac{1}{\sqrt{2}}\begin{pmatrix} 0 & \sqrt{2} & 0 & 0 \\ -1 & 0 & 1 & 0 \\ 1 & 0 & 1 & 0 \\ 0 & 0 & 0 & \sqrt{2} \end{pmatrix}. \tag{3.B.5}$$

Hence, the components of the total electron spin vector $\widetilde{\boldsymbol{S}}$, which reads as

$$\widetilde{\boldsymbol{S}} = \frac{1}{2}(\boldsymbol{\sigma}\otimes\mathbb{1} + \mathbb{1}\otimes\boldsymbol{\sigma'}) \tag{3.B.6}$$

in the basis $|s_1, s_2\rangle$, become in the singlet-triplet representation $S_i = U^\dagger \widetilde{S}_i U$, or particularly

$$S_x = \frac{1}{\sqrt{2}} \begin{pmatrix} 0 & 0 & 0 & 0 \\ 0 & 0 & 1 & 0 \\ 0 & 1 & 0 & 1 \\ 0 & 0 & 1 & 0 \end{pmatrix}, S_y = \frac{i}{\sqrt{2}} \begin{pmatrix} 0 & 0 & 0 & 0 \\ 0 & 0 & -1 & 0 \\ 0 & 1 & 0 & -1 \\ 0 & 0 & 1 & 0 \end{pmatrix}, S_z = \begin{pmatrix} 0 & 0 & 0 & 0 \\ 0 & 1 & 0 & 0 \\ 0 & 0 & 0 & 0 \\ 0 & 0 & 0 & -1 \end{pmatrix} \tag{3.B.7}$$

in the order $\{|0,0\rangle, |1,1\rangle, |1,0\rangle, |1,-1\rangle\}$. Thus, the singlet and triplet sector decouple.

Appendix 3.C: Sum Formula

In singlet-triplet representation the sum over spin indices s_1, s_2 in Eq. (3.44) simplifies to

$$\begin{aligned} \sum_{s_1,s_2=\pm} \langle s_1, s_2|\hat{\mathcal{C}}|s_2, s_1\rangle = \\ = \mathrm{Tr}\left[\Lambda \hat{\mathcal{C}}^{(\pm)}\right] = \mathrm{Tr}\left[\Lambda U \hat{\mathcal{C}} U^\dagger\right] = \mathrm{Tr}\left[U^\dagger \Lambda U \hat{\mathcal{C}}\right] \\ = -\sum_{s,m_s} \chi_s \langle s, m_s|\hat{\mathcal{C}}(\mathbf{Q})|s, m_s\rangle \end{aligned} \tag{3.C.8}$$

where $\chi_0 = 1$, $\chi_1 = -1$, and

$$\Lambda = \begin{pmatrix} 1 & 0 & 0 & 0 \\ 0 & 0 & 1 & 0 \\ 0 & 1 & 0 & 0 \\ 0 & 0 & 0 & 1 \end{pmatrix} \tag{3.C.9}$$

and thus

$$U^\dagger \Lambda U = \begin{pmatrix} -1 & 0 & 0 & 0 \\ 0 & 1 & 0 & 0 \\ 0 & 0 & 1 & 0 \\ 0 & 0 & 0 & 1 \end{pmatrix}. \tag{3.C.10}$$

Selecting the eigenbasis of $\hat{\mathcal{C}}^{-1}$ with according eigenvalues E, we may also write

$$\sum_{s_1,s_2=\pm} \langle s_1, s_2|\hat{\mathcal{C}}|s_2, s_1\rangle = \sum_{i\in\{\pm1,0\}} \frac{1}{E_i^{\mathcal{T}}(\mathbf{Q})} - \frac{1}{E^{\mathcal{S}}(\mathbf{Q})}, \tag{3.C.11}$$

where $\mathcal{S}(\mathcal{T})$ denotes the singlet (triplet) sector.

Appendix 3.D: Relation between Triplet Basis and Spin Density Components

As shown in Ref. [67], there exists a unitary transformation between the spin diffusion equation, Eq. (2.4), and the Cooperon. Therefore, we obtain an according transformation between the spin density $\mathbf{s} = (s_x, s_y, s_z)^\top$ and the triplet vector $\tilde{\mathbf{s}} = (|1,1\rangle, |1,0\rangle, |1,-1\rangle)^\top$ of the Cooperon, which is

$$\tilde{\mathbf{s}} = U_{cd}\,\mathbf{s}, \tag{3.D.12}$$

with the unitary operator

$$U_{cd} = \begin{pmatrix} -1 & i & 0 \\ 0 & 0 & \sqrt{2} \\ 1 & i & 0 \end{pmatrix} / \sqrt{2}. \tag{3.D.13}$$

Part II

Persistent Spin Textures in Quantum Wells

CHAPTER 4

Electrons in Quantum Wells with General Crystal Orientation

In this chapter, we investigate the possibility of spin-preserving symmetries due to the interplay of Rashba and Dresselhaus SOC in n-doped zinc-blende semiconductor quantum wells of general crystal orientation. The well-established cases that give rise to such a scenario are restricted to quantum wells grown along [001], [110], or [111] direction, where the SOF is either purely in-plane, purely out-of-plane, or vanishes, respectively [25, 104]. However, also low-symmetry growth directions allow for such situations, and the orientation of the SOF with respect to the surface normal $\mathbf{n}$ can in principle be designed arbitrarily. In particular, it is shown that a conserved spin operator can be realized if and only if at least two growth-direction Miller indices agree in modulus. The according SOF has in general both in-plane and out-of-plane components and is always perpendicular to the shift vector of the corresponding persistent spin helix. We also analyze higher-order effects arising from the Dresselhaus term, and the impact of our results on weak (anti)localization corrections.

4.1 2D Electron Model Hamiltonian

We consider a 2DEG whose crystal orientation is defined by an arbitrary normal unit vector $\mathbf{n} = (n_x, n_y, n_z)$ with the underlying basis vectors $\hat{\boldsymbol{x}}$, $\hat{\boldsymbol{y}}$, and $\hat{\boldsymbol{z}}$ pointing along the crystal axes [100], [010], and [001], respectively. The Hamiltonian describing the lowest conduction subband in an infinite quantum square well is given by

$$\mathcal{H} = \frac{\hbar^2 k^2}{2m^*} + \boldsymbol{\Omega} \cdot \boldsymbol{\sigma}, \tag{4.1}$$

where m^* is the effective electron mass and $\boldsymbol{\sigma}$ denotes the vector of Pauli matrices. The effects due to Rashba (R) and Dresselhaus (D) SOC are comprised in the SOF $\boldsymbol{\Omega} = \boldsymbol{\Omega}_\mathrm{R} + \boldsymbol{\Omega}_\mathrm{D}^{(1)} + \boldsymbol{\Omega}_\mathrm{D}^{(3)}$ with the dominant contributions

$$\boldsymbol{\Omega}_\mathrm{R} = \alpha\,(\mathbf{k} \times \mathbf{n})\,, \quad \boldsymbol{\Omega}_\mathrm{D}^{(1)} = \beta^{(1)}\,\boldsymbol{\kappa}, \tag{4.2}$$

where $\kappa_x = 2n_x(n_y k_y - n_z k_z) + k_x(n_y^2 - n_z^2)$ and analogous for the other components by cyclic index permutation (cf. Sec. 1.4) [103, 104]. In this formulation, the

electron wave vector $\mathbf{k}$ is constrained by $\mathbf{k}\cdot\mathbf{n}=0$. The field coefficients are given by $\alpha = r_{41}^{6c6c}\,\mathcal{E}_0$ and $\beta^{(1)} = b_{41}^{6c6c}\,[(\pi/a)^2 - k^2/4]$. Hereby, the Rashba SOC strength α is characterized by an electric field $\boldsymbol{\mathcal{E}} = \mathcal{E}_0\mathbf{n}$ as a result of a potential gradient in growth direction $\mathbf{n}$ of the quantum well. In contrast, the Dresselhaus parameter $\beta^{(1)}$ strongly depends on the quantum well width a. In the definition of $\beta^{(1)}$, the result of D'yakonov *et al.*, Ref. [103], is extended by including the effect of k-cubic Dresselhaus terms, focusing only on the lowest angular harmonics in k. The k-cubic terms reduce the Dresselhaus SOC strength $\beta^{(1)}$ by a factor that depends on the wave vector k which was already observed in Refs. [61, 144] for [001] 2DEGs. The impact of k-cubic Dresselhaus terms w.r.t. higher angular harmonics is described by the field $\mathbf{\Omega}_{\mathrm{D}}^{(3)}$. Commonly, these terms constitute an obstacle for the realization of SU(2) symmetry. We observe that only the [111] and [110] growth directions allow us to construct a collinear SOF despite the presence of $\mathbf{\Omega}_{\mathrm{D}}^{(3)}$. Yet, since the contribution $\mathbf{\Omega}_{\mathrm{D}}^{(3)}$ is usually very small, it will be neglected hereafter. It is discussed in more detail in App. 4.B.

4.2 Spin Diffusion Equation

To gather information about the spin relaxation, we study the impact of SOC on the spin diffusion equation for weak SOC and disorder in the regime of zero temperature (cf. Sec. 2.1). Selecting the Fourier representation with small wave vectors $\mathbf{k}$, $\mathbf{q}$, and frequencies ω, leads to the equation for the spin density $\mathbf{s}(\mathbf{q},\omega)$ [64, 67, 119]:

$$0 = \left(D_e q^2 - i\omega + 1/\hat{\tau}_{\mathrm{s}}^{(0)}\right)\mathbf{s} + \frac{4i\tau_e}{m^*}\,\langle(\mathbf{q}\cdot\mathbf{k})\,\mathbf{\Omega}\rangle\times\mathbf{s}. \tag{4.3}$$

Here, τ_{e} denotes the mean elastic scattering time, $D_e = v_F^2\tau_e/2$ the 2D diffusion constant with the Fermi velocity $v_F = \hbar k_F/m^*$. The corresponding DP spin-relaxation tensor is given by [117, 118]

$$\left(1/\hat{\tau}_{\mathrm{s}}^{(0)}\right)_{ij} = 4\tau_e/\hbar^2(\langle\mathbf{\Omega}^2\rangle\,\delta_{ij} - \langle\Omega_i\Omega_j\rangle). \tag{4.4}$$

The averaging $\langle\ldots\rangle$ is performed over all in-plane directions of $\mathbf{k}$ using the relation $\langle k_i k_j\rangle = (k_F^2/2)(\delta_{ij} - n_i n_j)$ [104]. It is practical to rewrite Eq. (4.3) by means of the spin diffusion operator $\Lambda_{\mathrm{sd}}(\mathbf{q})$, i.e., $0 = [D_e\Lambda_{\mathrm{sd}}(\mathbf{q}) - i\omega]\,\mathbf{s}$. Parameter configurations which yield a vanishing eigenvalue λ of Λ_{sd} at a specific $\mathbf{q} = \mathbf{q}_{\mathrm{min}}$ lead to an infinite spin lifetime. Thereby, we distinguish two cases depending on $\mathbf{q}_{\mathrm{min}}$: (i) for $\mathbf{q}_{\mathrm{min}} = 0$, the long-lived spin state does not precess in coordinate space, (ii) for $\mathbf{q}_{\mathrm{min}} = \mathbf{Q} \neq 0$, a persistent spin helix is formed.

4.3 Conditions for Persistent Spin States

In Fig. 4.1(a) we display the global minimum λ_{min} of the spectrum of Λ_{sd} in dependence of the 2DEG orientation. It is determined by identifying individually for

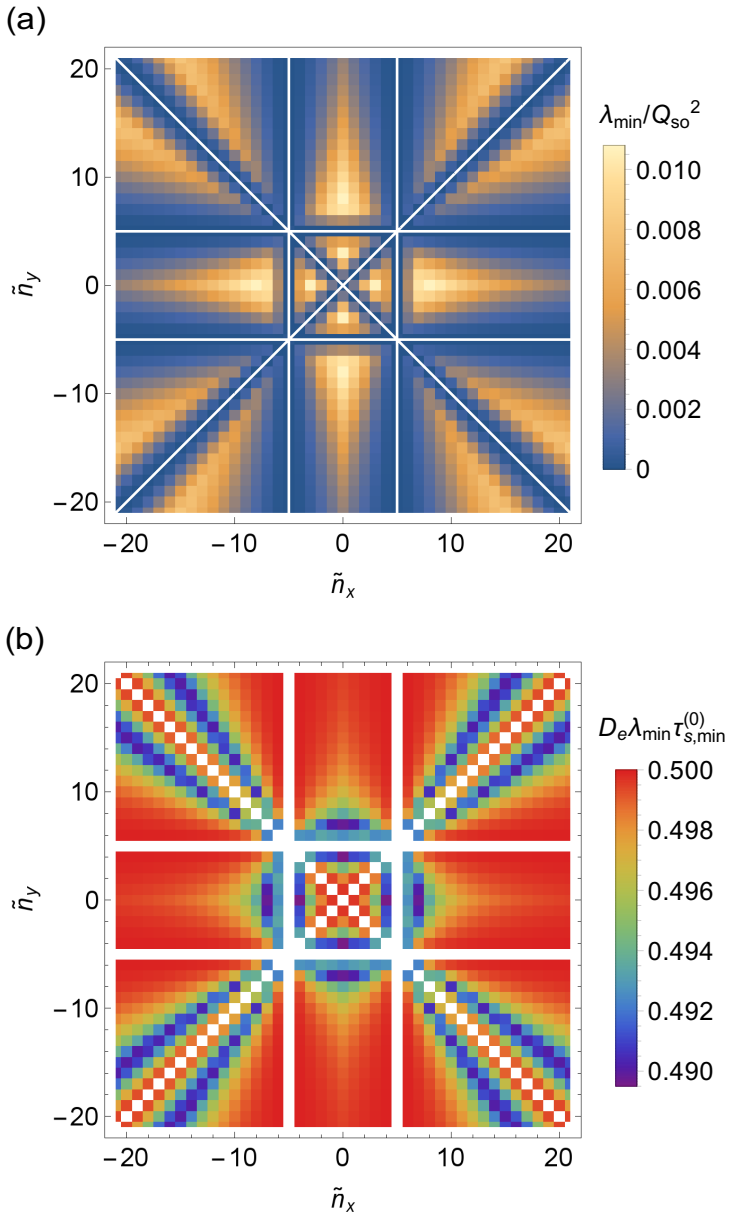

Fig. 4.1: (a) Global minimum $\lambda_{\min}$ (in terms of $Q_{so} = 4m\beta^{(1)}/\hbar^2$) of the spectrum of the spin diffusion operator Λ_{sd} for the optimal ratio of Rashba and Dresselhaus coefficients $\alpha/\beta^{(1)}$ for different growth directions $[\tilde{n}_x, \tilde{n}_y, 5]$ ($\tilde{n}_x, \tilde{n}_y \in \mathbb{Z}$). The white lines emphasize the vanishing minima. (b) Ratio between the global minimum $\lambda_{\min}$ and the minimum $1/(D_e\hat{\tau}^{(0)}_{s,\min})$ found by considering the spectrum at $\mathbf{q} = 0$ solely, which corresponds to the DP spin-relaxation tensor, Eq. (4.4). Along the white lines, both minima vanish exactly due to the SU(2) symmetry.

a 2DEG with the Miller indices $[\tilde{n}_x, \tilde{n}_y, 5]$ ($\tilde{n}_x, \tilde{n}_y \in \mathbb{Z}$), the optimal ratio of $\alpha/\beta^{(1)}$. Along the white lines, $\lambda_{\min}$ vanishes exactly. This indicates that a vanishing eigenvalue λ demands at least two equal indices $|n_i|$ of the normal vector $\mathbf{n}$. Rigorous analytical calculations confirm this supposition (cf. App. 4.A).

Thus, without loss of generality, we restrict our analysis to the first octant, i.e., $n_i > 0$, and for simplification set $n_x = n_y \equiv \eta$ and $n_z = \sqrt{1-2\eta^2}$ due to normalization. The relation to the polar angle θ w.r.t. [001] is given by $\eta = \sin(\theta)/\sqrt{2}$. Hence, the growth direction is defined by a plane which comprises all commonly known cases that allow for spin-preserving symmetries, i.e., [001], [111], and [110]. For an arbitrary $\eta \in \left[0, 1/\sqrt{2}\right]$ the Rashba and Dresselhaus coefficients need to fulfill the relation

$$\alpha/\beta^{(1)} = \Gamma_0 := (1-9\eta^2)\sqrt{1-2\eta^2}. \tag{4.5}$$

Inserting this particular condition in Eq. (4.1), we can rewrite the Hamiltonian in a form which reveals the SU(2) symmetry, that is,

$$\mathcal{H} = \frac{\hbar^2}{2m^*}\left[k^2 + (\mathbf{k}\cdot\mathbf{Q})\,\Sigma\right]. \tag{4.6}$$

The spin operator

$$\Sigma = \left(\sigma_x + \sigma_y + \frac{3\eta\sqrt{1-2\eta^2}}{3\eta^2-1}\sigma_z\right)/N \equiv \mathbf{\Pi}\cdot\boldsymbol{\sigma}, \tag{4.7}$$

with the normalization constant $N = \sqrt{2-3\eta^2}/|1-3\eta^2|$ is a conserved quantity, i.e., $[\mathcal{H}, \Sigma] = 0$. The direction of the collinear SOF is determined by the vector $\mathbf{\Pi}$. As a result, it is always perpendicular to the $[\bar{1}10]$ axis and, thus, also to the wave vector

$$\mathbf{Q} = \frac{Q_0}{\sqrt{2}}(-1, 1, 0), \tag{4.8}$$

with $Q_0 = |1-3\eta^2|\sqrt{1-3\eta^2/2}\,Q_{so}$ and $Q_{so} = 4m^*\beta^{(1)}/\hbar^2$, which induces the shift of the Fermi contours and describes the spin precession of the propagating electrons. The length $L_{so} := 2\pi/Q_0$ is denoted as spin precession length. It specifies the distance along $\mathbf{Q}$ that spin-polarized electrons need to propagate until their spin has performed a full precession cycle. The corresponding precession axis is given by the orientation of $\mathbf{\Pi}$. Note that an additional solution occurs for $\eta = 0$, that is, $\alpha = -\beta^{(1)}$, which results in $\mathbf{Q} = Q_0(1,1,0)/\sqrt{2}$ and $\Sigma = (\sigma_x - \sigma_y)/\sqrt{2}$ for a [001] confined 2DEG.

In Fig. 4.2, we display the characteristic quantities in case of a persistent spin helix symmetry in dependence of the quantum well growth direction. Here, ξ is defined as the polar angle between the surface normal $\mathbf{n}$ and the direction $\mathbf{\Pi}$ of the collinear SOF. Obviously, L_{so} reaches a minimum for a [001] orientation. For [111], i.e., $\eta = 1/\sqrt{3}$, the wave vector vanishes due to an overall vanishing SOF as the Rashba and Dresselhaus contributions cancel each other exactly. Another

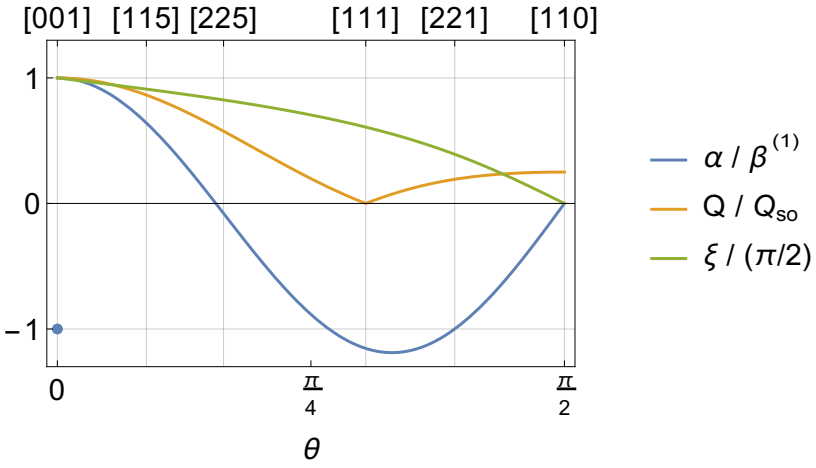

Fig. 4.2: Characteristic parameters in case of a persistent spin helix symmetry in dependence of the growth direction. Notice the degeneracy for $\alpha/\beta^{(1)}$ in the [001] direction.

peculiar situation occurs for $\eta = 1/3$. Similarly to a [110] 2DEG, it yields a conserved spin quantity for a vanishing Rashba SOC. As $\eta = 1/3$ corresponds to an irrational Miller index, this growth direction cannot be realized. Yet, it can be well approximated by, e.g., a [225] crystal vector.

4.4 Imprints on Weak (Anti)Localization

An indispensable tool to probe experimentally the DP spin relaxation are low-field magnetoconductivity measurements. As shown in Chap. 3, quantum interference in weakly disordered conductors, i.e., $E_F\tau_e/\hbar \gg 1$, leads to a correction to the Drude conductivity $\Delta\sigma$ which is highly sensitive to magnetic fields as they break the time-reversal invariance. Depending on the strength and structure of the SOF the contribution to the conductivity can be positive or negative, which is denoted as WL or WAL, respectively. Considering the standard white-noise model for the impurity potentials and weak disorder, we can write the 2D correction to the conductivity as (cf. Sec. 3.3.2) [61]

$$\Delta\sigma = \frac{2e^2}{h} \int\limits_{\mathcal{Q}<\sqrt{c_e}} \frac{d^2\mathcal{Q}}{(2\pi)^2} \left(\frac{1}{\mathcal{Q}^2 + c_\phi + c_\mathrm{B}} - \sum_{j\in\{\pm1,0\}} \frac{1}{\lambda_j/Q_{so}^2 + c_\phi + c_\mathrm{B}} \right), \tag{4.9}$$

with the conductance quantum $2e^2/h$. Moreover, we used the dimensionless orthogonal in-plane wave vectors of the 2DEG, $\boldsymbol{\mathcal{Q}} = (\mathcal{Q}_+, \mathcal{Q}_-)$ where $\mathcal{Q} = q/Q_\mathrm{so}$. Possible divergencies in the integral are removed by the upper and lower cutoffs $c_i = 1/(D_e Q_{so}^2 \tau_i)$, $i \in \{\phi, e, \mathrm{B}\}$, due to finite dephasing, elastic scattering and magnetic phase shifting rates, τ_ϕ^{-1}, τ_e^{-1}, and τ_B^{-1}, respectively. The latter takes into account external magnetic fields $\mathbf{B} = B\,\mathbf{n}$ perpendicular to the quantum well,

i.e., $1/\tau_\mathrm{B} = 2D_e e|B|/\hbar$ [147]. These fields are considered small enough that the Landau basis is not the appropriate choice. The spectrum of the Cooperon and the spin diffusion equation are identical as far as time-reversal symmetry is not broken [148]. As a consequence, the spin-relaxation rates, determined by the eigenvalues λ_j of the spin diffusion operator Λ_sd, become manifested in the gaps of the triplet eigenvalues of the Cooperon and, thus, directly enter Eq. (4.9). In case of a gapless mode, that is, a vanishing spin relaxation, this results in a negative contribution to the conductivity, i.e., WL, despite the presence of SOC and irrespective of its strength. Therefore, a gate-controlled crossover from WAL to WL provides a solid evidence of spin-preserving symmetries [23, 24]. The explicit form of Λ_sd, in case of two identical Miller indices, is given in App. 4.C.

4.5 Magnetoconductivity near SU(2) Symmetry

In the vicinity ϵ of the optimal ratio of Rashba and Dresselhaus SOC, i.e., $\alpha/\beta^{(1)} \mapsto \Gamma_0 + \epsilon$, where $\epsilon \ll 1$, the structure of the eigenvalues λ_j, $j \in \{0, \pm 1\}$, which are functions of the wave vector $\boldsymbol{\mathcal{Q}}$, can be approximated by three parabolas of the form

$$\lambda_j/Q_{so}^2 = \mathcal{Q}_+^2 + (\mathcal{Q}_- + j\zeta)^2 + \Delta_{|j|}. \tag{4.10}$$

The minima of $\lambda_{\pm 1}$ are shifted to finite in-plane wave vectors $\mathcal{Q}_- = \pm\zeta$ which are oriented along $[\bar{1}10]$, representing the long-lived helical spin states. Expanding Λ_sd to lowest order in ϵ and neglecting all $\mathbf{q}$-independent terms yields a shift $\zeta^2 \approx Q_0^2/Q_{so}^2 + \Delta_0 + \epsilon(1-3\eta^2)\sqrt{1-2\eta^2}$. Applying this and keeping only the leading terms in ϵ, one finds $\Delta_0 \approx 2\Delta_1 \approx \epsilon^2/4$. The gaps $\Delta_{|j|} = 1/(D_e Q_{so}^2 (\tau_s)_{|j|})$ are a consequence of the finite spin-relaxation rates $(\tau_\mathrm{s}^{-1})_{|j|}$ due to the broken SU(2) symmetry. We stress that the gap at $\boldsymbol{\mathcal{Q}} = 0$ is twice as large as the gap at $\boldsymbol{\mathcal{Q}} = (0, \pm\zeta)$. This fact is underlined by the results which are illustrated in Fig. 4.1(b). There, we compare the global minimum λ_min of the spectrum of the spin diffusion operator $\Lambda_\mathrm{sd}(\mathbf{q})$ with the one arising from the terms at $\mathbf{q} = 0$ purely, Eq. (4.4), for various growth directions. Besides the cases of SU(2) symmetry (white lines), the minima at $\mathbf{q} = 0$ are generally about a factor 2 larger than the minima λ_min. These observations highlight the superior spin lifetime of helical spin densities which was previously observed in planar and tubular 2DEGs with Rashba SOC [5, 61].

With this, the integral in Eq. (4.9) yields an analytical result, which solely depends on the quantities ζ and $\Delta_{0,1}$ and the cutoff parameters c_i, $i \in \{\phi, e, \mathrm{B}\}$:

$$\Delta\sigma \approx \frac{e^2}{2\pi h} \ln\left(\frac{4\Upsilon_{100}\Upsilon_{010}\Upsilon_{001}^2}{\Upsilon_{000}\Upsilon_{110}\left(\Upsilon_{101} - \zeta^2 + \sqrt{\upsilon}\right)^2} \right), \tag{4.11}$$

with the tensor $\Upsilon_{jkl} = c_\phi + c_\mathrm{B} + jc_e + k\Delta_0 + l\Delta_1$ and $\upsilon = \Upsilon_{101}^2 + 2\Upsilon_{\text{-}101}\zeta^2 + \zeta^4$. A particularly important characteristic feature for experimental probing is the gate control of the magnetoconductivity minima B_min where $\partial_B[\Delta\sigma(B)] = 0$ [22, 149].

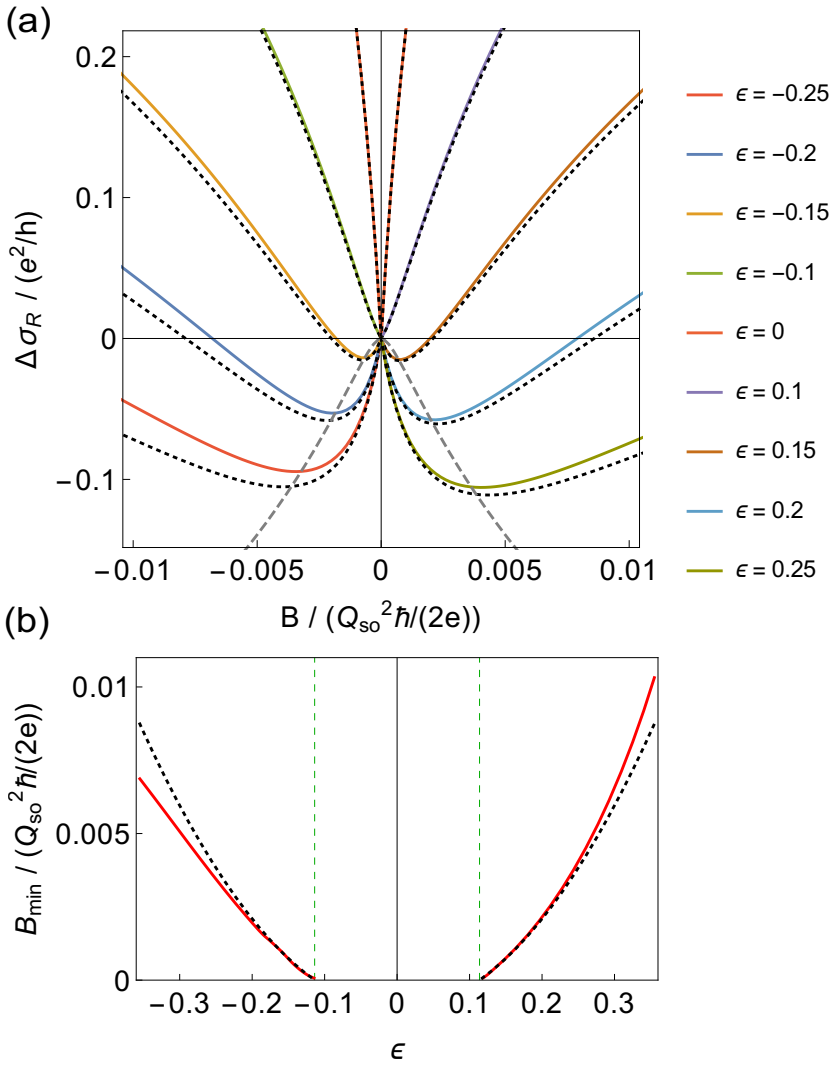

Fig. 4.3: 2DEG grown along [113] for $c_e/c_\phi = 10^3$ and $c_e = 1$ with $\alpha/\beta^{(1)}$ close to the SU(2) symmetry point. (a) Relative magnetoconductivity $\Delta\sigma_{\mathrm{R}}(B) = \Delta\sigma(B) - \Delta\sigma(0)$ for different values of ϵ. For compactness, we restrict the plots for $\epsilon < 0$ ($\epsilon > 0$) to negative(positive) magnetic fields. The colored lines correspond to exact numerical calculations, the black dotted lines to the approximate expression, Eq. (4.11). Gray dashed lines show the trend of the minima $\Delta\sigma(B_{\mathrm{min}})$ in dependence of ϵ. (b) The respective magnetoconductivity minimum as a function of ϵ. Red solid lines correspond to exact numerical calculations, black dotted and green dashed lines to approximate formulas.

Exploiting the fact that ϵ, c_ϕ, c_B, and c_e^{-1} are small quantities and neglecting the shift ζ, we can use Eq. (4.11) to derive an approximate expression for B_min as

$$B_\mathrm{min} \approx \frac{(\sqrt{5}-1)m^{*2}\widetilde{\alpha}^2}{2e\hbar^3} - \frac{\hbar}{2eD_e\tau_\phi}, \tag{4.12}$$

where we defined $\widetilde{\alpha} = \beta^{(1)}\epsilon$. According to this, the crossover from positive to negative magnetoconductivity appears at $\widetilde{\alpha}^2 \approx (1+\sqrt{5})\hbar^4/(4D_e m^{*2}\tau_\phi)$. These simple relations allow for a direct determination of SOC coefficients and dephasing rate without parameter fitting. The quadratic scaling $B_\mathrm{min} \propto \widetilde{\alpha}^2$ was recently confirmed in experiments [22, 149]. We stress that our numerical investigations indicate that the approximate formulas show generally better agreement for $\epsilon > 0$.

To give an example, we consider a [113] orientated 2DEG, which has gathered attention as it facilitates long spin lifetimes of 2D hole systems [150]. In Fig. 4.3(a) we demonstrate the gate-induced crossover from positive to negative relative magnetoconductivity $\Delta\sigma_\mathrm{R}(B) = \Delta\sigma(B) - \Delta\sigma(0)$ by varying the Rashba SOC strength, which is encapsulated in the quantity ϵ, around the SU(2) symmetry point. The colored lines correspond to the exact calculation by using Eqs. (4.3) and (4.9), the black dotted lines to the approximate expression, Eq. (4.11). The gray dashed lines depict the trend of the minimum $\Delta\sigma(B_\mathrm{min})$ obtained by Eqs. (4.11) and (4.12). The approximate formulas for the respective B_min and the horizontal offset (black dotted and green dashed lines) are compared to the exact numerical calculation (red solid lines) in Fig. 4.3(b).

4.6 Summary

In summary, we have identified general sufficient and necessary conditions for spin-preserving symmetries in 2DEGs of arbitrary growth directions. They demand a specific ratio of Rashba and Dresselhaus SOC for an arbitrary growth direction with at least two Miller indices equal in modulus. Going from [001] to [110], the corresponding collinear SOF gradually transforms from in-plane to out-of-plane, simultaneously modifying the spin precession length. Also, we determined two specific situations, i.e., [111] and [110], where the inclusion of higher angular harmonics of the Dresselhaus term continues to allow for a homogeneous persistent spin state. Furthermore, by analyzing the spectrum of the spin diffusion equation, we show that besides the cases of perfect SU(2) symmetry, the spin of the long-lived homogeneous spin state relaxes about a factor two faster than for the helical spin state. In addition, we derived analytical expressions for the magnetoconductivity and the location of its minimum around the SU(2) symmetry point. The latter enables a fitting-free experimental determination of the transport parameters. These results may trigger the interest for investigating 2DEGs with low-symmetry growth. It opens up new perspectives and supports the progress towards tailoring spintronic devices.

Appendix 4.A: Key Requirement for Miller Indices

In the following, we prove that the realization of a SU(2) symmetry in a 2DEG demands a growth direction with two Miller indices equal in modulus.

The Hamiltonian $\mathcal{H}_{\mathrm{so}}$ describing the SOC for a 2DEG, which is grown along an arbitrary normal unit vector $\mathbf{n} = (n_x, n_y, n_z)$ takes the form $\mathcal{H}_{\mathrm{so}} = \boldsymbol{\Omega}(\mathbf{k}) \cdot \boldsymbol{\sigma}$. Focusing on the first angular harmonics, the SOF $\boldsymbol{\Omega}$ consists of $\boldsymbol{\Omega} = \boldsymbol{\Omega}_{\mathrm{R}} + \boldsymbol{\Omega}_{\mathrm{D}}^{(1)}$. The respective Rashba (R) and Dresselhaus (D) SOF, $\boldsymbol{\Omega}_{\mathrm{R}}$ and $\boldsymbol{\Omega}_{\mathrm{D}}^{(1)}$, are defined in Eq. (4.2). We can reformulate $\mathcal{H}_{\mathrm{so}}$ as

$$\mathcal{H}_{\mathrm{so}} = \mathbf{k}^{\top} \Xi \, \boldsymbol{\sigma}, \tag{4.A.1}$$

with a k-independent tensor Ξ, which collects the wave vector coefficients of the according components of the SOF. In consequence of the 2D confinement, the wave vector obeys the relation $\mathbf{k} \cdot \mathbf{n} = 0$. Thus, without loss of generality, we assume $n_z \neq 0$ and replace $k_z = -(k_x n_x + k_y n_y)/n_z$ in $\boldsymbol{\Omega}$. Using this and setting $\Gamma = \alpha/\beta^{(1)}$ gives

$$\Xi = \beta^{(1)} \begin{pmatrix} 2n_x^2 + n_y^2 - n_z^2 + \Gamma \frac{n_x n_y}{n_z} & -\left(4n_x n_y + \Gamma \frac{n_x^2 + n_z^2}{n_z}\right) & (n_y^2 - n_x^2 + 2n_z^2)\frac{n_x}{n_z} + \Gamma n_y \\ 4n_x n_y + \Gamma \frac{n_y^2 + n_z^2}{n_z} & -\left(2n_y^2 + n_x^2 - n_z^2 + \Gamma \frac{n_x n_y}{n_z}\right) & -\left((n_x^2 - n_y^2 + 2n_z^2)\frac{n_y}{n_z} + \Gamma n_x\right) \\ 0 & 0 & 0 \end{pmatrix}. \tag{4.A.2}$$

In case of a SU(2) symmetry, the SOC Hamiltonian $\mathcal{H}_{\mathrm{so}}$ can be rewritten in the form $\mathcal{H}_{\mathrm{so}} = (\mathbf{k} \cdot \mathbf{Q})(\boldsymbol{\Pi} \cdot \boldsymbol{\sigma})$. In this formulation, both vectors $\mathbf{Q}$ and $\boldsymbol{\Pi}$ are required to be independent of k. The vector $\boldsymbol{\Pi}$ determines the direction of the collinear SOF and therefore the homogeneous persistent spin state. In contrast, the vector $\mathbf{Q}$ induces the shift of the Fermi contours and describes the spin precession of the persistent spin helix. Assuming this relation to hold, we can identify $\mathbf{a}_i = \mathbf{Q}\,\Pi_i$, $i \in \{1, 2, 3\}$, where $\mathbf{a}_i$ denotes the i-th column vector of Ξ. Hence, in order to obtain SU(2) symmetry, the column vectors $\mathbf{a}_i$ of Ξ need to be collinear. This yields three equations $\mathbf{a}_1 \times \mathbf{a}_2 = \mathbf{a}_3 \times \mathbf{a}_1 = \mathbf{a}_2 \times \mathbf{a}_3 = 0$ which are equivalent to

$$n_x\Gamma^2 + n_y n_z(10n_x^2 + n_y^2 + n_z^2)\Gamma = n_x[n_x^4 + 2(n_y^4 + n_z^4) - 3n_x^2(n_y^2 + n_z^2) - 11n_y^2 n_z^2], \tag{4.A.3}$$

$$n_y\Gamma^2 + n_z n_x(10n_y^2 + n_z^2 + n_x^2)\Gamma = n_y[n_y^4 + 2(n_z^4 + n_x^4) - 3n_y^2(n_z^2 + n_x^2) - 11n_z^2 n_x^2], \tag{4.A.4}$$

$$n_z\Gamma^2 + n_x n_y(10n_z^2 + n_x^2 + n_y^2)\Gamma = n_z[n_z^4 + 2(n_x^4 + n_y^4) - 3n_z^2(n_x^2 + n_y^2) - 11n_x^2 n_y^2]. \tag{4.A.5}$$

From $n_x = 0$ in Eq. (4.A.3) follows that either $\Gamma = 0$ or $n_y = 0$. The latter case corresponds to two equal indices. Using the solution $n_x = \Gamma = 0$ in Eq. (4.A.4) leads again to $n_y = 0$. As this allows to exclude the cases $n_x = n_y = 0$ from the discussion, we can eliminate Γ^2 by subtracting the distinct equations from each

other. Taking additionally into account normalization, i.e., $n_x^2 + n_y^2 + n_z^2 = 1$, one finds

$$\Gamma(n_x^2 - n_y^2) = \frac{n_x n_y}{n_z}(1 - 9n_z^2)(n_x^2 - n_y^2), \tag{4.A.6}$$

$$\Gamma(n_y^2 - n_z^2) = \frac{n_y n_z}{n_x}(1 - 9n_x^2)(n_y^2 - n_z^2), \tag{4.A.7}$$

$$\Gamma(n_z^2 - n_x^2) = \frac{n_z n_x}{n_y}(1 - 9n_y^2)(n_z^2 - n_x^2). \tag{4.A.8}$$

On condition that all indices $|n_i|$ are different from each other, we can cancel the factors $(n_i^2 - n_j^2)$. This, however, causes inconsistent solutions for Γ. As a result, at least two indices are required to be equal in modulus and we obtain three cases:

$$n_x = \pm n_y \;:\; \Gamma = \pm n_z - 9 n_x n_y n_z, \tag{4.A.9}$$

$$n_y = \pm n_z \;:\; \Gamma = \pm n_x - 9 n_x n_y n_z, \tag{4.A.10}$$

$$n_z = \pm n_x \;:\; \Gamma = \pm n_y - 9 n_x n_y n_z, \tag{4.A.11}$$

which includes the result of Chap. 4.

In the following section, we demonstrate that, in turn, starting from the assumption $n_x = n_y = \eta$, the relation $\Gamma = (1 - 9\eta^2)n_z$ must hold true in order to generate a collinear spin-orbit field. The latter induces SU(2) symmetry since it allows to reformulate the SOC Hamiltonian $\mathcal{H}_{\mathrm{so}}$ in the form $\mathcal{H}_{\mathrm{so}} = (\mathbf{k} \cdot \mathbf{Q})(\mathbf{\Pi} \cdot \boldsymbol{\sigma})$ as it is shown in Chap. 4.

Appendix 4.B: Impact of Higher Angular Harmonics

Again, we assume a 2DEG which is oriented along an arbitrary normal unit vector $\mathbf{n} = (n_x, n_y, n_z)$. The Hamiltonian $\mathcal{H}_{\mathrm{so}}$ which describes the SOC is written as

$$\mathcal{H}_{\mathrm{so}} = \mathbf{\Omega} \cdot \boldsymbol{\sigma} = (\mathbf{\Omega}_{\mathrm{R}} + \mathbf{\Omega}_{\mathrm{D}}) \cdot \boldsymbol{\sigma}, \tag{4.B.12}$$

where the Rashba SOF $\mathbf{\Omega}_{\mathrm{R}}$ is defined in Eq. (4.2). The full Dresselhaus SOF $\mathbf{\Omega}_{\mathrm{D}}$, including angular harmonics up to third order, is given by $\mathbf{\Omega}_{\mathrm{D}} = \mathbf{\Omega}_{\mathrm{D}}^{(1)} + \mathbf{\Omega}_{\mathrm{D}}^{(3)} = b_{41}^{6c6c}\boldsymbol{\nu}$ with the components [103, 104]

$$\begin{aligned}\nu_x = &\left(\frac{\pi}{a}\right)^2 \left[2n_x(n_y k_y - n_z k_z) + k_x(n_y^2 - n_z^2)\right] \\ &+ k_x\left(k_y^2 - k_z^2\right)\end{aligned} \tag{4.B.13}$$

and similar for ν_y and ν_z by cyclic index permutation. The parameter a denotes the width of the square well confinement along the growth direction, and γ_{D} a material and confinement specific parameter. In consequence of the 2D confinement, the wave vectors obey the relation $\mathbf{k} \cdot \mathbf{n} = 0$. In the given representation, the basis vectors $\hat{\boldsymbol{x}}$, $\hat{\boldsymbol{y}}$, and $\hat{\boldsymbol{z}}$ correspond to the principal crystal axes [100], [010], and [001], respectively.

It is convenient to rotate the Hamiltonian $\mathcal{H}_{\mathrm{so}}$ such that the z-axis of the transformed system is aligned with the 2DEG's growth direction. Focusing on the scenario where the persistent spin helix symmetry can be realized up to higher angular harmonics, we set $n_x = n_y \equiv \eta$ and $n_z = \sqrt{1-2\eta^2}$. For simplicity, we restrict to the first octant only, i.e., $\eta \in \left[0, 1/\sqrt{2}\right]$. The relation to the polar angle θ with respect to [001] yields $\eta = \sin(\theta)/\sqrt{2}$. With this, the rotation can be performed by means of the rotation matrix (cf. Sec. 1.4.5)

$$\mathcal{R} = \frac{1}{\sqrt{2}} \begin{pmatrix} n_z & -1 & \sqrt{2}\eta \\ n_z & 1 & \sqrt{2}\eta \\ -2\eta & 0 & \sqrt{2}n_z \end{pmatrix}. \tag{4.B.14}$$

The Hamiltonian in the rotated system, i.e., $\mathcal{H}'_{\mathrm{so}} = \boldsymbol{\Omega}' \cdot \boldsymbol{\sigma}'$, is obtained by replacing $\mathbf{k} \mapsto \mathcal{R} \cdot \mathbf{k}'$ and $\boldsymbol{\sigma} \mapsto \mathcal{R} \cdot \boldsymbol{\sigma}'$ with the according basis vectors $\hat{\boldsymbol{x}}' = (n_z, n_z, -2\eta)/\sqrt{2}$, $\hat{\boldsymbol{y}}' = (-1, 1, 0)/\sqrt{2}$, and $\hat{\boldsymbol{z}}' = (\eta, \eta, n_z)$.

After applying this transformation, the Rashba SOF lies in the plane of the quantum well and reads

$$\boldsymbol{\Omega}'_{\mathrm{R}} = \alpha k' \left(\sin(\varphi), -\cos(\varphi), 0\right), \tag{4.B.15}$$

with $\alpha = r_{41}^{6c6c}\mathcal{E}_0$ where r_{41}^{6c6c} is a material and confinement specific parameter and $\mathcal{E}_0$ results from an electric field $\boldsymbol{\mathcal{E}} = \mathcal{E}_0\hat{\boldsymbol{z}}'$ perpendicular to the 2DEG. Here, we introduced polar coordinates for the in-plane wave vectors, $k'_x = k'\cos(\varphi)$ and $k'_y = k'\sin(\varphi)$. The Dresselhaus SOF $\boldsymbol{\Omega}'_{\mathrm{D}}$ can be split into two contributions that contain the angular harmonics in $\mathbf{k}$ of the first and third order, $\boldsymbol{\Omega}'^{(1)}_{\mathrm{D}}$ and $\boldsymbol{\Omega}'^{(3)}_{\mathrm{D}}$, respectively. Thus, we find

$$\boldsymbol{\Omega}'_{\mathrm{D}} = \boldsymbol{\Omega}'^{(1)}_{\mathrm{D}} + \boldsymbol{\Omega}'^{(3)}_{\mathrm{D}}, \tag{4.B.16}$$

with the SOF w.r.t. the l-th angular harmonics

$$\boldsymbol{\Omega}'^{(l)}_{\mathrm{D}} = \beta^{(l)}k' \begin{pmatrix} b_1^{(l)}\sin(l\varphi) \\ b_2^{(l)}\cos(l\varphi) \\ b_3^{(l)}\sin(l\varphi)) \end{pmatrix}, \tag{4.B.17}$$

where $\beta^{(1)} = b_{41}^{6c6c}\left[(\pi/a)^2 - k'^2/4\right]$, $\beta^{(3)} = b_{41}^{6c6c}k'^2/4$, and the respective coefficients $b_j^{(l)}$ are comprised in the vectors

$$\mathbf{b}^{(1)} = \begin{pmatrix} (1+3\eta^2)n_z \\ (1-9\eta^2)n_z \\ -\sqrt{2}\eta(1-3\eta^2) \end{pmatrix}, \; \mathbf{b}^{(3)} = \begin{pmatrix} (1-3\eta^2)n_z \\ -(1-3\eta^2)n_z \\ 3\sqrt{2}\eta(1-\eta^2) \end{pmatrix}. \tag{4.B.18}$$

We note that each of the Dresselhaus fields lies in a plane which is defined by the corresponding normal vector $\mathbf{v}'^{(l)} = (b_3^{(l)}, 0, -b_1^{(l)})$. The planes coincide if $\eta = 0$ or

$\eta = 1/\sqrt{2}$, i.e., in case of a [001] or [110] 2DEG. In general, the field $\mathbf{\Omega}_{\mathrm{D}}^{\prime(3)}$ gives a correction $\mathbf{\Omega}_{\mathrm{D}}^{(3)} \cdot \boldsymbol{\sigma}$ to the Hamiltonian $\mathcal{H}$ in Eqs. (4.1) and (4.6). To this end, the Dresselhaus contribution due to third angular harmonics $\mathbf{\Omega}_{\mathrm{D}}^{\prime(3)} \cdot \boldsymbol{\sigma}'$ has to be back-transformed to the initial coordinate system corresponding to the principal crystal axes. This is achieved by replacing $\boldsymbol{\sigma}' \mapsto \mathcal{R}^{-1}\boldsymbol{\sigma}$, $\mathbf{k}' \mapsto \mathcal{R}^{-1}\mathbf{k}$, and using the relations $k'^3\cos(3\varphi) = k'_x(k'^2_x - 3k'^2_y)$ and $k'^3\sin(3\varphi) = -k'_y(k'^2_y - 3k'^2_x)$.

Typically, taking into account the effects of the third angular harmonics inhibits the realization of a perfect SU(2) symmetry. The spin rotation is no more *well-defined* as it depends on the electron's propagated path. Nonetheless, in the following we show that the [111] and [110] directions allow constructing a collinear SOF despite the presence of $\mathbf{\Omega}_{\mathrm{D}}{}^{(3)}$ which facilitates homogeneous persistent spin states. By adding the contributions $\mathbf{\Omega}'_{\mathrm{R}} + \mathbf{\Omega}_{\mathrm{D}}^{\prime(1)}$ it becomes obvious that a collinear SOF field is formed if the Rashba and Dresselhaus coefficients α and $\beta^{(1)}$ fulfill the relation

$$\alpha/\beta^{(1)} = b_2^{(1)} = (1 - 9\eta^2)\sqrt{1 - 2\eta^2}, \tag{4.B.19}$$

which generates the SU(2) symmetry as demonstrated in Chap. 4. Adopting this and focusing on the first angular harmonics yields the collinear field

$$\mathbf{\Omega}'_{\mathrm{R}} + \mathbf{\Omega}_{\mathrm{D}}^{\prime(1)} = \beta^{(1)}k'\sin(\varphi)(3\eta^2 - 1)\begin{pmatrix} -2n_z \\ 0 \\ \sqrt{2}\eta \end{pmatrix}. \tag{4.B.20}$$

Comparing with $\mathbf{\Omega}_{\mathrm{D}}^{\prime(3)}$, we observe that the collinearity is generally destroyed apart from two particular situations where $\eta = 1/\sqrt{3}$ or $\eta = 1/\sqrt{2}$, that is, the [111] or [110] direction, respectively. For [111], the SOF spanned by $\mathbf{\Omega}'_{\mathrm{R}} + \mathbf{\Omega}_{\mathrm{D}}^{\prime(1)}$ vanishes as both contributions cancel each other. The remaining field is given by $\mathbf{\Omega}_{\mathrm{D}}^{\prime(3)}$ which is collinear to the [111] direction. In case of a [110] 2DEG, we have $\mathbf{\Omega}'_{\mathrm{R}} = 0$ and the $\mathbf{\Omega}_{\mathrm{D}}^{\prime(3)}$ contribution is collinear to the [110] axis which coincides with the collinear field due to $\mathbf{\Omega}_{\mathrm{D}}^{\prime(1)}$.

Summarizing, we have demonstrated that choosing a growth direction which corresponds to identical Miller indices and focusing on the first angular harmonics opens the possibility to generate a collinear SOF. Also, we identified two specific scenarios, where the inclusion of higher angular harmonics does not destroy this collinearity and continues to allow for a homogeneous persistent spin state.

Appendix 4.C: Spin Diffusion Operator for Two Identical Miller Indices

Let us consider again a 2DEG grown along a crystal direction with two identical Miller indices with focus on the first octant, i.e., $n_x = n_y \equiv \eta$ and $n_z = \sqrt{1 - 2\eta^2}$ for $\eta \in \left[0, 1/\sqrt{2}\right]$. Analogously to the previous section, by replacing $\mathbf{q} \mapsto \mathcal{R} \cdot$

$\mathbf{q}'$ we choose the in-plane coordinate representation. Furthermore, we define the dimensionless in-plane wave vectors of the spin density as $\mathcal{Q}_+ = \mathcal{Q}\cos(\varphi)$ and $\mathcal{Q}_- = \mathcal{Q}\sin(\varphi)$ with $\mathcal{Q} = q'/Q_{so}$ which correspond to the basis vectors $\hat{\boldsymbol{x}}' = (n_z, n_z, -2\eta)/\sqrt{2}$ and $\hat{\boldsymbol{y}}' = (-1, 1, 0)/\sqrt{2}$, respectively. With these definitions, the spin diffusion operator can be written as

$$\Lambda_{\mathrm{sd}}/Q_{so}^2 = \begin{pmatrix} K & L & M \\ L^* & N & O \\ M^* & O^* & P \end{pmatrix}, \tag{4.C.21}$$

with the components

$$K = \mathcal{Q}^2 + \frac{1}{4}\left[1 + \Gamma^2 + \left(\Gamma^2 + 16\Gamma n_z - 3\right)\eta^2 + 43\eta^4 - 81\eta^6\right], \tag{4.C.22}$$

$$L = i\sqrt{2}\mathcal{Q}\sin(\varphi)\eta(2n_z + \Gamma) - \frac{1}{2}n_z\Gamma + \frac{1}{4}\left[(\Gamma^2 + 10n_z\Gamma - 9)\eta^2 + 58\eta^4 - 81\eta^6\right], \tag{4.C.23}$$

$$M = \frac{\eta}{4}[\Gamma(3 - 5\eta^2) + n_z(2 + \Gamma^2 - 2\eta^2)] - i\frac{\mathcal{Q}}{\sqrt{2}}\left\{[\Gamma + n_z(9\eta^2 - 1)]\cos(\varphi) + (\eta^2 - n_z\Gamma - 1)\sin(\varphi)\right\}, \tag{4.C.24}$$

$$N = K, \tag{4.C.25}$$

$$O = M - i\sqrt{2}\mathcal{Q}\sin(\varphi)(1 + n_z\Gamma - \eta^2), \tag{4.C.26}$$

$$P = K + \frac{1}{4}(1 - 3\eta^2)(1 + \Gamma^2 - 16\eta^2 + 27\eta^4), \tag{4.C.27}$$

where $\Gamma = \alpha/\beta^{(1)}$, $Q_{so} = 4m^*\beta^{(1)}/\hbar^2$, and higher angular harmonics $\propto \beta^{(3)}$ are neglected. The eigenvalues λ_j of Λ_{sd} directly enter Eq. 4.9, which yields the weak (anti)localization correction to the Drude conductivity.

CHAPTER 5

Strained 2D Hole Systems

We derive an effective Hamiltonian for a [001]-oriented quasi-2DHG in a strained zinc-blende semiconductor heterostructure including both Rashba and Dresselhaus SOC. In the presence of uniaxial strain along the ⟨110⟩ axes, we find a conserved spin quantity in the vicinity of the Fermi contours in the first valence subband. In contrast to the findings in Refs. [7, 26], this quantity meets realistic requirements for the Luttinger parameters. For more restrictive conditions, we even find a conserved spin quantity for vanishing strain, restricted to the vicinity of the Fermi surface.

5.1 Motivation

As seen in Chap. 1, the SOC for holes is distinct and much more complex than for electrons although the underlying fundamental mechanism, described by the Dirac equation, is the same. Since the conduction band, for most semiconductors, is an s-type energy band and the valence band is of p-type, the qualitative variation comes from the different total angular momentum, which is $j = 3/2$ in the valence band, giving rise to heavy and light holes (HH, LH) and the split-off holes. As the mixing of HH and LH strongly influences the SOC, the reduction of dimensionality, like in 2DHGs in semiconductor heterostructures, has an immediate effect [90]. This is due to the fact that the size quantization causes an energy separation between HH and LH states even at a vanishing in-plane Bloch wave vector, which affects the strength of the HH-LH mixing and thus the SOC at finite k-vectors. As a consequence, the magnitude of the SOC, especially the prefactor for Rashba SOC, depends sensitively on the confinement, as will be discussed in this chapter. Conversely, the Rashba SOC in the lowest conduction band is hardly affected by the size quantization (cf. Sec. 1.4 and Chap. 4). This is due to the s-type character of the energy band and also since the SOC is mainly determined by the energy gaps between the bulk bands. These energy gaps, however, do not differ significantly if adding a confinement. For a proper description of the hole system, compared to electron systems, a substantially higher number of SOC terms is needed and requires approximations for an analytical investigation at an early stage. Also, internal or external strain can yield significant consequences to the hole band structure (cf. Sec. 1.5). The reason is that it introduces additional couplings between the HH and LH bands, whereas - assuming a semiconductor

with a direct bandgap - the conduction band is only indirectly affected due to the interaction with the strain-altered valence band [81, 96, 106, 151]. Moreover, the cubic crystal structure of the semiconductor has an imprint on the symmetry of the hole spectrum as can be seen in the warping of the Fermi contours and these always follow the strained crystal symmetry.

Nonetheless, despite their complexity hole systems offer opportunities not available in electron systems and are particularly interesting for practical device applications for several reasons. First, the large effective mass m^* of holes compared to conduction band electrons diminishes the kinetic term such that contributions from SOC become more important. Secondly, the p-type character of the HH and LH states reduces the hyperfine interaction of the carrier spin with the nuclei (cf. Sec. 2.4). This allows in principle for long spin lifetimes and dephasing times [152, 153]. Another important aspect is the strength of the SOC in hole systems which can reach several meV in the splitting as, e.g., shown in GaAs/AlGaAs heterostructures [154, 155]. All these features of p-type systems facilitate a very effective manipulation of carrier spins and, hence, motivate further studies of hole gases in semiconductors as the one presented hereafter. Moreover, since in a 2DEG the conserved spin quantities are often limited by a k-cubic Dresselhaus contribution (cf. Chap. 4), the question arises whether this is also the case for the 2D hole systems.

An appealing continuation of the findings on spin-preserving symmetries in electron systems is the analysis of persistent spin states in hole systems as done recently in Refs. [7, 26]. However, these studies presuppose materials with strongly restricted and unusual band structures. Following Ref. [7], a strainless sample with both Rashba and Dresselhaus SOC allows for the existence of a persistent spin helix (PSH) in a 2DHG only in the case of a vanishing Luttinger parameter γ_3 with $\gamma_1 > 0$ and $\gamma_2 > 0$ [7]. Most of the semiconductors can only be properly described using a band model where $\gamma_2 < \gamma_3$, though (cf. Sec. 1.4.1) [70, 73, 156]. In Ref. [26], the PSH was found in the presence of finite strain and Rashba SOC where the condition for the Luttinger parameters is restricted by a different, however, also unusual condition $\gamma_2 = -\gamma_3$[1].

Aside from that, Refs. [7, 26] make use of a frequently applied approximation, in which all invariants in the bulk Hamiltonian are dropped that result from BIA and have relatively small expansion coefficients. This procedure may be justified in the bulk but, as recently shown, not necessarily for 2D systems. In 2DHGs, this approach leads to a model Hamiltonian with both Rashba and Dresselhaus SOC being essentially cubic in momentum [7, 91]. However, recent publications [92, 99], which are related to the seminal paper by Rashba and Sherman, Ref. [90], show that the relevance of the linear Dresselhaus terms in 2DHGs has been underestimated. Therefore, the above-mentioned estimations are questionable and fail at least for the standard compound GaAs.

In this chapter, we take into account linear and cubic Dresselhaus and Rashba

[1] A negative value of γ_2/γ_3 appears, e.g., when the lowest conduction band is not an s-type band as it is the case in diamond [157]. However, for diamond one finds only $\gamma_2/\gamma_3 \approx -0.16$ [157].

SOC as well as strain effects. With this, we identify conditions under which conserved spin quantities can be found for a wide range of semiconductors.

5.2 Hole Model Hamiltonian

The aim of our investigation is to identify the appropriate interplay between BIA (Dresselhaus SOC), a confining potential $V(\mathbf{r})$ (built-in and/or external) causing SIA, and strain (either externally imposed using, e.g., the piezoelectric effect or induced by the epitaxial growth process) which gives rise to a conserved spin quantity in the hole system. To find analytic conditions we derive an effective HH/LH-like 2×2 model, depending on the character of the topmost valence band. Starting point is a 4×4 model, which is derived from the extended Kane model and includes the Luttinger Hamiltonian. The respective terms were introduced and discussed in Sec. 1.4.

5.2.1 Effective 4×4 Hole Hamiltonian

The applied model which we use as a starting point for the investigation is an effective 4×4 Hamiltonian given by

$$\mathcal{H} = \mathcal{H}_{\mathrm{L}} + \mathcal{H}_{\mathrm{BIA}} + \mathcal{H}_{\mathrm{S}} + V. \tag{5.1}$$

The first term $\mathcal{H}_{\mathrm{L}}$ represents the Luttinger Hamiltonian for III-V semiconductors, Eq. (1.37). The second term $\mathcal{H}_{\mathrm{BIA}}$ accounts for the Dresselhaus SOC, Eq. (1.46). Furthermore, the effect of strain is described by the Bir-Pikus strain Hamiltonian $\mathcal{H}_{\mathrm{S}}$, Eq. (1.85). We assume the strain, with ϵ_{ij} being the symmetric strain tensor, to be uniaxial in-plane or biaxial in-plane. As a consequence, an in-plane strain with the tensor components ϵ_{xx}, ϵ_{yy}, ϵ_{xy} yields only one extra strain component, ϵ_{zz}. Thus, we set $\epsilon_{xz} = \epsilon_{yz} = 0$ in Eq. (1.85). Eventually, the potential $V = V_{\mathrm{E}} + V_{\mathrm{c}}$ includes the confining potential $V_{\mathrm{c}}(z)$ and the external potential $V_{\mathrm{E}}(z)$. The latter causes SIA which induces Rashba SOC. We assume the potential V to depend only on the z-coordinate, which is pointing in the growth direction [001] of the semiconductor heterostructure. More explicitly,

$$V_{\mathrm{E}}(z) = \mathbb{1}_{4\times4} \cdot e\,\mathcal{E}_z z, \tag{5.2}$$

and an infinite square well of width L with

$$V_{\mathrm{c}}(z) = \mathbb{1}_{4\times4} \cdot \begin{cases} 0 & \text{for } z \in [0, L]\,, \\ \infty & \text{otherwise.} \end{cases} \tag{5.3}$$

As pointed out in Sec. 1.4.4, the discontinuity of the potential V_{c} can result in non-Hermitian matrix elements of k_z^3. In our study, this problem does not occur since the responsible terms are neglected later on due to their insignificance. Furthermore, contributions due to boundary effects which result from the presence of heterointerfaces are assumed to be small. Such an interface can allow for additional HH-LH mixing [99, 158–160]. A possible alternation of the spin relaxation due to interface effects will be discussed elsewhere.

5.2.2 Effective 2 × 2 Model for the First Subband

In the following, we choose the basis states in such a way that the upper left block represents the HH the lower right block the LH subspace:

$$\mathcal{H} = \begin{pmatrix} \mathcal{H}_{\text{HH}} & \mathcal{H}_{\text{HH-LH}} \\ \mathcal{H}_{\text{LH-HH}} & \mathcal{H}_{\text{LH}} \end{pmatrix}. \tag{5.4}$$

The confinement in z-direction allows for a further simplification of the model to an effective 2×2 Hamiltonian using Löwdin's partitioning. The full Hamiltonian $\mathcal{H}$ is separated into two parts

$$\mathcal{H} = \mathcal{H}_0 + \mathcal{H}', \tag{5.5}$$

according to App. 1.A. The partition is, in general, not uniquely defined and different ways of splitting $\mathcal{H}$ are possible. For the given system, a meaningful decomposition is the one which allows a projection on the subspace of a particular HH or LH-like subband. Here, we select $\mathcal{H}_0$ to contain the diagonal elements of $\mathcal{H}_{\text{L}} + \mathcal{H}_{\text{S}} + V_{\text{c}}(z)$ at $k_x = k_y = 0$, and $\mathcal{H}'$ is treated as a perturbation with respect to the appropriate inverse splitting $1/\Delta_{\text{hl}}$, $(1/\Delta_{\text{hh}})$ between a HH-like and a LH(HH)-like subband. The energy splitting Δ_{hl} is due to both the spatial confinement in the [001] direction and the imposed strain.

According to the confinement, the eigenstates of $\mathcal{H}_0$ are given by $|j, m_j\rangle\,|n\rangle$, the product of the eigenstates of the total angular momentum $\mathbf{J}$ with $j = 3/2, m_j = \pm 1/2$ for LH and $m_j = \pm 3/2$ for HH and the subband index of z-quantization $n \in \mathbb{N}^+$. The eigenfunctions of the quantum well in position space read as $\langle z|n\rangle = \sqrt{2/L}\sin(z\,n\,\pi/L)$, which lead to the matrix elements of the k_i and z operators given in Eqs. (1.57)-(1.59). The eigenenergies of $\mathcal{H}_0$ (two-fold degenerate) according to the subspaces are given by

$$E_{\text{HH}}(n) = -\frac{\hbar^2}{2m_0}(\gamma_1 - 2\gamma_2)\,\langle k_z^2\rangle\,n^2, \tag{5.6}$$

$$E_{\text{LH}}(n) = -\frac{\hbar^2}{2m_0}(\gamma_1 + 2\gamma_2)\,\langle k_z^2\rangle\,n^2 + \delta, \tag{5.7}$$

where $\delta = b\,(\epsilon_{xx} + \epsilon_{yy} - 2\epsilon_{zz})$ corresponds to the diagonal shear strain tensor and $\langle k_z^2\rangle \equiv \langle 1|k_z^2|1\rangle$. For simplification, we subtracted an overall constant energy shift of $\Delta E = -\sum_i (a_v + 3b/4)\epsilon_{ii} - (3/2)b\epsilon_{zz}$. It becomes apparent that strain effects as well as the confining potential lift the degeneracy of HH and LH bands at $k_\parallel \equiv \sqrt{k_x^2 + k_y^2} = 0$.

In the following, the in-plane strain contribution will be rewritten, according to Ref. [26], defining an in-plane strain amplitude β and orientation θ as[2]

$$\beta^2 e^{2i\theta} := \frac{m_0}{\hbar^2\gamma_3}(b\,(\epsilon_{xx} - \epsilon_{yy}) + 2id\epsilon_{xy}). \tag{5.8}$$

[2]Note that the definition in Eq. (5.8) differs from the one given in Ref. [26] in the term proportional to d by a factor of $1/\sqrt{3}$.

The effective Hamiltonian for the lowest subband is now derived by Löwdin perturbation theory (see App. 1.A). Thereby, the lowest subband can be either a HH-like or a LH-like subband, depending on the magnitude and type of strain. Up to third order in the energy splitting it yields

$$\mathcal{H}_{\text{eff}} \approx \sum_{p=0}^{3} \mathcal{H}^{(p)} \tag{5.9}$$

$$= \sum_{p=0}^{3} \left(E_{\text{kin}}^{(p)} + V_{\text{eff}}^{(p)} \right) \cdot \mathbb{1}_{2\times 2} + \boldsymbol{\Omega}^{(p)} \cdot \boldsymbol{\sigma}, \tag{5.10}$$

with the Pauli matrices σ_i and the $\mathcal{H}^{(p)}$, where the superscript (p) indicates the order in the perturbation (cf. App. 1.A). Additionally, we will neglect terms of the order of $\mathcal{O}(k^4)$.

We would like to mention some properties of the perturbation theory first. Concerning the decomposition of the Hamiltonian, it should be stressed that if we instead choose $\mathcal{H}_0 = \mathcal{H}_{\text{L}} + \mathcal{H}_{\text{S}}$, that is, without the confinement potential, we can make use of the non-commutativity of the momentum operator k_z and the position operator z to derive a finite Rashba coefficient as done in Refs. [26, 70]. However, in this case, the energy splitting Δ_{hl} cannot be a result of the subband quantization, but only have strain as an origin. This approximation may be justified if the strain splitting is much larger than the subband splitting. Yet, since we consider a quasi 2D system, the subband splitting is an essential effect and we are thus to choose the partitioning as described above.

An important observation of the perturbation presented in this paper is that a finite Rashba SOF, resulting from the coupling between different subbands, can only be obtained by third or higher order perturbation theory. This is due to the fact that the diagonal elements of $\mathcal{H}'$, Eq. (5.5), and thus $\mathcal{E}_z$, are not yet involved in the second order, according to Eq. (1.A.6). In addition, it will be shown in the following that assuming a HH(LH)-like ground state it is necessary to include, in addition to the first LH(HH)-like subband, also the second HH(LH)-like subband in the perturbation procedure to obtain a finite contribution due to Rashba SOC.

Concerning the significance of the various Dresselhaus contributions in $\mathcal{H}_{\text{BIA}}$, Eq. (1.46), we mentioned earlier in Sec. 1.4.2, that in the bulk system keeping only the cubic term proportional b_{41}^{8v8v} is a good approximation. This is due to its large value compared to the other cubic terms as shown explicitly in App. 5.A.1. However, the size quantization causes an additional linear Dresselhaus contribution for HHs that would not appear if only the term proportional b_{41}^{8v8v} was considered. For the light holes, the situation is different as the term proportional b_{41}^{8v8v} already yields a linear term which clearly dominates over the remaining linear contributions. As a result, we will take into account the effect of the k-linear terms generated in the first-order perturbation by the terms proportional C_k, b_{42}^{8v8v} and b_{51}^{8v8v} only in case of a HH-like ground state and neglect them in case of a LH-like ground state. The coefficient b_{52}^{8v8v} yields only a small cubic term which can be disregarded. Based on its large value, for higher order BIA corrections we incorporate solely terms

proportional to b_{41}^{8v8v}.

Depending on the nature of the strain, the splitting can lead to either a lowest HH-like or LH-like subband. If we, e.g., specify to the case of uniaxial compressive stress in [110] direction, we obtain $\delta < 0$ since $\epsilon_{xx} = \epsilon_{yy} < 0$ and $\epsilon_{zz} > 0$ [106]. Therefore, the splitting between HH and LH is enhanced and the topmost subband is HH for arbitrary material since $\gamma_i > 0$. Consequently, we have to distinguish two cases:

(i) System with a HH-like Ground State

Assuming the ground state being HH-like and applying third-order Löwdin perturbation theory, we get for the part of the Hamiltonian which is proportional to unity in spin space, according to Eq. (5.10),

$$E_{\mathrm{kin,HH}} = E_{\mathrm{kin},+}, \tag{5.11}$$

$$V_{\mathrm{eff,HH}} = V_{\mathrm{eff},+}(\Delta_{\mathrm{h1,h2}}), \tag{5.12}$$

where we defined

$$\begin{aligned} E_{\mathrm{kin},\pm} = & -\frac{\hbar^2}{m_0}\left(\gamma_1 \pm \gamma_2\right) k_\parallel^2 \pm \frac{1}{\Delta_{\mathrm{h1,l1}}}\left\{\frac{3}{4}\left(b_{41}^{8v8v}\left\langle k_z^2\right\rangle\right)^2 k_\parallel^2 \right. \\ & \left. + \frac{3\hbar^4}{2m_0^2}\beta^2\gamma_3^2\left[\frac{\gamma_2}{\gamma_3}\left(k_x^2 - k_y^2\right)\cos(2\theta) + 2k_x k_y \sin(2\theta)\right]\right\} \end{aligned} \tag{5.13}$$

and

$$\begin{aligned} V_{\mathrm{eff},\pm}(\Delta) = & \sum_i \left(a_v + \frac{3}{4}b\right)\epsilon_{ii} + \frac{3}{2}b\epsilon_{zz} - \frac{\hbar^2\left\langle k_z^2\right\rangle}{2m_0}\left(\gamma_1 \mp 2\gamma_2\right) + \frac{e\mathcal{E}_z L}{2} \\ & \pm \frac{3\hbar^4}{4m_0^2\Delta_{\mathrm{h1,l1}}}\beta^4\gamma_3^2 + \frac{256L^2e^2\mathcal{E}_z^2}{81\Delta}. \end{aligned} \tag{5.14}$$

The energy gaps are given by $\Delta_{\mathrm{ln,hm}} = E_{\mathrm{LH}}(n) - E_{\mathrm{HH}}(m)$ and $\Delta_{\mathrm{hn,lm}}$ analogously. The effective vector field $\mathbf{\Omega}$ due to Rashba and Dresselhaus SOC, which is modified by the presence of strain, yields

$$\mathbf{\Omega}_{\mathrm{HH}} = \mathbf{\Omega}_+ \tag{5.15}$$

with components given by

$$\begin{aligned} \Omega_{x,\pm} = & \lambda_{\mathrm{R},\pm}\left\{\pm\left(\gamma_2 \pm 2\gamma_3\right)k_x^2 k_y \mp \gamma_2 k_y^3 + \beta^2\gamma_3\left[\pm k_y\cos(2\theta) + k_x\sin(2\theta)\right]\right\} \\ & + \eta_\pm k_x + \lambda_{\mathrm{D},\pm}\left\{k_x k_y^2\left(\gamma_2 \mp 2\gamma_3\right) - k_x^3\gamma_2\right. \\ & \left. + \beta^2\gamma_3\left[\pm k_y\left(\frac{k_x^2}{\langle k_z^2\rangle} - 1\right)\sin(2\theta) + k_x\left(\frac{k_y^2}{\langle k_z^2\rangle} - 1\right)\cos(2\theta)\right]\right\}, \end{aligned} \tag{5.16a}$$

$$\begin{aligned}\Omega_{y,\pm} = & \pm\lambda_{\mathrm{R},\pm}\left\{\pm\left(\gamma_2\pm2\gamma_3\right)k_xk_y^2\mp\gamma_2k_x^3+\beta^2\gamma_3\left[k_y\sin(2\theta)\mp k_x\cos(2\theta)\right]\right\}\\ & \pm\eta_\pm k_y+\lambda_{\mathrm{D},\pm}\Bigg\{\pm k_x^2k_y\left(\gamma_2\mp2\gamma_3\right)\mp k_y^3\gamma_2\\ & +\beta^2\gamma_3\left[k_x\left(\frac{k_y^2}{\langle k_z^2\rangle}-1\right)\sin(2\theta)\mp k_y\left(\frac{k_x^2}{\langle k_z^2\rangle}-1\right)\cos(2\theta)\right]\Bigg\},\end{aligned}\tag{5.16b}$$

$$\Omega_{z,\pm}=0.\tag{5.16c}$$

Here, the Dresselhaus coefficients $\eta_\pm$, $\lambda_{\mathrm{D},\pm}$ and the Rashba coefficient $\lambda_{\mathrm{R},\pm}$ are given by

$$\eta_+ = -\frac{\sqrt{3}}{2}C_k-\frac{3}{4}\left(b_{42}^{8v8v}+b_{51}^{8v8v}\right)\langle k_z^2\rangle\tag{5.17}$$

$$\eta_- = -b_{41}^{8v8v}\langle k_z^2\rangle\tag{5.18}$$

$$\lambda_{\mathrm{D},\pm} = \pm\frac{3\hbar^2}{2m_0\Delta_{\mathrm{h1,l1}}}b_{41}^{8v8v}\langle k_z^2\rangle,\tag{5.19}$$

$$\lambda_{\mathrm{R},+} = \frac{128\hbar^4e\mathcal{E}_z\gamma_3}{9\pi^2m_0^2\Delta_{\mathrm{h1,l1}}\Delta_{\mathrm{h1,h2}}},\tag{5.20}$$

$$\lambda_{\mathrm{R},-} = \frac{128\hbar^4e\mathcal{E}_z\gamma_3}{9\pi^2m_0^2\Delta_{\mathrm{l1,h1}}\Delta_{\mathrm{l1,l2}}}.\tag{5.21}$$

The index $(\pm)$ distinguishes the case of a system with a HH-like ground state $(+)$ from the one with a LH-like ground state $(-)$.

Notice that given a vanishing γ_3 the dominant contribution due to Rashba SOC vanishes, too. Only a contribution as a result of the coupling to conduction bands is left, which is of higher than third order. More precisely, in the bulk system, for most semiconductors, the dominant invariant in the extended Kane model, which is present due to SIA, is given by (cf. Eq. (1.49))

$$\mathcal{H}_{8v8v}^{\mathrm{SIA}}=r_{41}^{8v8v}((k_y\mathcal{E}_z-k_z\mathcal{E}_y)J_x+\mathrm{c.p.}).\tag{5.22}$$

If the bulk system is reduced to an effective two-dimensional system, the according counterpart of this term in an effective 2×2 Hamiltonian can be calculated using Löwdin perturbation theory as done above, keeping the factor r_{41}^{8v8v} unchanged. However, as mentioned in Ref. [7], for a HH-like ground state this resulting term is of higher order than the one given proportional to λ_{R} (although represented by the same invariants). This can be understood by recalling the root of the coefficient r_{41}^{8v8v}: It is the coupling between valence and conduction bands. In contrast, if a confinement is present, the contribution resulting from Rashba SOC in the effective HH system is dominated by the splitting between HH and LH-like subbands. In the case of a LH-like ground state an additional k-linear Rashba term proportional to r_{41}^{8v8v} appears already in third-order perturbation theory. The angular momentum matrix J_x is zero in the HH subspace but has finite matrix elements in the LH subspace. Since the prefactor r_{41}^{8v8v} contains terms which are inversely proportional to the band gap [70], this contribution can be neglected since

we assume the conduction bandgap to be much larger than the subband splitting. The contribution stemming from BIA has a different nature: The parameter b_{41}^{8v8v}, which is connected with the invariant $(\{k_x, k_y^2 - k_z^2\}J_x + \text{c.p.})$ in the Kane model, is mainly defined through the valence band Γ_{8v} and conduction band Γ_{6c} gap E_0. Thus, it is hardly affected by the subband quantization. Moreover, in contrast to the Rashba contribution, the corresponding Dresselhaus term in the confined system appears already in second order of the applied perturbation. Hence, we also neglect higher-order contributions due to BIA.

(ii) System with a LH-like Ground State

According to Eqs. (5.6) and (5.7), on condition that $\delta > 2\hbar^2\pi^2\gamma_2/(m_0L^2)$ the ground state of the valence band is the first LH-like subband. As in the case of a HH-like ground state, we do not obtain a z-component in the effective SO field. However, in first-order Löwdin perturbation theory, Eq. (1.A.4), we obtain an additional linear term η_- and a cubic term $\mathbf{\Omega}_b$ proportional to b_{41}^{8v8v}. Furthermore, terms appear in third order which couple the electric field $\mathcal{E}_z$ with the Dresselhaus term proportional to b_{41}^{8v8v}, App. 5.A.2. Since the SOC is a small correction, these terms are much smaller than the one not mixing both factors. Thus, according to the previous case of a HH-like ground state, we have

$$E_{\text{kin,LH}} = E_{\text{kin},-}, \tag{5.23}$$

$$V_{\text{eff,LH}} = V_{\text{eff},-}(\Delta_{\text{l1,l2}}) + \delta. \tag{5.24}$$

The effective vector field $\mathbf{\Omega}$ due to Rashba and Dresselhaus SOC yields

$$\mathbf{\Omega}_{\text{LH}} = \mathbf{\Omega}_- + \mathbf{\Omega}_b \tag{5.25}$$

with the additional term

$$\mathbf{\Omega}_b = b_{41}^{8v8v}\left\{k_x k_y^2, -k_x^2 k_y, 0\right\}^\top. \tag{5.26}$$

5.2.3 Summarized Results

In summary, by developing an effective 2×2 model for a 2DHG we worked out the dominant contributions due to strain (β, θ), Rashba (λ_R) and Dresselhaus SOC (η, λ_D) to be considered in Eq. (5.10). The interplay between strain and Rashba or Dresselhaus SOC yields additional terms that are linear respectively linear as well as cubic in momentum. Thereby, we find that in contrast to the Rashba contribution the according Dresselhaus term in the confined system appears already in second-order Löwdin perturbation theory. In respect of finding a conserved spin quantity, we extracted the effective vector fields $\mathbf{\Omega}_{\text{HH}}$ for a HH-like ground state and $\mathbf{\Omega}_{\text{LH}}$ for a LH-like ground state in Eqs. (5.15) and (5.25). The fields cover a wide parameter space. In the next section, this will allow for identifying conserved spin quantities that do not require parameter configurations which are difficult to realize in real materials (e.g., $\gamma_3 = 0$ in Ref. [7], $\gamma_2 = -\gamma_3$ in Ref. [26]). Thus, it facilitates the detection of long-lived spin states in experiments.

5.3 Conserved Spin Quantity

Following the analysis of Ref. [18], our goal is to identify a conserved quantity Σ which is directly connected to k-independent eigenspinors. The general ansatz is

$$\Sigma = s_0 \mathbb{1}_{2\times 2} + \mathbf{s}\cdot\boldsymbol{\sigma}. \tag{5.27}$$

For this quantity to be conserved, it has to fulfill the relation $[\Sigma, \mathcal{H}_{\text{eff}}] = 0$ which is true for

$$\Omega_x s_z = \Omega_y s_z = 0 \quad \wedge \quad \Omega_y s_x - \Omega_x s_y = 0. \tag{5.28}$$

We are going to prove that one can find two solutions to this problem given by

$$\Sigma_\xi = \sum_{\mathbf{k}, k=k_{\parallel F}} \sum_{\alpha\beta} c^\dagger_{\mathbf{k}\alpha}(\sigma_x + \xi\sigma_y)_{\alpha\beta} c_{\mathbf{k}\beta}, \tag{5.29}$$

with $\xi = \pm$, if either the strain is absent or its direction fulfills

$$\theta = \pm\frac{\pi}{4} \equiv \chi\frac{\pi}{4}. \tag{5.30}$$

Here, $c^\dagger_{\mathbf{k}\alpha}$ creates a HH(LH) in the spin state $\alpha = \pm$ for $m_j = \pm 3/2$ ($m_j = \pm 1/2$). We assume that the Fermi wave vector $k_{\parallel F}$ does not deviate much from rotational symmetry and thus can be replaced by its angular average value $k_{\parallel F} \equiv \langle k_{\parallel F}\rangle_\varphi$ [7, 26]. This situation holds for materials close to axial symmetry, i.e., $\gamma_2 = \gamma_3$, and a small strain amplitude β. Therefore, we transform $\{k_x, k_y\}^\top$ into polar coordinates, $k_{\parallel F}\{\cos(\varphi), \sin(\varphi)\}^\top$. Thus, if a hole, with a spin state given by $\{1, \pm\exp(\xi i\pi/4)\}^\top/\sqrt{2}$ and $k = k_{\parallel F}$ is injected into the two-dimensional system (including spin-independent scattering processes) its spin is not randomized.

For the in-plane strain, the direction condition basically requires symmetric normal strain components $\epsilon_{xx} = \epsilon_{yy}$ and a non-vanishing shear strain component ϵ_{xy}. This situation can be generated by $\langle 110\rangle$ uniaxial strain [106]. We demonstrate this explicitly in App. 5.B for an experimental setup by use of a piezo crystal as done by Habib *et al.* in Ref. [161].

As we will see in the following, the constraint on the wave vector $\mathbf{k}$ of persistent spin states is crucial since it reveals that we found no conserved spin quantity for the whole k-space but only for the averaged Fermi contour. However, this constraint is not surprising when we recall the case of persistent spin states in [001]-oriented 2DEGs (cf. Sec. 2.1 and Chap. 4). If the SO terms are linear in the wave vector, the condition for the existence of persistent spin states is fulfilled if the Rashba SOC coefficient is equal to the one for the linear Dresselhaus term. In this special case, the SOF is collinear in the whole k-space. If the cubic Dresselhaus term is included, we cannot find a quantity Σ which commutes with the Hamiltonian $\mathcal{H}$ at every wave vector, though. Nevertheless, if the SOC terms are Fourier decomposed and only the lowest harmonics in the azimuthal angle is considered, one finds a condition for long-lived spin states. In contrast to the case without the cubic contribution, the found symmetry is, however, bound to an appropriate energy. This can also

be seen in the spin-relaxation rates in diffusive 2DEGs as well as planar quantum or cylindrical wurtzite nanowires with SOC (cf. Chaps. 4 and 8) [61, 146]. One does not only find an additional spin-relaxation term due to the cubic Dresselhaus term but also a shift of the linear Dresselhaus coefficient. This shift depends on the Fermi energy.

In the following (as in the previous section), we consider separately the case of a HH-like ground state and the LH-like ground state. For the sake of simplicity, we apply the following replacements:

$$\lambda_{\mathrm{D},\pm} = n_{\mathrm{HH/LH}}\lambda_{\mathrm{R},\pm}, \tag{5.31}$$

$$\gamma_3 = \Gamma\gamma_2, \tag{5.32}$$

$$\beta = Bk_{\parallel F}, \tag{5.33}$$

$$\langle k_z^2\rangle = \left(\frac{k_{\parallel F}}{\kappa}\right)^2, \tag{5.34}$$

and for the HH-like state additionally

$$\eta_+ = \eta_0\gamma_2\left\langle k_z^2\right\rangle \lambda_{\mathrm{D},+}. \tag{5.35}$$

In contrast to the discussed effect of the cubic Dresselhaus in an 2DEG, we will find persistent and not only long-lived spin states.

5.3.1 Conserved Spin Quantity in Case of a HH-like Ground State

Making use of the definitions above and setting $n \equiv n_{\mathrm{HH}}$ for simplicity, we obtain for Σ_ξ the following equation according to Eq. (5.28):

$$0 = \Omega_{y,+} - \xi\Omega_{x,+} \tag{5.36}$$

$$\begin{aligned} &= (\cos(\varphi) - \xi\sin(\varphi))\left\{B^2\Gamma\xi\left(n+\xi\right) + \chi\left[\xi + n(\eta_0/\kappa^2 - 1)\right]\right. \\ &\quad \left. + \left[B^2\kappa^2 n\Gamma + 2\chi\left(1+\Gamma+n\xi\left(\Gamma-1\right)\right)\right]\cos(\varphi)\sin(\varphi)\right\}. \end{aligned} \tag{5.37}$$

This equation is fulfilled independently of the polar angle φ if the ratio between Dresselhaus and Rashba SOC strength n and the strain strength factor B satisfy the relations

$$n_{\xi,\chi}^{(\pm)} = \xi\frac{2\left(1+\Gamma\right)}{2\left(1-\Gamma\right) - (\xi\chi)\Gamma\kappa^2\left(B_{\xi,\chi}^{(\pm)}\right)^2} \tag{5.38}$$

and

$$B_{\xi,\chi}^{(\pm)} = \sqrt{\frac{\xi\chi\left(4-\kappa^2\right) \pm \mathcal{W}}{2\Gamma\kappa^2}}, \tag{5.39}$$

where

$$\mathcal{W} = \sqrt{\kappa^4 + 8\left(1+\Gamma\right)\eta_0 - 8\left(1+2\Gamma\right)\kappa^2 + 16}, \tag{5.40}$$

and $-B_{\xi,\chi}^{(\pm)}$ are also solutions.

If the C_k term in Eq. 5.17 can be neglected,[3] real solutions for $B^{(\pm)}_{\xi,\chi}$ are only found for $\kappa \in A_{\mathrm{sgn}(\xi\cdot\chi)}$ where

$$A_+ = \left[0, 2\sqrt{1+2\Gamma-2\sqrt{(1+\Gamma)\,(\Gamma-\eta_0/8)}}\right], \tag{5.41}$$

$$A_- = \left[2\sqrt{1+2\Gamma+2\sqrt{(1+\Gamma)\,(\Gamma-\eta_0/8)}}, \infty\right) \tag{5.42}$$

if $\mathrm{Im}(A_{\mathrm{sgn}(\xi\cdot\chi)}) = 0$ which usually holds as typically $\Gamma > 0$ and $\eta_0 < 0$.

In absence of strain, that is, $\beta = 0$, the formulas above yield the following requirements on the ratio n and for the Fermi wave vector $k_{\|F}$ to get Σ_ξ:

$$n_0 \equiv n = \xi\frac{1+\Gamma}{1-\Gamma}, \tag{5.43}$$

$$k_0 \equiv k_{\|F} = \sqrt{\frac{\eta_+}{2\gamma_2\lambda_{\mathrm{D},+}}\frac{1+\Gamma}{\Gamma}}. \tag{5.44}$$

In this scenario, the SOF even vanishes at a specific value k_0 of the Fermi wave vector in the axially symmetric case, i.e., $\Gamma = 1$. For this purpose, both linear and cubic Dresselhaus contributions are crucial. Hence, this solution was not existent in our previous publication Ref. [7]. The axially symmetric case demands a vanishing Rashba contribution, $\lambda_{\mathrm{R},+}/\lambda_{\mathrm{D},+} \approx 0$. However, for the most semiconductors Γ ranges from 1 to 1.5. Thus, the cubic Dresselhaus SOC strength has to outweigh the Rashba SOC strength, i.e., $|\lambda_{\mathrm{D},+}| > |\lambda_{\mathrm{R},+}|$.

More peculiar solutions occur for $\Gamma \neq 1$ or in the presence of strain. For certain parameter configurations, the SOF becomes collinear on the averaged Fermi contour. As a consequence, this SU(2) spin rotation symmetry gives rise to a persistent spin helix [19]. For a start, by setting $\Gamma = -1$, $\chi = \xi = 1$ we can recover the solutions presented by Sacksteder *et al.* in Ref. [26]. In this case, we obtain $n = 0$, which is obvious since Dresselhaus SOC was not considered in Ref. [26], and $B = 1$, which is consistent with their results. It is remarkable that the presence of the linear Dresselhaus term, which was not considered either by Sacksteder *et al.*, does not alter the result. Note that here, too, the solution for the conserved spin quantity is bound to an averaged Fermi contour by Eq. (5.33). Moreover, recalling Eq. (5.28), one finds for these particular parameters a conserved spin quantity for every direction θ, given by

$$\Sigma = \sin(\theta)\sigma_x - \cos(\theta)\sigma_y, \tag{5.45}$$

which generalizes the result from the previous publication. Yet, we emphasize that the condition $\Gamma = -1$ is rather unusual for most materials (cf. Sec. 1.4.1).

Regarding the realization of persistent spin states in experiments, it is of interest to analyze whether the constraints allow for realistic parameters (i.e., typical for

[3] The full expression is given in App. 5.C.

III-V semiconductors). Thus, we present a concrete example for the conserved quantities Σ_ξ. At this, we assume $\gamma_3 - \gamma_2 > 0$, Eq. (1.44), and $\gamma_i > 0$ to hold and choose, as an example, $\Gamma = 1.2$ for the plots of $n^{(\pm)}_{\xi,\chi}$ and $B^{(\pm)}_{\xi,\chi}$, Fig. 5.1. In order to draw a general picture and for simplicity we neglected the linear Dresselhaus contribution, i.e., $\eta_0 \to 0$. In the range A_+, i.e., $\xi = \chi$ that comprises realistic values for κ (e.g., $\kappa = 0.3$ for a confinement width $L = 100\,\text{Å}$ and a small Fermi vector $k_{\parallel F} = 0.01\,\text{Å}^{-1}$) solutions are displayed in Fig. 5.1(a,b). The solutions with a small B value, $B^{(-)}_{-,-}$ in Fig. 5.1(b), are preferable since in this case, the deformation of the Fermi contour is small. In addition, it is reasonable to assume that $n > 1$, since the Dresselhaus contribution is usually larger than the Rashba contribution. The domain A_- ($\xi = -\chi$) shown in Fig. 5.1(c,d) is less realistic. Having large values of κ implies a large width of the quantum well and a high Fermi energy which leads to populations in higher subbands where the model loses its validity. Also, for a large Fermi energy the Fermi contour is strongly deformed as can be understood by examining the term proportional to $\beta^2\gamma_3^2$ of the kinetic energy, Eq. (5.13). A spherical approximation becomes inappropriate. Moreover, if a strong strain is applied to the sample the appropriate model Hamiltonian needs to include also the coupling to the split-off band.

For future devices like the spin field-effect-transistor, it is not only of interest to find persistent spin states. In fact, samples are favorable where the injected particles undergo only a well-defined spin-rotation. Thereby the initial spin state, with $\mathbf{k}$ being a good quantum number, is not necessarily an eigenstate. Here, *well-defined* means that the rotation only depends on the distance between the injection and detection position. For n-type systems, this condition was first analyzed in Ref. [18]. Concerning a 2DHG as described in this paper, a spin-conserving condition, which is valid for spin states with arbitrary wave vectors, cannot be found: The condition is limited to the averaged Fermi contour. For these states, we can find an additional condition so that their precession depends only on the distance. At this, a necessary condition is an elastic scattering from impurities. The corresponding effective vector field in the case where the Eqs. (5.38) and (5.39) hold has the structure given by

$$\mathbf{\Omega}_{\text{HH}} = (k_x + \xi k_y)\varphi^{(\pm)}(k_x, k_y) \begin{pmatrix} \xi \\ 1 \\ 0 \end{pmatrix} \Bigg|_{k_x^2 + k_y^2 = k_{\parallel F}^2} . \tag{5.46}$$

In the case where $(k_x + \xi k_y)\varphi^{\pm}(k_x, k_y)$ depends linearly on k_i ($k_{\parallel F}$ is a constant), the mentioned spin-rotation is only distant dependent. Here, one finds

$$\varphi^{(\pm)}(k_x, k_y) = \frac{k_{\parallel F}^2 \gamma_2 \lambda_{R,+}}{\kappa^2(\pm\xi\chi\mathcal{W} + 4\Gamma - \kappa^2)} \Bigg[2(4 \pm \xi\chi\mathcal{W})(1 + \Gamma) - (2 \pm \xi\chi\mathcal{W} + 6\Gamma)\kappa^2 + \kappa^4 + \xi 8(\Gamma^2 - 1)\kappa^2 \frac{k_x k_y}{k_{\parallel F}^2} \Bigg]. \tag{5.47}$$

Thus, the special case where a well-defined spin rotation occurs can only be found if $\Gamma \equiv \gamma_3/\gamma_2 = \pm 1$.

5.3.2 Conserved Spin Quantity in Case of a LH-like Ground State

Analogously, it is possible to find conserved spin quantities if the ground state is LH-like. Yet, the structure of the SOF is more complex since it contains an additional first-order term due to Dresselhaus SOC, Eq. (5.26). As stated above, an [110] uniaxial compressive strain leads to $\delta < 0$ and therefore cannot be used. It is commonly known that for in-plane biaxial tensile stress LH ground state can be created but in that case ϵ_{xy} vanishes [106]. Consequently, combined strain effects are necessary to generate the required condition. Nonetheless, we stress that we do not demand a strong in-plane strain amplitude for identifying a conserved spin quantity. In fact, an appropriate tensor component ϵ_{zz} is necessary. This component is encapsulated in the splitting

$$\Delta_{\mathrm{h1,ln}} = \frac{\hbar^2}{2m_0} \langle k_z^2 \rangle \left[\left(n^2 - 1\right) \gamma_1 + 2 \left(n^2 + 1\right) \gamma_2 \right] - \delta, \tag{5.48}$$

and thus in the SOC strength. For simplicity, we set $n \equiv n_{\mathrm{LH}}$. Hence, the calculation of the conserved quantity is the same as before and valid as long as the deformation of the Fermi contour is not excessively strong. In this case, we find for the parameters $n_{\xi,\chi}^{(\pm)}$ and $B_{\xi,\chi}^{(\pm)}$ the relations

$$n_{\xi,\chi}^{(\pm)} = \frac{6\left(\Gamma - 1\right)}{3\chi\Gamma \left(B_{\xi,\chi}^{(\pm)}\right)^2 \kappa^2 - 2\xi \left(3\left(\Gamma + 1\right) + 2\mathcal{Q}\right)} \tag{5.49}$$

and

$$B_{\xi,\chi}^{(\pm)} = \sqrt{\frac{\xi\chi \left(4\mathcal{Q} - 3\kappa^2 + 12\right) \pm \mathcal{P}}{6\Gamma\kappa^2}}, \tag{5.50}$$

where we defined

$$\mathcal{P} = \sqrt{16\left(\mathcal{Q} + 3\Gamma\right)^2 + 24\kappa^2 \left(\mathcal{Q} + 6\Gamma - 3\right) + 9\kappa^4}, \tag{5.51}$$

$$\mathcal{Q} = \frac{\Delta_{\mathrm{l1,h1}}}{\left|\left(\Delta_{\mathrm{l1,h1}}\big|_{\delta=0}\right)\right|}. \tag{5.52}$$

The parameters $n_{\xi,\chi}^{(\pm)}$ and $B_{\xi,\chi}^{(\pm)}$ are plotted in Fig. 5.1(e,f) for $\Gamma = 1.2$ and $\mathcal{Q} = 1$ which is equivalent to an energy shift $\delta = 2\left|\left(\Delta_{\mathrm{l1,h1}}\big|_{\delta=0}\right)\right|$. We only find real solutions for $B_{\xi,\chi}^{(+)}$ and $n_{\xi,\chi}^{(+)}$. In contrast to the HH-like ground state for a realistic system with $\Gamma > 1$ we do not find a conserved spin quantity if strain is absent.

In the last part of this section, we apply the insights on the conserved spin quantity to a prominent semiconductor.

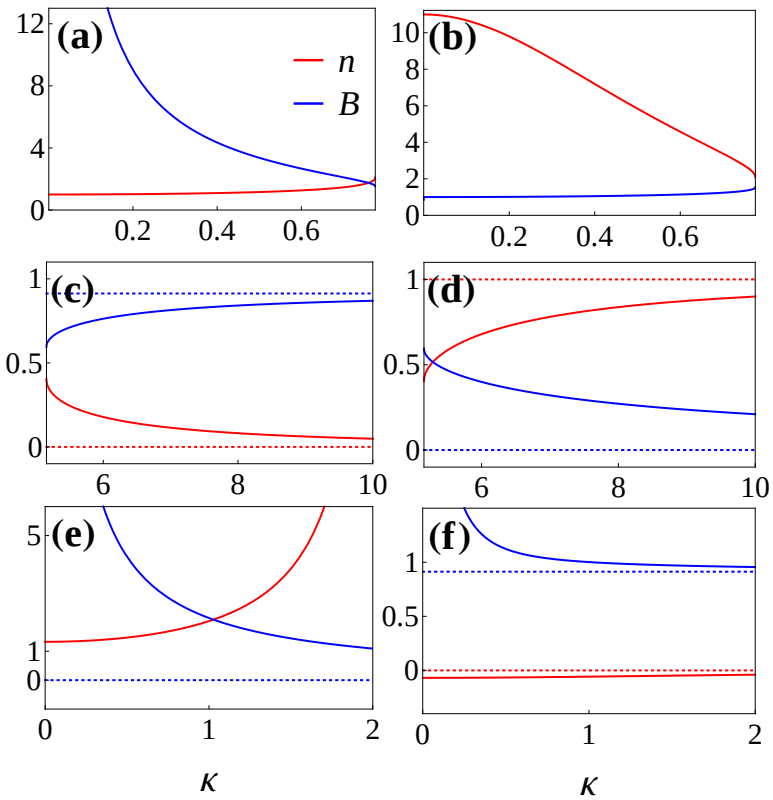

Fig. 5.1: Parameter configurations for $n^{(\pm)}_{\xi,\chi}$ and $B^{(\pm)}_{\xi,\chi}$ which yield the conserved spin quantity Σ_ξ for $\theta = \chi\pi/4$ in case of a HH-like ((a)-(d)) and LH-like ((e)-(f)) ground state. The ratio between the Luttinger parameter γ_3 and γ_2 is set to $\Gamma = 1.2$ and the linear Dresselhaus contribution is neglected, i.e., $\eta_0 \to 0$. The domain for κ is A_+ for $\xi = \chi$ and A_- else. The dashed lines indicate the according asymptotes at large width of the quantum well. (a) $n^{(+)}_{\xi,\chi}$ and $B^{(+)}_{\xi,\chi}$, (b) $n^{(-)}_{\xi,\chi}$ and $B^{(-)}_{\xi,\chi}$ for $\xi = \chi = -1$. If $\xi = \chi = 1$ holds only the sign of n is inverted. (c) $n^{(+)}_{\xi,\chi}$ and $B^{(+)}_{\xi,\chi}$, (d) $n^{(-)}_{\xi,\chi}$ and $B^{(-)}_{\xi,\chi}$ for $\xi = -\chi = 1$. Interchanging of ξ and χ only changes the sign of n. (e) $n^{(+)}_{\xi,\chi}$ and $B^{(+)}_{\xi,\chi}$ which yield the conserved spin quantity Σ_- for $\xi = \chi = -1$ and (f) $\xi = -\chi = -1$. The case $\xi = 1$ reverses only the sign of n.

5.3.3 Example: p-doped InSb

We choose p-doped InSb as an example to contrast the strained case yielding a conserved spin quantity with the one of a strainless sample. We assume a confinement in [001] direction with a depth of $L = 100\,\text{Å}$. To guarantee a low filling, we set $k_{\|F} = 0.01\,\text{Å}^{-1}$. The used parameters here are listed in App. 1.C. Further, we assume the additional splitting due to strain between HH and LH-like subbands to vanish, $\delta = 0$. Choosing an external electric field of $\mathcal{E}_z = 1.6\,\text{kV/cm}$ and a [110] tensile strain direction ($\epsilon_{xy} > 0$), i.e., $\xi = \chi = 1$, allows for a persistent spin polar-

ization in [110] direction. Since we can assume a HH-like ground state, we apply Eq. (5.38) and (5.39) and obtain the parameter for the in-plane strain strength to be $B_{1,1}^{(-)} = 0.74$ and the corresponding ratio between Dresselhaus and Rashba SOC strength to be $n_{1,1}^{(-)} = -20.7$.

In Fig. 5.2(d) the resulting effective SOF is plotted and compared to the case where the [110] stress is absent, Fig. 5.2(c). A stream plot, Fig. 5.2(a,b) shows that without strain, Fig. 5.2(a), the vector field vanishes approximately at $k_0 = 6.9 \times 10^{-3}\,\text{Å}^{-1}$, which is illustrated by the blue dotted circle. We see that even though the condition Eq. (5.43) on n_0 for the spin-preserving symmetry in the strainless case is not perfectly fulfilled, i.e., $n_{1,1}^{(-)} > n_0 = -29.6$, the location where the field disappears is still well described by k_0 in Eq. (5.44). Additionally, there is one source in the vector field at $k_{\parallel} = 0$. Including strain, Fig. 5.2(b), gives rise to two additional sources that are centered at the crossing of the Fermi contour and the $[1\bar{1}0]$ axis. This can be understood by considering the factor $(k_x + \xi k_y)$ in Eq. (5.46). At these two sources, the vector field components are suppressed which are not collinear with the [110] direction. The Fermi contours split due to the SOC. Without strain, they are only slightly deformed as consequence of the band warping. If strain is present, the deviation of rotational symmetry of the contours is enhanced. The deformation is most intense in the [110] and $[1\bar{1}0]$ direction. To guide the viewer's eye, we give in Fig. 5.2(e,f) a detailed picture of the SOF acting on the outer Fermi contour. In the case of strain the vectors lie parallel to the [110] direction. As discussed above, the plots also show that the preserved spin quantity is limited to the averaged Fermi contour. The vector field regions which are non-collinear are strongly suppressed, though. This leads to a reduction of spin relaxation even in the case of a general spin state injected into the 2DHG.

Influence of Linear Dresselhaus Terms

Moreover, we want to emphasize that in the chosen parameter regime the effect of the linear Dresselhaus contribution is only small. Fig. 5.3 shows how the field modifies if the linear Dresselhaus term proportional to η_+ is neglected. The strain-induced additional field sources move to a marginally lower Fermi wave vector by $\epsilon = 3.1 \times 10^{-3}\,\text{Å}^{-1}$ where the conserved spin quantity is reobtained. To first order in η_+ the shift ϵ can be generally estimated by

$$\epsilon = \frac{\eta_+}{\sqrt{2}\beta\gamma_3} \left\{ (\lambda_{\mathrm{D},+} + \lambda_{\mathrm{R},+}) \left[\frac{\beta^2 \lambda_{\mathrm{D},+}}{\langle k_z^2 \rangle} + 2(\lambda_{\mathrm{D},+} + \lambda_{\mathrm{R},+}) \right] \right\}^{-1/2} . \tag{5.53}$$

We stress that the influence of the linear BIA terms becomes even smaller for increasing Fermi wave vector k_F and in other materials such as GaAs is less significant.

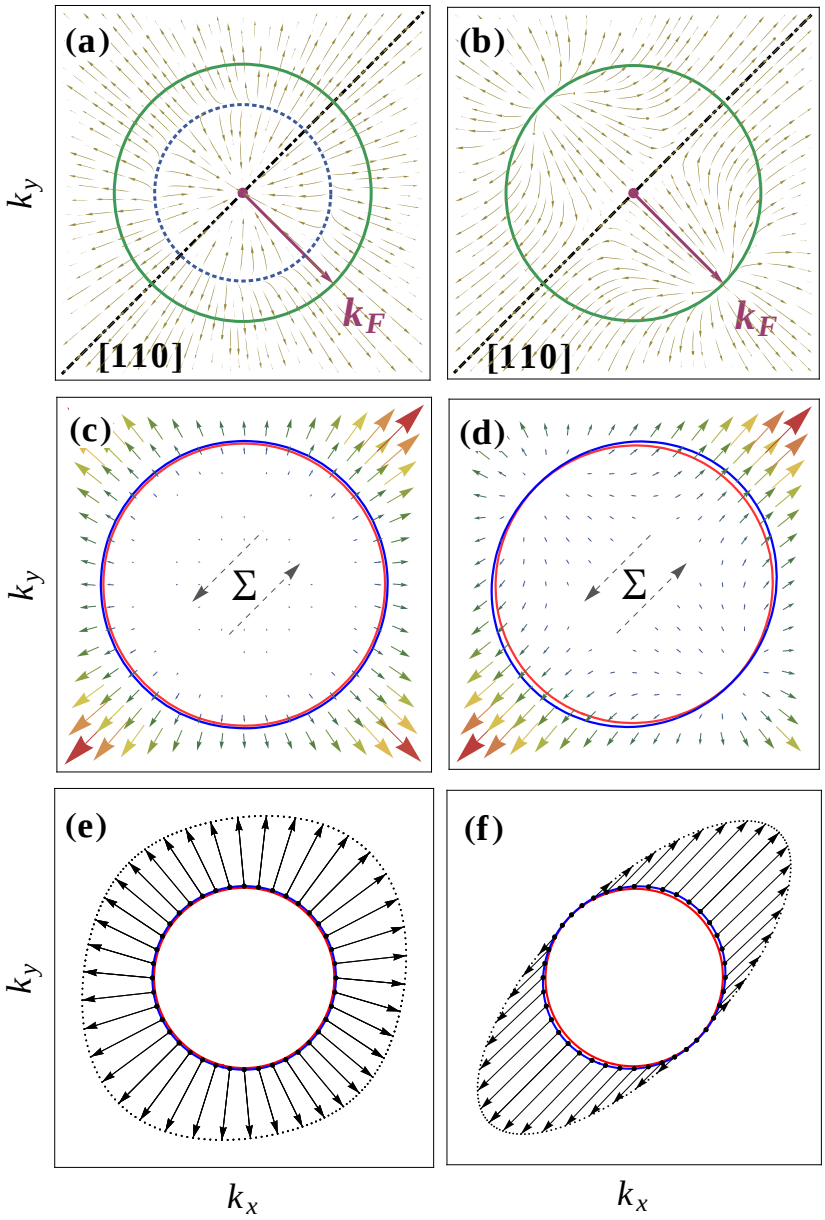

Fig. 5.2: Comparison of the SOF without applied strain (left column) and the case where strain gives rise to a conserved spin quantity Σ in case of a HH-like ground state. In the presented case the SOC strengths are $\lambda_{\mathrm{D},+} = -42.5\,\mathrm{eV\AA}^3$, $\lambda_{\mathrm{R},+} = 2.05\,\mathrm{eV\AA}^3$ and $\eta_+ = -34.1 \times 10^{-3}\,\mathrm{eV\AA}$. (a) and (b) Stream plot of the effective SOF. The green circle indicates the axially symmetric Fermi contour. The blue dotted circle corresponds to $k_0 = 6.9 \times 10^{-3}\,\mathrm{\AA}^{-1}$ where the field vanishes approximately. (c) and (d) Vector field and Fermi contours. The gray arrows indicate the spin polarization. (e) and (f) Detailed picture of the SOF that operates at the outer Fermi contour.

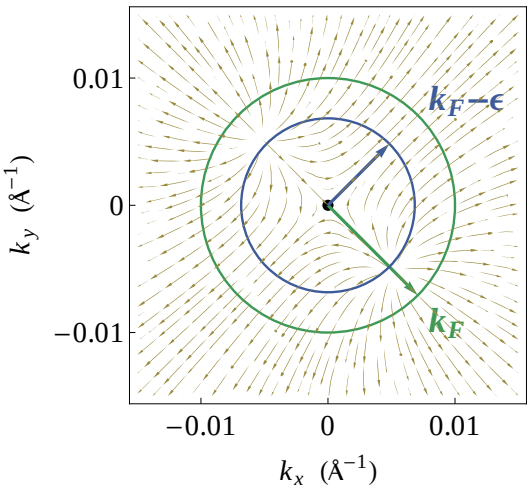

Fig. 5.3: Stream plot of the effective SOF without linear Dresselhaus contribution, i.e., $\eta_+ \to 0$, in case of a HH-like ground state. The strain-induced sources of the field move to a slightly lower Fermi wave vector by $\epsilon = 3.1 \times 10^{-3}\,\text{Å}^{-1}$ where the spin-preserving symmetry is recreated.

5.4 Summary

Summarizing, we identified conserved spin quantities in a [001]-oriented 2DHG in semiconductors with zinc-blende structure. Thereby, we derived the dominant contribution to the SOF due to Rashba SOC directly from an electric field $\mathcal{E}_z$, which was missing in our previous publication, Ref. [7]. The significant effect due to Rashba SOC is only controlled by the subband gaps and not, as in the case of Dresselhaus SOC, by the conduction band gap. In view of recent publications, we also included the effect of linear Dresselhaus SOC terms, whose significance was pointed out in Refs. [92, 99] to be underestimated. The proper determination of the SOF enabled us to conclude that there are two possibilities for long-lived spin states. In respect of an unstrained sample, such states exist only for heavy holes. It requires a certain ratio of cubic Rashba and Dresselhaus SOC strength defined solely by the Luttinger parameters γ_2 and γ_3. Other spin-preserving symmetries occur in presence of strain for both a HH-like and LH-like ground state. Here, a non-vanishing [110] shear strain component ϵ_{xy} and a symmetric in-plane normal strain $\epsilon_{xx} = \epsilon_{yy}$ are essential. We have recovered the conserved spin quantity presented in Ref. [26] for the special case where $\gamma_2/\gamma_3 = -1$. In all circumstances, owing to the presence of both linear and cubic terms due to SOC the persistent spin states are bound to a Fermi contour. We have also demonstrated that only for this case and for $\gamma_2/\gamma_3 = 1$ one finds a spin rotation of a spin on the averaged Fermi contour which only dependents on the distance between the injection and detection position. Moreover, we have shown that for the existence of a conserved spin quantity in semiconductors, which are accessible for experiments (e.g., systems

with $\gamma_2/\gamma_3 \approx 1$), the interplay between Dresselhaus SOC, Rashba SOC and possibly strain is crucial.

In this way, shear strain has turned out to be a key component for an efficient manipulation of spin lifetime in 2D hole systems of zinc-blende structure.

Appendix 5.A: Utilized Approximations

5.A.1 Dominant Invariants for the Cubic BIA Spin Splitting in Bulk Semiconductors

Our starting point is the extended Kane model excluding contributions from remote bands, i.e., $C_k = 0$. The remaining invariants for the Γ_{8v} band block in this model, which give rise to cubic BIA spin splitting, are given by Eq. (1.46). In order to determine the coefficients, Löwdin's partitioning in the energy gaps at the Γ-point in the extended Kane model can be applied. In Tab. 1.18, the coefficients in third-order perturbation theory have been listed for several compounds. It reveals that in the bulk compared to b_{41}^{8v8v}, the terms proportional to b_{42}^{8v8v}, b_{51}^{8v8v} and b_{52}^{8v8v} can be neglected. As an example, we compare the extended Kane model with the effective 4×4 model used in this chapter by calculating the absolute value $|\Delta E|$. The latter is the BIA spin splitting calculated for both LH and HH states in GaAs for $\mathbf{k}||[110]$ in the bulk system. The result is plotted in Fig. 5.4 and shows very good agreement between both models. Deviations are only present at large k-values.

Note, however, that for a certain choice of parameters for the $\mathbf{k}\cdot\mathbf{p}$ model higher-order corrections to the coefficients can be significant, as recently shown in Ref. [92]. For a comparison of $\mathcal{H}_{\mathrm{BIA}}$ with the terms used in Ref. [90] or Ref. [92], it is useful to recast Eq. (1.46) for $C_k = 0$ in the form

$$\begin{aligned}\mathcal{H}_{\mathrm{BIA}} = b_{41}^{8v8v}(\mathbf{J}\cdot\boldsymbol{\kappa}) + b_{42}^{8v8v}\sum_{\alpha} J_\alpha^3\kappa_\alpha + (b_{52}^{8v8v} - b_{51}^{8v8v}) \\ \times\sum_{\alpha} V_\alpha k_\alpha\left(k_\alpha^2 + \frac{1}{(b_{52}^{8v8v}/b_{51}^{8v8v})-1}k^2\right),\end{aligned} \tag{5.A.1}$$

with $V_x = \{J_x, J_y^2 - J_z^2\}_{(s)}$, J_α and $\kappa_x = k_x(k_y^2 - k_z^2)$ (and corresponding terms). The relation between the coefficients used in Ref. [90] and the one in Eq. (1.46) are thus given by

$$b_{41}^{8v8v} = \frac{i}{6}PP'Q\frac{1}{E_0}\left(\frac{13}{E_0'} - \frac{5}{E_0'+\Delta_0'}\right) \hat{=} \alpha_v + \frac{13}{8}\delta\alpha_v, \tag{5.A.2}$$

$$b_{42}^{8v8v} = \frac{2i}{3}PP'Q\frac{1}{E_0}\left(\frac{1}{E_0'} - \frac{1}{E_0'+\Delta_0'}\right) \hat{=} -\frac{1}{2}\delta\alpha_v, \tag{5.A.3}$$

$$b_{51}^{8v8v} = \frac{2i}{9}PP'Q\frac{1}{E_0}\left(\frac{1}{E_0'+\Delta_0'} - \frac{1}{E_0'}\right) \hat{=} -\frac{1}{6}\delta\alpha_v, \tag{5.A.4}$$

$$b_{52}^{8v8v} = \frac{4i}{9}PP'Q\frac{1}{E_0}\left(\frac{1}{E_0'} - \frac{1}{E_0'+\Delta_0'}\right) \hat{=} \frac{1}{3}\delta\alpha_v, \tag{5.A.5}$$

with P, P' Q, Δ_0, Δ_0', and Δ^- as defined in Eqs. (1.29)-(1.34). Notice that there is a difference in the application of perturbation theory to get the prefactors: According to Eq. [19a] in Ref. [162], e.g., one finds for $\Delta_0' \approx 0$ the term, which corresponds to b_{42}^{8v8v}, to be

$$b_{42}^{8v8v} \sim PP'Q\frac{1}{E_0(E_0+E_0')}. \tag{5.A.6}$$

In contrast, Eq. (5.A.3) vanishes if Δ_0' can be neglected.

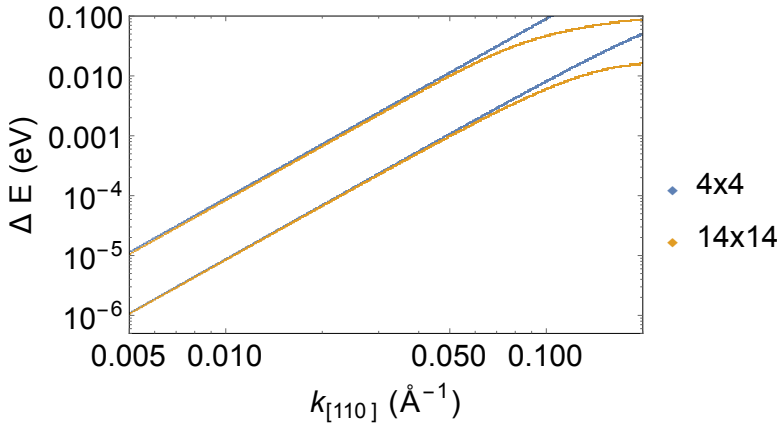

Fig. 5.4: Absolute value $|\Delta E|$ of the BIA spin splitting of LH and HH states in GaAs for $\mathbf{k}||[110]$ in the bulk system. The results are obtained by means of diagonalization of the full 14×14 matrix of the extended Kane model (orange) and the effective 4×4 model used in this thesis (blue), following Ref. [70]. Here, contributions from remote bands to the extended Kane model are excluded.

5.A.2 LH-like Valence Band Ground State: Mixing of the Electric Field and Dresselhaus Term

Assuming a LH-like valence band ground state and applying Löwdin perturbation to third order, terms appear in third order which couple the electric field $\mathcal{E}_z$ with the Dresselhaus term proportional to b_{41}^{8v8v},

$$\begin{aligned}
\Omega_{\mathrm{mix},x}^{(3)} &= -\frac{256e\mathcal{E}_z b_{41}^{8v8v}}{27\Delta_{\mathrm{l1,l2}}^2}\left(2b_{41}^{8v8v}k_y(k_x^2-k_y^2)+e\mathcal{E}_z k_x\right), \\
\Omega_{\mathrm{mix},y}^{(3)} &= -\frac{256e\mathcal{E}_z b_{41}^{8v8v}}{27\Delta_{\mathrm{l1,l1}}^2}\left(2b_{41}^{8v8v}k_y(k_x^2-k_y^2)-e\mathcal{E}_z k_x\right), \\
\Omega_{\mathrm{mix},z}^{(3)} &= 0. \qquad (5.A.7)
\end{aligned}$$

Since we assume the SOC to be a small correction, these terms are negligible compared to the terms proportional to $\lambda_{\mathrm{R},\pm}$, $\lambda_{\mathrm{D},\pm}$ or η_-, Eqs. (5.18)-(5.21). Therefore, we disregard these terms in the calculation of the conserved spin quantity.

Appendix 5.B: Uniaxial Strain via Piezo Crystals

Experimentally, an uniaxial strain can be conveniently implemented by the application of a piezo crystal since the deformation is tunable. In this setup, as done by Habib *et al.* in Ref. [161], the sample is fixed at one side of the piezo crystal where we align the poling direction of the piezo with the [110] direction. Depending on the polarity of the applied voltage, the piezo crystal extends (shrinks) along its poling direction and simultaneously shrinks (extends) perpendicular to it. Assuming

the deformation is completely transmitted to the sample, we can relate the strain coefficients of the sample, where the principal axes correspond to the three ⟨100⟩ axes, to the strain coefficients of the piezo, which can be directly measured. We define the transferred strain parallel to the poling and perpendicular to it as $\epsilon'_{\parallel}$ and $\epsilon'_{\perp}$. Since due to *Hooke's law* an in-plane strain generates also a finite out-of-plane component, the strain tensor of the sample becomes

$$\boldsymbol{\epsilon} = \frac{1}{2}\begin{pmatrix} \epsilon'_{\parallel}+\epsilon'_{\perp} & \epsilon'_{\parallel}-\epsilon'_{\perp} & 0 \\ \epsilon'_{\parallel}-\epsilon'_{\perp} & \epsilon'_{\parallel}+\epsilon'_{\perp} & 0 \\ 0 & 0 & -\frac{2C_{12}}{C_{11}}\left(\epsilon'_{\parallel}+\epsilon'_{\perp}\right) \end{pmatrix}, \tag{5.B.8}$$

where C_{12} and C_{11} are stiffness tensor components depending on the sample's material (cf. Sec. 1.5.1). It becomes clear that in this situation the in-plane normal strain is symmetric, i.e., $\epsilon_{xx} = \epsilon_{yy}$, and the shear strain component $\epsilon_{xy} \neq 0$ as $\epsilon'_{\parallel}$ and $\epsilon'_{\perp}$ have opposite sign, which corresponds to the situation demanded in Sec. 5.3.

Appendix 5.C: Domain

If the C_k term in Eq. (5.17) cannot be neglected, the real solutions for $B^{(\pm)}_{\xi,\chi}$ are only found for $\kappa \in A_{\mathrm{sgn}(\xi\cdot\chi)}$, where

$$A_+ = \left[0, 2\sqrt{1+2\Gamma+\frac{\sqrt{3}}{2}\frac{C_k}{\tilde{\lambda}_{\mathrm{D}}}(1+\Gamma)-2\sqrt{(1+\Gamma)\,\Lambda}}\right], \tag{5.C.9}$$

$$A_- = \left[2\sqrt{1+2\Gamma+\frac{\sqrt{3}}{2}\frac{C_k}{\tilde{\lambda}_{\mathrm{D}}}(1+\Gamma)+2\sqrt{(1+\Gamma)\,\Lambda}}, \infty\right), \tag{5.C.10}$$

with

$$\Lambda = \frac{1}{2\tilde{\lambda}_{\mathrm{D}}^2}\left\{6C_k^2(1+\Gamma)+8\sqrt{3}C_k\tilde{\lambda}_{\mathrm{D}}(1+2\Gamma)+\tilde{\lambda}_{\mathrm{D}}\left[3k_{\parallel F}^2(b_{42}^{8v8v}+b_{51}^{8v8v})+32\Gamma\tilde{\lambda}_{\mathrm{D}}\right]\right\} \tag{5.C.11}$$

and $\tilde{\lambda}_{\mathrm{D}} = \gamma_2 k_{\parallel F}^2 \lambda_{\mathrm{D},+}$.

Part III

Spin Relaxation and Conductivity in Nanowires

CHAPTER 6

Zinc-Blende Nanowires with 2D Tubular Conductive Channel

The weak (anti)localization correction is computed analytically for electrons in tubular semiconductor nanowires of zinc-blende type. We include linear Rashba and Dresselhaus SOC and compare wires of standard growth directions ⟨100⟩, ⟨111⟩, and ⟨110⟩. The motion on the quasi-2D dimensional surface is considered diffusive in both directions: transversal as well as along the cylinder axis. It is shown that Dresselhaus and Rashba SOC similarly affect the spin-relaxation rates. For the ⟨110⟩ growth direction, the long-lived spin states are of helical nature. We detect a crossover from WL to WAL depending on SOC strength as well as dephasing and scattering rate. The theory is fitted to experimental data of an undoped ⟨111⟩ InAs nanowire device which exhibits a top-gate-controlled crossover from positive to negative magnetoconductivity. Thereby, we extract transport parameters where we quantify the distinct types of SOC individually.

6.1 Model Hamiltonian for Tubular 2DEG

6.1.1 Bulk Model

We start with the bulk Hamiltonian $\mathcal{H}$ for electrons in the Γ_{6c} conduction band with SOC as

$$\mathcal{H} = \frac{\hbar^2 k^2}{2m^*} + \mathcal{H}_\mathrm{R} + \mathcal{H}_\mathrm{D}^{[001]}. \tag{6.1}$$

with the effective electron mass m^*. The term $\mathcal{H}_\mathrm{R}$ corresponds to the bulk Rashba Hamiltonian, Eq. (1.48), and the term $\mathcal{H}_\mathrm{D}^{[001]}$ to the bulk Dresselhaus Hamiltonian,[1] Eq. (1.45). In this definition, the basis vectors correspond to the ⟨100⟩ crystal axes. Since we also consider ⟨111⟩ and ⟨110⟩ nanowires, we rotate the Hamiltonian such that the new basis vectors are aligned with the new crystal axes. In general, we define the z-axis to be parallel to the wire's growth direction. As shown in Sec. 1.4.5, the rotation can be performed by means of the rotation operator $\mathcal{R}$, which transforms an arbitrary vector $\mathbf{v}$ as $\mathbf{v} \mapsto \mathcal{R}(\phi, \theta)\,\mathbf{v}$, where θ denotes the polar and ϕ

[1] Here, the superscript indicates that the z-axis is oriented along the [001] crystal axis.

the azimuth angle of the former coordinate system, that is, $\theta = \arccos\left(1/\sqrt{3}\right)$ and $\phi = \pi/4$ for $\langle 111\rangle$ nanowires and $\theta = \pi/2$ and $\phi = \pi/4$ for $\langle 110\rangle$ nanowires. An additional rotation about the transformed z-axis can be applied to choose the alignment of the $\hat{\boldsymbol{x}}$ and $\hat{\boldsymbol{y}}$ basis vectors with the crystallographic axes of the new system as desired. Here, we select for $\langle 111\rangle$ nanowires the Cartesian basis system as $\hat{\boldsymbol{x}} \parallel [11\bar{2}]$, $\hat{\boldsymbol{y}} \parallel [\bar{1}10]$, $\hat{\boldsymbol{z}} \parallel [111]$ and for $\langle 110\rangle$ nanowires as $\hat{\boldsymbol{x}} \parallel [\bar{1}10]$, $\hat{\boldsymbol{y}} \parallel [001]$, $\hat{\boldsymbol{z}} \parallel [110]$. The Rashba Hamiltonian is invariant with respect to a rotation of the crystal provided that the electric field rotates analogously. However, in confined systems the Dresselhaus Hamiltonian depends on the crystal orientation (see also Sec. 4). In the transformed coordinate systems, it takes the form

$$\begin{aligned}\mathcal{H}_{\mathrm{D}}^{[111]} = \frac{b_{41}^{6c6c}}{2\sqrt{3}} \Big\{ &\left[-k_y\left(k_x^2 + k_y^2 + 2\sqrt{2}k_xk_z - 4k_z^2\right)\right]\sigma_x \\ &+ \left[k_y^2\left(k_x + \sqrt{2}k_z\right) + k_x\left(k_x^2 - \sqrt{2}k_xk_z - 4k_z^2\right)\right]\sigma_y \\ &+ \left[\sqrt{2}k_y\left(3k_x^2 - k_y^2\right)\right]\sigma_z\Big\}\end{aligned} \tag{6.2}$$

and

$$\mathcal{H}_{\mathrm{D}}^{[110]} = b_{41}^{6c6c}\left\{\frac{1}{2}k_z\left(k_x^2 + 2k_y^2 - k_z^2\right)\sigma_x - 2k_xk_yk_z\sigma_y + \frac{1}{2}k_x\left(-k_x^2 + 2k_y^2 + k_z^2\right)\sigma_z\right\}. \tag{6.3}$$

Semiconductor nanowires often exhibit a cross-sectional geometry of a hexagon [53]. Nevertheless, for simplicity, we will assume the nanowire to have cylindrical symmetry in the following. Thus, we introduce cylindrical coordinates.

6.1.2 Coordinate Transformation

The Cartesian and the cylindrical coordinates are related through the equations

$$r = \sqrt{x^2 + y^2}, \tag{6.4}$$

$$\phi = \arctan\left(\frac{y}{x}\right), \tag{6.5}$$

where the inverse tangent is suitably defined to take the correct quadrant of (x, y) into account. Hence, in a cylindrical system the wave vector $\mathbf{k} = (k_x, k_y, k_z)^\top$ and the vector of Pauli matrices $\boldsymbol{\sigma} = (\sigma_x, \sigma_y, \sigma_z)^\top$ transform into

$$\mathbf{k} = \hat{\mathbf{r}}\, k_r + \hat{\boldsymbol{\phi}}\, k_\phi + \hat{\mathbf{z}}\, k_z, \tag{6.6}$$

$$\boldsymbol{\sigma} = \hat{\mathbf{r}}\, \sigma_r + \hat{\boldsymbol{\phi}}\, \sigma_\phi + \hat{\mathbf{z}}\, \sigma_z, \tag{6.7}$$

where $k_r = -i\partial_r$, $k_\phi = -\frac{i}{r}\partial_\phi$, $k_z = -i\partial_z$. The orthonormal unit vectors in the Cartesian basis are

$$\hat{\mathbf{r}} = \begin{pmatrix}\cos(\phi)\\ \sin(\phi)\\ 0\end{pmatrix}, \quad \hat{\boldsymbol{\phi}} = \begin{pmatrix}-\sin(\phi)\\ \cos(\phi)\\ 0\end{pmatrix}, \quad \hat{\mathbf{z}} = \begin{pmatrix}0\\ 0\\ 1\end{pmatrix}. \tag{6.8}$$

Therefore, the time-independent Schrödinger equation for $\mathcal{H}$ becomes

$$\left[-\frac{\hbar^2}{2m^*}\left(\partial_r^2 + \frac{1}{r}\partial_r + \frac{1}{r^2}\partial_\phi^2 + \partial_z^2\right) + V(\mathbf{r}) + \mathcal{H}_\mathrm{R} + \mathcal{H}_\mathrm{D}\right] |\psi\rangle = E\,|\psi\rangle\,, \tag{6.9}$$

where we included a position-dependent potential $V(\mathbf{r})$ that causes a structural confinement to be discussed in the following subsection. We identify in the component k_ϕ the angular momentum operator along the z axis: $\mathcal{L}_z = -i\hbar\partial_\phi$. The transformation into the cylindrical coordinate system has an important consequence. In the new Hamiltonian position operators r, ϕ occur and one has to take account of the non-commutativity with the momentum operators k_r, k_ϕ. These position operators are also implicitly contained in k_ϕ, k_r, σ_r, and σ_ϕ. Yet, since $[k_r, \sigma_i] = [k_\phi, \sigma_i] = 0$ where $i \in \{x, y, z\}$, it is often convenient to keep the Pauli matrices Cartesian. The Pauli matrices in cylindrical coordinates and the relevant commutation relations are given in the Apps. 6.A and 6.B. Owing to these commutators, the Hermiticity of the derived model Hamiltonian is often not obvious [163].

6.1.3 Tubular System

Hereafter, we follow the procedure used to derive a quasi-1D dimensional Hermitian Hamilton operator for mesoscopic rings in presence of SOC as done in Refs. [164–166].

In order to obtain the tubular geometry of the nanowire, we consider a radial harmonic confinement potential $V(\mathbf{r}) = V(r) = \frac{1}{2}m^*\omega^2(r-R)^2$ which forces the electron wave function to be localized at a narrow region around the cylinder radius R.[2] R is assumed to be large in comparison with the mean radial extent of the wave function. If the potential is steep enough, the particles fill the lowest radial eigenmode only. Hence, we can treat the Hamiltonian perturbatively by separating

$$\mathcal{H} = \mathcal{H}_0 + \mathcal{H}_1, \tag{6.10}$$

where

$$\mathcal{H}_0 = -\frac{\hbar^2}{2m^*}\left(\partial_r^2 + \frac{1}{r}\partial_r\right) + \frac{1}{2}m^*\omega^2(r-R)^2, \tag{6.11}$$

$$\mathcal{H}_1 = -\frac{\hbar^2}{2m^*}\left(\frac{1}{r^2}\partial_\phi^2 + \partial_z^2\right) + \mathcal{H}_\mathrm{R} + \mathcal{H}_\mathrm{D}. \tag{6.12}$$

In the limit of a 2D tubular system, we can neglect the term $\frac{1}{r}\partial_r$ in comparison with ∂_r^2. Thus, the Schrödinger equation for $\mathcal{H}_0$ reduces to a 1D harmonic oscillator equation. The normalized eigenfunction for the lowest radial mode is given by

$$\langle r|R_0\rangle = \left(\frac{\gamma}{\sqrt{\pi}R}\right)^{1/2} \exp\left[-\frac{\gamma^2}{2}(r-R)^2\right], \tag{6.13}$$

[2] Utilization of a harmonic potential is particularly convenient since most of the matrix elements take a simple form.

where $\gamma^2 = m^*\omega/\hbar$ and the ground state eigenenergy $E_{R_0} = \hbar\omega/2$. The 2D approximation is justified since

$$\frac{\langle \frac{1}{r}\partial_r \rangle}{\langle \partial_r^2 \rangle} \approx -\frac{e^{-\gamma^2 R^2}}{\sqrt{\pi}\gamma R} \overset{\gamma R\to\infty}{\longrightarrow} 0 \tag{6.14}$$

for $\gamma R \gg 1$. Note that in order to obtain analytical expressions the integrals have to be extended to $r\,\epsilon\,[-\infty,\infty]$. This, however, is applicable since we assume $\langle r|R_0\rangle \approx 0$ for $r \leq 0$.[3] In this approximation, Eq. (6.14) vanishes exactly.

The quasi-2D tubular Hamiltonian is now defined as

$$\mathcal{H}_{\text{tube}} \equiv \langle R_0|\mathcal{H}_1|R_0\rangle\,. \tag{6.15}$$

Making use of the fact that $\gamma R \gg 1$ and the SOC terms are assumed to be small compared to the kinetic part of the Hamiltonian, we keep only terms of the order of $\mathcal{O}(1/r)$ in the Dresselhaus Hamiltonian. The remaining relevant matrix elements are given in App. 6.C. We stress that in contrast to a 2DEG the matrix elements for the momentum operator along the confinement direction $\langle k_r^3\rangle$ and $\langle k_r\rangle$ do not vanish. The latter was disregarded in Ref. [167] by parity arguments which do not hold for a cylindrical system. In fact, it is possible to show that independent of the exact form of $V(\mathbf{r})$ one obtains $\langle k_r\rangle = i/(2R)$, which we prove in App. 6.D. Since the model results from $\mathbf{k}\cdot\mathbf{p}$ theory, using an expansion of $\mathbf{k}$ around the Γ point, we can also neglect the subordinate terms $\propto k_z^2$ and obtain a fully linearized version of the Dresselhaus SOC:

$$\begin{aligned}\mathcal{H}_{\text{D}}^{[001],2\text{D}} = \beta\Big\{&\sigma_r\left[\frac{1}{2}\sin(2\phi)k_\phi - 2\cos(2\phi)\,\langle k_r\rangle\right] - \sigma_\phi\left[\cos(2\phi)k_\phi + \frac{5}{2}\sin(2\phi)\,\langle k_r\rangle\right]\\ &+\sigma_z\cos(2\phi)k_z\Big\},\end{aligned} \tag{6.16}$$

$$\begin{aligned}\mathcal{H}_{\text{D}}^{[111],2\text{D}} = \frac{\beta}{2\sqrt{3}}\Big\{&\sigma_r\left[-\sqrt{2}\sin(3\phi)k_z - k_\phi\right] + \sigma_\phi\left[\langle k_r\rangle - \sqrt{2}\cos(3\phi)k_z\right]\\ &+\sigma_z\,3\sqrt{2}\Big[\cos(3\phi)k_\phi + 3\sin(3\phi)\,\langle k_r\rangle\Big]\Big\},\end{aligned} \tag{6.17}$$

$$\begin{aligned}\mathcal{H}_{\text{D}}^{[110],2\text{D}} = \frac{\beta}{8}\Big\{&\sigma_r\Big[\cos(\phi) + 3\cos(3\phi)\Big]k_z - \sigma_\phi\Big[11\sin(\phi) + 3\sin(3\phi)\Big]k_z\\ &+\sigma_z\Big\{\Big[\sin(\phi) + 9\sin(3\phi)\Big]k_\phi - \Big[\cos(\phi) + 27\cos(3\phi)\Big]\,\langle k_r\rangle\Big\}\Big\},\end{aligned} \tag{6.18}$$

with $\beta = b_{41}^{6c6c}\,\langle k_r^2\rangle$. Quite recently, the tubular Dresselhaus Hamiltonian for the [111] growth direction has also been derived by Kokurin in Ref. [168] in a similar way, using a different alignment of the x and y-axes.

Concerning the Rashba SOC, we can distinguish two different sources for an electric field. First, similarly to the case of a planar 2DEG, we assume a constant

[3] For $R\gamma > 2$ the deviation $\Delta = |\,\langle R_0|R_0\rangle - 1| \propto 10^{-4}$ and $\langle \frac{1}{r}\partial_r\rangle\,/\,\langle\partial_r^2\rangle \propto 10^{-3}$.

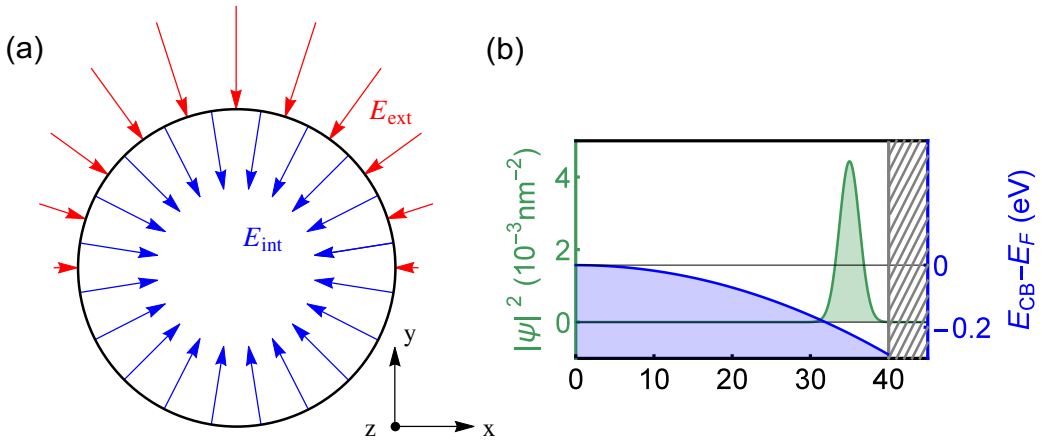

Fig. 6.1: (a) Internal (blue) and external (red) electric field that lead to Rashba SOC in a nanowire (here, $E_{\text{int}}, E_{\text{ext}} < 0$). The internal field can be a consequence of Fermi level pinning, the external due to a gate voltage. Fig. (b) sketches the situation of a nanowire with radius $R_0 = 40\,\text{nm}$. Here, the electron probability density $|\psi|^2$ (green) is focused at $R = 35\,\text{nm}$ below the surface and extends over an area of about 10 nm for a confinement parameter $\gamma = 0.55\,\text{nm}^{-1}$. The blue line illustrates the bending of the conduction band (CB) edge due to Fermi (F) level pinning. The resulting radial confinement is modeled by a harmonic potential in this work.

and homogeneous internal electric field pointing in the direction of the confinement, i.e., $\boldsymbol{\mathcal{E}}_{\text{int}} = \mathcal{E}_{\text{int}}\,\hat{\mathbf{r}}$ with $\mathcal{E}_{\text{int}}$ being constant. This field is a consequence of Fermi level pinning, which can be altered by doping. Second, since the Rashba effect can be modified externally by a gate voltage, we simulate a realistic situation for the experiment as the one performed by Heedt *et al.*, Ref. [59]. There, the gate electrode is laterally fixed (in this model chosen to be in the $\hat{\mathbf{y}}$ direction) to the wire leading to an inhomogeneous field. We approximate it by $\boldsymbol{\mathcal{E}}_{\text{ext}} = \mathcal{E}_{\text{ext}}\sin(\phi)\Theta(\phi)\Theta(\pi-\phi)\,\hat{\mathbf{r}}$ where Θ is the Heaviside function. Both fields and the resulting radial confinement for the wave function are schematically depicted in Fig. 6.1. Since the field $\boldsymbol{\mathcal{E}}_{\text{ext}}$ depends on the polar angle ϕ that does not commute with k_ϕ, we need to symmetrize the Rashba Hamiltonian in Eq. (1.48) in order to obtain a Hermitian operator. Consequently, we find for the Rashba SOC contribution

$$\begin{aligned}\mathcal{H}_{\text{R}}^{\text{2D}} = {}& \alpha_{\text{int}}\Big[\sigma_\phi k_z - \sigma_z k_\phi\Big] \\ & + \alpha_{\text{ext}}\Theta(\phi)\Theta(\pi-\phi)\Big\{\sigma_\phi\sin(\phi)k_z + \sigma_z\Big[\cos(\phi)\,\langle k_r\rangle - \sin(\phi)k_\phi\Big]\Big\}, \end{aligned} \tag{6.19}$$

with $\alpha_{\text{int/ext}} = r_{41}^{6c6c}\mathcal{E}_{\text{int/ext}}$. In Eqs. (6.16)-(6.19) the order of the operators ϕ, k_ϕ, σ_r, and σ_ϕ is crucial. The internal Rashba Hamiltonian has been set up previously [121, 169] to study spin dynamics in cylindrical 2DEGs and similarly in curved 1D wires [170].

At this point, we emphasize that this derivation is fundamentally different from

a previous model considered by Magarill *et al.*, Ref. [171], and Manolescu *et al.*, Ref. [172]. These authors used the Rashba and linearized Dresselhaus Hamiltonian of a [001] confined 2DEG and transformed the in-plane Cartesian coordinates into the in-plane coordinates of the cylinder surface. In other words, they described a 2DEG wrapped around a core to form the shell of a hollow cylinder. In case of the Rashba contribution (referring to the internal part of $\mathcal{H}_{\mathrm{R}}^{\mathrm{2D}}$), both situations do not differ. The reason is that the intrinsic electric field is equivalent as in both cases it is assumed to penetrate the surface perpendicularly, i.e., the field is collinear with the confinement direction. However, as in both scenarios the structure of the crystal in the layer is different, the Dresselhaus contribution will be distinct as well. The model of Refs. [171] and [172] requires a deformation of the crystal structure. Thus, if the radius R of this cylinder is small the effects due to strain are presumably very important. On the other hand, if the radius R of the cylinder is large the situation becomes nearly equivalent to a flat 2D system with a periodic boundary condition for one of the in-plane vectors. The approach used in this publication does not assume a deformed crystal and strain effects are less relevant. Moreover, it was shown in Ref. [56] that the crystal structure in the shell of a core/shell nanowire can adopt the structure of the core. Therefore, a rolled-up 2DEG seems not to be the proper model for a realistic core/shell nanowire.

Returning to our model, we can express the quasi-2D Hamiltonian $\mathcal{H}_{\mathrm{tube}}$ as a matrix with the normalized basis functions

$$\langle \phi | \, l \rangle = \frac{1}{\sqrt{2\pi}} \exp(il\phi), \tag{6.20}$$

$$\langle z | \, k_z \rangle = \frac{1}{\sqrt{L}} \exp(ik_z z), \tag{6.21}$$

where l is the angular momentum quantum number. Moreover, we assume periodic boundary conditions in axial direction with periodicity L leading to plane wave solutions with the quasi-continuous quantum number k_z. It is worth to mention that in a system with only internal Rashba SOC the Hamiltonian commutes with the z-component of the total angular momentum operator, i.e., $\mathcal{J}_z = \mathcal{L}_z + \frac{\hbar}{2}\sigma_z$ [169]. Yet, as soon as external Rashba or Dresselhaus SOC are incorporated the total angular momentum $j = l \pm 1/2$ is no more a good quantum number.

6.1.4 Spin Conservation on the Tubular Surface

Commonly, in systems with SOC the spin rotation symmetry is broken. As the spin precession depends on the momentum of the carrier, scattering in a diffusive semiconductor with inversion asymmetry randomizes the spin which results in DP spin relaxation (cf. Sec. 2.1). In Part II we have seen that in planar 2D electron or hole systems the interplay of Rashba SOC, Dresselhaus SOC, and possibly strain effects can lead to spin-preserving symmetries which are robust against spin-independent disorder. Similarly, Trushin *et al.*[121] showed that in a rolled-up 2DEG a certain ratio of Rashba SOC strength and curvature radius leads to a conservation of the tangential spin component $\frac{\hbar}{2}\sigma_\phi$.

In the tubular nanowires studied in this article, we assume diffusive motion and treat the transverse momentum k_ϕ in the same way as k_z, as a quasi-continuous quantity. We will average over all in-plane momenta and azimuthal angles, which will become clear in the subsequent section. As a result, the interplay between Rashba and Dresselhaus SOC does not lead to a suppressed DP spin relaxation in a tubular nanowire grown along the high-symmetry directions $\langle 001 \rangle$ or $\langle 111 \rangle$. We can refer this characteristic to the fact that in general Rashba and Dresselhaus SOC exhibit a different ϕ-dependence. The mismatch is particularly pronounced for the internal Rashba contribution as it is independent of ϕ. Thus, the interplay between Rashba and Dresselhaus cannot generate a collinear field independent of its azimuthal location. On the other hand, for $\langle 110 \rangle$ nanowires due to their lower symmetry we will observe that the internal Rashba as well as the Dresselhaus SOC compete with the external Rashba SOC. Therefore, the ratios of interaction strengths modify the spin-relaxation rate. Moreover, we will find that both Rashba and Dresselhaus SOC yield an additional shift of the Cooperon triplet spectra that cause an insuppressible spin relaxation. It is also to mention that the particular scenario found by Trushin *et al.* [121] is not reflected in our results for the Cooperon spectrum. We attribute this property to the azimuthal averaging which diminishes the curvature effects.

6.2 Quantum Correction to the Conductivity

In this section, we compute the weak (anti)localization correction $\Delta\sigma$ for the 2D tubular system. Along with the usual preconditions as specified in Sec. 3.3, the motion of the electrons is considered to be diffusive in longitudinal as well as transversal direction of the 2D cylindrical shell. According to Eq. (3.45), the conductivity correction can be written as

$$\Delta\sigma = \frac{2e^2}{h}\frac{\hbar D_e}{\mathcal{V}}\mathrm{Re}\left(\sum_{\mathbf{Q}}\sum_{s,m_s}\chi_s \langle \mathbf{Q}| \langle s, m_s|\hat{\mathcal{C}}(\hat{\mathbf{Q}})|s, m_s\rangle |\mathbf{Q}\rangle\right), \tag{6.22}$$

where we restored the trace over the wave vectors $\mathbf{Q}$ for reasons of comprehensibility. Aside from the definitions as introduced in Sec. 3.3.2, here $\mathcal{V}$ denotes the surface of the nanowire and D_e the 2D diffusion constant, i.e., $D_e = v_F^2\tau_e/2$. Below, we follow the approaches of Refs. [61, 67, 173, 174] to compute the Cooperon (Hamiltonian) and the magnetoconductivity correction.

6.2.1 Cooperon Hamiltonian

The sum in the auxiliary function $I(\hat{\mathbf{Q}})$, Eq. (3.39), averages over all intermediate electron wave vectors $\mathbf{q}$ of the scattering events. As stated before, we assume diffusive motion not only along the cylinder axis but also along the circumference. This assumption holds true as long as the mean-free path is much smaller than the circumference of the nanowire. Such a situation is similar to a disordered planar 2D

system and therefore we will treat it analogously. As a consequence, the electron wave vector $\mathbf{q}$ is considered as a continuous variable and replaced by the Fermi wave vector $\mathbf{q} = \mathbf{k}_F$. With this, we average over all directions of the in-plane wave vector and the azimuthal angles. It is worth to mention, that in flat quantum wires, the specular scattering at the lateral confinement requires conservation of the spin current which yields an additional boundary condition for the Cooperon equation [67, 175]. This, however, does not apply to periodic boundary conditions and is therefore irrelevant for the tubular system.

Defining the in-plane wave vector $\mathbf{k}_\parallel = (k_\phi, k_z)^\top = k_\parallel \left(\cos(\vartheta), \sin(\vartheta)\right)^\top$ of the cylinder's tangent space, the Cooperon propagator $\hat{\mathcal{C}}$ in Fourier space, Eq. (3.43), simplifies to

$$\hat{\mathcal{C}}(\hat{\mathbf{Q}}) = \tau \left(1 - \int_0^{2\pi} \frac{\mathrm{d}\phi}{2\pi} \int_0^{2\pi} \frac{\mathrm{d}\vartheta}{2\pi} \frac{1}{1 - i\tau\hat{\Sigma}}\right)^{-1} \tag{6.23}$$

where

$$\hat{\Sigma} = \mathcal{H}(\hat{\mathbf{Q}} - \mathbf{k}_F, \boldsymbol{\sigma}) - \mathcal{H}(\mathbf{k}_F, \boldsymbol{\sigma}'). \tag{6.24}$$

The integral represents the averaging over the azimuth angle ϕ of the cylinder and the angle ϑ between the in-plane Fermi wave vector components[4] k_ϕ and k_z in the tangent space corresponding to a certain angle ϕ. A more detailed derivation is given in App. 6.E. In the following, we assume the ratio $\kappa \equiv \langle k_r \rangle / (ik_\parallel)$ to be small. This holds true for $8\pi n_{2\mathrm{D}} R^2 \gg 1$ which can be seen when rewritten in terms of the 2D electron density n_{2D} as $\kappa^2 = (4R^2k_F^2 + 1)^{-1} = (8\pi n_{2\mathrm{D}} R^2 + 1)^{-1}$ by means of the relation $k_\mathrm{F} = \sqrt{2\pi n_{2\mathrm{D}}}$. Therefore, we can approximate $k_F^2 = \langle k_r \rangle^2 + k_\parallel^2 \approx k_\parallel^2$ and $D_e \approx \tau_e v_\parallel^2/2$ since $v_F = \hbar k_F/m^*$.

We account for small magnetic fields $\mathbf{B} = \nabla \times \mathbf{A}$ purely by the principle of minimal coupling and substitute the wave vectors $\mathbf{Q} \to \mathbf{Q} + 2e\mathbf{A}/\hbar$. We choose the magnetic field $\mathbf{B} = B\,\hat{\mathbf{y}}$ which is related to the vector potential $\mathbf{A}$, here, represented in Landau gauge as

$$\mathbf{A} = -Bx\hat{\mathbf{z}} = -BR\cos(\phi)\hat{\mathbf{z}}. \tag{6.25}$$

On the cylinder surface, the magnetic field, as well as the vector potential, are inhomogeneous and the vector potential has no out-of-plane component.

If we drop all terms in $\hat{\Sigma}$ that do not contain the Fermi velocity, which gives the dominant contribution, we obtain

$$\hat{\Sigma} \approx -\left(\hbar\hat{\mathbf{Q}} + 2e\mathbf{A} + 2m^*\hat{\boldsymbol{a}}\boldsymbol{S}\right)\mathbf{v}_F. \tag{6.26}$$

The matrix $\hat{\boldsymbol{a}}$ contains the Rashba and Dresselhaus SOC and is listed in App. 6.F for the different growth directions. Furthermore, the total electron spin vector $\boldsymbol{S}$ in the of singlet-triplet states representation is given in App. 3.B. Advantageously, in this representation the singlet ($\mathcal{S}$) and the triplet ($\mathcal{T}$) sectors decouple from each other and can be treated separately.

[4] In the following, we drop the index F for compactness.

At last, we define the Cooperon Hamiltonian as

$$H_{\mathcal{C}}(\hat{\mathbf{Q}}) = (\hbar D_e \hat{\mathcal{C}}(\hat{\mathbf{Q}}))^{-1} \tag{6.27}$$

and perform the integral in Eq. (6.23) by Taylor expanding the integrand to second order in $\left(\hbar\hat{\mathbf{Q}} + 2e\mathbf{A} + 2m\hat{\boldsymbol{a}}\boldsymbol{S}\right)$ and find the Cooperon Hamiltonian in units of Q_{so}^2 with $Q_{so} = 2m\beta/\hbar^2$ as

$$\begin{aligned}\frac{H_{\mathcal{C}}^{\xi}(\hat{\boldsymbol{\mathcal{Q}}})}{Q_{so}^2} = &\left(\mathcal{Q}_\phi^2 + \mathcal{Q}_z^2 + \mathcal{B}^2 R_{so}^2\right) \mathbb{1}_{4\times4} - 2\left(\lambda_1 + \frac{\lambda_2}{\pi}\right)\mathcal{Q}_\phi S_z - \frac{1}{2}\lambda_2 \mathcal{Q}_z S_x \\ &+ \lambda_1\left[\frac{2}{3\pi}\lambda_2\left(2S_x^2 + S_y^2 + 3S_z^2\right) - \sqrt{2}\mathcal{B}R_{so}S_y\right] + \lambda_1^2\left[\frac{1}{2}\left(S_x^2 + S_y^2\right) + S_z^2\right] \\ &+ \frac{\lambda_2^2}{16}\left[3S_x^2 + S_y^2 + 4\left(1 - 2\kappa^2\right)S_z^2\right] - \frac{2\sqrt{2}}{3\pi}\lambda_2\mathcal{B}R_{so}S_y + \mathcal{F}^{\xi}. \end{aligned} \tag{6.28}$$

The terms $\mathcal{F}^{\xi}$ result from Dresselhaus SOC and thus depend on the growth direction ξ of the nanowire as

$$\mathcal{F}^{[001]} = \frac{1}{16}\left[\left(5 - 82\kappa^2\right)\left(S_x^2 + S_y^2\right) + 8S_z^2\right] + \frac{\lambda_2}{8}\left(3 - 2\kappa^2\right)\{S_x, S_z\}, \tag{6.29}$$

$$\begin{aligned}\mathcal{F}^{[111]} = &\frac{1}{8}\left(S_x^2 + S_y^2 + 6S_z^2\right) - \frac{1}{12}\left(S_x^2 + S_y^2 + 163S_z^2\right)\kappa^2 \\ &+ \frac{\lambda_2}{4\sqrt{3}}\left[\left(1 - 2\kappa^2\right)\{S_y, S_z\} - \sqrt{2}\{S_x, S_y\}\right], \end{aligned} \tag{6.30}$$

$$\begin{aligned}\mathcal{F}^{[110]} = &\frac{3}{2}\mathcal{Q}_z S_x + \frac{1}{64}\left[38S_x^2 + 32S_y^2 + \left(41 - 730\kappa^2\right)S_z^2\right] \\ &+ \frac{\lambda_2}{16}\left[\left(2\kappa^2 - 1\right)S_z^2 - 7S_x^2 - 4S_y^2\right]. \end{aligned} \tag{6.31}$$

Here, we define the dimensionless parameters

$$\mathcal{Q}_i = \frac{Q_i}{Q_{so}}, \quad \lambda_1 = \frac{\alpha_{\text{int}}}{\beta}, \quad \lambda_2 = \frac{\alpha_{\text{ext}}}{\beta}, \quad \kappa = \frac{\langle k_r\rangle}{ik_{\parallel}}, \quad \mathcal{B} = \frac{\sqrt{2}eB}{\hbar Q_{so}^2}, \quad R_{so} = R\,Q_{so}. \tag{6.32}$$

Note that in Eq. (6.28) we neglect the terms

$$\frac{1}{\hbar D_e Q_{so}^2}\left(i\langle Q_r\rangle\langle v_r\rangle + \langle Q_r\rangle^2\langle v_r\rangle^2\tau_e\right)\mathbb{1}_{4\times4}. \tag{6.33}$$

This is justified as the first term is proportional to τ_e^{-1} since $D_e \propto \tau_e$, which is in accordance with the case without SOC as shown in Ref. [138]. The second term can be dropped because $\langle Q_r\rangle^2\langle v_r\rangle^2 \propto R^{-4}$ and thus it is very small for a large radius. The Cooperon Hamiltonian is therefore Hermitian and we will discuss its spectrum hereafter.

6.2.2 Spectrum Analysis

Analytical Expressions for the Eigenvalues

In general, there is no simple analytical expression for the eigenvalues of the full Cooperon Hamiltonian in Eq. (6.28). Partly, this is attributed to the reduction of

symmetry by the external Rasbha, the Dresselhaus SOC for wires along [110] and the magnetic field. Yet, we can provide solutions of simple structure for certain particular situations. This will be useful for estimating the spin-relaxation rates and determining the conductivity correction in Sec. 6.2.3.

Since the magnetic field is considered to be small, it is reasonable to neglect the off-diagonal terms $\propto \mathcal{B}$ in Eq. (6.28). The magnetic field will, hence, merely cause a shift $\mathcal{B}^2 R_{so}^2$ of the entire spectrum. Note that this is equivalent to treating the magnetic field by means of a magnetic phase shift rate τ_B that breaks the time-reversal invariance, which gives for diffusive wire cross-sections $1/\tau_B = 2D_e e^2 R^2 B^2$ [142, 176].

If the surface conductive channel is a consequence of Fermi level pinning, the internal Rashba and Dresselhaus SOC can be comparably large and compete with each other. Yet, here we consider the Dresselhaus SOC to be the dominant mechanism as it strongly depends on the confinement due to the matrix element $\langle k_r^2 \rangle$ which is only a few tens of nanometers in a realistic nanowire [44, 169, 177]. Also, in a situation where the gate is wrapped around the nanowire the resulting field is collinear to the internal field and therefore renormalizes the internal Rashba coefficient [47, 178, 179]. Moreover, in core/shell systems the band bending can be much lower [55]. Thus, the Rashba SOC will constitute a small perturbation whereas the internal outweighs the external as the latter is due to a gate voltage and can be chosen arbitrarily small.

In line with this, considering the high-symmetry growth directions [001] and [111], we can provide an approximate solution for the band structure by neglecting all off-diagonal elements proportional to λ_2. We stress that these eigenvalues are *exact* for vanishing external Rashba contribution, i.e., $\lambda_2 = 0$ (and neglected off-diagonal magnetic field terms). In case of the low-symmetry direction [110] owing to finite off-diagonal Dresselhaus terms we find an exact solution only by neglecting *all* Rashba contributions, i.e., $\lambda_1 = \lambda_2 = 0$. Thus, the spectrum of the Cooperon Hamiltonian is given by

$$E_{\mathcal{S}}/Q_{so}^2 = \mathcal{Q}_\phi^2 + \mathcal{Q}_z^2 + \mathcal{B}^2 R_{so}^2, \tag{6.34}$$

$$E_\chi^\xi/Q_{so}^2 \approx E_{\mathcal{S}}/Q_{so}^2 + \mathcal{M}_\chi^\xi, \tag{6.35}$$

where for the high-symmetry directions we obtain

$$\mathcal{M}_{\mathcal{T}_0}^{[001]} = f_0 + \frac{5}{8} - \frac{41}{4}\kappa^2, \tag{6.36}$$

$$\mathcal{M}_{\mathcal{T}_{\pm1}}^{[001]} = f_\pm + \frac{13}{16} - \frac{41}{8}\kappa^2, \tag{6.37}$$

and

$$\mathcal{M}_{\mathcal{T}_0}^{[111]} = f_0 + \frac{1}{4} - \frac{1}{6}\kappa^2, \tag{6.38}$$

$$\mathcal{M}_{\mathcal{T}_{\pm1}}^{[111]} = f_\pm + \frac{7}{8} - \frac{163}{12}\kappa^2, \tag{6.39}$$

with

$$f_0 = \lambda_1^2 + \frac{2}{\pi}\lambda_1\lambda_2 + \frac{1}{4}\lambda_2^2, \tag{6.40}$$

$$f_\pm = \frac{3}{2}\lambda_1^2 + \frac{1}{2}\left(\frac{3}{4} - \kappa^2\right)\lambda_2^2 + \frac{3}{\pi}\lambda_1\lambda_2 \pm 2\left(\lambda_1 + \frac{1}{\pi}\lambda_2\right)\mathcal{Q}_\phi \tag{6.41}$$

and for the low-symmetry direction without Rashba SOC

$$\mathcal{M}_{\mathcal{T}_0}^{[110]} = \frac{73}{64} - \frac{10}{64}\kappa^2, \tag{6.42}$$

$$\mathcal{M}_{\mathcal{T}_{\pm 1}}^{[110]} = \frac{1}{128}\left[149 - 730\kappa^2 \pm \sqrt{36864\mathcal{Q}_z^2 + (9 - 730\kappa^2)^2}\right]. \tag{6.43}$$

Here, the Cooperon momentum operator $\hat{\boldsymbol{\mathcal{Q}}}$ is expressed in the basis given in Eqs. (6.20) and (6.21). Thus, the Cooperon momentum along the cylinder axis $\mathcal{Q}_z$ is quasi-continuous and the transverse Cooperon momentum becomes $\mathcal{Q}_\phi = n/R_{so}$, where n is the number of the transverse Cooperon mode.

The exact energy spectra of the Cooperon Hamiltonian Eq. (6.28) are displayed in Figs. 6.2, 6.3, 6.4, and 6.5 for $\mathcal{B} = \kappa = 0$. For better perceptibility, we illustrate $\mathcal{Q}_\phi$ as a continuous quantity, which corresponds to the case where $R_{so} \gg 1$. In all figures the black solid line corresponds to the singlet mode, which is independent of the SOC, and the black dashed lines to the case where Rashba SOC is absent.

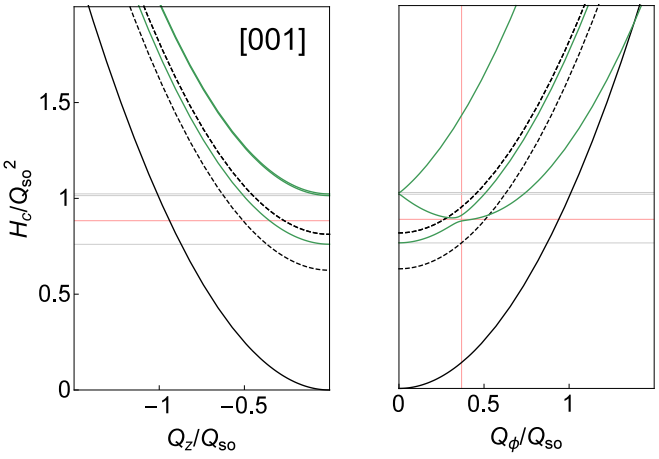

Fig. 6.2: Spectrum of the Cooperon Hamiltonian for [001] nanowires with parameter configurations $\lambda_1 = 0.4$ and $\lambda_2 = -0.1$ for $\mathcal{B} = \kappa = 0$ (green). Dashed lines correspond to vanishing Rashba SOC and black solid line to the singlet mode. The grid lines are plotted by use of the approximate formulas $\Delta_\chi^{[001]}$ (gray) and $\delta_\phi^{[001]}$ for $\mathcal{Q}_\phi^{\min,[001]}$ (red). The grid lines are plotted using the approximate formulas derived in Sec. 6.2.2.

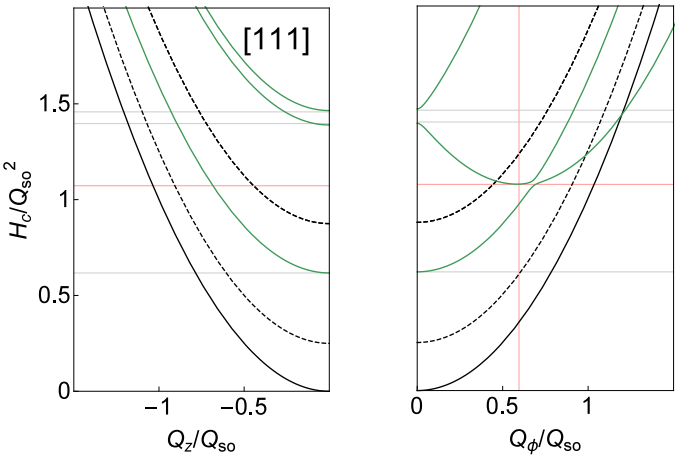

Fig. 6.3: Spectrum of the Cooperon Hamiltonian for [111] nanowires with parameter configurations $\lambda_1 = 0.5$ and $\lambda_2 = 0.3$ for $\mathcal{B} = \kappa = 0$ (green). Dashed lines correspond to vanishing Rashba SOC and black solid line to the singlet mode. The grid lines are plotted by use of the approximate formulas $\Delta_\chi^{[111]}$ (gray) and $\delta_\phi^{[111]}$ for $\mathcal{Q}_\phi^{\min,[111]}$ (red). The grid lines are plotted using the approximate formulas derived in Sec. 6.2.2.

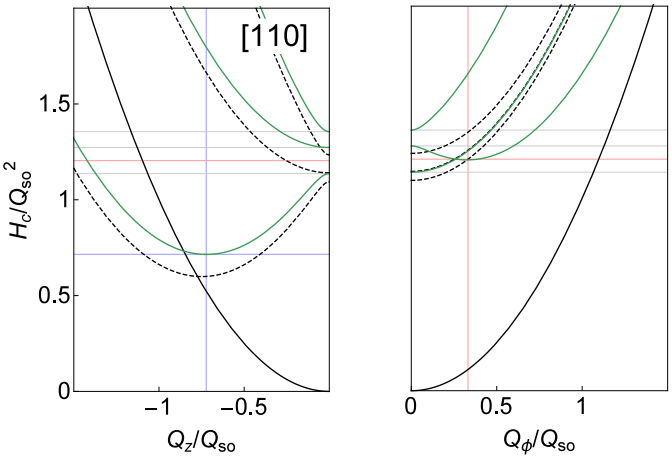

Fig. 6.4: Spectrum of the Cooperon Hamiltonian for [110] nanowires with parameter configurations $\lambda_1 = 0.3$ and $\lambda_2 = 0.1$ for $\mathcal{B} = \kappa = 0$ (green). Dashed lines correspond to vanishing Rashba SOC and black solid line to the singlet mode. The grid lines are plotted by use of the approximate formulas $\Delta_\chi^{[110]}$ (grey), $\delta_\phi^{[110]}$ for $\mathcal{Q}_\phi^{\min,[110]}$ (red) and $\delta_z^{[110]}$ for $\mathcal{Q}_z^{\min,[110]}$ (blue). The grid lines are plotted using the approximate formulas derived in Sec. 6.2.2.

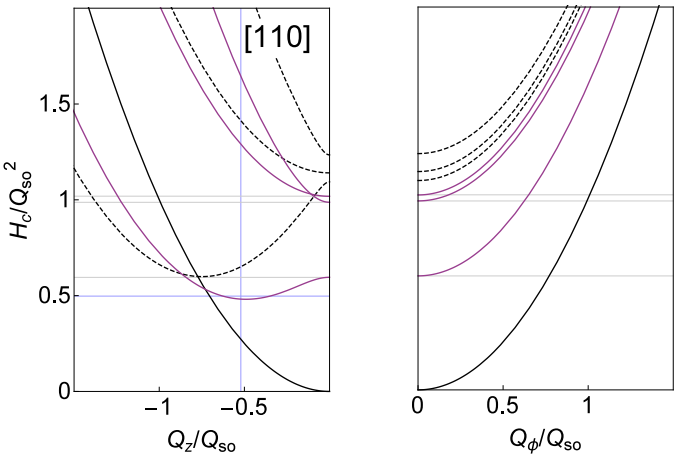

Fig. 6.5: Spectrum of the Cooperon Hamiltonian for [110] nanowires with optimal parameter configurations for a lowest possible gap along $\mathcal{Q}_z$ with $\lambda_1 = -0.901$ and $\lambda_2 = 0.305$ for $\mathcal{B} = \kappa = 0$ (green). Dashed lines correspond to vanishing Rashba SOC and black solid line to the singlet mode. The grid lines are plotted by use of the approximate formulas $\Delta_\chi^{[110]}$ (grey) and $\delta_z^{[110]}$ for $\mathcal{Q}_z^{\mathrm{min},[110]}$ (blue). The grid lines are plotted using the approximate formulas derived in Sec. 6.2.2.

Spin-Relaxation Gaps

As the spectrum of the Cooperon and the spin diffusion equation are identical as far as the time-reversal symmetry is not broken, i.e., $B = 0$, the minima of the triplet eigenvalues of the Cooperon Hamiltonian are direct measures of the spin-relaxation rate and thus of particular interest [64, 67]. In Eq. (6.28) all terms that are linear in momentum $\mathcal{Q}$ can shift the minimum of two triplet eigenmodes to a finite momentum. Any mode that is gapless at finite $\mathcal{Q}$ reveals a persistent spin helix, which has been demonstrated in 2DEGs for a certain ratio of linear Dresselhaus and Rashba SOC strength (cf. Sec. 2.1 and Chap. 4). However, only in growth direction [110] there is a $\mathcal{Q}$-dependent Dresselhaus term. This reflects an earlier statement that the interplay with Rashba cannot be used to control the minimum and suppress the spin relaxation for $\langle 001\rangle$ and $\langle 111\rangle$ nanowires. Also, we see from Eqs. (6.29)-(6.31) that even for $\mathcal{Q}$-independent terms there is no coupling between Dresselhaus and internal Rashba SOC in any growth direction. We only find a coupling between Dresselhaus and external Rashba as well as internal and external Rashba. These $\mathcal{Q}$-independent terms cause a positive shift of the triplet spectrum and thereby an insuppressible spin relaxation. Hence, a gapless mode cannot be found. This contradicts the conjecture of previous authors, Refs. [36, 41, 42, 45, 46, 180], that Dresselhaus SOC in [111] is absent and, hence, cannot cause spin relaxation. In the following, we analyze the position and value of the minima for $\mathcal{B} = 0$ which can be related to spin-relaxation rates. The latter we will denote

as spin-relaxation gaps.

First of all, we note that κ is the only parameter which lowers the triplet eigenenergies at $\boldsymbol{\mathcal{Q}} = 0$. It is remarkable as this quantity depends on the radius R of the nanowire. Nevertheless, it is assumed to be small since we consider $n_{2\mathrm{D}}R^2 \gg 1$. Therefore, we will neglect κ for simplicity in the following discussion.

Since the Rashba SOC constitutes a small perturbation, we can estimate the spin-relaxation gaps $\Delta_\chi^\xi \equiv E_\chi^\xi\left(\boldsymbol{\mathcal{Q}}=0\right)/Q_{so}^2$ by Taylor expanding the exact eigenvalues in terms of λ_i as

$$\Delta_{\mathcal{T}_0}^{[001]} \approx \lambda_1^2 + \frac{2}{\pi}\lambda_1\lambda_2 + \frac{1}{16}\lambda_2^2 + \frac{5}{8}, \tag{6.44}$$

$$\Delta_{\mathcal{T}_{\pm1}}^{[001]} \approx \frac{3}{2}\lambda_1^2 + \frac{9\mp1}{3\pi}\lambda_1\lambda_2 + \frac{15\pm1}{32}\lambda_2^2 + \frac{13}{16}, \tag{6.45}$$

$$\Delta_{\mathcal{T}_0}^{[111]} \approx \lambda_1^2 + \frac{2}{\pi}\lambda_1\lambda_2 + \frac{29}{120}\lambda_2^2 + \frac{1}{4}, \tag{6.46}$$

$$\Delta_{\mathcal{T}_{\pm1}}^{[111]} \approx \frac{3}{2}\lambda_1^2 + \frac{3}{\pi}\lambda_1\lambda_2 + \frac{91}{240}\lambda_2^2 + \frac{7}{8} \pm \frac{|\lambda_2|}{4\sqrt{6}}, \tag{6.47}$$

$$\Delta_{\mathcal{T}_0}^{[110]} \approx \lambda_1^2 + \frac{2}{\pi}\lambda_1\lambda_2 + \frac{1}{4}\lambda_2^2 - \frac{11}{16}\lambda_2 + \frac{35}{32}, \tag{6.48}$$

$$\Delta_{\mathcal{T}_{\pm1}}^{[110]} \approx \frac{3}{2}\lambda_1^2 + \frac{9\pm1}{3\pi}\lambda_1\lambda_2 + \frac{6\pm1}{16}\lambda_2^2 - \frac{13\pm3}{32}\lambda_2 + \frac{76\pm3}{64}. \tag{6.49}$$

The twofold degeneracy of the eigenvalues $E_{\mathcal{T}_{\pm1}}^\xi$ at $\boldsymbol{\mathcal{Q}} = 0$ is lifted for [110] nanowires and also, independent of the growth direction, in presence of an external Rashba contribution owing to the lower symmetry. An important observation at this point is that in absence of Rashba SOC the lowest spin-relaxation gap is given for [111] nanowires by $\Delta_{\mathcal{T}_0}^{[111]} = 1/4$. Thus, it is reasonable to assume that the spin relaxation due to Dresselhaus SOC is lowest for nanowires grown along [111].

Analogously, let us call the spin-relaxation gap, where a minimum in one of the triplet modes occurs at finite values of $\mathcal{Q}_i$, $\delta_i^\xi \equiv E_{\mathcal{T}_{\min}}^\xi\left(\mathcal{Q}_i = \mathcal{Q}_i^{\min,\xi}\right)/Q_{so}^2$. For arbitrary ξ we can approximately locate the position of the minima at finite $\mathcal{Q}_\phi$ at $\mathcal{Q}_\phi^{\min,\xi} = \pm\left(\lambda_1 + \lambda_2/\pi\right)$ by neglecting all off-diagonal elements.[5] The spin-relaxation gap δ_ϕ^ξ at this position and in this approximation for $\mathcal{Q}_z = 0$ is about

$$\delta_\phi^{[001]} \approx a + \frac{13}{16}, \tag{6.50}$$

$$\delta_\phi^{[111]} \approx a + \frac{7}{8}, \tag{6.51}$$

$$\delta_\phi^{[110]} \approx a - \frac{13}{32}\lambda_2 + \frac{19}{16}, \tag{6.52}$$

where

$$a = \frac{1}{2}\lambda_1^2 + \frac{1}{\pi}\lambda_1\lambda_2 + \left(\frac{3}{8} - \frac{1}{\pi^2}\right)\lambda_2^2. \tag{6.53}$$

[5] For [110] this assumption is rather crude due to off-diagonal Dresselhaus contributions.

Depending on Rashba SOC, we can obtain a situation where the lowest minima are at finite values of $\mathcal{Q}_\phi$. To linear order in λ_2 the domain $\mathcal{P}^\xi$ where the lowest minimum is at $\boldsymbol{\mathcal{Q}} = 0$, that is, $\lambda_1 \in \mathcal{P}^\xi$, is

$$\mathcal{P}^{[001]} = \left(-\sqrt{\frac{3}{8}} - \frac{\lambda_2}{\pi}, \sqrt{\frac{3}{8}} - \frac{\lambda_2}{\pi}\right), \tag{6.54}$$

$$\mathcal{P}^{[111]} = \left(-\frac{\sqrt{5}}{2} - \frac{\lambda_2}{\pi}, \frac{\sqrt{5}}{2} - \frac{\lambda_2}{\pi}\right), \tag{6.55}$$

$$\mathcal{P}^{[110]} = \left(-\sqrt{\frac{3}{4}} - \left[\frac{1}{\pi} + \frac{3\sqrt{3}}{8}\right]\lambda_2,\ \sqrt{\frac{3}{4}} - \left[\frac{1}{\pi} - \frac{3\sqrt{3}}{8}\right]\lambda_2\right). \tag{6.56}$$

However, in any case where the lowest minimum is at finite $\mathcal{Q}_\phi$, this spin-relaxation gap is larger than compared to the case without Rashba SOC. Therefore, it is reasonable to say that the spin direction of the long-lived spin states is homogeneous in coordinate space.

Contrary to the other cases, the [110] direction reveals also a shifted minimum along $\mathcal{Q}_z$. As a result, the states with the longest spin lifetime are of helical nature along the wire axis. Expanding the exact eigenvalues to first order in λ_i and setting $\mathcal{Q}_\phi = 0$, we obtain

$$\mathcal{Q}_z^{\min,[110]} = \pm\frac{3\sqrt{255}}{64} \mp \frac{87}{64}\sqrt{\frac{3}{85}}\lambda_2, \tag{6.57}$$

which yields the spin-relaxation gap

$$\delta_z^{[110]} \approx \frac{2455}{4096} - \frac{463}{2048}\lambda_2 + \frac{79}{64}\lambda_1^2 + \frac{21}{8\pi}\lambda_1\lambda_2 + \frac{1093}{4096}\lambda_2^2. \tag{6.58}$$

It is the lowest gap in the [110] triplet spectrum until the Rashba contribution becomes very large, that is, $|\lambda_1| > 1.45$ for pure internal or $\lambda_2 < -28.4 \vee \lambda_2 > 1.03$ for pure external Rashba SOC. We find an optimal value of $\delta_z^{[110]} \approx 0.498$ for $\lambda_1 \approx -0.305$ and $\lambda_2 \approx 0.901$ within our approximations.

In what follows, we apply the previously derived approximate formulas to compute the correction to the Drude conductivity.

6.2.3 Magnetoconductivity Correction

As shown in App. 3.C, selecting the eigenbasis of the Cooperon Hamiltonian, the Eq. (6.22) simplifies to

$$\Delta\sigma(B) = \frac{2e^2}{h}\frac{1}{\mathcal{V}}\sum_{\mathbf{Q}}\left(\frac{1}{E^{\mathcal{S}}(\mathbf{Q})} - \sum_{i\in\{\pm1,0\}}\frac{1}{E_i^{\mathcal{T}}(\mathbf{Q})}\right), \tag{6.59}$$

where the E_i^j are the eigenvalues of the Cooperon Hamiltonian, Eq. (6.28). Note the opposite sign of the singlet and triplet eigenvalues. The dominance of the singlet or triplet sector determines whether the conductivity correction results in WL or WAL.

Since the ϕ angular dependence is removed by the averaging over Fermi contour in Eq. (6.23), there is no coupling between the transverse Cooperon modes. In experiment the infrared and ultraviolet divergence is eliminated due to a finite dephasing and elastic scattering time, τ_ϕ and τ_e, respectively. Therefore, we insert a lower cutoff c_ϕ due to dephasing and an upper cutoff c_e due to elastic scattering.

Consequently, in terms of Q_{so} Eq. (6.59) becomes

$$\Delta\sigma(B) = \frac{2e^2}{h}\frac{1}{2\pi^2 R_{so}}\sum_{n=-l_{\max}}^{l_{\max}}\int_0^{\sqrt{c_e}} d\mathcal{Q}_z \left(\frac{1}{E^{\mathcal{S}}(\mathcal{Q}_z,n)/Q_{so}^2 + c_\phi} - \sum_{i\in\{\pm1,0\}}\frac{1}{E_i^{\mathcal{T}}(\mathcal{Q}_z,n)/Q_{so}^2 + c_\phi}\right), \tag{6.60}$$

where

$$l_{\max} = \lfloor\sqrt{c_e}R_{so}\rfloor, \tag{6.61}$$
$$c_e = 1/(D_e\tau_e Q_{so}^2), \tag{6.62}$$
$$c_\phi = 1/(D_e\tau_\phi Q_{so}^2) \tag{6.63}$$

and $\lfloor ...\rfloor$ denotes the next lower integer number. For the growth directions [001] and [111], we can further simplify Eq. (6.60) if we consider the approximate eigenvalues of the Cooperon Hamiltonian. In this case, the integral can be computed analytically and yields

$$\Delta\sigma(B) = \frac{2e^2}{h}\frac{1}{2\pi^2 R_{so}}\sum_{n=-l_{\max}}^{l_{\max}}\left\{\frac{\arctan\left(\sqrt{c_e}\left[E^{\mathcal{S}}(Q_z=0,n)/Q_{so}^2 + c_\phi\right]^{-1/2}\right)}{\left[E^{\mathcal{S}}(Q_z=0,n)/Q_{so}^2 + c_\phi\right]^{1/2}} - \sum_{i\in\{\pm1,0\}}\frac{\arctan\left(\sqrt{c_e}\left[E_i^{\mathcal{T}}(Q_z=0,n)/Q_{so}^2 + c_\phi\right]^{-1/2}\right)}{\left[E_i^{\mathcal{T}}(Q_z=0,n)/Q_{so}^2 + c_\phi\right]^{1/2}}\right\}, \tag{6.64}$$

with the approximate eigenmodes E_i^j [Eqs. (6.34) and (6.35)] of the Cooperon Hamiltonian evaluated at $Q_z = 0$.

In Fig. 6.6, we picture the conductivity correction without magnetic and external electric field for a $\langle 111\rangle$ nanowire. A crossover from WL to WAL appears depending on the dephasing time and the elastic scattering time. The crossover from negative to positive magnetoconductivity is shown in Figs. 6.7 which is due to an increase of the lower cutoff c_ϕ. Here, we defined the relative magnetoconductivity as $\Delta\sigma_R \equiv \Delta\sigma(B) - \Delta\sigma(B=0)$. Note that this can also be achieved by reducing the SOC strength which is encapsulated in the quantity Q_{so}. It is worth mentioning that both crossovers do not necessarily coincide. Moreover, in contrast

to a planar wire with hard wall boundaries as shown in Ref. [67] we do not find a crossover in dependency of the wire width W which corresponds to the circumference $2\pi R$ of the tubular nanowire. This is due to the fact that no motional narrowing occurs due to periodic boundary conditions.

By fitting theory to data from experiment one can extract the Rashba and Dresselhaus SOC strengths. These are related to the spin-relaxation rate $1/\tau_\mathrm{s}$ through

$$\frac{1}{\tau_s} = D_e E_\chi^\xi\Big|_{\mathcal{B}=0}, \tag{6.65}$$

where E_χ^ξ are the triplet eigenvalues of the Cooperon Hamiltonian without magnetic field. The relaxation thus depends on the given spin state. With the aid of the global minimum of the triplet spectrum, one can estimate the minimal spin-relaxation rate, though. For the most systems, it is reasonable to assume that those gaps are given by $\Delta_{\mathcal{T}_0}^{[001]}$, $\Delta_{\mathcal{T}_0}^{[111]}$, or $\delta_z^{[110]}$ in Eqs. (6.44), (6.46) and (6.58), depending on the growth direction of the nanowire. For pure internal Rashba SOC, i.e., $\alpha_\mathrm{ext} = \beta = 0$, the spin-relaxation rate at $Q = 0$ yields

$$\frac{1}{\tau_s} = 4m^{*2} D_e \alpha_\mathrm{int}^2/\hbar^4, \tag{6.66}$$

which is identical to the case of a planar 2DEG grown along the [001] crystal axis as derived by D'yakonov *et al.* in Ref. [103] and also found in early studies on WL/WAL [144, 146]. We point out that for large Rashba SOC, the global minimum is shifted to finite momenta $Q \neq 0$, though. In case of pure internal Rashba SOC the resulting spin-relaxation rate is about a factor 2 smaller due to the gap $\delta_\phi \approx \lambda_1^2/2 = \Delta_{\mathcal{T}_0}/2$, which was also noticed by Kettemann in Ref. [61]. Owing to the discrete nature of Q_ϕ in our model, however, such states are not necessarily available in the given nanowire system.

In the last part of this section, we fit the derived formulas for the magnetoconductivity correction to experimental data of an exemplary semiconductor nanowire.

6.2.4 Experimental Data Fitting: InAs Nanowire

As an example, we present the fitting results for the magnetoconductance measurements in an undoped top-gated ⟨111⟩ InAs nanowire.[6] The nanowire is grown by selective area metal-organic vapor phase epitaxy [181]. Subsequently, the InAs nanowire is transferred to a Si/SiO_2 substrate and contacted electrically via electron beam lithography. The nanowire segment in-between the source and drain contacts is covered with $LaLuO_3$ high-k dielectric and a metallic gate electrode, [59] giving rise to an external electric field distribution as depicted schematically in Fig. 6.1(a). Magnetoresistance measurements are performed in a pumped flow cryostat at a temperature of 1.7 K using a low-frequency (33 Hz) lock-in setup with

[6] This device corresponds to *Device A* in Ref. [59].

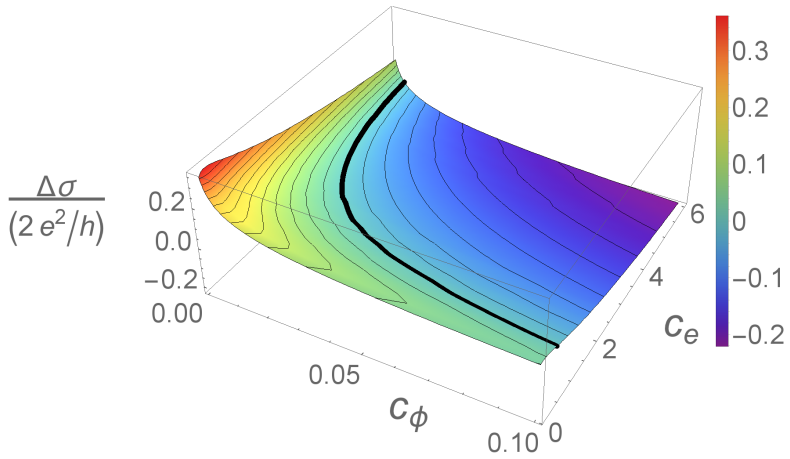

Fig. 6.6: Crossover from WL to WAL in a $\langle 111 \rangle$ nanowire for $\mathcal{B} = \kappa = \lambda_2 = 0$, $\lambda_1 = 0.3$ and $R_{so} = 30$.

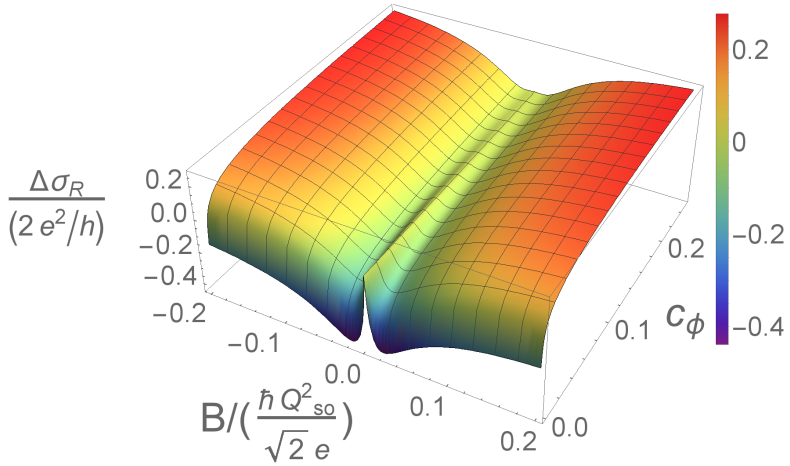

Fig. 6.7: Relative magnetoconductivity $\Delta\sigma_R \equiv \Delta\sigma(B) - \Delta\sigma(B = 0)$ in a $\langle 111 \rangle$ nanowire for $\kappa = \lambda_2 = 0$, $\lambda_1 = 0.3$, $R_{so} = 30$ and $c_e = 10$.

an ac bias current of 10 nA. As can be seen in Fig. 6.8, the device exhibits a gate-induced crossover from positive to negative magnetoconductivity - which is usually associated with a crossover from WL to WAL. The same characteristic behavior has been recently observed in several experiments [41, 42, 47].

The utilization of InAs for nanowires is highly popular [41, 42, 44, 47–50, 59]. In nanowires grown from this material the common problem of carrier depletion at the surface is avoided as consequence of Fermi level pinning [44]. The narrow bandgap of InAs results in large Rashba and Dresselhaus SOC coefficients[70] $r_{41}^{6c6c} = 117.1\,\mathrm{eÅ}^2$ and $b_{41}^{6c6c} = 27.18\,\mathrm{eVÅ}^3$, respectively. The effective mass is given by $m^* = 0.026\,m_0$ where m_0 is the bare electron mass [169]. In line with the experimental setup of Ref. [59], we consider a free length of the nanowire of $L = 2.6\,\mu\mathrm{m}$ and a radius of $R_0 = 40\,\mathrm{nm}$ where the radial position R of the maximum of the wave function is estimated to be at $R = 35\,\mathrm{nm}$. Using the relation $\Delta G = (2\pi R/L)\Delta\sigma$, we can determine the conductivity correction from the macroscopic conductance correction ΔG of the probed nanowire sample. Moreover, we use the field-effect mobility $\mu = 1000\,\mathrm{cm^2V^{-1}s^{-1}}$ and 3D electron density $n_{3D} = 5.1 \times 10^{17}\,\mathrm{cm^{-3}}$ where the 2D electron density can be approximated by $n_{2\mathrm{D}} = n_{3\mathrm{D}}R_0^2/(2R)$. By means of the relation $\mu = e\tau_e/m^*$, we find a mean free path of $l_e = 17.9\,\mathrm{nm}$ which yields the ratio $l_e/(2\pi R_0) = 0.08$. The diffusivity condition around the circumference is, hence, well fulfilled. Also, the parameter configuration satisfies the Ioffe-Regel criterion with $(E_F\tau_e/\hbar)^{-1} = 0.41$ and $\kappa = 0.05$ is indeed small.

We determine an appropriate fitting value for the internal Rashba contribution of $\alpha_{\mathrm{int}} = -74\,\mathrm{meVÅ}$. The respective internal electric field, that arises from Fermi level pinning, is $\mathcal{E}_{\mathrm{int}} = -6.3 \times 10^6\,\mathrm{V/m}$, whose magnitude is in agreement with previous simulations [44, 59]. Accordingly, the Dresselhaus SOC strength is found to be $\beta = 41\,\mathrm{meVÅ}$ which corresponds to a ratio $\lambda_1 = -1.8$ and confinement parameter $\gamma = 0.55\,\mathrm{nm^{-1}}$. The radial extent of the wave function is pictured in Fig. 6.1(b). In Fig. 6.8 we plot the relative magnetoconductivity correction $\Delta\sigma_{\mathrm{R}} = \Delta\sigma(B) - \Delta\sigma(B = 0)$ for an increasing external top-gate voltage V_g or Rashba contribution $\alpha_{\mathrm{ext}} \propto \lambda_2$, respectively. A crossover from positive to negative magnetoconductivity due to a growing SOC strength occurs. The symbol-dotted lines in Fig. 6.8 illustrate the experimental data, the solid lines the fitted relative magnetoconductivity correction using Eq. (6.60). Each magnetoconductivity curve represents an average of 25 individual measurements in a 500 mV gate voltage interval. In this way, we can ensure that the superimposed universal conductance oscillations are averaged out. It is shown in Fig. 6.9(a), that the scaling between the external Rashba parameter $|\alpha_{\mathrm{ext}}|$ and the gate voltage V_g is roughly linear. The extracted spin-relaxation and dephasing lengths l_s and l_ϕ, respectively, are displayed in Fig. 6.9(b) in dependence of an external gate voltage V_g. For a pure internal Rashba contribution, i.e., $\lambda_2 = 0$, we detect a spin-relaxation length of $l_{\mathrm{s}} = \sqrt{D_e\tau_s} = 191\,\mathrm{nm}$ by means of Eqs. (6.65) and (6.46). It decreases simultaneously with an increasing external gate voltage. In contrast, the dephasing length remains relatively constant at $l_\phi \approx 100\,\mathrm{nm}$. We stress that, here, we assume the quantum well to remain unchanged as the gate voltage increases. For high voltages the

quantum well width can be expected to become smaller. However, as consequence of the asymmetry of the external Rashba contribution the associated non-axial symmetric deformation of the quantum well is not comprised in our model for Dresselhaus SOC.

In contrast to previous works, we were able to quantify the Rashba and Dresselhaus SOC parameters individually for a zinc-blende type nanowire with surface charge accumulation layer. The close agreement with experiment in the presented example suggests that the developed model provides reliable information about the transport parameters.

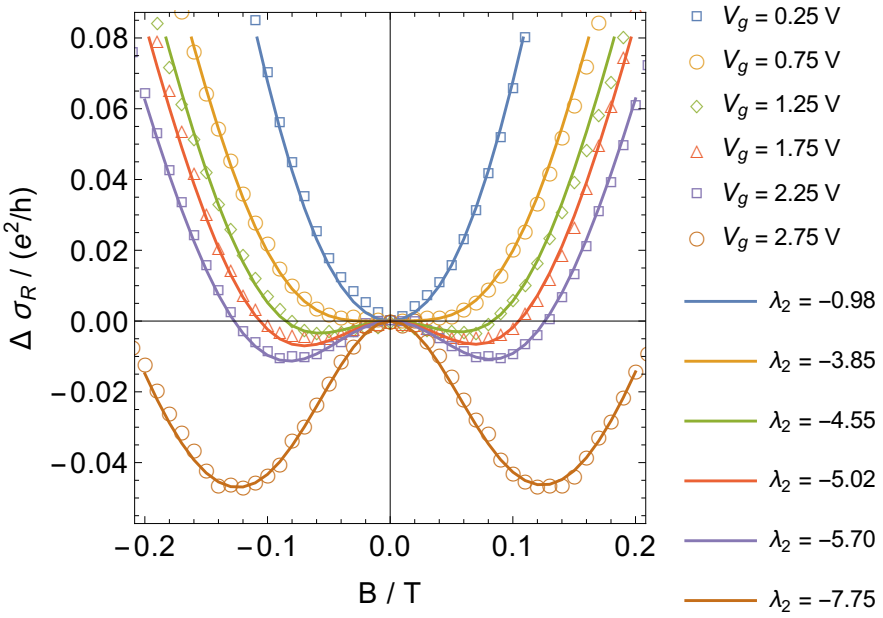

Fig. 6.8: Gate-controlled crossover from positive to negative magnetoconductivity $\Delta\sigma_R \equiv \Delta\sigma(B) - \Delta\sigma(B=0)$ in a $\langle 111\rangle$ InAs nanowire. The symbol-dotted lines correspond to experimental data for different top-gate voltages V_g which is fitted by theory (solid lines) using Eq. (6.60) and varying the external Rashba SOC strength $\alpha_{\text{ext}} \propto \lambda_2$.

6.3 Summary

Summarizing, we have developed models to describe linear Rashba and Dresselhaus SOC effects in zinc-blende semiconductor nanowires of growth directions $\langle 001\rangle$, $\langle 111\rangle$ and $\langle 110\rangle$. In the considered systems the transport is governed by electron states near the surface which can be a result of Fermi level pinning or radial confinement in core/shell nanowires. Motivated by recent experiments [59], the Rashba SOC is composed of two parts: an internal and an external contribution. The internal one is due to an axial symmetric homogeneous electric field induced

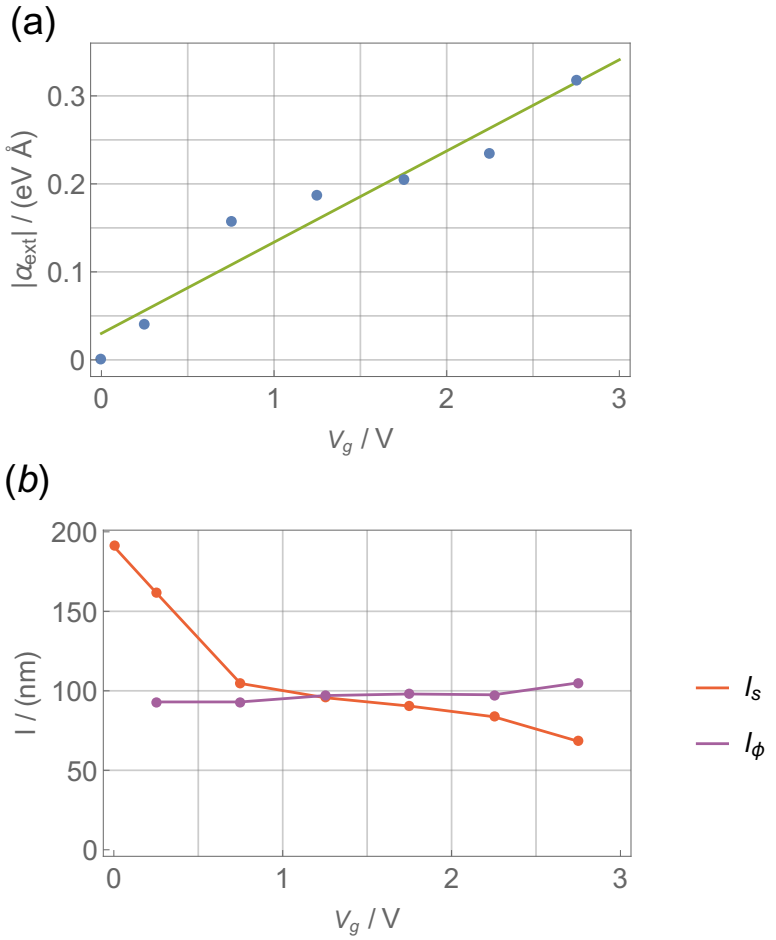

Fig. 6.9: Extracted fitting parameters for a ⟨111⟩ InAs nanowire. (a) External Rashba SOC strength $|\alpha_{\text{ext}}|$ as well as (b) spin-relaxation and dephasing length l_s and l_ϕ, respectively, in dependence of a top-gate voltage V_g.

by Fermi surface pinning or/and a wrap-around gate. The external one results from an external gate which causes an also axial symmetric but inhomogeneous field that penetrates only one side of the nanowire. Moreover, we anticipate that the microscopic crystal structure in the nanowire does not differ from the bulk. This leads to a Dresselhaus SOC which is fundamentally different to previous approaches [171, 172] that modeled rolled-up [001] confined 2DEGs. Compared with the latter, the Dresselhaus SOC depends on the azimuthal location at the surface of the nanowire.

We have computed the Cooperon Hamiltonian following former approaches [61, 67, 173, 174]. The electron motion on the cylindrical surface was treated diffusive in both in-plane coordinates. It is shown that the Dresselhaus SOC causes a gap for the triplet eigenmodes and, hence, an insuppressible spin relaxation. This contradicts the conjecture of previous authors, Refs. [36, 41, 42, 45, 46, 180], that Dresselhaus SOC is absent in $\langle 111 \rangle$ nanowires and, hence, cannot cause spin relaxation. Nevertheless, we found the lowest gap for the $\langle 111 \rangle$ growth direction which indicates a lower spin relaxation than for $\langle 001 \rangle$ or $\langle 110 \rangle$ nanowires. A zero-gap mode for certain interplay of Rashba and Dresselhaus SOC which reflects spin-preserving symmetries was not found. For the $\langle 110 \rangle$ nanowires, we observed an additional shift of the minima of the Cooperon modes for the momentum along the wire axis whose value and position depends also on Rashba SOC. In most cases, it represents the global minimum of the spectrum. As a consequence, the states with the longest spin lifetime are of helical nature.

Finally, we derived the quantum mechanical correction to the Drude conductivity. We detected a crossover from negative to positive magnetoconductivity depending on the dephasing time and the SOC strengths. A significant dependency on the wire radius was not found which was attributed to periodic boundary conditions along the circumference of the cylinder. By fitting the developed theory to data from low-field magnetoconductance measurements in a $\langle 111 \rangle$ InAs nanowire we extracted spin-relaxation and dephasing rates as well as SOC strengths. We were able to quantify the Rashba and Dresselhaus SOC parameters individually. Both contributions were shown to be likewise significant in a nanowire with surface accumulation layer.

As a final remark, we want to emphasize that studying the magnetoconductance behavior in a nanowire is a particularly delicate task. The reason is that gating or doping can change the potential landscape or the electron density in such a way that the electron states transform from the surface states (2D) to volume states (3D) in the nanowire. As the conductivity corrections in 2D and 3D are fundamentally different [138], it is often not clear which model applies. Additionally, it is ambiguous whether a gate-induced crossover from positive to negative magnetoconductivity is solely attributed to an increase of Rashba SOC or accompanied by a dimensional crossover. This provides an incentive for further investigations of the weak (anti)localization in nanowires where the electron states cover the entire volume. We address this topic in the following chapter.

Appendix 6.A: Pauli Matrices in Cylindrical Coordinates

$$\sigma_r = \begin{pmatrix} 0 & e^{-i\phi} \\ e^{i\phi} & 0 \end{pmatrix}, \quad \sigma_\phi = \begin{pmatrix} 0 & -ie^{-i\phi} \\ ie^{i\phi} & 0 \end{pmatrix}, \quad \sigma_z = \begin{pmatrix} 1 & 0 \\ 0 & -1 \end{pmatrix}. \tag{6.A.1}$$

Appendix 6.B: Commutator Relations

$$\begin{aligned}
[k_\phi, \cos(\phi)] &= (i/r)\sin(\phi), && (6.B.2)\\
[k_\phi, \sin(\phi)] &= -(i/r)\cos(\phi), && (6.B.3)\\
[k_\phi, \sigma_\phi] &= (i/r)\sigma_r, && (6.B.4)\\
[k_\phi, \sigma_r] &= -(i/r)\sigma_\phi, && (6.B.5)\\
[k_r, 1/r] &= i/r^2, && (6.B.6)\\
[k_r, k_\phi] &= (i/r)k_\phi. && (6.B.7)
\end{aligned}$$

Appendix 6.C: Matrix Elements

The matrix elements with respect to the lowest radial mode $|R_0\rangle$ are

$$\begin{aligned}
\langle 1/r \rangle &= 1/R, && (6.C.8)\\
\langle 1/r^2 \rangle &= 1/R^2, && (6.C.9)\\
\langle k_r \rangle &= i/(2R), && (6.C.10)\\
\langle k_r^2 \rangle &= \gamma^2/2, && (6.C.11)\\
\langle k_r^3 \rangle &= 3i\gamma^2/(4R) \\
&= 3\langle k_r \rangle \langle k_r^2 \rangle, && (6.C.12)\\
\langle 1/r \cdot k_r \rangle &= 0, && (6.C.13)\\
\langle 1/r \cdot k_r^2 \rangle &= \gamma^2/(2R). && (6.C.14)
\end{aligned}$$

Appendix 6.D: Radial Momentum Expectation Value

In this section, we prove that it is not substantial to choose a harmonic radial confinement in order to obtain $\langle k_r \rangle = i/(2R)$. A similar proof was demonstrated in Ref. [164]. Let $|R_0\rangle$ be the lowest radial mode of the Hamiltonian with an arbitrary potential $V(\mathbf{r})$ that confines the wave function $\langle r|R_0\rangle \equiv \rho_0$ to a region around R. The wave function is demanded to vanish exactly at the limits $r = 0$ and $r \to \infty$. We now define $|R_0\rangle \equiv |R_0'\rangle / \sqrt{r}$ and obtain

$$\langle R_0'|\frac{1}{r}\partial_r|R_0'\rangle = \langle R_0|\partial_r + \frac{1}{2r}|R_0\rangle = \langle \partial_r \rangle + \frac{1}{2R}. \tag{6.D.15}$$

On the other hand, partial integration gives

$$\langle R_0'|\frac{1}{r}\partial_r|R_0'\rangle = \int_0^\infty \mathrm{d}r\,(\rho_0')^*\frac{\mathrm{d}\rho_0'}{\mathrm{d}r} = |\rho_0'|^2\Big|_0^\infty - \int_0^\infty \mathrm{d}r\,\rho_0'\left(\frac{\mathrm{d}\rho_0'}{\mathrm{d}r}\right)^*. \tag{6.D.16}$$

Since $|\rho_0'|^2\Big|_0^\infty = r\,|\rho_0|^2\Big|_0^\infty = 0$, the Eq. (6.D.16) must be purely imaginary. However, given the fact that the Hermiticity of the operator $\frac{1}{r}\partial_r$ requires a real expectation value, $\langle R_0'|\frac{1}{r}\partial_r|R_0'\rangle$ has to vanish identically.

Appendix 6.E: Auxiliary Function in the Tubular System

The auxiliary function $I(\hat{\mathbf{Q}})$ in Eq. (3.39) is evaluated at the Fermi energy E_F. For small values of $\mathbf{Q}$ and $\hbar/\tau$ we approximate $I(\hat{\mathbf{Q}})$ in the following way. For the quasi-2D momentum of the electron we have $\mathbf{q} = (\langle q_r\rangle, q_\phi, q_z)^\top$ and $|\mathbf{q}\rangle = |q_\phi\rangle\,|q_z\rangle$. Defining $(q_\phi, q_z)^\top = (q_\parallel\cos(\vartheta), q_\parallel\sin(\vartheta))^\top$ and the Fermi wave vector $\mathbf{k}_F$ we find with the 2D density of states per spin $\nu_0 = \mathcal{V}m^*/(2\pi\hbar^2)$ and the surface of the nanowire $\mathcal{V}$

$$\begin{aligned} I(\hat{\mathbf{Q}}) &= \frac{\hbar}{2\pi\nu_0\tau_e}\sum_{\mathbf{q}}\langle\mathbf{q}|\,\mathcal{G}^{\mathrm{R}}(\hat{\mathbf{q}},\boldsymbol{\sigma})\mathcal{G}^{\mathrm{A}}(\hat{\mathbf{Q}}-\hat{\mathbf{q}},\boldsymbol{\sigma'})\,|\mathbf{q}\rangle \\ &\approx \frac{1}{\nu_0}\int_0^{2\pi}\frac{\mathrm{d}\phi}{2\pi}\sum_{q_\phi,q_z}\frac{1}{1-i\tau_e\hat{\Sigma}/\hbar}\delta(E_F-\mathcal{H}(\mathbf{q})) \\ &\approx \int_0^{2\pi}\frac{\mathrm{d}\phi}{2\pi}\int_0^{2\pi}\frac{\mathrm{d}\vartheta}{2\pi}\frac{1}{1-i\tau_e\hat{\Sigma}/\hbar}\Big|_{\mathbf{q}=\mathbf{k}_F}, \end{aligned} \tag{6.E.17}$$

where $\hat{\Sigma} = \mathcal{H}(\hat{\mathbf{Q}}-\mathbf{k}_F,\boldsymbol{\sigma}) - \mathcal{H}(\mathbf{k}_F,\boldsymbol{\sigma'})$.

Appendix 6.F: Spin-Orbit Coupling Matrices

The SOC matrix $\hat{\boldsymbol{a}} = \hat{\boldsymbol{a}}_{\mathrm{D}}^{\xi} + \hat{\boldsymbol{a}}_{\mathrm{R}}$ comprises the Dresselhaus SOC for the different wire directions $\xi \in \{[001],[111],[110]\}$ as well as internal and external Rashba SOC, i.e., $\hat{\boldsymbol{a}}_{\mathrm{R}} = \hat{\boldsymbol{a}}_{\mathrm{R}}^{\mathrm{int}} + \hat{\boldsymbol{a}}_{\mathrm{R}}^{\mathrm{ext}}$. If we chose the basis for convenience in the order $\{\hat{\mathbf{r}},\hat{\boldsymbol{\phi}},\hat{\mathbf{z}}\}$, the matrices are written as

$$\hat{\boldsymbol{a}}_{\mathrm{D}}^{[001]} = \frac{\beta}{\hbar}\begin{pmatrix} -2\cos(2\phi) & -\frac{5}{2}\sin(2\phi) & 0 \\ \frac{1}{2}\sin(2\phi) & -\cos(2\phi) & 0 \\ 0 & 0 & \cos(2\phi) \end{pmatrix},$$

$$\hat{\boldsymbol{a}}_{\mathrm{D}}^{[111]} = \frac{\beta}{2\sqrt{3}\hbar}\begin{pmatrix} 0 & 1 & 9\sqrt{2}\sin(3\phi) \\ -1 & 0 & 3\sqrt{2}\cos(3\phi) \\ -\sqrt{2}\sin(3\phi) & -\sqrt{2}\cos(3\phi) & 0 \end{pmatrix},$$

$$\hat{\boldsymbol{a}}_{\mathrm{D}}^{[110]} = \frac{\beta}{8\hbar}\begin{pmatrix} 0 & 0 & -\cos(\phi) - 27\cos(3\phi) \\ 0 & 0 & \sin(\phi) + 9\sin(3\phi) \\ \cos(\phi) + 3\cos(3\phi) & -11\sin(\phi) - 3\sin(3\phi) & 0 \end{pmatrix}, \tag{6.F.18}$$

and

$$\hat{\boldsymbol{a}}_{\mathrm{R}}^{\mathrm{int}} = \frac{\alpha_{\mathrm{int}}}{\hbar}\begin{pmatrix} 0 & 0 & 0 \\ 0 & 0 & -1 \\ 0 & 1 & 0 \end{pmatrix}, \quad \hat{\boldsymbol{a}}_{\mathrm{R}}^{\mathrm{ext}} = \frac{\alpha_{\mathrm{ext}}}{\hbar}\Theta(\phi)\Theta(\pi-\phi)\begin{pmatrix} 0 & 0 & \cos(\phi) \\ 0 & 0 & -\sin(\phi) \\ 0 & \sin(\phi) & 0 \end{pmatrix}. \tag{6.F.19}$$

CHAPTER 7

Cylindrical 3D-Diffusive Zinc-Blende Nanowires

Hereafter, we study the effects of SOC on the magnetoconductivity in 3D-diffusive cylindrical semiconductor nanowires. Following up on our previous investigations on tubular semiconductor nanowires (cf. Chap. 6), we focus in this chapter on nanowire systems where no surface accumulation layer is formed but instead the electron wave function extends over the entire cross-section. We take into account the Dresselhaus SOC resulting from a zinc-blende lattice and the Rashba SOC, which is controlled by a lateral gate electrode. The spin-relaxation rate due to Dresselhaus SOC is found to depend neither on the spin density component nor on the wire growth direction and is unaffected by the radial boundary. In contrast, the Rashba spin-relaxation rate is strongly reduced for a wire radius that is smaller than the spin precession length. The derived model is fitted to the data of magnetoconductance measurements of a heavily doped back-gated InAs nanowire and transport parameters are extracted. At last, we compare our results to previous theoretical and experimental studies and discuss the occurring discrepancies.

7.1 Formulation of the Bulk Problem

7.1.1 Hamiltonian for Bulk Electrons

Analogously to the previous chapter, the Hamiltonian $\mathcal{H}$ which describes bulk electrons in the lowest conduction band of a zinc-blende type semiconductor with SOC reads as

$$\mathcal{H} = \frac{\hbar^2 k^2}{2m^*} + \mathcal{H}_{\mathrm{R}} + \mathcal{H}_{\mathrm{D}}. \tag{7.1}$$

with the Rashba and Dresselhaus SOC Hamiltonians, $\mathcal{H}_{\mathrm{R}}$ and $\mathcal{H}_{\mathrm{D}}$ as defined in Eqs. (1.48) and (1.45), respectively. In this definition, the underlying basis vectors $\{\hat{\mathbf{x}}, \hat{\mathbf{y}}, \hat{\mathbf{z}}\}$ point along the crystal axes [100], [010], and [001]. We begin with the assumption that the electrons in the wire experience a nearly homogeneous electric field perpendicular to the wire axis. In Sec. 7.1.2 we will see that the choice of the wire axis and the perpendicular electric field is arbitrary as the Rashba and Dresselhaus SOC do not mix with each other in the Cooperon and the effect of

the Dresselhaus SOC is independent of the crystal direction. Thus, without loss of generality, we define the wire axis to be oriented along $\hat{\mathbf{z}}$ and the electric field as $\boldsymbol{\mathcal{E}} = \mathcal{E}\hat{\mathbf{y}}$.

7.1.2 3D Conductivity Correction and Cooperon

In contrast to the previous chapter, the motion of the electrons is considered to be diffusive in all three spatial directions. Using the definitions and preconditions as given in Sec. 3.3.2, the conductivity correction is written as

$$\Delta\sigma = \frac{2e^2}{h}\frac{\hbar D_e}{\mathcal{V}}\mathrm{Re}\left(\sum_{\mathbf{Q}}\sum_{s,m_s}\chi_s\,\langle s,m_s|\hat{\mathcal{C}}(\hat{\mathbf{Q}})|s,m_s\rangle\right), \tag{7.2}$$

where in the present case $\mathcal{V}$ denotes the volume of the cylindrical nanowire and D_e the 3D diffusion constant, i.e., $D_e = v_F^2\tau_e/3$. As SOC constitutes a small perturbation to the kinetic part in the Hamiltonian $\mathcal{H}$ and the main contribution to the Cooperon results from terms near $Q = 0$, the Cooperon propagator $\hat{\mathcal{C}}$ can be approximated by (cf. Eq. (3.43))

$$\hat{\mathcal{C}}(\mathbf{Q}) = \frac{\tau_e}{\hbar}\left(1 - \int\frac{d\Omega}{4\pi}\frac{1}{1 - i\tau_e\hat{\Sigma}(\mathbf{Q})/\hbar}\right)^{-1}, \tag{7.3}$$

where $\hat{\Sigma}(\mathbf{Q}) = \mathcal{H}(\mathbf{Q} - \mathbf{k}_F, \boldsymbol{\sigma}) - \mathcal{H}(\mathbf{k}_F, \boldsymbol{\sigma'})$ and the integral is performed over all angles Ω of the Fermi wave vector $\mathbf{k}_F$. In 3D the Fermi contour is nearly spherical and the integral is continuous. For weak disorder, i.e., $E_F\tau_e/\hbar \gg 1$, we may further approximate $\hat{\Sigma}(\mathbf{Q}) \approx -\mathbf{v}_F(\hbar\mathbf{Q} + 2m^*(\hat{\mathbf{a}}_\mathrm{R} + \hat{\mathbf{a}}_\mathrm{D})\mathbf{S})$ with the total electron spin vector $\boldsymbol{S}$ in the singlet-triplet basis as defined in App. 3.B. The matrix $\hat{\mathbf{a}}_\mathrm{R}(\hat{\mathbf{a}}_\mathrm{D})$ contains the contributions due to Rashba (Dresselhaus) SOC, i.e.,

$$\hat{\mathbf{a}}_\mathrm{R} = \frac{\alpha_\mathrm{R}}{\hbar}\begin{pmatrix} 0 & 0 & 1 \\ 0 & 0 & 0 \\ -1 & 0 & 0 \end{pmatrix}, \tag{7.4}$$

and

$$\hat{\mathbf{a}}_\mathrm{D} = \frac{b_{41}^{6c6c}}{\hbar}\begin{pmatrix} k_y^2 - k_z^2 & 0 & 0 \\ 0 & k_z^2 - k_x^2 & 0 \\ 0 & 0 & k_x^2 - k_y^2 \end{pmatrix}, \tag{7.5}$$

where $\alpha_\mathrm{R} = r_{41}^{6c6c}\mathcal{E}$. For convenience and in analogy to the previous chapter, we define the Cooperon Hamiltonian $\hat{H}_\mathcal{C} = (\hbar D_e\hat{\mathcal{C}})^{-1}$. An additional Taylor expansion of the integrand in Eq. (7.3) to second order in $(\hbar\mathbf{Q} + 2m(\hat{\mathbf{a}}_\mathrm{R} + \hat{\mathbf{a}}_\mathrm{D})\mathbf{S})$, yields

$$\hat{H}_\mathcal{C}/Q_{so}^2 = (\boldsymbol{\mathcal{Q}} + 2e\boldsymbol{\mathcal{A}}_s/\hbar)^2 + \lambda_\mathrm{D}\mathbf{S}^2/2, \tag{7.6}$$

in terms of the dimensionless momenta $\mathcal{Q}_i = Q_i/Q_{so}$ with $Q_{so} = 2m\alpha_\mathrm{R}/\hbar^2 = 2\pi/L_{so}$ where L_{so} is the Rashba spin precession length. This approximation is valid in the diffusive regime when the SOC energy is small in comparison to the scattering energy $\hbar/\tau_e$, which is also the necessary precondition for the DP spin relaxation. The impact of large SOC on the conductivity was studied in 2D systems in Refs. [182–184]. Similar to the 2D and quasi-1D cases (cf. Chap. 6 and Ref. [61]), the effect of Rashba SOC becomes manifest in an effective vector potential $\mathbf{A}_s = Q_{so}\boldsymbol{\mathcal{A}}_s$ where $\boldsymbol{\mathcal{A}}_s = \hbar/(2e)(S_z, 0, -S_x)^\top$ and therefore couples to the Cooperon momentum. In contrast, the Dresselhaus SOC leads to a term $\propto \lambda_\mathrm{D} = 8\Gamma^2/35$, where $\Gamma = k_F^2 b_{41}^{6c6c}/\alpha_\mathrm{R}$, which does not couple to the wave vector $\boldsymbol{\mathcal{Q}}$ and is diagonal in the triplet sector. Thus, it gives rise to a spin-relaxation rate which is identical for all components of the spin density. We stress that unlike in tubular wires (cf. Chap. 6) the Dresselhaus contribution does not mix with the Rashba contribution and does not depend on the growth direction of the wire due to the averaging over the Fermi contour. Hence, the result applies to any zinc-blende nanowire irrespective of the growth direction and for an arbitrarily oriented electric field perpendicular to the wire axis.

7.2 Finite-Size Effects on the Diffusion in Mesoscopic Nanowires

7.2.1 Impact of a Radial Boundary Condition

Owing to the finite-size geometry of the nanowire, the Cooperon has to be complemented by a boundary condition. The impact of the boundary becomes relevant if the dephasing length is larger than the nanowire diameter. As the length of the nanowire typically largely exceeds its radial extension, we assume periodic boundary conditions along the wire axis for simplicity. For an insulating surface and spin-conserving boundary the condition reads as [61, 175, 185, 186]

$$\hat{\mathbf{n}} \cdot (\boldsymbol{\nabla} + 2ie\mathbf{A}_s/\hbar)\,\hat{\mathcal{C}}|_{\mathcal{S}} = 0, \tag{7.7}$$

where $\hat{\mathbf{n}}$ denotes the normal vector of the surface $\mathcal{S}$. This condition accounts for a specular boundary, which is plausible since the nanowires possess only a small degree of surface roughness [187]. Aside from that, in the transverse diffusive regime the ramifications of a diffusive boundary are insignificant [188]. The equation above can be simplified to a Neumann boundary condition, i.e., $\hat{\mathbf{n}} \cdot (\boldsymbol{\nabla}\hat{\mathcal{C}}')|_{\mathcal{S}} = 0$, by applying a non-Abelian gauge transformation. Thereby, the Cooperon (and with it the Cooperon Hamiltonian) is transformed as $\hat{\mathcal{C}} \to \hat{\mathcal{C}}' = U_A \hat{\mathcal{C}} U_A^\dagger$ with the unitary transformation operator $U_A = \exp[i2e\,(\hat{\mathbf{n}} \cdot \mathbf{A}_s)(\hat{\mathbf{n}} \cdot \mathbf{r})/\hbar]$. In this case, the lowest Cooperon mode $|0\rangle$ corresponds to a solution which has a vanishing wave vector perpendicular to the surface, i.e., $\hat{\mathbf{n}} \cdot \mathbf{Q} = 0$, and is thus constant in coordinate space along $\hat{\mathbf{n}}$. [175]

For a cylindrical nanowire, we identify $\hat{\mathbf{n}} = \hat{\boldsymbol{\rho}}$ and the surface $\mathcal{S}$ is defined by the constraint $\rho = R$ where R is the radius of the wire and we introduced the standard

cylindrical coordinates (ρ, ϕ, z) with the corresponding basis vectors $\{\hat{\boldsymbol{\rho}}, \hat{\boldsymbol{\phi}}, \hat{\boldsymbol{z}}\}$. Accordingly, the unitary transformation operator reads as $U_A = \exp[i2e\,(\hat{\boldsymbol{\rho}} \cdot \mathbf{A}_s)\rho/\hbar] = \exp[iQ_{so}xS_z]$ and the boundary condition becomes $\hat{\boldsymbol{\rho}} \cdot (\boldsymbol{\nabla}\hat{\mathcal{C}}')|_{\rho=R} = 0$. Using this, we obtain the transformed Cooperon Hamiltonian $\hat{H}'_{\mathcal{C}}$ as

$$\begin{aligned}\hat{H}'_{\mathcal{C}}/Q_{so}^2 = \boldsymbol{\mathcal{Q}}^2 &- 2\mathcal{Q}_z\left[\cos(Q_{so}x)S_x - \sin(Q_{so}x)S_y\right] \\ &+ \cos^2(Q_{so}x)S_x^2 + \sin^2(Q_{so}x)S_y^2 \\ &- \sin(Q_{so}x)\cos(Q_{so}x)\{S_x, S_y\} + \lambda_{\mathrm{D}}\mathbf{S}^2/2. \end{aligned} \tag{7.8}$$

The Dresselhaus contribution remains unchanged since $[S_i, \mathbf{S}^2] = 0$.

A suitable and generic real space basis for the transformed Cooperon (Hamiltonian) which satisfies the Neumann boundary condition is

$$\langle \mathbf{r}|n, l, Q_z\rangle = J_l^{(n)}(\rho)e^{il\phi}e^{iQ_z z}/N_{nl}, \tag{7.9}$$

with the angular momentum quantum number $l \in \mathbb{Z}$, the continuous plane wave number Q_z along the wire axis, and an appropriate normalization constant N_{nl}. The radial dependence is given by the Bessel function of the first kind $J_l^{(n)} := J_l(\rho\,\zeta_{n,|l|}/R)$, where $\zeta_{n,|l|}$ signifies the n-th radial extremum ($n \in \mathbb{N}_+$) of the Bessel function of $J_l(\rho)$. Additionally, we define $J_l^{(0)} = \delta_{l,0}$ which corresponds to a constant solution in the cross-sectional plane and constitutes the lowest mode of $\hat{H}'_{\mathcal{C}}$, usually denoted as zero-mode $|0\rangle$, i.e., $|0\rangle \equiv |n = 0, l = 0, Q_z\rangle$.

The zero-mode is of central interest since it allows to determine the spin states with the longest spin lifetime in narrow wires. These states are also characteristic to the conductance correction in transport as they yield the predominant contribution. In particular, if the wire is thin enough that the lowest Cooperon mode is well separated from the others, the transformed Cooperon Hamiltonian $\hat{H}'_{\mathcal{C}}$ can be evaluated only for the lowest mode, i.e., $\langle 0|\hat{H}'_{\mathcal{C}}|0\rangle$. This approach, which is often termed zero-mode approximation [61, 175, 186], is used in the following to obtain analytical expressions for the spin-relaxation rates and compute the magnetoconductance correction.

However, it is essential to notice that, due to the gauge transformation, the lowest mode is position-dependent in the (untransformed) system. More precisely, the real space representation of the lowest mode of the Cooperon Hamiltonian $\hat{H}_{\mathcal{C}}$ is in fact $U_A^\dagger\,\langle \mathbf{r}|0\rangle$. Consequently, the corresponding long-lived spin states have in general a rather complex helical structure in real space and are, therefore, often experimentally not accessible. Only in narrow wires, if the spin precession length is much larger than the boundary separation, the eigenstates are nearly homogeneous in real space. Exemplary in this context are optical orientation measurements or spin lasers, where the spin densities are homogeneously excited along the wire axis [39, 189, 190]. This becomes particularly important in wurtzite nanowires due to the presence of intrinsic k-linear SOC terms. For this reason, we will pay special attention to this scenario in Sec. 8.2.2 of the next chapter.

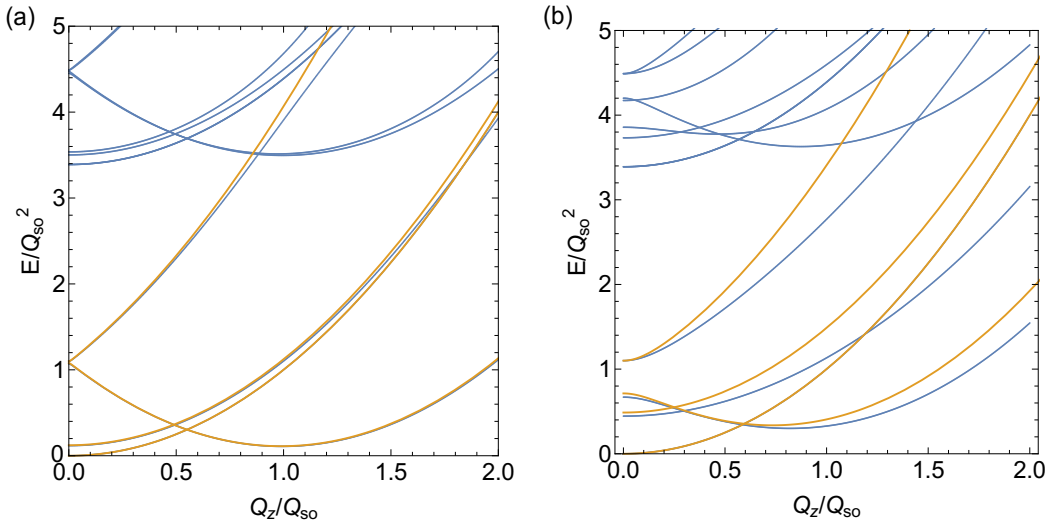

Fig. 7.1: Comparison of the zero-mode approximation (yellow), Eqs. (7.10), (7.11) and (7.12), with the exact diagonalization of $\hat{H}'_{\mathcal{C}}$ (blue) truncated to $n_{max} = 4$ and $|l_{max}| = 4$ for $\lambda_D = 0.1$ and (a) $Q_{so}R = 0.3$ and (b) $Q_{so}R = 1.5$.

7.2.2 Zero-Mode Approximation

In order to obtain an analytical result for the spin-relaxation rates and the magnetoconductance correction, the transformed Cooperon $\hat{\mathcal{C}}'$ is evaluated for the lowest mode $|0\rangle$, called zero-mode. Using this approximation, the eigenvalues of $\langle 0|H'_{\mathcal{C}}|0\rangle$ read as

$$E_S^{(0)}/Q_{so}^2 = \mathcal{Q}_z^2, \tag{7.10}$$

$$E_{T,0}^{(0)}/Q_{so}^2 = \mathcal{Q}_z^2 + \lambda_{\mathrm{D}} + a_{so}/2, \tag{7.11}$$

$$E_{T,\pm}^{(0)}/Q_{so}^2 = \mathcal{Q}_z^2 + \lambda_{\mathrm{D}} + 1 - a_{so}/4 \pm \frac{1}{4}\sqrt{a_{so}^2 + 64(1-b_{so})^2\mathcal{Q}_z^2}, \tag{7.12}$$

where we introduced $a_{so} = 1-2J_1(2Q_{so}R)/(2Q_{so}R)$ and $b_{so} = 1-2J_1(Q_{so}R)/(Q_{so}R)$ with the Bessel function of the first kind J_1. We stress that the spectrum is identical for a planar wire if $\lambda_D = 0$ and the function $2J_1(x)/x$ is replaced by $\sin(x)/x$ [61]. In Fig. 7.1 we compare the zero-mode approximation with exact diagonalization for different values of $Q_{so}R$. As the zero-mode approximation provides reliable results for small values of $Q_{so}R < 1$ [67], we can write the triplet spectrum as

$$E_{T,0}^{(0)}/Q_{so}^2 = \mathcal{Q}_z^2 + \Delta_0, \tag{7.13}$$

$$E_{T,\pm}^{(0)}/Q_{so}^2 = (\mathcal{Q}_0 \pm |\mathcal{Q}_z|)^2 + \Delta_1. \tag{7.14}$$

where $\Delta_0 = \lambda_{\mathrm{D}} + a_{so}/2$, $\Delta_1 = \lambda_{\mathrm{D}} + 2b_{so} - a_{so}/4$, and $\mathcal{Q}_0 = 1 - b_{so}$. This has the following advantages. First, we capture the most important features of the spectrum, that is, the minima of the triplet modes Δ_j, which are direct measures of the spin-relaxation rates. For $E_{T,\pm}^{(0)}$ the minimum is shifted to finite momenta

$\mathcal{Q}_z = \pm\mathcal{Q}_0$ and the corresponding long-lived spin densities are, therefore, of helical structure. Second, the simple form of the spectrum allows to derive a closed-form expression for the magnetoconductance correction later on.

7.2.3 Spin Relaxation in Narrow Wires

The DP spin-relaxation rate is related to the gaps in the Cooperon spectrum via the relation $(1/\tau_s)_j = D_e E_{T,j}$. Hence, in general, $(1/\tau_s)_j$ depends on the Cooperon wave vector $\mathbf{Q}$ as well as on the orientation of the given spin state which is subject to a random walk. For a spatially homogeneous spin density, $\mathbf{Q} = 0$, the result is equivalent to the eigenvalues of the DP spin-relaxation tensor (cf. Sec. 2.1).

In the bulk, the 3D Cooperon can be simply evaluated in the basis of plane waves. For $\mathbf{Q} = 0$, the Cooperon Hamiltonian, Eq. (7.6), is diagonal in the basis of spin density components, App. 3.D, leading to the 3D spin-relaxation rates $(1/\tau_s)_{ii} = D_e Q_{so}^2(\lambda_\mathrm{D} + 1 + \delta_{i,y})$ where $i \in \{x, y, z\}$. Unlike Rashba SOC, the Dresselhaus SOC affects the spin relaxation of all spin density components in the same way.

In presence of a radial boundary condition, the corresponding gauge transformation leads to a position dependence of the eigenstates of the Cooperon Hamiltonian $H_\mathcal{C}$. In App. 7.A, the Cooperon Hamiltonian $H_\mathcal{C}$ in zero-mode approximation is given in the basis of spin density components. For $Q_z = 0$, the s_z component is fully decoupled and independent of the location on the wire cross-section. As a consequence, a spin density which is homogeneously polarized along the wire axis is an eigenstate of the Cooperon Hamiltonian and decays according to the spin-relaxation rate $(1/\tau_s)_{zz} = D_e Q_{so}^2(\lambda_\mathrm{D} + 1)$. Remarkably, this rate is independent of the wire radius to all orders in $Q_{so}R$ within the zero-mode approximation. In fact, it is identical to the 3D spin-relaxation rate. The remaining two (unnormalized) eigenstates $\mathbf{a}_{\parallel,j}$, where $\mathbf{a}_{\parallel,-} = (\tan(Q_{so}x), 1, 0)^\top$ and $\mathbf{a}_{\parallel,+} = (1, -\tan(Q_{so}x), 0)^\top$, with the according spin-relaxation rates $(1/\tau_s)_{\parallel,j} = D_e Q_{so}^2(\delta_{j,-} \pm a_{so}/2 + \lambda_\mathrm{D})$ lie in the plane of the cross-section and depend on the position as depicted in Fig. 7.2.

In analogy to numerous previous works [61, 103, 144–146], we define hereafter the spin-relaxation rate of the system $1/\tau_s$ as the minimal rate for $\mathcal{Q}_z = 0$, which is $1/\tau_s \equiv (1/\tau_s)_{\parallel,+} = D_e Q_{so}^2(a_{so}/2 + \lambda_\mathrm{D})$. In the limit of $Q_{so}R \ll 1$, corresponding to a radius R much smaller than the Rashba spin precession length L_{so}, we replace $a_{so} \to 4b_{so} \to (Q_{so}R)^2/2$, which gives,

$$\frac{1}{\tau_s} = \frac{k_F^2 \mathcal{E}^2 (r_{41}^{6c6c})^2 \tau_e}{3\hbar^2} (Q_{so}R)^2 + \frac{32 k_F^6 (b_{41}^{6c6c})^2 \tau_e}{105\hbar^2} \tag{7.15}$$

to second order in $Q_{so}R$. Noting further that since $Q_{so}x \leq Q_{so}R \ll 1$, the respective eigenstate is $\mathbf{a}_{\parallel,+} \approx (1, 0, 0)^\top$. In accordance with Ref. [61], the first term in Eq. (7.15) is strongly suppressed in wires with small radii. However, compared to Ref. [61] the first term is a factor 2 smaller if we associated $R = W/2$, where W is the width of the planar quantum wire. The Dresselhaus-dependent spin-relaxation rate was also obtained in Ref. [191]. Notably, as seen from Eq. (7.14), the global

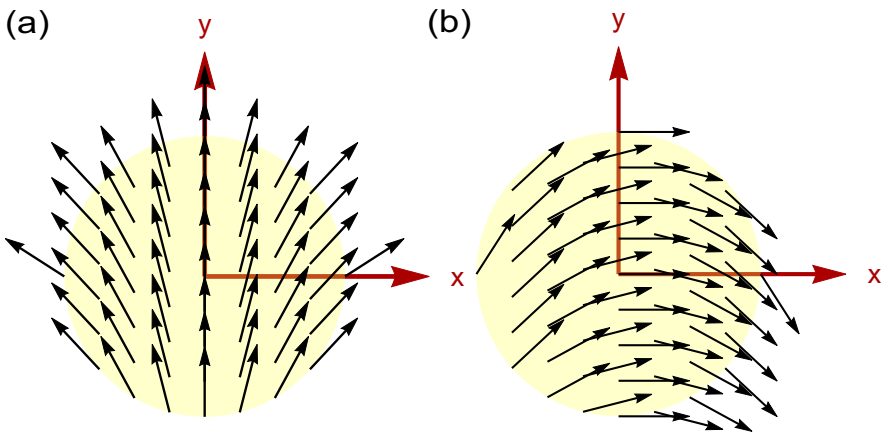

Fig. 7.2: Eigenstates (a) $\mathbf{a}_{\parallel,-}/\|\mathbf{a}_{\parallel,-}\|$ and (b) $\mathbf{a}_{\parallel,+}/\|\mathbf{a}_{\parallel,+}\|$ of the Cooperon Hamiltonian in zero-mode approximation, App. 7.A, for $Q_{so}R = 1$. Both states lie in the plane of the nanowire cross-section (yellow).

minimum of the spectrum is found at finite wave vectors $\mathcal{Q}_z = \pm\mathcal{Q}_0$ and given by Δ_1 which is for small λ_D approximately half as large as Δ_0. This outlines the superior spin lifetime of helical spin densities, which was observed earlier in planar and tubular 2DEGs (cf. Chaps. 4 and 6).

7.2.4 General Remarks

First, we would like to point out some general observations on the structure of the Cooperon Hamiltonian $\hat{H}_\mathcal{C}$, Eq. (7.6), with respect to the presence of a generic SOC contribution. Linear and cubic SOC terms can be always expanded in terms of first- and third-degree spherical harmonics in the wave vector $\mathbf{k}$. Only the first-degree spherical harmonic terms can be rewritten in form of an effective vector potential $\mathbf{A}_s$ in the Cooperon Hamiltonian. In the present case, e.g., the bulk Dresselhaus SOC consists only of third-degree spherical harmonic terms, which leads to the structure of Eq. (7.6). Owing to the effective vector potential, the minimum of $\hat{H}_\mathcal{C}$ is shifted to finite Cooperon wave vectors $\mathbf{Q}_\mathrm{min}$.

This has important consequences when the Cooperon Hamiltonian is subject to an insulating spin-conserving boundary condition as a result of a finite-size geometry (cf. Sec. 7.2.1). In particular, the component of the effective vector field $\mathbf{A}_s$ which is perpendicular to the surface is removed by a gauge transformation U_A. Thereby, the component of the minimum in direction of the boundary, i.e., $\hat{\mathbf{n}}\cdot\mathbf{Q}_\mathrm{min}$, is shifted to a zero wave vector after the transformation, i.e., $U_A(\hat{\mathbf{n}}\cdot\mathbf{Q}_\mathrm{min})U_A^\dagger = 0$. Since the lowest Cooperon mode typically corresponds to a constant solution in coordinate space, $\langle 0|\hat{\mathbf{n}}\cdot\mathbf{Q}|0\rangle = 0$ holds true and the remaining gauge-transformed (and therefore position-dependent) terms are averaged along the confined directions. This generates a suppression of the spin-relaxation rate in small wires (in zero-mode approximation), which is denoted as motional narrowing as it is observed in the cylindrical wire in this thesis and also earlier in planar quantum

wires [61, 67, 173]. In both cases, the spin relaxation due to first-degree spherical harmonic SOC terms is strongly suppressed for wires of widths much smaller than the spin precession length. A finite relaxation remains, however, due to the third-degree spherical harmonic contributions.

Hence, the effect of motional narrowing is expected to be maximal if the entire effective vector potential $\mathbf{A}_s$ is removed. In fact, such a scenario occurs in wurtzite nanowires grown along the [0001] axis as we will discuss in the next chapter, Chap. 8. Here, the cylindrical nanowire takes an outstanding role as it has a boundary in radial direction for the Cooperon, in contrast to the planar quantum wire that has a boundary along one Cartesian coordinate only.

7.3 Magnetoconductance Correction

7.3.1 Magnetic Dephasing

For experimental probing, we need to take into account the phase breaking due to a magnetic field. Disregarding SOC, the Cooperon propagator $\hat{\mathcal{C}}$ in real space is defined through the diffusion equation [175, 185]

$$\left[\hbar D_e(i\boldsymbol{\nabla} - 2e\mathbf{A}/\hbar)^2 + \hbar/\tau_\phi\right]\hat{\mathcal{C}}(\mathbf{r}-\mathbf{r}') = \delta(\mathbf{r}-\mathbf{r}'), \tag{7.16}$$

with the magnetic vector potential $\mathbf{A}$ and the dephasing rate τ_ϕ. This equation has the general solution

$$\hat{\mathcal{C}}(\mathbf{r}-\mathbf{r}') = \sum_n \Phi_n^*(\mathbf{r}')\Phi_n(\mathbf{r})/(\hbar D_e E_n + \hbar/\tau_\phi), \tag{7.17}$$

where Φ_n solve the eigenvalue equation $(i\boldsymbol{\nabla} - 2e\mathbf{A}/\hbar)^2\Phi_n(\mathbf{r}) = E_n\Phi_n(\mathbf{r})$ with the according eigenenergy E_n. If we choose a gauge such that the vector potential has no component perpendicular to the surface, i.e., $\hat{\mathbf{n}}\cdot\mathbf{A} = 0$, the vector potential does not affect the boundary condition, Eq. (7.7). For small magnetic fields, we can treat the terms $\propto \mathbf{A}$ in the eigenvalue equation perturbatively in zero-mode approximation. Assuming a Coulomb gauge with $\langle 0|\mathbf{A}|0\rangle = 0$, we obtain in lowest order the magnetic phase shift rate as

$$1/\tau_B = D_e\,(2e/\hbar)^2\,\langle 0|\mathbf{A}^2|0\rangle\,, \tag{7.18}$$

where the expectation value is equivalent to the average taken over the sample geometry. The same expression is found by Beenakker *et al.* in Ref. [192].

If a cylindrical nanowire with the surface vector $\hat{\mathbf{n}} = \hat{\boldsymbol{\rho}}$ is placed in a magnetic field perpendicular ($\mathbf{B}_\perp = B\hat{\mathbf{y}}$) or parallel ($\mathbf{B}_\parallel = B\hat{\mathbf{z}}$) to the growth axis $\hat{\mathbf{z}}$, the corresponding vector potentials that fulfill the above-mentioned criteria are $\mathbf{A}_\perp = By\,\hat{\mathbf{z}}$ and $\mathbf{A}_\parallel = B(x\,\hat{\mathbf{y}} - y\,\hat{\mathbf{x}})/2$. Consequently, the respective magnetic phase shift rates become $1/\tau_{B,\perp} = D_e\,(eBR/\hbar)^2$ and $1/\tau_{B,\parallel} = 1/\,(2\tau_{B,\perp})$. Note that here the magnetic field is assumed to be small enough such that the free magnetic length $\widetilde{l}_B = \sqrt{\hbar/(2e|B|)}$ exceeds the wire width [185].

7.3.2 Zero-Mode Magnetoconductance Correction

To support the experimental probing by means of transport measurements, we provide analytical formulas for the magnetoconductance correction $\Delta G(B)$. For cylindrical semiconductor nanowires of length L and radius R, the macroscopic magnetoconductance correction ΔG follows the relation $\Delta G(B) = (\pi R^2/L)\Delta\sigma(B)$. More explicitly, using the groundwork of the preceding sections, we find in zero-mode approximation

$$\Delta G^{(0)}(B) = \frac{2e^2}{h}\frac{1}{L\pi}\int_0^{1/l_e} \mathrm{d}Q_z \left(\frac{1}{Q_z^2 + l_\phi^{-2} + l_B^{-2}} - \sum_{j\in\{0,\pm\}} \frac{1}{E_{T,j}^{(0)}(Q_z) + l_\phi^{-2} + l_B^{-2}} \right), \tag{7.19}$$

with the characteristic length scales $l_i = \sqrt{D_e \tau_i}$ where $i \in \{e, \phi, B\}$. The magnetic dephasing length l_B depends on the orientation of the external magnetic field as shown in the previous section. In diffusive approximation, l_e is the shortest of all length scales. In order to make the effects of the radial boundary relevant the dephasing lengths l_ϕ and l_B should exceed the diameter d of the nanowire.

We stress that the upper cutoff of the integral due to the mean free path l_e, to remove the divergence, is strictly speaking only required in 2D. Neglecting the upper limit $\sqrt{c_e}$ and using the simplified triplet spectrum for $Q_{so}R < 1$, Eqs. (7.13) and (7.14), we obtain the closed-form expression

$$\Delta G^{(0)}(B) = \frac{2e^2}{h}\frac{1}{2L}\left(\frac{1}{\sqrt{l_\phi^{-2} + l_B^{-2}}} - \sum_{j\in\{0,\pm\}} \frac{1}{\sqrt{l_\phi^{-2} + l_B^{-2} + l_{s,j}^{-2}}} \right), \tag{7.20}$$

where $l_{s,j} := \left(E_{T,j,min}^{(0)}\right)^{-1/2}$ is the spin-relaxation length of the j-th long-lived spin state according to the three lowest minima of the triplet spectrum, that are, $E_{T,0,min}^{(0)}/Q_{so}^2 = \Delta_0$ and $E_{T,\pm,min}^{(0)}/Q_{so}^2 = \Delta_1$.

Going beyond zero-mode approximation requires the numerical diagonalization of the full multiband Cooperon (Hamiltonian). As a result, writing down a closed-form expression as in Eq. (7.20) is not possible anymore. Yet, if the wire diameter is small enough and the separation between the modes is much larger than the broadening due to SOC, we might neglect the SOC-induced intermode mixing. In this case, we can simply write

$$\Delta G = \sum_q \Delta G^{(q)}, \tag{7.21}$$

where for each $\Delta G^{(q)}$ the Cooperon (Hamiltonian) is, analogously to the calculation of $\Delta G^{(0)}$, projected on the q-th Cooperon mode, i.e., $\langle q|\hat{H}'_{\mathcal{C}}|q\rangle$ where $|q\rangle = |n, l, Q_z\rangle$ and $n \in \mathbb{N}_0$, $l \in \mathbb{Z}$, and $Q_z \in \mathbb{R}$ as defined in Sec. 7.2.1. The impact of small magnetic fields can be treated by including the corresponding magnetic vector potential $\mathbf{A}$ via minimal coupling in the Cooperon Hamiltonian, i.e., $\mathbf{Q} \to \mathbf{Q} + 2e\mathbf{A}/\hbar$ in Eq. (7.6).

In the following section we apply the developed model to fit magnetoconductance measurements.

7.3.3 Experimental Data Fitting

Exemplarily, we present the fitting results for a heavily n-doped InAs nanowire. As previously shown [59, 68], the electrons in undoped InAs nanowires are confined to a narrow layer beneath the surface due to Fermi level pinning and the transport is governed by surface states. However, a controlled doping allows the electrons to distribute over the entire volume and thereby change the dimensionality and transport topology to that of a quasi-3D channel [54, 59, 68].

The studied sample corresponds to *Device D* of Ref. [59] and possesses the following parameters. Adopting the findings of Ref. [70], the narrow band gap of InAs results in large Rashba and Dresselhaus SOC coefficients $r_{41}^{6c6c} = 117.1\,\text{eÅ}^2$ and $b_{41}^{6c6c} = 27.18\,\text{eVÅ}^3$, respectively. Moreover, the effective mass is given by $m^* = 0.026\,m_0$ where m_0 is the bare electron mass [169]. In line with the experimental setup of Ref. [59], we consider a length of the nanowire of $L = 2.18\,\mu\text{m}$ and a radius of $R = 47.5\,\text{nm}$. Moreover, we use the field-effect mobility $\mu = 600\,\text{cm}^2\text{V}^{-1}\text{s}^{-1}$ and the 3D electron density $n_{3D} = 5 \times 10^{18}\,\text{cm}^{-3}$. The change of the back-gate voltage V_g from 5 V to 60 V yields an increase of the electron density by a factor of 1.5, whereas the mobility is assumed to remain relatively unchanged. By means of the relations $\mu = e\tau_e/m^*$ and $k_F = (3\pi^2 n_{3D})^{1/3}$, we find a mean free path $l_e = v_F\tau_e$ between 21 nm and 24 nm. Accordingly, $\hbar/(E_F\tau_e)$ ranges from 0.14 to 0.18 and therefore the *Ioffe-Regel* criterion is generally well fulfilled.

Fig. 7.3 depicts a gate-induced crossover from positive to negative relative magnetoconductance $\Delta G_R \equiv \Delta G(B) - \Delta G(B = 0)$, which is usually associated with a crossover from WL to WAL. The experiments are performed at a temperature of $T = 4\,\text{K}$ and the magnetic field is oriented perpendicular to the wire axis, i.e., $\tau_B = \tau_{B,\perp}$ (cf. Sec. 7.3.1). In order to average out the superimposed universal conductance oscillations, each magnetoconductance curve represents the mean value of roughly 200 individual measurements in 20 V gate voltage intervals. We fitted Eq. (7.19) by changing the effective Dresselhaus parameter $\alpha_\text{D} = b_{41}^{6c6c}k_F^2$ according to the modifications of the electron density and by adjusting the Rashba parameter α_R, or equivalently the strength of the internal electric field $|\mathcal{E}|$. The resulting electric field increases with the gate voltage from $1.7 \times 10^7\,\text{V/m}$ to $3.1 \times 10^7\,\text{V/m}$. The Rashba and effective Dresselhaus SOC strengths are shown in Fig. 7.4(a). A slight deviation from the typically expected linear V_g-dependence of α_R is attributed to deviations from a homogeneous electric field within the wire. We point out, that the precondition for the zero-mode approximation, $Q_{so}R < 1$, is strictly speaking not perfectly fulfilled for large voltages. More precisely, $Q_{so}R$ ranges from 0.64 to 1.16. However, by comparing the exact diagonalization with the zero-mode approximation, cf. Fig. 7.1, it becomes obvious that the most important characteristics of the spectrum, the minima, are barely changed and the application of the zero-mode approximation is here still justified. Furthermore, using the relation $l_s = \sqrt{D_e\tau_s}$ with

$1/\tau_s \equiv (1/\tau_s)_{\parallel,+}$ as defined in Sec. 7.2.3 (and in the limit $Q_{so}R \ll 1$ in Eq. (7.15)), we can extract the spin-relaxation and dephasing lengths, l_s and l_ϕ, respectively, which are shown in Fig. 7.4(b). At $V_g = 5\,\mathrm{V}$ the spin-relaxation length l_s exceeds the dephasing length l_ϕ, which reflects the observation of WL in Fig. 7.3. Hence, a controlled application of a gate voltage allows to reduce the spin-relaxation length roughly by a factor of 3.

Critical Discussion and Comparison with Previous Results

Hereafter, we follow with a critical discussion and compare our gathered data with previous experiments on similar n-doped InAs nanowire devices [46–49]. In these works, the magnetoconductance data are analyzed by means of a 1D magnetoconductance formula [193], which does not consider the mesoscopic details of the system. In App. 7.B, we use this formula to fit the magnetoconductance data of our device. Aside from the obvious discrepancy between experimental data and theory, it shows disagreements with our findings above.

First, we remark that even for a vanishing back-gate voltage a finite Rashba strength α_R will remain, which was also seen in Refs. [46–49]. We attribute this to the fact that even for zero gate voltage an intrinsic electric field due to Fermi level surface pinning will remain. Aside from that, for small voltages other spin-relaxation mechanisms can become important, above all, the EY mechanism due to the large electron density through doping (cf. Chap. 2). However, we emphasize that the modification of the electron density in our sample alters the EY spin-relaxation rate by a factor of 1.7 [130]. Since we detect an increase of the spin-relaxation rate by a factor of 9.5, it is not possible to explain this behavior within EY theory. Nevertheless, the strength of the extracted Rashba parameter α_R should be treated with caution as it comprises a contribution of additional spin-relaxation rates.

Secondly, although similar transport parameters are found in Refs. [46–49], the variation of the dephasing length l_ϕ with the gate voltage in the according fits is most striking. In most of these works, the dephasing length increases with the gate voltage which is usually justified by a reduced electron-electron interaction through an increase of the electron density. Some authors even observed a decrease of l_ϕ with increasing gate voltage [48] or oscillations [46]. It is most pronounced in Refs. [46, 47, 49], where the dephasing length suddenly changes by about 100 nm near the WL regime. In App. 7.B, we show that the application of the 1D magnetoconductance formula of Ref. [193] to our nanowire device likewise leads to an unusual trend for l_ϕ. This behavior is not seen in our device with our magnetoconductance model, where the dephasing length remains nearly constant. However, we find that in our model an unambiguous fitting of the magnetoconductance curve in the WL regime, in contrast to the WAL regime and opposed to the model in Ref. [193], is barely possible. Note that we could also fit for a lower value of l_ϕ for $V_g = 5\,\mathrm{V}$ which would further increase the spin-relaxation length and diminish the saturation value for α_R. However, as we do not see any indication of a change of l_ϕ in the WAL regime,

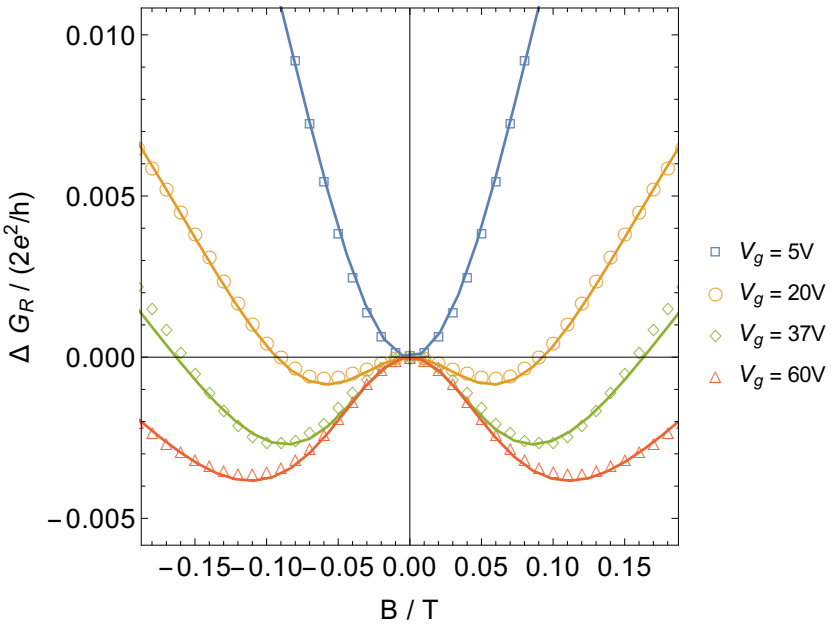

Fig. 7.3: Gate-controlled crossover from positive to negative relative magnetoconductance $\Delta G_R \equiv \Delta G(B) - \Delta G(B = 0)$ in a doped $\langle 111 \rangle$ InAs nanowire. The symbol-dotted lines correspond to experimental data for different back-gate voltages V_g, which are fitted by theory (solid lines) using Eq. (7.19) and varying the Rashba and effective Dresselhaus SOC strengths as shown in Fig. 6.9(a).

we assume that a similar value holds in the WL regime. This finding supports the need of taking into account details on the mesoscopic scale of the nanowire as presented in this paper in order to obtain reliable transport parameters.

Based on our observations, we suggest that for dephasing the electron-electron interaction may be not as effective as previously assumed in a largely doped sample as considered here. This would be in agreement with the findings in disordered 3D metal films [194]. On the other hand, the change of the electron density in our investigated system is possibly too low in order to make a reliable statement. Also, as the extracted dephasing length exceeds the diameter d of the wire, we expect the geometric properties to play an important role in a similar manner as it is the case for the magnetic dephasing. In planar quantum wires with a width smaller than the dephasing length, electron-electron interaction has been identified as the predominant mechanism [195]. For further studies, we propose, therefore, (a) the development of a theoretical description of the inelastic scattering mechanisms as a function of temperature, electron density, and system size for a quasi-3D cylindrical wire and (b) an experimental investigation to see which mechanisms really apply. This would support a reliable parameter fitting in the WL regime and thereby enable a correct determination of the zero gate voltage spin-relaxation processes.

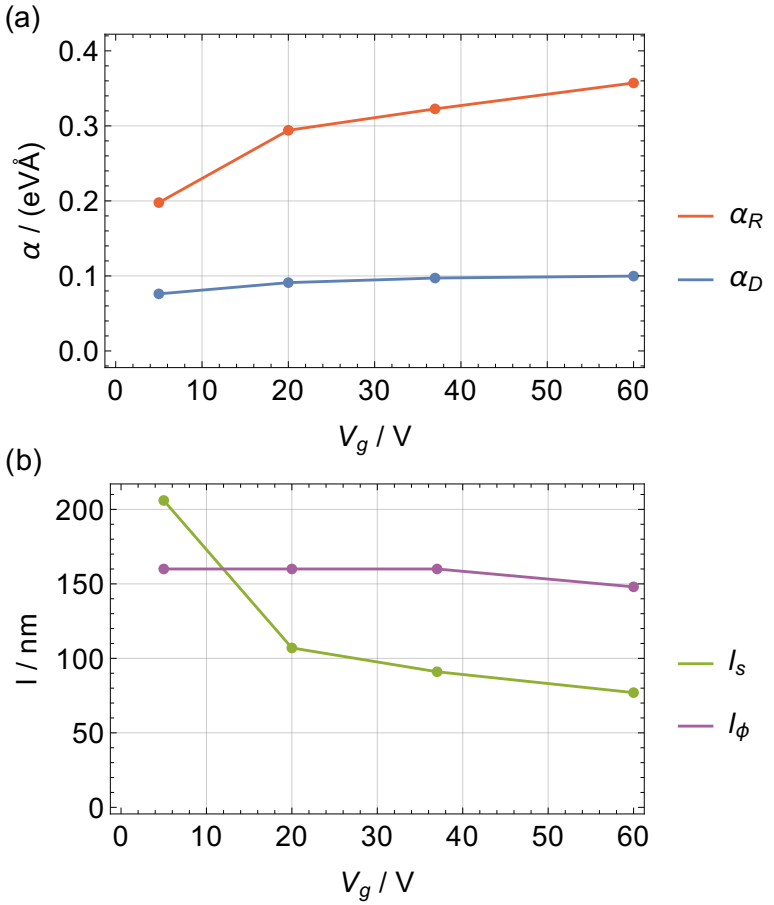

Fig. 7.4: Extracted fitting parameters for a doped ⟨111⟩ InAs nanowire. We show in (a) the Rashba and effective Dresselhaus SOC strength α_{R} and $\alpha_{\mathrm{D}} = b_{41}^{6c6c} k_F^2$, and in (b) the spin-relaxation and dephasing length l_s and l_ϕ, respectively, in dependence of the back-gate voltage V_g.

7.4 Summary and Perspective

We studied the effects of SOC on the quantum conductivity correction for semiconductor nanowires with zinc-blende structure. The spin relaxation due to Dresselhaus SOC is found to be the same for all spin components, independent of the wire growth direction and the wave vector of the spin density, and not affected by a change of the wire radius. Contrarily, in presence of Rashba SOC the relaxation depends on the spin component. A homogeneous spin density that is polarized along the $\hat{\mathbf{x}}$-axis decays according to Eq. (7.15) if the wire radius is smaller than the spin precession length. However, the long-lived spin states have helical structure in real space. Similarly to the planar wire [61], the relaxation due to Rashba SOC is strongly suppressed for small wire widths. Interestingly, a homogeneously excited spin density along the wire axis does not exhibit any dependence on the wire radius

and is therefore not subject to motional narrowing. The derived expressions for the magnetoconductance correction are fitted to the data of magnetoconductance measurements of a heavily doped back-gated InAs nanowire. We find good agreement between theory and experiment and reasonable transport parameters. For comparison, we also apply the 1D magnetoconductance formula of Kurdak *et al.* [193], which has been frequently used by other authors [41–43, 45–49]. The fitted curves show larger deviations from the experimental observations and an unusual trend of the dephasing length.

We stress that the developed model holds for 3D-diffusive nanowires and a crossover to the quasi-ballistic regime is not included. For the latter case, it is plausible to assume that the Dresselhaus spin-relaxation rate will decrease due to the reduction of the number of contributing channels as shown in Ref. [173] for planar wires and in the following chapter for wurtzite nanowires. Additionally, the effects of surface roughness will start to play a noticeable role [188]. It is also to mention that semiconductor nanowires are often polytypic with zinc-blende and wurtzite segments or even pure wurtzite phase, even though the underlying semiconductor material has zinc-blende lattice in the bulk [57, 196]. As the SOC in the wurtzite phase is fundamentally different, distinct characteristics concerning conductivity and spin relaxation can be expected. For this reason, we perform further model calculations in the next chapter, where we take into account the exact wurtzite SOC Hamiltonian.

Appendix 7.A: Zero-Mode Cooperon Hamiltonian

Relevant in experiments is the relaxation process of the spin density **s**. Due to the gauge transformation U_A the eigenstates of the Cooperon Hamiltonian $H_\mathcal{C}$ depend on the position on the cross-section. We can write the triplet sector of the Cooperon Hamiltonian in the basis of the spin density components by reverting the gauge transformation after projecting the transformed Cooperon Hamiltonian on the zero-mode and applying the basis transformation to the triplet sector as defined in App. 3.D. More precisely, the triplet sector of the Cooperon Hamiltonian in the basis of the spin density components $\{s_x, s_y, s_z\}$ reads in terms of Q_{so}^2 as

$$\begin{pmatrix} a & d & e \\ d^* & b & f \\ e^* & f^* & c \end{pmatrix}, \tag{7.A.1}$$

where

$$\begin{aligned} a &= c - \frac{1}{2} + \frac{1}{2}(a_{so} - 1)\cos(2Q_{so}x), \\ b &= c - \frac{1}{2} - \frac{1}{2}(a_{so} - 1)\cos(2Q_{so}x), \\ c &= \mathcal{Q}_z^2 + \lambda_\mathrm{D} + 1, \\ d &= -\frac{1}{2}(a_{so} - 1)\sin(2Q_{so}x), \\ e &= -2i\mathcal{Q}_z(b_{so} - 1)\sin(2Q_{so}x), \\ f &= -2i\mathcal{Q}_z(b_{so} - 1)\cos(2Q_{so}x). \end{aligned} \tag{7.A.2}$$

Notably, for $\mathcal{Q}_z = 0$ the s_z component is decoupled and independent of the location on the wire cross-section and the wire radius. Consequently, a spin density which is homogeneously polarized along the wire axis is not subject to motional narrowing in zero-mode approximation.

Appendix 7.B: Experimental Data Fitting with Kurdak *et al.*'s Formula

Here, we demonstrate the application of the 1D magnetoconductance formula of Kurdak *et al.*, Ref. [193], to the nanowire device discussed in Sec. 7.3.3. This model is frequently used for the theoretical analysis of semiconductor nanowire devices [41–43, 45–49]. In case of a diffusive wire of length L, the magnetoconductance correction reads as

$$\Delta G(B) = \frac{2e^2}{h}\frac{1}{2L}\left[3\left(\frac{1}{l_\phi^2} + \frac{4}{3l_s^2} + \frac{1}{l_B^2}\right)^{-1/2} - \left(\frac{1}{l_\phi^2} + \frac{1}{l_B^2}\right)^{-1/2}\right], \tag{7.B.3}$$

with the dephasing, spin-relaxation, magnetic dephasing length, l_ϕ, l_s, and l_B, respectively. For the magnetic dephasing length, we used our relation for a perpendicular magnetic field, that is, $l_B = \sqrt{D_e \tau_{B,\perp}}$ as derived in Sec. 7.3.1 which is more appropriate for a cylindrical wire. Note that compared to the definition in Refs. [192, 197], here also $l_B \propto |B|^{-1}$ holds true. In Fig. 7.5 we show the relative magnetoconductance correction $G_R = \Delta G(B) - \Delta G(0)$ and the accordingly obtained fitting parameters. Remarkably, in strong contradiction to the observations using our model, cf. Sec. 7.3.3, the extracted dephasing length shows a monotonous decrease with the gate voltage which is rather unphysical. Also, the spin-relaxation length is nearly twice as large for small gate voltages. Aside from that, a strong discrepancy between the experimental data and theory in the WAL regime is obvious. As a consequence of these observations, we suggest that a more appropriate model should be used.

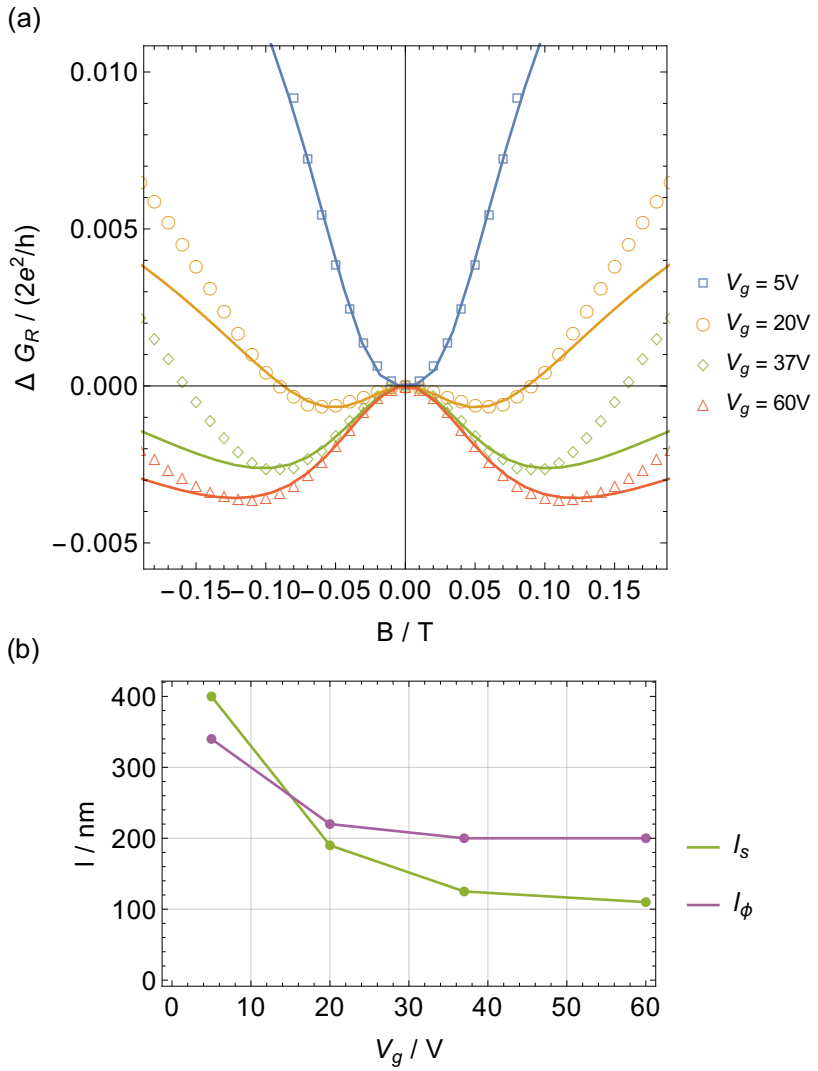

Fig. 7.5: (a) Gate-controlled crossover from positive to negative relative magnetoconductance $\Delta G_R \equiv \Delta G(B) - \Delta G(B = 0)$ in a doped $\langle 111 \rangle$ InAs nanowire. The symbol-dotted lines correspond to experimental data for different back-gate voltages V_g, which are fitted by the 1D magnetoconductance formula of Kurdak *et al.* [193] (solid lines), and adjusting the dephasing and spin-relaxation lengths, l_ϕ and l_s, as shown in (b).

CHAPTER 8

Cylindrical 3D-Diffusive Wurtzite Nanowires

Nanowires built of non-nitride III-V semiconductor materials are often found in wurtzite phase even if the underlying material has zinc-blende structure in the bulk [198–205]. As this allows for the utilization of materials with large SOC such as InSb, GaSb, or InAs and SOC effects are generally more prominent in wurtzite systems due to their reduced symmetry, these systems are particularly attractive for spintronics [206]. Motivated by this, we theoretically investigate the DP spin-relaxation properties in wurtzite semiconductor nanowires and their impact on the quantum correction to the conductivity. Analogously to the previous chapter, the nanowires are considered diffusive in three spatial directions and of cylindrical shape. Although the lifetime of the long-lived spin states is limited by the dominant k-linear spin-orbit contributions in the bulk, these terms show almost no effect in the finite-size nanowires. Here, the spin lifetime is essentially determined by the small k-cubic spin-orbit terms and nearly independent of the wire radius. At the same time, these states possess in general a complex helical structure in real space that is modulated by the spin precession length induced by the k-linear terms. For this reason, the experimentally detected spin relaxation largely depends on the ratio between the nanowire radius and the spin precession length as well as the type of measurement (cf. Fig. 8.1). In particular, it is shown that while a variation of the radius hardly affects the magnetoconductance correction, which is governed by the long-lived spin states, the change in the spin lifetime observed in optical experiments can be dramatic. We compare our results with recent experimental studies on wurtzite InAs nanowires.

8.1 Theoretical Groundwork

8.1.1 Electrons in the Wurtzite Lattice

The bulk electrons in the Γ_{7c} conduction band of a wurtzite type semiconductor with SOC are described by the Hamiltonian

$$\mathcal{H} = \frac{\hbar^2 k^2}{2m^*} + \mathcal{H}_{\mathrm{so}}^{\mathrm{ext}} + \mathcal{H}_{\mathrm{so}}^{\mathrm{int}}. \tag{8.1}$$

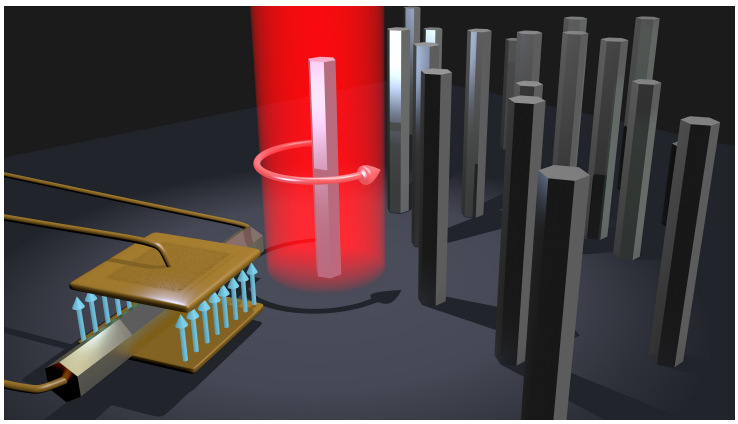

Fig. 8.1: Illustration of the two experimental techniques that can lead to very dissimilar results for the spin lifetime (cf. Secs. 8.2.2 and 8.2.3). While probing the magnetoconductance (left) under influence of a gate-induced electric field determines the lifetime of the long-lived helical spin states, micro-photoluminescence measurements [189] (center) follow the relaxation process of a homogeneous spin density which is excited by circularly polarized light.

The terms

$$\mathcal{H}_{\mathrm{so}}^{\mathrm{ext}} = \alpha_{\mathrm{R}}^{\mathrm{ext}}(k_x\sigma_z - k_z\sigma_x), \tag{8.2}$$

$$\mathcal{H}_{\mathrm{so}}^{\mathrm{int}} = \left[\gamma_{\mathrm{R}}^{\mathrm{int}} + \gamma_{\mathrm{D}}\left(bk_z^2 - k_\perp^2\right)\right](k_y\sigma_x - k_x\sigma_y), \tag{8.3}$$

with $k_\perp^2 = k_x^2 + k_y^2$ and $\alpha_{\mathrm{R}}^{\mathrm{ext}} = \gamma_{\mathrm{R}}^{\mathrm{ext}}\mathcal{E}$ denote the extrinsic (ext) and intrinsic (int) Rashba (R) and the Dresselhaus (D) SOC contributions with the material specific parameters $\gamma_{\mathrm{R}}^{\mathrm{int}}, \gamma_{\mathrm{R}}^{\mathrm{ext}}, \gamma_{\mathrm{D}}$, and b, the electric field strength $\mathcal{E}$, and the effective electron mass m^*, which is here considered isotropic [101, 104, 207]. In this notation, the $\hat{\mathbf{z}}$-axis corresponds to the [0001] crystal axis (c-axis). As in the previous chapter for zinc-blende systems, we assume that the electrons in the wire experience a nearly homogeneous electric field perpendicular to the wire axis. Without loss of generality, it is aligned with the system's $\hat{\mathbf{y}}$-axis, i.e., $\boldsymbol{\mathcal{E}} = \mathcal{E}\hat{\mathbf{y}}$, and results in the external Rashba contribution $\mathcal{H}_{\mathrm{so}}^{\mathrm{ext}}$.

8.1.2 3D Cooperon and the Radial Boundary

Since the following analysis is completely analogous to the study of the 3D-diffusive zinc-blende nanowires, we adopt the respective definitions and preconditions given in Chap. 7. Equivalently to Sec. 7.1.2, the 3D Cooperon propagator $\hat{\mathcal{C}}$ can be written as

$$\hat{\mathcal{C}}(\mathbf{Q}) = \frac{\tau_e}{\hbar}\left(1 - \int \frac{\mathrm{d}\Omega}{4\pi}\frac{1}{1 - i\tau_e\hat{\Sigma}(\mathbf{Q})/\hbar}\right)^{-1}, \tag{8.4}$$

where $\hat{\Sigma}(\mathbf{Q}) \approx -\mathbf{v}_F(\hbar\mathbf{Q} + 2m^*\hat{\mathbf{a}}\mathbf{S})$. Here, the matrix $\hat{\mathbf{a}}$ comprises the intrinsic and extrinsic SOC contributions resulting from the electric field and the inversion

asymmetry of the wurtzite lattice, i.e.,

$$\hat{\mathbf{a}} = \begin{pmatrix} 0 & -a_{\text{int}} & a_{\text{ext}} \\ a_{\text{int}} & 0 & 0 \\ -a_{\text{ext}} & 0 & 0 \end{pmatrix}, \tag{8.5}$$

with

$$a_{\text{ext}} = \alpha_{\text{R}}^{\text{ext}}/\hbar, \quad a_{\text{int}} = \left[\gamma_{\text{R}}^{\text{int}} + \gamma_{\text{D}}\left(bk_z^2 - k_\perp^2\right)\right]/\hbar.$$

For reasons of expediency and in accordance with previous chapters, we focus hereafter on the Cooperon Hamiltonian $\hat{H}_{\mathcal{C}} = (\hbar D_e \hat{\mathcal{C}})^{-1}$. A Taylor expansion of the integrand in Eq. (8.4) to second order in $(\hbar\mathbf{Q} + 2m^*\hat{\mathbf{a}}\mathbf{S})$, yields

$$\hat{H}_{\mathcal{C}} = \left[\mathbf{Q} + 2e\mathbf{A}_s/\hbar\right]^2 + \Delta_s. \tag{8.6}$$

The effect of SOC becomes manifest in two different ways which origins from the distinct spherical harmonic decomposition of the SOC contributions in the wave vector $\mathbf{k}$. (i) The SOC terms due to the first-degree spherical harmonics in the wave vector $\mathbf{k}$ lead to an effective vector potential $\mathbf{A}_s = \mathbf{A}_s^{\text{ext}} + \mathbf{A}_s^{\text{int}}$, where

$$\mathbf{A}_s^{\text{ext}} = \alpha_{\text{R}}^{\text{ext}} m^*/(e\hbar)(S_z, 0, -S_x)^\top, \tag{8.7}$$

$$\mathbf{A}_s^{\text{int}} = \left[\gamma_R^{\text{int}} + \delta_D^{(1)}\right] m^*/(e\hbar)(-S_y, S_x, 0)^\top, \tag{8.8}$$

with $\delta_D^{(1)} = (b-4)\gamma_D k_F^2/5$, and therefore couples to the Cooperon momentum. (ii) In addition, we find an intrinsic spin-relaxation term $\Delta_s = \delta_D^{(3)}(S_x^2 + S_y^2)$, where

$$\delta_D^{(3)} = \frac{32}{175}\left((1+b)\gamma_D m^* k_F^2/\hbar^2\right)^2, \tag{8.9}$$

which is a result of the third-degree spherical harmonics in the Dresselhaus field and is independent of the Cooperon momentum. The decomposition of the intrinsic SOC Hamiltonian $\mathcal{H}_{\text{so}}^{\text{int}}$, Eq. (8.3), in terms of spherical harmonics is demonstrated in the App. 8.A. Notably, in the analogous zinc-blende system the intrinsic SOC contains only third-degree spherical harmonic terms and does not give rise to an effective vector potential but solely leads to a contribution Δ_s that is diagonal in the triplet basis (cf. Eq. (7.6)).

The minima of the triplet eigenmodes $E_{T,j}$ are direct measures of the spin-relaxation rate $(1/\tau_s)_j$ of a certain polarized spin density $\mathbf{s}$ via the relation $(1/\tau_s)_j = D_e E_{T,j}$. For this reason, the minima of the spectrum are of particular interest as they allow to identify long-lived spin density states. In contrast to the term Δ_s in case (ii), the effective vector potential $\mathbf{A}_s$ is capable of shifting the global minimum of an eigenvalue to finite wave vectors $\mathbf{Q}$ and thereby giving rise to helical spin states with longer spin lifetimes than the homogeneous counterpart ($Q_z = 0$). Moreover, the SOC-induced vector potential $\mathbf{A}_s$ plays a crucial role in case of a boundary condition for the Cooperon.

As shown in Sec. 7.2.1, the finite-size geometry of the nanowire requires a radial boundary condition for the Cooperon, that is,

$$\hat{\boldsymbol{\rho}} \cdot (\boldsymbol{\nabla} + 2ie\mathbf{A}_s/\hbar)\, \hat{\mathcal{C}}|_{\rho=R} = 0. \tag{8.10}$$

The boundary condition for the Cooperon gives rise to a multisubband system. Without SOC each subband is fourfold spin degenerate. In presence of SOC, each Cooperon subband splits into one singlet and three triplet bands, which are in general non-degenerate. We can simplify above equation to a Neumann boundary condition, i.e., $\hat{\boldsymbol{\rho}} \cdot (\boldsymbol{\nabla}\hat{\mathcal{C}}')|_{\rho=R} = 0$, by performing a gauge transformation of the Cooperon (and simultaneously the Cooperon Hamiltonian), that is, $\hat{\mathcal{C}} \to \hat{\mathcal{C}}' = U_A \hat{\mathcal{C}} U_A^\dagger$, with the unitary transformation operator $U_A = \exp[i2e\,(\hat{\boldsymbol{\rho}} \cdot \mathbf{A}_s)\rho/\hbar]$. The transformed Cooperon Hamiltonian $\hat{H}'_{\mathcal{C}}$ can then be diagonalized using the basis given in Eq. (7.9) which fulfills the Neumann boundary condition. An approximative solution that allows to obtain analytical expressions can be found by projecting the $\hat{H}'_{\mathcal{C}}$ on the lowest subband $|0\rangle$ named *zero-mode*. The zero-mode represents the spin states with the longest spin lifetime and gives rise to the dominant conductance correction.

As a downside of the mutual interplay of intrinsic and extrinsic SOC effects, the transformed Cooperon Hamiltonian $\hat{H}'_{\mathcal{C}}$ has an ample and complex structure. Dealing with the resulting symbolic expressions is a delicate task and we shall discuss only specific situations analytically. In the following section, we focus only on the intrinsic SOC.

8.2 Intrinsic Spin Relaxation

The dynamics of a local spin density $\mathbf{s} = \mathbf{s}(\mathbf{r}, t)$ follows the spin diffusion equation (cf. Ref. [67] and Eq. (2.4))

$$0 = \partial_t\, \mathbf{s} + D_e \hat{H}_{\mathrm{SD}}\, \mathbf{s}. \tag{8.11}$$

An initial spin density $\mathbf{s}_0$ evolves in time as $\mathbf{s}_t = \exp(-D_e \hat{H}_{\mathrm{SD}} t)\, \mathbf{s}_0$. The spin diffusion Hamiltonian $\hat{H}_{\mathrm{SD}}$ is related to the Cooperon Hamiltonian $\hat{H}_{\mathcal{C}}$ via the unitary transformation $\hat{H}_{\mathrm{SD}} = U_{cd}^\dagger \hat{H}_{\mathcal{C}} U_{cd}$, where U_{cd} is defined in App. 3.D. Consequently, by analyzing the Cooperon Hamiltonian we can study the temporal and spatial evolution of a spin density. In the following subsections, we omit the effects of a lateral gate electrode, i.e., $\alpha_{\mathrm{R}}^{\mathrm{ext}} = 0$.

8.2.1 Spin Relaxation in the Bulk

In the bulk, the Cooperon Hamiltonian $\hat{H}_{\mathcal{C}}$, Eq. (8.6), can be diagonalized in the basis of plane waves $\langle \mathbf{r}|\mathbf{Q}\rangle \propto \exp(i\mathbf{Q}\cdot\mathbf{r})$ with the continuous wave vectors Q_i. Then, the eigenvalues read as

$$E_S = \mathbf{Q}^2, \tag{8.12}$$

$$E_{T,\pm} = \mathbf{Q}^2 + \frac{3}{2}\left(Q_{so}^2 + \delta_D^{(3)}\right) \pm \frac{1}{2}\sqrt{16Q_\perp^2 Q_{so}^2 + \left(Q_{so}^2 + \delta_D^{(3)}\right)^2}, \tag{8.13}$$

$$E_{T,0} = \mathbf{Q}^2 + Q_{so}^2 + \delta_D^{(3)}, \tag{8.14}$$

where $Q_\perp^2 = Q_x^2 + Q_y^2$ and $Q_{so} = 2m(\gamma_R^{\text{int}} + \delta_D^{(1)})/\hbar^2 = 2\pi/L_{so}$, where L_{so} denotes the spin precession length due to the intrinsic SOC. Consequently, the spin-relaxation rates for homogeneously polarized spin densities, i.e., $\mathbf{Q} = \mathbf{0}$, are

$$\left(\tau_s^{-1}\right)_\perp^{\text{hom}} = \left(\tau_s^{-1}\right)_z^{\text{hom}}/2 = D_e(Q_{so}^2 + \delta_D^{(3)}), \tag{8.15}$$

where the z-polarized densities decay twice as fast as the states in the x-y-plane ($\perp$). Yet, for $\delta_D^{(3)} < 3Q_{so}^2$ (which is usually fulfilled) the spin densities with the longest spin lifetime are homogeneous along the c-axis but have helical structure in the x-y-plane. Their spin decays according to $(1/\tau_s)^{\text{helix}} = D_e E_{T,-}(Q_\perp = Q_0, Q_z = 0)$, that is,

$$\left(\frac{1}{\tau_s}\right)^{\text{helix}} = D_e\left[\frac{7}{16}Q_{so}^2 + \frac{11}{8}\delta_D^{(3)} - \frac{1}{16}\left(\frac{\delta_D^{(3)}}{Q_{so}}\right)^2\right], \tag{8.16}$$

at the finite wave vectors perpendicular to the c-axis

$$Q_0 = \frac{1}{4}\sqrt{15Q_{so}^2 - 2\delta_D^{(3)} - \left(\frac{\delta_D^{(3)}}{Q_{so}}\right)^2}. \tag{8.17}$$

Disregarding the typically small cubic SOC term $\propto \delta_D^{(3)}$, the relaxation rate is about half as large as for the homogeneous long-lived state. We can identify the corresponding helical spin density as

$$\mathbf{s}(\mathbf{r}, t) \propto \left[\frac{\mathbf{q}}{\|\mathbf{q}\|}\Sigma\cos(\mathbf{q}\cdot\mathbf{r}) + \hat{\boldsymbol{z}}\sin(\mathbf{q}\cdot\mathbf{r})\right]\exp\left(-t/\tau_s^{\text{helix}}\right) \tag{8.18}$$

with $\Sigma \approx (15Q_{so}^2 + 4\delta_D^{(3)})/(3\sqrt{15}Q_{so}^2)$ to lowest non-vanishing order in $\delta_D^{(3)}$. The wave vector $\mathbf{q}$ lies in the x-y-plane and has the length $\|\mathbf{q}\| = Q_0$. For $\delta_D^{(3)} \to 0$ the solutions coincide with the result for the 2D Rashba system as discussed in Refs. [64, 67, 208].

8.2.2 Spin Dynamics in the Nanowire

As described in Sec. 8.1.2 (or in greater detail in Sec. 7.2.1 for zinc-blende wires), in order to simplify the boundary condition, required by the finite-size geometry of the wire, we apply a gauge transformation to the Cooperon Hamiltonian. The transformed Cooperon Hamiltonian $\hat{H}'_{\mathcal{C}}$ is found as

$$\hat{H}'_{\mathcal{C}} = \boldsymbol{Q}^2 + \frac{\delta_D^{(3)}}{4}\Big\{3\mathbf{S}^2 - S_z^2 - \frac{1}{2}(S_+^2 e^{-2i\phi} + S_-^2 e^{2i\phi})$$

$$+\left[\mathbf{S}^2-3S_z^2+\frac{1}{2}(S_+^2e^{-2i\phi}+S_-^2e^{2i\phi})\right]\cos(2Q_{so}\rho)$$

$$-2\Big[\{S_x,S_z\}\cos(\phi)+\{S_y,S_z\}\sin(\phi)\Big]\sin(2Q_{so}\rho)\Big\} \tag{8.19}$$

with $S_\pm = S_x \pm iS_y$. We stress that the gauge transformation removes the effective vector potential $\mathbf{A}_s^{\text{int}}$ completely and only quadratic wave vectors $\mathbf{Q}^2$ remain. As in the bulk, the global minimum with respect to the wave vector Q_z of the spectrum is found at $Q_z = 0$.

Long-Lived Spin States and Diffusive-Ballistic Crossover

An analytical result for the lowest eigenvalues can be obtained by evaluating the transformed Cooperon Hamiltonian in *zero-mode approximation*, i.e., $\langle 0|\hat{H}'_{\mathcal{C}}|0\rangle$. The boundary-induced shift of the first excited mode is of the order of $\langle 1,0,0|Q_\perp^2|1,0,0\rangle \propto R^{-2}$. On the other hand, the spin-orbit broadening within each mode is of the order of $\delta_D^{(3)}$. Consequently, we can estimate the zero-mode to be well separated if $\delta_D^{(3)}R^2 \ll 1$ holds. Under these circumstances, the eigenvalues of $\langle 0|\hat{H}'_{\mathcal{C}}|0\rangle$ read as

$$E_S^{(0)} = Q_z^2, \tag{8.20}$$

$$E_{T,\pm}^{(0)} = Q_z^2 + \delta_D^{(3)}\left(\frac{5}{4}+\frac{a_{so}}{2}\right), \tag{8.21}$$

$$E_{T,0}^{(0)} = Q_z^2 + \delta_D^{(3)}\left(\frac{3}{2}-a_{so}\right), \tag{8.22}$$

where we introduced

$$a_{so} = \left[1-\cos(2R_{so})-2R_{so}\sin(2R_{so})\right]/(2R_{so})^2, \tag{8.23}$$

and $R_{so} = Q_{so}R$. Asymptotically, we obtain $a_{so} \to -1/2$ for $R_{so} \to 0$ and $a_{so} \to 0$ for $R_{so} \to \infty$.

We focus again on the long-lived spin states, which are found for a homogeneous spin polarization along the c-axis, i.e., $Q_z = 0$. The eigenvalues are displayed in Fig. 8.2 in dependence of R_{so}. Besides the slight increase (decrease) of the eigenvalue $E_{T,\pm}^{(0)}$ ($E_{T,0}^{(0)}$) for small R_{so}, the eigenvalues show R_{so}-periodic oscillations with decreasing amplitude. We emphasize that the amplitudes depend solely on the term $\delta_D^{(3)}$, which is usually small compared to Q_{so}^2. Hence, the resulting spin-relaxation rates show very little dependence on the thickness of the nanowire. Since these rates enter the leading-order conductance correction, the latter will be hardly affected by any changes in the nanowire radius either. Owing to the gauge transformation, the according eigenvectors of $H_{\mathcal{C}}$ are position-dependent in the cross-sectional plane. More precisely, the (unnormalized) eigenvectors $\mathbf{a}_j$, which are associated with the triplet eigenvalues $E_{T,j}^{(0)}$ in Eqs. (8.21) and (8.22) for $Q_z = 0$, take the form

$$\mathbf{a}_+ = (\cos(\phi), \sin(\phi), -\tan(Q_{so}\rho))^\top, \tag{8.24}$$

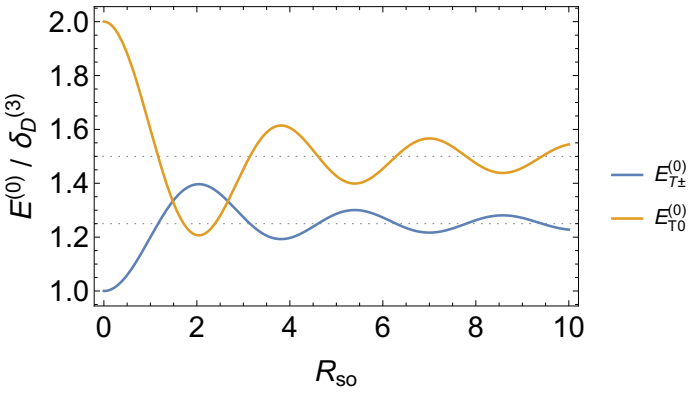

Fig. 8.2: Lowest eigenvalues of the Cooperon Hamiltonian for $Q_z = 0$ in zero-mode-approximation in dependence of the dimensionless radius R_{so} and in absence of external electric fields, i.e., $\alpha_{\mathrm{R}}^{\mathrm{ext}} = 0$.

$$\mathbf{a}_- = (-\sin(\phi), \cos(\phi), 0)^\top, \tag{8.25}$$

$$\mathbf{a}_0 = (\cos(\phi)\tan(Q_{so}\rho), \sin(\phi)\tan(Q_{so}\rho), 1)^\top, \tag{8.26}$$

in the basis of spin density components $\{s_x, s_y, s_z\}$. The eigenvectors $\mathbf{a}_\pm$ are not uniquely defined as the corresponding eigenvalues are degenerate.

In the *1D-diffusive* limit, i.e., $R_{so} \ll 1$, we can write $\mathbf{a}_+ = \hat{\boldsymbol{\rho}}$, $\mathbf{a}_- = \hat{\boldsymbol{\phi}}$, and $\mathbf{a}_0 = \hat{\mathbf{z}}$ since $Q_{so}\rho \leq R_{so}$. We stress that for $R_{so} \to 0$ the corresponding eigenvalues are identical to the ones resulting from bulk spin-relaxation term Δ_s in Eq. (8.6) giving rise to the spin-relaxation rates in Eq. (8.15) for $Q_{so} = 0$, i.e.,

$$\left(\tau_s^{-1}\right)_\perp^{\mathrm{1D}} = \left(\tau_s^{-1}\right)_z^{\mathrm{1D}} /2 = D_e \delta_D^{(3)}. \tag{8.27}$$

The equivalent result is obtained by considering only the DP spin-relaxation tensor, Eq. (2.2), for the bulk system and taking only into account the Dresselhaus contribution due to the higher spherical harmonics $(\mathcal{H}_{\mathrm{so}}^{\mathrm{int}})_{(3)}$ (cf. App. 8.A). Hence, the spin relaxation resulting from the first-degree spherical harmonic contribution $(\mathcal{H}_{\mathrm{so}}^{\mathrm{int}})_{(1)}$ is absent for $R_{so} \to 0$. As for small densities the k-linear contribution, which is comprised in $(\mathcal{H}_{\mathrm{so}}^{\mathrm{int}})_{(1)}$, is expected to be dominant, the spin lifetime is significantly enhanced in wires with small radii. Aside from that, it is to mention that for third-degree spherical harmonic SOC terms the mean free scattering time τ_e is lowered to τ_e/u, where $1 \leq u \leq 9$ depending on the type of scattering process, e.g., $u = 1$ for isotropic and $u = 9$ for small-angle scattering [104, 146]. This can further reduce the spin-relaxation rate of the long-lived spin states in the nanowire. The impact on the bulk spin-relaxation rate, e.g., Eqs. (8.15) and (8.16), is less important due to the dominance of the spin-relaxation rate resulting from k-linear SOC terms.

At last, we discuss the *diffusive-ballistic transition* regime, in which the nanowire radius is not only much smaller than the spin precession length but also

of the order of the mean free path l_e, i.e., $R_{so} \ll 1 \wedge R/l_e \sim 1$. As shown in Ref. [173], the number of the conducting channels decreases with the reduction of the wire width. This leads to a suppression of the cubic SOC terms $(\mathcal{H}_{\rm so}^{\rm int})_{(3)}$, which are responsible for the spin-relaxation rate for $R_{so} \ll 1$. We can account for the diffusive-ballistic crossover by replacing the integral over the Fermi surface in Eq. (8.4) by a sum over all modes as shown in detail in App. 8.B. For simplicity, we treat the size-quantization according to a square wire along $\hat{\mathbf{z}}$ with side lengths W and hard-wall boundaries. Consequently, two quantum numbers occur, which are labeled by n and p with $n, p \in [1, N]$ where N denotes the maximum quantum number. In Fig. 8.3, we show how the parameter $\delta_D^{(3)}$ decreases to $\xi\delta_D^{(3)}$ due to the reduction of contributing modes via the wire side length W or maximum quantum number N. The decay can be well fitted with $\xi \propto \ln(k_F W)$.

We stress that in the diffusive-ballistic crossover regime the above modifications are plausible and explain further decrease of the spin-relaxation rate. However, in the pure transversal ballistic regime, the subband structure of the system is fully resolved, which has dramatic consequences on the DP spin-relaxation mechanism. Owing to k_z-mirror symmetry of the Hamiltonian of the wurtzite nanowires, the spin degeneracy is *not* lifted along the crystal c-axis. As a consequence, there is obviously no spin-rotation about a spin-orbit induced effective magnetic field (spin-orbit field) and hence no DP spin relaxation. This is a remarkable difference to, e.g., the transversal ballistic planar quantum wires with Rashba SOC. In a strictly one-dimensional limit, there are two kinds of persistent spin states, that is, (a) a homogeneous spin density which is polarized along the (uni-directional) spin-orbit field and (b) the persistent spin helix perpendicular to it [116]. In Ref. [209] it is shown that in the multisubband Rashba wire the persistent spin helix disappears. Responsible for this are inter-subband transitions which lead to a non-commutativity of the time-evolution operator $U(k_z)$ for reversed paths along the channel, i.e., $[U(k_z), U(-k_z)] \neq 0$. In a multisubband wurtzite nanowire the commutativity is trivially given since $U(k_z) = U(-k_z)$.

Decay of a Homogeneous Spin Density

Optical spin injection in semiconductor nanowires typically generates collective spin excitations, that are polarized along the wire axis and homogeneously distributed throughout the entire volume [189]. In general, such spin densities do not constitute eigenstates of the spin diffusion/Cooperon Hamiltonian and one has to solve the respective initial value problem.

Regarding this, we can set $Q_z = 0$ and only focus on the dynamics in the cross-sectional plane ($\perp$). Then the initial spin density $\mathbf{s}_0$ at the time $t = 0$ is defined as

$$\mathbf{s}_0(\mathbf{r}) = \hat{\mathbf{z}}\,\Theta(R-\rho)/(\pi R^2), \tag{8.28}$$

where Θ denotes the Heaviside function and the total average spin

$$\boldsymbol{\mathcal{S}}(t) = \int \mathrm{d}^2 r_\perp\, \mathbf{s}(\mathbf{r}, t) \tag{8.29}$$

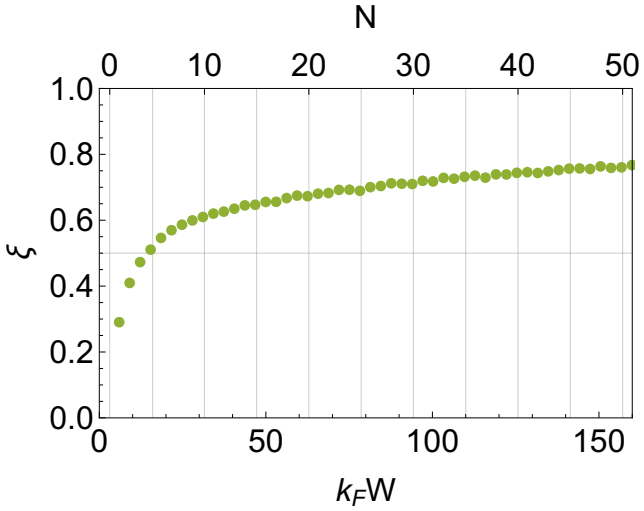

Fig. 8.3: Factor of reduction ξ of the spin-relaxation contribution due to diffusive-ballistic crossover, i.e., $\delta_D^{(3)} \to \xi\delta_D^{(3)}$, in dependence of $k_F W$ or the maximal quantum number N.

is normalized at $t = 0$ with respect to the cross-sectional plane, i.e., $\|\boldsymbol{\mathcal{S}}(0)\| = 1$. The temporal and spatial evolution of the spin density according to Eq. (8.11) yields

$$\mathbf{s}(\mathbf{r}, t) = U_{cd}^{\dagger} U_A^{\dagger} \exp(-D_e \hat{H}'_{\mathcal{C}} t) \cdot \mathbf{s}'_0, \tag{8.30}$$

where $\mathbf{s}'_0 = U_A U_{cd} \mathbf{s}_0$ or explicitly

$$\mathbf{s}'_0(\mathbf{r}) = \frac{\Theta(R-\rho)}{\pi R^2} \left[\frac{\sin(Q_{so}\rho)}{\sqrt{2}} \left(e^{i\phi} \left|1,-1\right\rangle - e^{-i\phi} \left|1,1\right\rangle \right) + \cos(Q_{so}\rho) \left|1,0\right\rangle \right], \tag{8.31}$$

represents the initial state in the singlet-triplet basis in the gauge-transformed system. It is practical, to expand $\mathbf{s}'_0$ in the basis $\langle \mathbf{r}|n,l,Q_z=0\rangle$, Eq. (7.9), that fulfills the Neumann boundary condition of $\hat{H}'_{\mathcal{C}}$. Apparently, the deviation of the initial state from the zero-mode $\langle \mathbf{r}|0\rangle$, which is constant in real space, becomes stronger with increasing values of R_{so}. As a consequence, the inclusion of higher modes and thereby larger spin-relaxation rates in the expansion becomes more relevant. In absence of the SOC terms in $\hat{H}'_{\mathcal{C}}$ the functions $\langle \mathbf{r}|n,l,0\rangle$ constitute the eigenbasis. Hence, we can estimate the boundary-induced spin-relaxation rates by $(1/\tau_s)_{n,|l|} := D_e \langle n,l,0|Q_\perp^2|n,l,0\rangle = D_e(\zeta_{n,|l|}/R)^2$. This has a significant impact on the total spin-relaxation rate even for small values of R_{so}.

In Fig. 8.4, we display the numerically computed total spin-relaxation rate $(1/\tau_s)_z$ in terms of the 1D-diffusive rate $(1/\tau_s)_z^{1D}$, Eq. (8.27), in dependence of R_{so} and for different ratios of $Q_{so}^2/\delta_D^{(3)}$. The rate $(1/\tau_s)_z$ is defined by the time, after which the z-component of the total spin is decayed to the factor $\mathcal{S}_z(t)/\mathcal{S}_z(0) = e^{-1}$

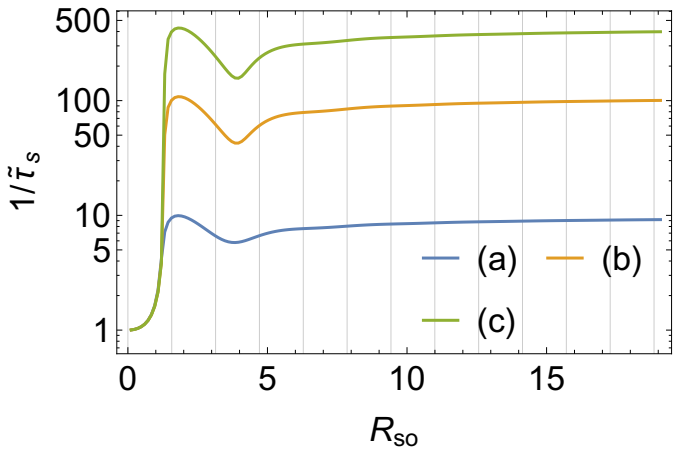

Fig. 8.4: Total spin-relaxation rate in terms of the 1D-diffusive rate, i.e., $1/\tilde{\tau}_s := (\tau_s)_z^{1D}/(\tau_s)_z$, for a homogeneously z-polarized spin density in dependence of the radius R_{so} for (a) $Q_{so}^2 = 18\,\delta_D^{(3)}$, (b) $Q_{so}^2 = 220\,\delta_D^{(3)}$, and (c) $Q_{so}^2 = 880\,\delta_D^{(3)}$.

of its initial value. Notice that, here a single-exponential fit is not necessarily reliable for the extraction of the spin-relaxation rate since a single-exponential decay is only given for an eigenstate. Most striking is the massive increase of the spin-relaxation rate for small values of R_{so}. The peak in the relaxation rate occurs almost precisely at $R_{so} = \pi/2$. We can understand this behavior by noting that for $R_{so} = \pi/2$ the $|1, \pm 1\rangle$-components of $\mathbf{s}_0'$ can be well represented by the basis functions $\langle \mathbf{r}|n = 1, l = \mp 1, 0\rangle$. The respective boundary-induced relaxation rate is given by $(1/\tau_s)_{1,|1|} = D_e(2\zeta_{1,1}/\pi)^2 Q_{so}^2$, which is remarkably of the order of magnitude of the *bulk* spin-relaxation rate. Similar but less pronounced resonances occur at larger integer values of $R_{so}/(\pi/2)$. As the radius R_{so} further increases, the influence of higher modes gains more and more weight and the mixing of the modes becomes larger, which is depicted in Fig. 8.5. Nevertheless, the total increment is weakened by the simultaneously decreasing significance of the boundary-induced relaxation rates, which scale with $\propto R_{so}^{-1}$. At last, we illustrate in Fig. 8.6 the dynamical evolution of a spin density for the radius $R_{so} = 10$, where the corresponding (gauge-transformed) initial state $\mathbf{s}_0'$ strongly deviates from a spatially homogeneous distribution. Similar characteristic behavior was observed in planar quantum wires [64]. The relaxation process of the local spin density $\mathbf{s}(\mathbf{r}, t)$ is strongly inhomogeneous and locally accelerated due to the fast-decaying modes. As the optical measurement typically provides information about the average spin $\boldsymbol{\mathcal{S}}(t)$, the long-lived spin states are masked by the fast-decaying modes. Note, that also in 2D systems an accelerated decay can be found if the initial state is spatially not homogeneous [120].

In conclusion, we found a dramatic change of the total average spin-relaxation rate for an initially homogeneously z-polarized spin density with the wire radius. Within the range of $0 < R/L_{so} \leq 1/4$ (with $l_e < R$) the spin-relaxation rate varies

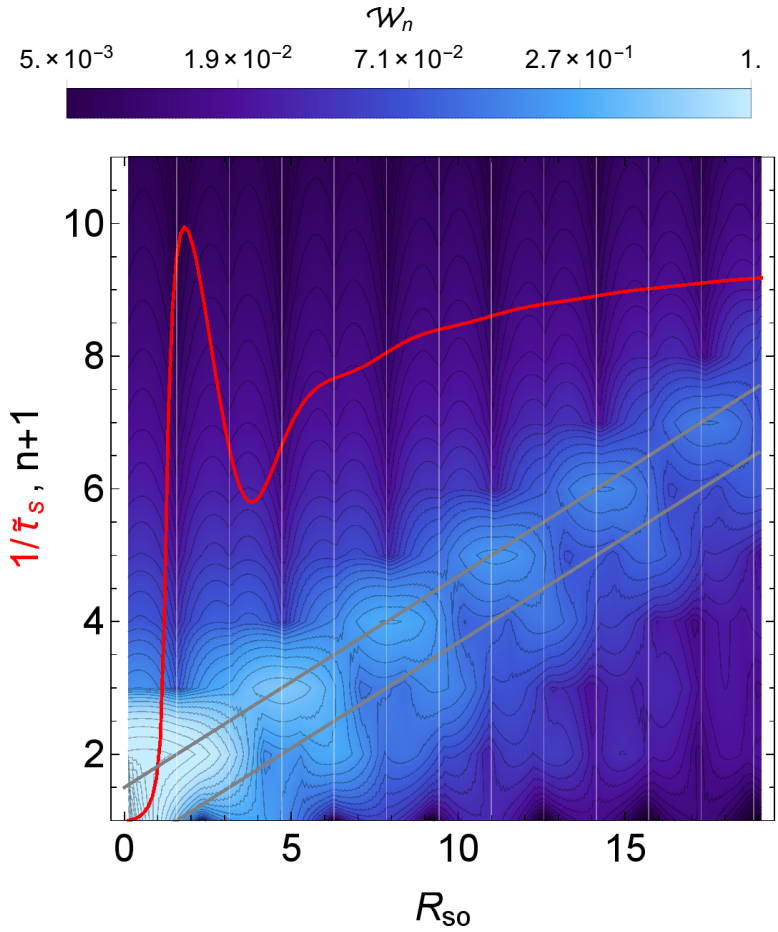

Fig. 8.5: The red solid line shows again the total spin-relaxation rate $1/\tilde{\tau}_s$ as displayed in Fig. 8.4(a) in dependence of the radius R_{so}. The density plot in the background visualizes the relative weight $\mathcal{W}_n$ of the n-th radial Cooperon modes $J_l^{(n)}$, that gives the dominant contribution in the expansion of the initial state $\mathbf{s}_0'$. For better perceptibilty, we summed over all contributing angular momentum quantum numbers in the expansion coefficients c_{nl}, i.e., $\mathcal{W}_n \propto \sum_{l\in\{0,\pm1\}} |c_{nl}|$, where $c_{nl} = \int \mathrm{d}^2 r_\perp \, \langle n, l, 0|\mathbf{r}\rangle \, \mathbf{s}_0'$. The gray solid lines illustrate that the dominance of $J_l^{(n)}$ increases with the radius R_{so} in discrete steps of approximately $R_{so} = n\pi/2$ for even and odd n, respectively.

from the very small 1D-diffusive rate to a rate which is of the order of the bulk spin-relaxation rate. This peculiar feature should be directly detectable in optical spin injection measurements [189]. We stress that, this behavior cannot be observed in zinc-blende nanowires since the homogeneous initial state, Eq. (8.28), constitutes an eigenstate that is independent of the wire radius (cf. Chap. 7). This is a consequence of the missing effective vector potential in Eq. (8.10) which in turn is due to the lack of first-degree spherical harmonic intrinsic SOC terms, in particular, the k-linear contribution.

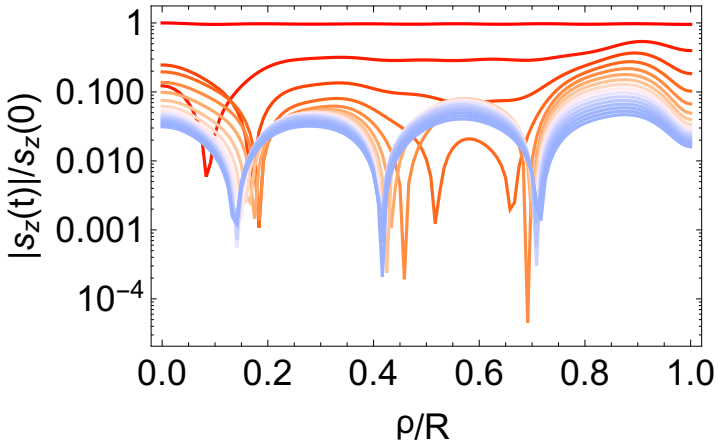

Fig. 8.6: Temporal and spatial evolution of a homogeneously z-polarized spin density for $Q_{so}^2 = 18\delta_D^{(3)}$ and $R_{so} = 10$ in time-steps of $\Delta t = \tau_s$ from red to blue from $t = 0$ to $t = 15\tau_s$, respectively.

8.2.3 Conclusive Remarks and Example

The intrinsic spin relaxation in bulk wurtzite semiconductors is dominated by the k-linear SOC terms. In nanowires, however, owing to the interplay of the particular form of the wurtzite SOC Hamiltonian and the finite-size geometry, there exist special long-lived spin states. The lifetimes of these states are mainly determined by the k-cubic SOC terms and are, thus, much longer than what is found in the bulk. At the same time, the long-lived spin states have in general a complex helical texture in real space, which is very sensitive to the system parameters, especially, the ratio of the spin precession length L_{so} to the nanowire radius R. Magnetoconductance measurements of the weak (anti)localization always detect the lifetimes of the long-lived spin states irrespective of their texture. In contrast, optical spin orientation determines the lifetime of some specifically configured state, which in most cases strongly deviates from the long-lived spin states. Therefore, the extracted lifetimes in both experiments can differ drastically. In particular, opposed to the magnetoconductance measurement the optical measured lifetime is highly sensitive to the nanowire radius. They alter from the very long lifetime in narrow wires, which coincides with the lifetime of the long-lived spin states, to a

very short lifetime, which is of the order of magnitude of the bulk lifetime.

Example: InAs Nanowire in Wurtzite Phase

In order to emphasize the significance of the results, we provide a concrete example of a wurtzite InAs nanowire grown along the [0001]-axis. The spin relaxation in these systems has been experimentally investigated recently in Refs. [48, 50] by means of magnetoconductance measurements. Both studies use nanowires with diameters of about 80 nm and carrier densities which correspond to a 3D electron density $n \sim 10^{17}\,\mathrm{cm}^{-3}$. The authors extract values for the spin-relaxation length from fitting using different theoretical models. Ref. [50] applies the model of Kettemann [61] developed for diffusive planar wires with DP spin relaxation. On the other hand, Ref. [48] uses the 1D magnetoconductance model of Kurdak *et al.* [193] (see also App. 7.B), which is developed for ballistic planar wires. As already pointed out in Ref. [48], we emphasize that in both situations the utilized model does not include an accurate description of the wurtzite nanowire. Ref. [50] observes spin-relaxation lengths of 75 nm and 100 nm for two different samples and a fixed gate voltage. In Ref. [48] various gating techniques are used which yield spin-relaxation lengths of 150-170 nm for low gate voltages.

For a comparison with our findings, we consider an average effective mass m^* of the Γ_7 conduction band of wurtzite InAs as $m^* = (2m^*_\perp + m^*_\parallel)/3$, where $m^*_\parallel = 0.042\,m_0$, $m^*_\perp = 0.037\,m_0$, and m_0 denotes the bare electron mass [210, 211]. The respective SOC coefficients read as $\gamma_R^{\mathrm{int}} = 0.3\,\mathrm{eV\AA}$, $\gamma_D = 132.5\,\mathrm{eV\AA}^3$, and $b = -1.24$ [207]. The Fermi wave vector k_F can be estimated from the 3D electron density n as $k_F = (3\pi^2 n)^{1/3}$. The DP spin-relaxation length is related to the spin lifetime τ_s as $l_s = \sqrt{D_e \tau_s}$. Let us concentrate on the relaxation of spin states that are homogeneously polarized in real space since the bulk eigenstates coincide with the nanowire eigenstates in the 1D-diffusive limit. In Fig. 8.7, we compare the spin precession length and the spin-relaxation lengths of the bulk and the long-lived spin states in the 1D-diffusive limit with the spin-relaxation rates Eqs. (8.15) and (8.27), respectively. In general, the density-modulation enters through the parameters $\delta_D^{(1)}$ and $\delta_D^{(3)}$, which result from the k-cubic SOC terms. Remarkably, the spin precession length, i.e., $L_{so} = \pi\hbar^2/[m(\gamma_R^{\mathrm{int}} + \delta_D^{(1)})]$, diverges for a large density of $n = 3.4 \times 10^{18}\,\mathrm{cm}^{-3}$ since the coefficients $\delta_D^{(1)}$ and γ_R cancel each other. In this case, the bulk spin-relaxation lengths are solely determined by the k-cubic terms and, therefore, the relaxation lengths of bulk and long-lived spin states coincide.

Focusing on the regime of low to moderate electron densities, i.e., $n < 10^{18}\,\mathrm{cm}^{-3}$, the spin precession length alters only insignificantly, i.e., $L_{so} = 200-350\,\mathrm{nm}$. Moreover, the spin-relaxation lengths of the long-lived spin states ($> 1\,\mu\mathrm{m}$) are at least two orders of magnitude larger than the bulk spin-relaxation lengths ($< 60\,\mathrm{nm}$). As we have seen above, for nanowires with diameter $d > L_{so}/2 = 100 - 175\,\mathrm{nm}$ the optical measurement will detect a spin-relaxation length that is of the order of magnitude of the relaxation length in the bulk. This is in strong contrast to the magnetoconductance measurement, which probes the spin relaxation of the long-

lived spin states and hardly changes with the radius (cf. Fig. 8.2). Hence, there is a large discrepancy between experimental characterization methods. These findings also indicate that in Refs. [48, 50] the obtained spin-relaxation lengths predominantly result from the externally induced Rashba SOC, assuming that the results do not largely deviate due to the employed magnetoconductance model. This reasoning is also in agreement with the presumptions made in Ref. [50]. Last, it should be mentioned that for InAs in the low-density range additional SOC effects due to Fermi level surface pinning may become relevant (cf. Chap. 6 and Refs. [68, 169]). Their impact on the intrinsic spin relaxation in wurtzite nanowires shall be discussed elsewhere.

We conclude that it will be a delicate task to gain information about the intrinsic spin relaxation and the SOC coefficients from both experimental techniques. In magnetoconductance measurements owing to the long-lived spin states the intrinsic relaxation features can be easily covered by the externally induced Rashba terms due to electrical gating. On the other hand, in optical spin orientation the long-lived spin states are only excited in the 1D diffusive limit, where $R/L_{so} \ll 1$. Beyond this regime, the measured lifetime corresponds to a superposition of states and can strongly differ from the one of the long-lived spin states.

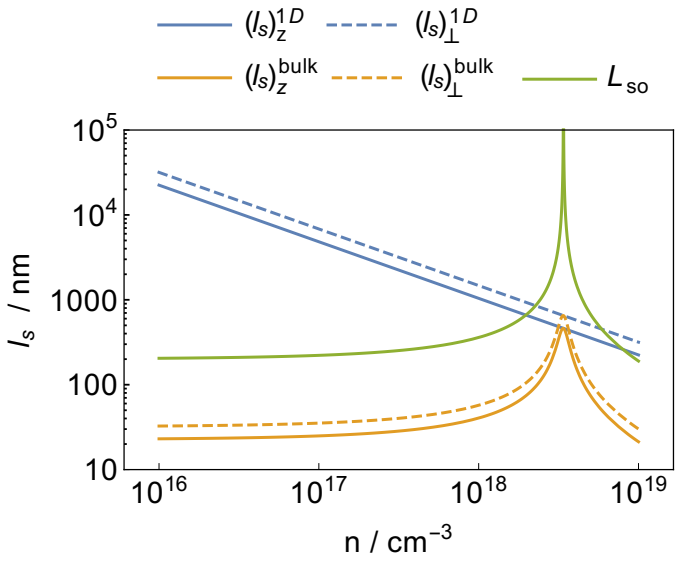

Fig. 8.7: Dependence of the spin precession length L_{so} and spin-relaxation lengths l_s on the 3D electron density n in wurtzite InAs. The relaxation lengths of the bulk and long-lived spin states in the 1D-diffusive limit are labeled with $(l_s)_{z,\perp}^{\mathrm{bulk}}$ and $(l_s)_{z,\perp}^{\mathrm{1D}}$, respectively.

8.3 Magnetoconductance Correction

8.3.1 Nanowire with a Lateral Gate Electrode

To establish a connection to transport experiments and, thereby, enable a different experimental approach, we shall focus on the impact of the extrinsic SOC on the Cooperon modes in the following. The external spin manipulation by electrical gating is a central component in magnetoconductance measurements as well as for the realization of all-electrical spintronic devices.

Due the combination of intrinsic and extrinsic SOC contributions a straightforward gauge transformation of the Cooperon Hamiltonian is impractical. In order to yet still obtain a useful analytical result, we may approximate the gauge-transformed Cooperon Hamitonian H'_C by expanding it in terms of $Q_{so}\rho$ ($Q'_{so}\rho$) up to second order, which is well justified for wires of width smaller than the spin precession length, i.e., $Q_{so}\rho(Q'_{so}\rho) \leq R_{so}(R'_{so}) \ll 1$. Here we defined $R'_{so} = Q'_{so}R$ with $Q'_{so} = 2m\alpha_{\mathrm{R}}^{\mathrm{ext}}/\hbar^2$, which is related to the spin precession length L_{so}^{ext} induced by the extrinsic SOC via $L_{so}^{\mathrm{ext}} = 2\pi/Q_{so}^{\mathrm{ext}}$. Using this simplification, the triplet eigenvalues in zero-mode approximation read as

$$E_{T,0}^{(0)} = Q_z^2 + \frac{1}{4}\left[Q_{so}'^2\varrho_{so}^2 + \delta_D^{(3)}\left(4 + R_{so}^2\right)\right], \tag{8.32}$$

$$E_{T,\pm}^{(0)} = Q_z^2 + \frac{1}{8}\Big[Q_{so}'^2(8 - \varrho_{so}^2) \pm \sqrt{\kappa(Q_z)} + \delta_D^{(3)}(12 - R_{so}^2)\Big], \tag{8.33}$$

where $\varrho_{so} = \sqrt{R_{so}^2 + R_{so}'^2}$ and

$$\begin{aligned}\kappa(Q_z) = {} & 4Q_z^2Q_{so}'^2(\varrho_{so}^2 - 8)^2 + Q_{so}'^4\varrho_{so}^4 + 2\delta_D^{(3)}Q_{so}'^2\left[4R_{so}'^2 - R_{so}^2(4 + R_{so}'^2) + 3R_{so}^4\right] \\ & + (\delta_D^{(3)})^2\left[\left(4 - 3R_{so}^2\right)^2 + R_{so}^2R_{so}'^2\right].\end{aligned} \tag{8.34}$$

By expanding up to second order in $R_{so}(R'_{so})$, one can easily verify that the correct results are obtained for the pure intrinsic and pure extrinsic SOC cases (cf. Sec. 8.2.2 and Sec. 7.2.2, respectively). In order to derive a closed-form expression for the magnetoconductivity, we consider below the two limiting cases, where either the extrinsic or intrinsic SOC dominates and the eigenvalues $E_{T,\pm}^{(0)}$ can be approximated by parabolas. More precisely, for $\eta := \delta_D^{(3)}/(4Q_{so}'^2) > 1$ the eigenvalue $E_{T,-}^{(0)}$ exhibits one or otherwise two minima (cf. Fig. 8.8). The derived expressions are compared in Fig. 8.9 to the numerical calculation of the spectrum with the full gauge-transformation and to the approximated spectrum in Eqs. (8.32) and (8.33).

Low Extrinsic Spin-Orbit Coupling and Homogeneous Spin Density

For small external fields, i.e., $Q'_{so}/Q_{so} \ll 1$, the term in κ, which couples to the wave vector Q_z can be neglected and the global minimum of the spectrum is found at

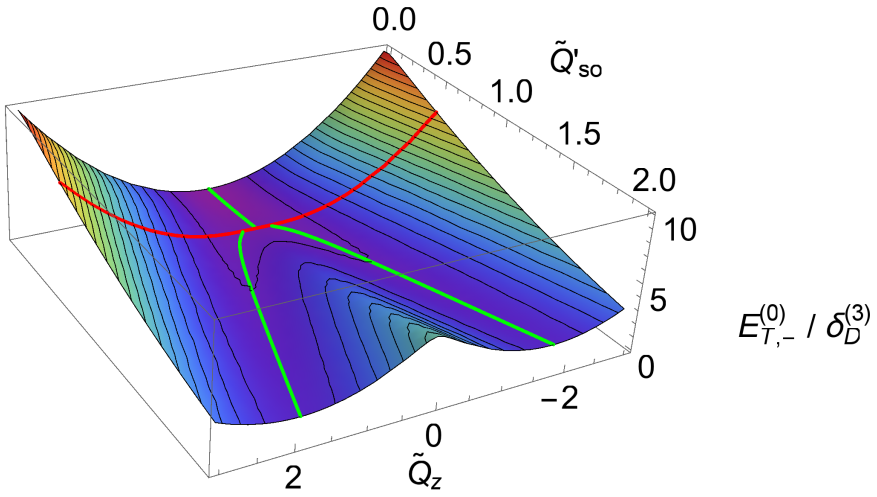

Fig. 8.8: Eigenvalue $E^{(0)}_{T,-}$ in terms of $\delta^{(3)}_D$ in dependence of $\tilde{Q}'_{so} = Q'_{so}/\sqrt{\delta^{(3)}_D}$ and $\tilde{Q}_z = Q_z/\sqrt{\delta^{(3)}_D}$. The green lines depict the minimum $E^{(0)}_{T,-}(Q_z = 0)$, Eq. (8.35), for $4Q'^2_{so} < \delta^{(3)}_D$ and $E^{(0)}_{T,-}(|Q_{z,0}|)$, Eq. (8.39), elsewise. The red line marks the bifurcation point $4Q'^2_{so} = \delta^{(3)}_D$.

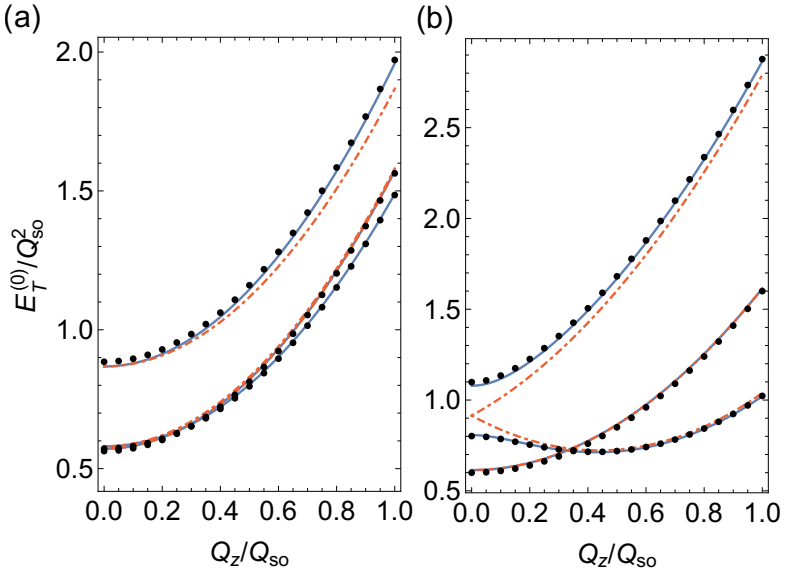

Fig. 8.9: Triplet eigenvalues $E^{(0)}_{T,j}$ in terms of Q^2_{so} for $R_{so} = 0.75$, $\delta^{(3)}_D/Q^2_{so} = 0.5$ in the case of (a) dominant intrinsic SOC, i.e., $\eta = 12.5$, or (b) dominant extrinsic SOC, i.e., $\eta = 0.5$. The black dotted lines correspond to the exact eigenvalues of the full gauge-transformed Cooperon Hamiltonian $H'_{\mathcal{C}}$ in zero-mode approximation. The blue solid lines depict the approximative analytic solution for the eigenvalues, Eqs. (8.32) and (8.33), and the red dot-dashed lines to the simplified solutions in the limiting cases of either dominant intrinsic SOC or dominant extrinsic SOC.

$Q_z = 0$. In this case, the triplet eigenvalues $E^{(0)}_{T,\pm}$ simplify to gaped unit parabolas, i.e.,

$$E^{(0)}_{T,-} = Q_z^2 + Q_{so}'^2\left(1 - R_{so}'^2/4\right) + \delta_D^{(3)}\left(1 + R_{so}^2/4\right), \tag{8.35}$$

$$E^{(0)}_{T,+} = Q_z^2 + Q_{so}'^2\left(1 - R_{so}^2/4\right) + \delta_D^{(3)}\left(2 - R_{so}^2/2\right), \tag{8.36}$$

to second order in $R_{so}(R'_{so})$.

In analogy and for better comparison to many other previous investigations (cf. Refs. [61, 144, 146] and Chaps. 6 and 7) the spin lifetime is defined here by the global minimum of the spectrum at $Q_z = 0$, which describes the decay of a spin density, that is homogeneously excited along the wire axis. Even though it is determined by the relative strength of the extrinsic and intrinsic SOC, in the limit $R_{so} \to 0$ and $R'_{so} \to 0$ the lowest eigenvalue is always given by $E^{(0)}_{T,0}(0)$. Therefore, we define here

$$\frac{1}{\tau_s} = D_e E^{(0)}_{T,0}(0). \tag{8.37}$$

The eigenvectors of $\hat{H}_{\mathcal{C}}$, that correspond to the eigenvalues $E^{(0)}_{T,j}(0)$ are $\mathbf{b}_0 = \hat{\mathbf{x}}, \mathbf{b}_- = \hat{\mathbf{y}}$, and $\mathbf{b}_+ = \hat{\mathbf{z}}$ in the basis of spin density components to lowest order in $Q_{so}\rho$ ($Q'_{so}\rho$).

Strong Extrinsic Spin-Orbit Coupling

In the Sec. 7.3.3, we have seen that for zinc-blende wires a dominating external field was necessary to observe WAL characteristics. The latter are urgent for an unambigious parameter fitting. For $\eta < 1$, the minimum of $E^{(0)}_{T,-}$ moves to finite wave vectors

$$|Q_{z,0}| = \frac{Q'_{so}}{16\sqrt{1-\eta^2}}\left[\eta R_{so}'^2\left(1+2\eta\right) - \eta R_{so}^2\left(1+10\eta\right) + 2\left(8\eta^2 - 8 + \rho_{so}^2\right)\right] \tag{8.38}$$

to second order in $R_{so}(R'_{so})$, which yields the gap

$$E^{(0)}_{T,-}(|Q_{z,0}|) = \frac{Q_{so}'^2}{8}\left[\varrho_{so}^2 + \eta\left(48 - 3R_{so}^2 - R_{so}'^2\right) + 2\eta^2\left(5R_{so}^2 - R_{so}'^2 - 4\right)\right] \tag{8.39}$$

to second order in $R_{so}(R'_{so})$. Using this, we can rewrite the eigenvalues $E^{(0)}_{T,\pm}$ as

$$E^{(0)}_{T,\pm} = \left(|Q_{z,0}| \pm |Q_z|\right)^2 + E^{(0)}_{T,-}(|Q_{z,0}|). \tag{8.40}$$

For large extrinsic SOC, the gap $E^{(0)}_{T,-}(|Q_{z,0}|)$ turns into the global minimum of the spectrum, which underlines again the superiority of helical spin states and was also seen in other systems (cf. Refs. [61, 64, 67, 173] and Chaps. 4, 6 and 7). Neglecting the term $\propto \eta^2$, we can estimate the transition to occur at

$$\eta \approx \frac{\varrho_{so}^2}{16 - 11R_{so}^2 - R_{so}'^2} \leq 1/2, \tag{8.41}$$

for $R_{so} \wedge R'_{so} \leq 1$. Note that for $\eta \ll 1$, the gap is about half as large as the global minimum for $Q_z = 0$, i.e., $E^{(0)}_{T,0}(0)$.

8.3.2 Zero-Mode Magnetoconductance Correction

In the case that $\delta_D^{(3)} R^2 \ll 1$, we can write the leading-order magnetoconductance correction $\Delta G(B)$, analogously to zinc-blende nanowires (cf. Sec. 7.3.2), for the wurtzite counterpart in zero-mode approximation as

$$\Delta G^{(0)}(B) = \frac{2e^2}{h} \frac{1}{L\pi} \int_0^{1/l_e} \mathrm{d}Q_z \left(\frac{1}{Q_z^2 + l_\phi^{-2} + l_B^{-2}} - \sum_{j\in\{0,\pm\}} \frac{1}{E_{T,j}^{(0)}(Q_z) + l_\phi^{-2} + l_B^{-2}} \right), \tag{8.42}$$

where L denotes the nanowire length, l_ϕ the dephasing length, and l_e the mean free path. The magnetic dephasing length $l_B = \sqrt{D_e \tau_B}$ is computed in Sec. 7.3.1 for distinct orientations of the external magnetic field.

In the limiting cases of purely intrinsic as well as either dominant intrinsic or extrinsic SOC and neglecting the upper limit of the integral, we obtain the closed-form expression

$$\Delta G^{(0)}(B) = \frac{2e^2}{h} \frac{1}{2L} \left(\frac{1}{\sqrt{l_\phi^{-2} + l_B^{-2}}} - \sum_i \frac{1}{\sqrt{l_\phi^{-2} + l_B^{-2} + l_{s,i}^{-2}}} \right), \tag{8.43}$$

where $l_{s,i} := \left(E_{T,i,min}^{(0)} \right)^{-1/2}$ is the spin-relaxation length of the i-th long-lived spin state according to the three lowest minima of the triplet eigenvalues. (i) For purely intrinsic SOC and $\delta_D^{(3)} R^2 \ll 1$, the minima can be replaced by Eqs. (8.21) and (8.22) for $Q_z = 0$. Regarding small radii $R_{so}(R'_{so})$ and (ii) dominating intrinsic SOC, the $E_{T,i,min}^{(0)}$ are given by the gaps at $Q_z = 0$, i.e., Eqs. (8.32), (8.35), and (8.36), or (iii) for dominating extrinsic SOC, we find one minima at $E_{T,0}^{(0)}(0)$, Eq. (8.32), and the other two both at $E_{T,-}^{(0)}(|Q_{z,0}|)$, Eq. (8.39).

On the other hand, considering small radii $R_{so}(R'_{so})$ but arbitrary ratios of extrinsic and intrinsic SOC, the integral in Eq. (8.42) has to be solved numerically by using Eqs. (8.32) and (8.33). Each of these cases allows a direct comparison with low-field magnetoconductance measurements and the extraction of transport parameters of the individual systems. As an important aspect, we emphasize that the leading-order magnetoconductance correction is governed by the minimum in the spin-relaxation rate. The corresponding long-lived spin states can, however, be difficult to realize in other experimental approaches.

8.4 Summary and Conclusion

We have studied the effects of a cylindrical boundary on the spin-relaxation properties in wurtzite semiconductor nanowires. The nanowires were assumed to be grown along the [0001] crystal axis and of approximately cylindrical shape. The electron motion was considered diffusive transversally as well as longitudinally with

respect to the nanowire axis. In addition to the intrinsic SOC, the influence of an additional side-gate induced extrinsic Rashba SOC was taken into account. Within zero-mode approximation for the Cooperon we derived explicit expressions for the leading-order magnetoconductance correction.

At this point, we summarize the previous observations and discuss the differences and similarities to zinc-blende semiconductor nanowires and planar quantum wires focusing primarily on the boundary effects on the intrinsic spin relaxation [3, 61, 62, 64, 67, 173] . In general, the SOC terms can be sorted in terms of spherical harmonics. Only the first-degree spherical harmonics give rise to an effective vector potential $\mathbf{A}_s$, which constitutes the key element in the boundary condition for the Cooperon, Eq. (8.10). In order to fulfill the boundary condition for the Cooperon, the component of the effective vector potential normal to the boundary, is removed by gauge transformation, e.g., $\hat{\boldsymbol{\rho}} \cdot \mathbf{A}_s$ in case of the cylindrical wire. This has two important consequences. (i) The spin-relaxation rates, associated with the first-degree spherical harmonics of the removed vector potential, are suppressed. This gives rise to long-lived spin states with lifetimes much longer than in the bulk. (ii) At the same time, these states assume a complex helical structure in real space, which depends on the spin precession length induced by the first-degree spherical harmonics SOC terms.

In zinc-blende nanowires, the Dresselhaus SOC consists solely of third-degree spherical harmonics. Due to the absence of an effective vector potential, the boundary condition for the Cooperon is independent of the SOC and the lowest eigenstates (zero-mode) are constant in real space with respect to the cross-sectional plane. The according intrinsic spin relaxation is therefore independent of the wire radius and identical with the bulk system. The situation is fundamentally different in both wurtzite nanowires and planar zinc-blende quantum wires. Owing to the presence of an effective vector potential, the boundary effect strongly reduces the minimal spin-relaxation rates. In wurtzite wires, the intrinsic vector potential lies completely in the cross-sectional plane. Therefore, it is entirely removed by the gauge-transformation and the spin-relaxation rate of the long-lived spin states is purely limited by the third-degree spherical harmonic SOC terms. This rate is also hardly affected by any changes in the radius. In quantum wires, the impact of the boundary is less significant since a share of the vector potential remains. The respective minimal spin-relaxation rate still depends on first-degree spherical harmonic terms. However, it can be further suppressed in the 1D-diffusive limit leading to the well-known $1/\tau_s \propto W^2$ scaling with the wire width W [61].

As stated above, the corresponding long-lived spin states exhibit, in general, a complex helical structure across the cross-section. An experimental preparation of such states can be challenging. In Sec. 8.2, it was demonstrated that in wurtzite nanowires the optically-measured spin-relaxation rate for a homogeneously z-polarized spin density shows a significant dependence on the wire radius whereas the spin-relaxation rates of the long-lived eigenstates hardly varies. More precisely, below the critical radius $R = L_{so}/4$ the spin-relaxation rate massively decreases from the large bulk-like rate, mainly defined by the k-linear SOC terms, to a tiny

rate, that is given by the k-cubic SOC terms and corresponds to the long-lived spin states. The reason is that, depending on the radius and the spin precession length, the real space structure of the initial state can strongly deviate from the long-lived eigenstate. Therefore, a comparison between the experimentally-extracted spin-relaxation rates may be delusive. Similar results can be expected for planar quantum wires. Remarkably, however, this does not apply to zinc-blende nanowires since the homogeneous initial state corresponds to a long-lived eigenstate and is independent of the wire radius.

On the other hand, the minima in the relaxation rate play a crucial role as they enter the leading-order quantum correction to the conductivity. In wurtzite systems with purely intrinsic SOC, the minimum is determined by the parameter $\delta_D^{(3)}$, which results from the cubic Dresselhaus terms and is, thus, typically very small. As a consequence, the characteristic WAL minimum, which is often required for unambiguous parameter fitting [3], is expected to appear at very low magnetic fields. An exemplary comparison in Sec. 8.2.3 of our predictions with recent experiments [48, 50] indicates that the intrinsic SOC effects can be easily obscured by the extrinsic effects due to the utilization of an external gate. To avoid this situation, we suggest transport experiments in which the electron density is modulated. Since the spin-relaxation rate is via $\delta_D^{(3)}$ highly sensitive to variations in the electron density, the magnetoconductance correction can be manipulated efficiently, e.g., by doping. In case of a constant elastic scattering time τ_e, a dependence of $(\tau_s)_z^{1\mathrm{D}} \propto n_{3D}^{-2}$ should be observed, similar to a bulk zinc-blende system [212, 213] but in contrast to a bulk wurtzite system [214]. For $\tau_s/\tau_\phi < 1.14$, where τ_s is defined in Eq. (8.37), a crossover from positive to negative magnetoconductance should be found [3, 5].

To conclude, magnetoconductance measurements of the weak (anti)localization correction are convenient to extract transport parameters of the system. They constitute also a practical tool to identify the lowest possible spin-relaxation rates and determine parameter configurations, which minimize them. However, these experiments do not provide any information on the structure of the corresponding eigenstates. Therefore, drawing general conclusions for the spin-relaxation rate can be sometimes misleading. The spin-relaxation rate depends always on the device geometry as well as the structure and orientation of the prepared state, where the latter can be controlled in optical experiments. Therefore, optical and transport experiments are complementary tools, which together enable a reliable overall picture.

Appendix 8.A: Intrinsic Spin-Orbit Coupling

A spherical harmonic decomposition of the intrinsic SOC Hamiltonian $\mathcal{H}_{\rm so}^{\rm int} = \sum_l (\mathcal{H}_{\rm so}^{\rm int})_{(l)}$, Eq. (8.3), with respect to the angular momentum l, results in the two contributions, i.e., $l \in \{1, 3\}$,

$$(\mathcal{H}_{\rm so}^{\rm int})_{(1)} = \left[\gamma_{\rm R}^{\rm int} + \frac{\gamma_{\rm D}(b-4)k^2}{5}\right](k_y\sigma_x - k_x\sigma_y), \tag{8.A.1}$$

$$(\mathcal{H}_{\rm so}^{\rm int})_{(3)} = \frac{\gamma_{\rm D}(b+1)}{5}\left(4k_z^2 - k_\perp^2\right)(k_y\sigma_x - k_x\sigma_y). \tag{8.A.2}$$

where $k_\perp^2 = k_x^2 + k_y^2$ and $k^2 = k_x^2 + k_y^2 + k_z^2$. In the ungated nanowire, the contribution $(\mathcal{H}_{\rm so}^{\rm int})_{(1)}$ is completely removed by the gauge transformation due to the boundary condition Eq. (8.10). Thus, the second term $(\mathcal{H}_{\rm so}^{\rm int})_{(3)}$ is responsible for the DP spin relaxation in narrow nanowires. It gives rise to the bulk spin-relaxation term in Eq. (8.9).

Appendix 8.B: Diffusive-Ballistic Crossover

As soon as the wire width becomes comparable to the mean free path, i.e. $W \sim l_e$, the condition of the transverse diffusivity is no more well fulfilled. In the diffusive-ballistic crossover regime, the number of states for scattering becomes finite. Depending on the confinement, the number of available states will decrease with reduction of the wire width. Hence, we can include the crossover to the quasi-ballistic case by replacing the continuous integration over the Fermi surface in Eq. (8.4) by a sum over all discrete modes [173]. More precisely, when computing the Cooperon we are dealing with integrals I of the form

$$I = \frac{1}{4\pi k_F^2}\int \mathrm{d}^3k\, \delta(k_F - |\mathbf{k}|) f(\mathbf{k}), \tag{8.B.3}$$

where the Fermi contour is approximated to be spherical. Due to symmetry, odd terms in k_i vanish after integration. Consequently, we can write I as an integral over the unit sphere $\mathbf{u} = (u_x, u_y, u_z) = (k_x, k_y, k_z)/k_F$ in Cartesian coordinates, that is,

$$I = \frac{2}{\pi}\int_0^1 \mathrm{d}u_x \int_0^{\sqrt{1-u_x^2}} \mathrm{d}u_y \, \frac{f(u_x, u_y, \sqrt{1-u_x^2-u_y^2})}{\sqrt{1-u_x^2-u_y^2}}. \tag{8.B.4}$$

For simplicity, we treat the size-quantization according to a square wire along $\hat{\mathbf{z}}$ with side lengths W and hard-wall boundaries along the $\hat{\mathbf{x}}$ and $\hat{\mathbf{y}}$ axes. The maximum number of modes N along $\hat{\mathbf{x}}$ (or $\hat{\mathbf{y}}$) is approximately $N = \lfloor\sqrt{s^2-1}\rfloor$ where $s = k_F W/\pi$ and $\lfloor\chi\rfloor$ denotes the integer part of χ. Thus, by replacing $u_x = n/s$ and $u_y = p/s$ with $n, p \in [1, N]$ we can express the (continuous) integral

in Eq. (8.B.4) by a (discrete) sum over all channels, that is,

$$I = \frac{2}{\pi s} \sum_{n=1}^{N} \sum_{p=1}^{\sqrt{1+N^2-n^2}} \frac{f(\frac{n}{s}, \frac{p}{s}, \sqrt{1-\left(\frac{n}{s}\right)^2 - \left(\frac{p}{s}\right)^2})}{\sqrt{s^2-n^2-p^2}}. \tag{8.B.5}$$

In Fig. 8.3, we demonstrate the impact of the discretization on the parameter $\delta_D^{(3)}$, which is responsible for the finite spin-relaxation rate even for $R_{so} \to 0$.

Future Prospects

In this thesis, we have addressed the fundamental issue of spin relaxation in selected semiconductor nanostructures. The studied mechanism is of D'yakonov-Perel' type, which is most prominent in diffusive systems that lack inversion symmetry.

It was demonstrated that in quantum wells due to the interplay of Rashba, Dresselhaus SOC, and strain additional symmetries emerge that give rise to persistent spin states. While the existence of the persistent spin states in electron systems is unambiguously proven by now, the experimental evidence for holes remains to be shown. In comparison to the electron system, an experimental verification is more challenging for holes as it requires not only the appropriate tuning of the Rashba and Dresselhaus SOC but also demands a certain amount of uniaxial shear strain. Here, magnetotransport measurements of the weak (anti)localization might be particularly suited since a gate-electrode allows an adjustment of the Rashba SOC strength. The necessary additional strain can be implemented, for instance, by utilization of a piezo crystal. A crossover from WL to WAL will give a clear indication for the existence of long-lived spin states. In this context, a theoretical description would be desirable as it allows to quantify the involved transport parameters. Since an appropriate model is not available, experimenters so far employed models that were developed for electron systems [215–218]. These models fail to describe the weak (anti)localization in a realistic 2D hole system, where the SOC is much more complex and the linear and cubic SOC terms non-trivially interfere. In particular, due to the absence of the strain-induced SOC terms, the WAL-WL transition due to the spin-preserving symmetry cannot be reproduced. This gives strong incentive for further theoretical modeling.

Another way to slow down the spin relaxation consists of confining the spatial region for diffusion and guiding the propagating spins along narrow channels. We have shown that in 3D-diffusive zinc-blende and wurtzite nanowires such a reduced spin decay appears. It is especially pronounced in wurtzite systems as the k-linear SOC terms become ineffective. On the other hand, the tubular zinc-blende nanowires seem to be less affected by the finite size. This, however, can be attributed to the theoretical model, which implied periodic boundary conditions around the wire circumference. Also, for certain small radii, one basic presumption of this model, a much larger wire radius compared to the radial extent of the wave function in the confined region, is not justified anymore. As this already indicates, semiconductor nanowires are particular delicate objects since they can have very distinct mesoscopic features, which makes theoretical model building challenging. The physical observables naturally depend on the characteristic length scales: the system size, the dephasing length, the elastic mean free path, the Fermi wave-

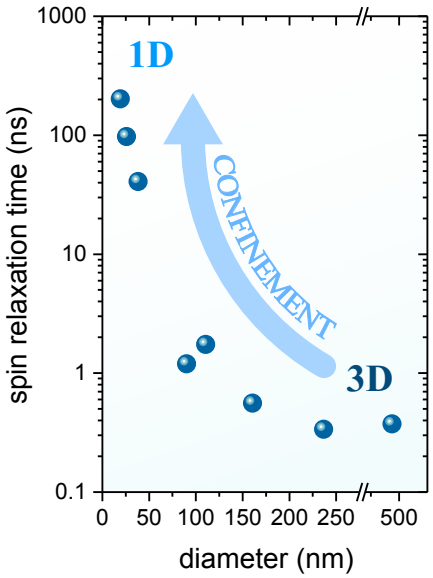

Fig. 8.10: Spin-relaxation time of an optically injected spin density, that is homogeneously polarized along the wire axis [1]. The reduction of the nanowire diameter yields a considerable increase in the relaxation time.

length, and the spin precession length. While in these structures the diameter is typically smaller the dephasing length if the temperature is sufficiently low, the situation is less obvious for the mean free path. Although most nanowires can assumed to be diffusive along the wire axis, the transversal motion can be either diffusive or ballistic. Depending on the regime, different spin-relaxation properties will be observed. At the same time, the relevance and even the dominance of the contributing spin-relaxation processes can change.

Exemplary in this context is our recent experimental study on intrinsic GaAs nanowires in the wurtzite phase oriented along the [0001]-axis [1]. Here, a strong suppression of the spin relaxation is found as the wire diameter is reduced (cf. Fig. 8.10), which is in agreement with our findings in Chap. 8. Yet, if we quantitatively compare the measured values with our theoretical predictions, we see striking differences. Since these wires are undoped and of high crystalline phase purity, we can attribute this inconsistency to the fact that the transversal diffusive approximation does not hold for these wires and our model does not apply. Aside from that, upon decreasing the nanowire diameter below 50 nm, we find clear signatures of quantum confinement (cf. Fig. 8.11). In the present case of wurtzite nanowires, the resulting subbands are spin-degenerate along the [0001]-direction. This indicates that the DP mechanism, for diffusive motion along the wire axis, should be inefficient. Thus, the question remains: which mechanism does actually limit the spin lifetime and how does it scale with the diameter?

In general, we notice that for thin nanowires, the diameter may become comparable to the Fermi wavelength and the electronic subband structure becomes relevant. This holds also for the tubular systems if the nanowires are thin and clean

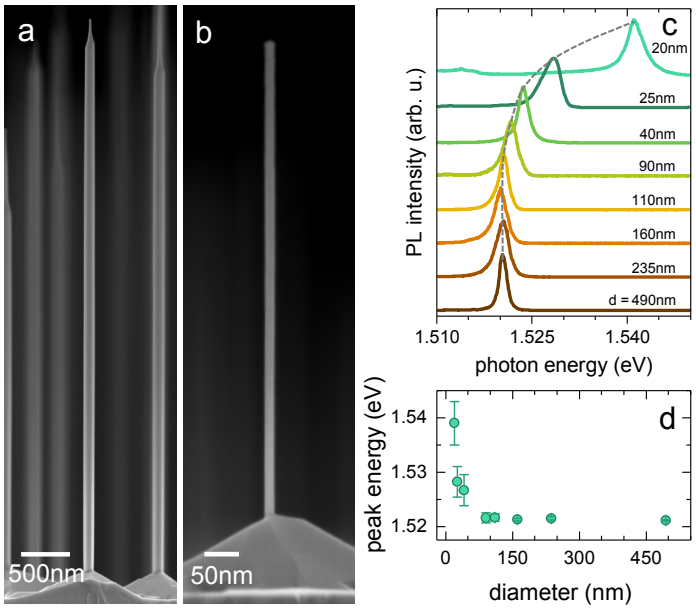

Fig. 8.11: Scanning electron micrographs of GaAs nanowires of diameters (a) $d = 113\,\mathrm{nm}$ and (b) $d = 22\,\mathrm{nm}$ [1]. The significant diameter-dependent shift below $d = 50\,\mathrm{nm}$ (c) in the photoluminescence (PL) intensity to higher photon energies and (d) in the peak energy of the emission is a clear indicator of quantum confinement effects.

enough to enable a ballistic phase-coherent propagation of the carriers around the circumference. In the current state of knowledge, the spin-relaxation properties in multisubband systems are not yet well-established although considerable ramification on each of the contributing spin-relaxation process can be expected.

To conclude, the study in the present thesis covers nanowires that are typically of the order of $\sim 100\,\mathrm{nm}$ where the transport is often diffusive and quantum size effects are negligible (apart from the radial confinement in tubular systems). As the experimental device preparation techniques become more and more advanced, the transition to other regimes becomes possible. Here, the transport is transversal ballistic and the electronic subband structure is fully resolved. In this regime, we anticipate a significant alteration of the spin-related phenomena, which in many cases will be sensitive to the diameter as it influences the number of occupied subbands. Consequently, additional theoretical investigations are strongly required.

Aside from the focus on the weak (anti)localization in this thesis, the tubular nanowires are also paradigmatic systems to study other arising mesoscopic phenomena like the Aharonov-Bohm [219, 220], the Aharonov-Casher [221, 222], the Altshuler-Aronov-Spivak effect [223, 224], as well as the emergence of persistent charge and spin currents [225, 226]. Here, new interesting features may occur as a result of the combination of the radial confinement and the specific Dresselhaus SOC Hamiltonians as derived in Chap. 6 for different growth directions. In regard to this, our approach should be extended to account for the wurtzite phase,

which frequently appears in nanowires even though the underlying semiconductor material has a zinc-blende lattice in the bulk. The axial symmetry of the wurtzite SOC Hamiltonian could allow for special symmetries that, similar to the planar 2D systems, for instance, yield persistent spin states due to the interplay with the Rashba SOC or curvature effects.

In summary, the quantum wells and nanowires are extremely rich in mesoscopic and quantum phenomena. Despite the intensive research over the past decades, plenty of open questions remain to be answered and there is still a wide room for new discoveries.

Acknowledgments

The past years of my life were devoted to an intensive study of the spin phenomena in semiconductor nanostructures. Although or maybe because the work demanded considerable efforts, it was a great experience and caused a positive development on an intellectual as well as personal level. I learned that accuracy, patience, perseverance, and certainly also frustration tolerance are essential character traits for being a good researcher. There is a large number of people who helped to increase my knowledge and add my fingerprint to the world of research by putting it down in form of publications and my doctoral thesis.

First of all, I want to thank Prof. Dr. John Schliemann for offering me the opportunity to join his research group and work on my doctoral thesis. He gave me a great freedom of choice to follow my own ideas. This created a very relaxed environment in which my creativity could flourish. I had always enough room to make my own decisions which nurtured my independence and that I am convinced is a great value. I am very thankful for his guidance and also his efforts to provide the necessary financial support via the DFG Grants No. 336985961 and No. SFB 689. In particular, I owe my gratitude to Dr. Paul Wenk. When we first met in the tutorial class of John's *Condensed-Matter Theory* lecture, I had the strong feeling that a collaboration with him would be enjoyable, instructive, and productive. My instincts turned out right because without his support I would certainly not have accomplished so many nice results. Working together with Paul has always been fun and I am sure he will make a great professor one day. Moreover, I am very grateful for the experimental collaborations with the groups of Prof. Dr. Thomas Schäpers and Prof. Dr. Dominique Bougeard and, in particular, their group members Dr. Sebastian Heedt and Florian Dirnberger. The interaction was always very pleasant and considerably enhanced the outcome of our research. Special thanks to Prof. Dr. Francisco Mireles for his great hospitality when I visited Ensenada and for his friendship. I also want to acknowledge the help of Martin Wackerl for making pretty Feynman diagrams in LaTeX and for proof-reading my thesis. Furthermore, I appreciate the numerous fruitful and motivating discussions with Dr. Tiago Campos, Dr. Lin Chen, Prof. Dr. Dimitrie Culcer, Prof. Dr. Szabolcs Csonka, Dr. Tobias Dollinger, Prof. Dr. J. Carlos Egues, Prof. Dr. Jaroslav Fabian, Dr. Paulo E. Faria Junior, Tobias Frank, Dr. Martin Gmitra, Dr. Christian Gradl, Prof. Dr. Tobias Korn, Prof. Dr. Klaus Richter, Dr. Markus Schwemmer, Prof. Dr. Roland Winkler, and Patrick Zellekens, among others. Also, I am very grateful to Prof. Dr. Ulrich Zülicke and Prof. Dr. Michele Governale for providing me the opportunity to continue my scientific career at the Victoria University in Wellington. Finally, I want to thank my whole family, especially my parents, who believed in me and gave me encouragement and support during my entire study.

References

[1] F. Dirnberger, M. Kammermeier, P. E. Faria Junior, J. König, M. Forsch, C. Schüller, T. Korn, J. Schliemann, P. Wenk, and D. Bougeard, (2018), submitted to *Phys. Rev. Lett.*

[2] M. Kammermeier, P. Wenk, F. Dirnberger, D. Bougeard, and J. Schliemann, Phys. Rev. B **98**, 035407 (2018).

[3] M. Kammermeier, P. Wenk, J. Schliemann, S. Heedt, Th. Gerster, and Th. Schäpers, Phys. Rev. B **96**, 235302 (2017).

[4] M. Kammermeier, P. Wenk, and J. Schliemann, Phys. Rev. Lett. **117**, 236801 (2016).

[5] M. Kammermeier, P. Wenk, J. Schliemann, S. Heedt, and Th. Schäpers, Phys. Rev. B **93**, 205306 (2016).

[6] P. Wenk, M. Kammermeier, and J. Schliemann, Phys. Rev. B **93**, 115312 (2016).

[7] T. Dollinger, M. Kammermeier, A. Scholz, P. Wenk, J. Schliemann, K. Richter, and R. Winkler, Phys. Rev. B **90**, 115306 (2014).

[8] M. Kammermeier, *Strained Hole Systems with Rashba and Dresselhaus Spin-Orbit Coupling*, Master's thesis, University of Regensburg (2014).

[9] G. E. Moore, Electronics **38** (1965).

[10] V. K. Joshi, Eng. Sci. Technol. Int. J. **19**, 1503 (2016).

[11] N. Kim, T. Austin, D. Baauw, T. Mudge, K. Flautner, J. Hu, M. Irwin, M. Kandemir, and V. Narayanan, Computer **36**, 68 (2003).

[12] M. Stockinger, *Optimization of Ultra-Low-Power CMOS Transistors*, Ph.D. thesis, Vienna University of Technology (2000).

[13] S. Datta and B. Das, Appl. Phys. Lett. **56**, 665 (1990).

[14] H. C. Koo, J. H. Kwon, J. Eom, J. Chang, S. H. Han, and M. Johnson, Science **325**, 1515 (2009).

[15] Y. H. Park, J. W. Choi, H.-J. Kim, J. Chang, S. H. Han, H.-J. Choi, and H. C. Koo, Sci. Rep. **7**, 46671 (2017).

[16] Th. Schäpers, *Semiconductor Spintronics*, De Gruyter Textbook (De Gruyter, 2016).

[17] M. I. D'yakonov and V. I. Perel', Sov. Phys. Solid State **13**, 3023 (1972), [Fiz. Tverd. Tela **13**, 3581 (1971)].

[18] J. Schliemann, J. C. Egues, and D. Loss, Phys. Rev. Lett. **90**, 146801 (2003).

[19] B. A. Bernevig, J. Orenstein, and S.-C. Zhang, Phys. Rev. Lett. **97**, 236601 (2006).

[20] J. D. Koralek, C. P. Weber, J. Orenstein, B. A. Bernevig, S.-C. Zhang, S. Mack, and D. D. Awschalom, Nature **458**, 610 (2009).

[21] Y. Kunihashi, M. Kohda, and J. Nitta, Phys. Rev. Lett. **102**, 226601 (2009).

[22] S. Faniel, T. Matsuura, S. Mineshige, Y. Sekine, and T. Koga, Phys. Rev. B **83**, 115309 (2011).

[23] M. P. Walser, C. Reichl, W. Wegscheider, and G. Salis, Nat. Phys. **8**, 757 (2012).

[24] M. Kohda, V. Lechner, Y. Kunihashi, T. Dollinger, P. Olbrich, C. Schönhuber, I. Caspers, V. V. Bel'kov, L. E. Golub, D. Weiss, K. Richter, J. Nitta, and S. D. Ganichev, Phys. Rev. B **86**, 081306 (2012).

[25] J. Schliemann, Rev. Mod. Phys. **89**, 011001 (2017).

[26] V. E. Sacksteder and B. A. Bernevig, Phys. Rev. B **89**, 161307 (2014).

[27] K. Richter, *Semiclassical Theory of Mesoscopic Quantum Systems* (Springer, 2000).

[28] V. Mourik, K. Zuo, S. M. Frolov, S. R. Plissard, E. P. A. M. Bakkers, and L. P. Kouwenhoven, Science **336**, 1003 (2012).

[29] A. Das, Y. Ronen, Y. Most, Y. Oreg, M. Heiblum, and H. Shtrikman, Nat. Phys. **8**, 887 (2012).

[30] L. Hofstetter, S. Csonka, J. Nygård, and C. Schönenberger, Nature **461**, 960 (2009).

[31] J. A. van Dam, Y. V. Nazarov, E. P. A. M. Bakkers, S. De Franceschi, and L. P. Kouwenhoven, Nature **442**, 667 (2006).

[32] S. Heedt, I. Wehrmann, K. Weis, R. Calarco, H. Hardtdegen, D. Grützmacher, Th. Schäpers, C. Morgan, and D. E. Bürgler, "Toward spin electronic devices based on semiconductor nanowires," in *Future Trends in Microelectronics* (John Wiley & Sons, Inc., 2013) pp. 328–339.

[33] A. B. Greytak, C. J. Barrelet, Y. Li, and C. M. Lieber, Appl. Phys. Lett. **87**, 151103 (2005).

[34] J. Xiang, W. Lu, Y. Hu, Y. Wu, H. Yan, and C. M. Lieber, Nature **441**, 489 (2006).

[35] S. Nadj-Perge, S. M. Frolov, E. P. A. M. Bakkers, and L. P. Kouwenhoven, Nature **468**, 1084 (2010).

[36] S. Nadj-Perge, V. S. Pribiag, J. W. G. van den Berg, K. Zuo, S. R. Plissard, E. P. A. M. Bakkers, S. M. Frolov, and L. P. Kouwenhoven, Phys. Rev. Lett. **108**, 166801 (2012).

[37] P. Krogstrup, H. I. Jørgensen, M. Heiss, O. Demichel, J. V. Holm, M. Aagesen, J. Nygård, and A. Fontcuberta i Morral, Nat. Photonics **7**, 306 (2013).

[38] X. Dai, S. Zhang, Z. Wang, G. Adamo, H. Liu, Y. Huang, C. Couteau, and C. Soci, Nano Lett. **14**, 2688 (2014).

[39] P. E. Faria Junior, G. Xu, J. Lee, N. C. Gerhardt, G. M. Sipahi, and I. Žutić, Phys. Rev. B **92**, 075311 (2015).

[40] X. Dai, A. Messanvi, H. Zhang, C. Durand, J. Eymery, C. Bougerol, F. H. Julien, and M. Tchernycheva, Nano Lett. **15**, 6958 (2015).

[41] A. E. Hansen, M. T. Björk, I. C. Fasth, C. Thelander, and L. Samuelson, Phys. Rev. B **71**, 205328 (2005).

[42] S. Dhara, H. S. Solanki, V. Singh, A. Narayanan, P. Chaudhari, M. Gokhale, A. Bhattacharya, and M. M. Deshmukh, Phys. Rev. B **79**, 121311 (2009).

[43] X.-J. Hao, T. Tu, G. Cao, C. Zhou, H.-O. Li, G.-C. Guo, W. Y. Fung, Z. Ji, G.-P. Guo, and W. Lu, Nano Lett. **10**, 2956 (2010).

[44] S. Estévez Hernández, M. Akabori, K. Sladek, C. Volk, S. Alagha, H. Hardtdegen, M. G. Pala, N. Demarina, D. Grützmacher, and Th. Schäpers, Phys. Rev. B **82**, 235303 (2010).

[45] I. van Weperen, B. Tarasinski, D. Eeltink, V. S. Pribiag, S. R. Plissard, E. P. A. M. Bakkers, L. P. Kouwenhoven, and M. Wimmer, Phys. Rev. B **91**, 201413 (2015).

[46] P. Roulleau, T. Choi, S. Riedi, T. Heinzel, I. Shorubalko, T. Ihn, and K. Ensslin, Phys. Rev. B **81**, 155449 (2010).

[47] D. Liang and X. P. Gao, Nano Lett. **12**, 3263 (2012).

[48] Z. Scherübl, G. Fülöp, M. H. Madsen, J. Nygård, and S. Csonka, Phys. Rev. B **94**, 035444 (2016).

[49] K. Takase, Y. Ashikawa, G. Zhang, K. Tateno, and S. Sasaki, Sci. Rep. **7**, 930 (2017).

[50] T. S. Jespersen, P. Krogstrup, A. M. Lunde, R. Tanta, T. Kanne, E. Johnson, and J. Nygård, Phys. Rev. B **97**, 041303 (2018).

[51] L. J. Lauhon, M. S. Gudiksen, D. Wang, and C. M. Lieber, Nature **420**, 57 (2002).

[52] B. A. Wacaser, K. Deppert, L. S. Karlsson, L. Samuelson, and W. Seifert, J. Cryst. Growth **287**, 504 (2006).

[53] S. A. Fortuna and X. Li, Semicond. Sci. Technol. **25**, 024005 (2010).

[54] S. Wirths, K. Weis, A. Winden, K. Sladek, C. Volk, S. Alagha, T. E. Weirich, M. von der Ahe, H. Hardtdegen, H. Lüth, N. Demarina, D. Grützmacher, and Th. Schäpers, J. Appl. Phys. **110**, 053709 (2011).

[55] C. Blömers, T. Rieger, P. Zellekens, F. Haas, M. I. Lepsa, H. Hardtdegen, Ö. Gül, N. Demarina, D. Grützmacher, H. Lüth, and Th. Schäpers, Nanotechnology **24**, 035203 (2013).

[56] F. Haas, K. Sladek, A. Winden, M. von der Ahe, T. E. Weirich, T. Rieger, H. Lüth, D. Grützmacher, Th. Schäpers, and H. Hardtdegen, Nanotechnology **24**, 085603 (2013).

[57] Z. Zhang, Z. Lu, H. Xu, P. Chen, W. Lu, and J. Zou, Nano Res. **7**, 1640 (2014).

[58] S. d'Hollosy, M. Jung, A. Baumgartner, V. A. Guzenko, M. H. Madsen, J. Nygård, and C. Schönenberger, Nano Lett. **15**, 4585 (2015).

[59] S. Heedt, I. Otto, K. Sladek, H. Hardtdegen, J. Schubert, N. Demarina, H. Lüth, D. Grützmacher, and Th. Schäpers, Nanoscale **7**, 18188 (2015).

[60] M. Speckbacher, J. Treu, T. J. Whittles, W. M. Linhart, X. Xu, K. Saller, V. R. Dhanak, G. Abstreiter, J. J. Finley, T. D. Veal, and G. Koblmüller, Nano Lett. **16**, 5135 (2016).

[61] S. Kettemann, Phys. Rev. Lett. **98**, 176808 (2007).

[62] A. G. Mal'shukov and K. A. Chao, Phys. Rev. B **61**, R2413 (2000).

[63] A. A. Kiselev and K. W. Kim, Phys. Rev. B **61**, 13115 (2000).

[64] P. Schwab, M. Dzierzawa, C. Gorini, and R. Raimondi, Phys. Rev. B **74**, 155316 (2006).

[65] Th. Schäpers, V. A. Guzenko, M. G. Pala, U. Zülicke, M. Governale, J. Knobbe, and H. Hardtdegen, Phys. Rev. B **74**, 081301 (2006).

[66] A. W. Holleitner, V. Sih, R. C. Myers, A. C. Gossard, and D. D. Awschalom, New J. Phys. **9**, 342 (2007).

[67] P. Wenk and S. Kettemann, Phys. Rev. B **81**, 125309 (2010).

[68] V. E. Degtyarev, S. V. Khazanova, and N. V. Demarina, Sci. Rep. **7**, 3411 (2017).

[69] F. Schwabl, *Advanced Quantum Mechanics* (Springer, 2008).

[70] R. Winkler, *Spin-Orbit Coupling Effects in Two-Dimensional Electron and Hole Systems*, Springer Tracts in Modern Physics, Vol. 191 (Springer-Verlag, Berlin, 2003).

[71] F. Schwabl, *Quantum Mechanics* (Springer, 2007).

[72] L. H. Thomas, Nature **117**, 514 (1926).

[73] P. Yu and M. Cardona, *Fundamentals of Semiconductors: Physics and Materials Properties*, Graduate Texts in Physics (Springer, 2010).

[74] J. Fabian, A. Matos-Abiague, C. Ertler, P. Stano, and I. Zutic, Acta Phys. Slovaca **57**, 565 (2007).

[75] E. O. Kane, J. Phys. Chem. Solids **1**, 249 (1957).

[76] L. C. L. Y. Voon and M. Willatzen, *The $k \cdot p$ Method* (Springer, 2009).

[77] N. W. Ashcroft and M. D. N., *Festkörperphysik* (Oldenburg Verlag, 2013).

[78] T. Ihn, *Semiconductor Nanostructures* (Oxford, 2011).

[79] U. Rössler, Solid State Commun. **49**, 943 (1984).

[80] H. Mayer and U. Rössler, Phys. Rev. B **44**, 9048 (1991).

[81] M. Cardona, N. E. Christensen, and G. Fasol, Phys. Rev. B **38**, 1806 (1988).

[82] A. M. Cohen and G. E. Marques, Phys. Rev. B **41**, 10608 (1990).

[83] M. S. Dresselhaus, *Application of Group Theory to the Physics of Solids* (Springer, 2002).

[84] G. L. Bir and G. E. Pikus, *Symmetry and Strain-induced Effects in Semiconductors* (Wiley/Halsted Press, 1974).

[85] J. M. Luttinger, Phys. Rev. **102**, 1030 (1956).

[86] A. Scholz, T. Dollinger, P. Wenk, K. Richter, and J. Schliemann, Phys. Rev. B **87**, 085321 (2013).

[87] O. Madelung, *Semiconductors* (Springer, 1982).

[88] H. A. Kramers, Proc. Amsterdam Acad. **33**, 959 (1930).

[89] G. Dresselhaus, Phys. Rev. **100**, 580 (1955).

[90] E. Rashba and E. Sherman, Phys. Lett. A **129**, 175 (1988).

[91] D. V. Bulaev and D. Loss, Phys. Rev. Lett. **95**, 076805 (2005).

[92] M. V. Durnev, M. M. Glazov, and E. L. Ivchenko, Phys. Rev. B **89**, 075430 (2014).

[93] Y. A. Bychkov and E. I. Rashba, J. Phys. C: Solid State Phys. **17**, 6039 (1984).

[94] Y. Bychkov and E. I. Rashba, JETP Lett. **39**, 78 (1984), [Pis'ma Zh. Eksp. Teor. Fiz. **39**, No. 2, 66 (1984)].

[95] S. Datta, *Quantum Transport* (Cambridge University Press, 2005).

[96] Y. Sun, S. E. Thompson, and T. Nishida, *Strain Effects in Semiconductors: Theory and Device Applications* (Springer, 2010).

[97] S. Datta, *Electronic Transport in Mesoscopic Systems* (Cambridge University Press, 1997).

[98] G. E. Simion and Y. B. Lyanda-Geller, Phys. Rev. B **90**, 195410 (2014).

[99] J.-W. Luo, A. N. Chantis, M. van Schilfgaarde, G. Bester, and A. Zunger, Phys. Rev. Lett. **104**, 066405 (2010).

[100] P. S. Alekseev and M. O. Nestoklon, Phys. Rev. B **95**, 125303 (2017).

[101] M. Wu, J. Jiang, and M. Weng, Phys. Rep. **493**, 61 (2010).

[102] O. Krebs, D. Rondi, J. L. Gentner, L. Goldstein, and P. Voisin, Phys. Rev. Lett. **80**, 5770 (1998).

[103] M. D'yakonov and V. Y. Kachorovskii, Sov. Phys. Semicond. **20**, 110 (1986), [Fiz. Tekh. Poluprovodn. **20**, 178 (1986)].

[104] I. Zutic, J. Fabian, and S. Das Sarma, Rev. Mod. Phys. **76**, 323 (2004).

[105] S. Thompson, M. Armstrong, C. Auth, S. Cea, R. Chau, G. Glass, T. Hoffman, J. Klaus, Z. Ma, B. Mcintyre, A. Murthy, B. Obradovic, L. Shifren, S. Sivakumar, S. Tyagi, T. Ghani, K. Mistry, M. Bohr, and Y. El-Mansy, IEEE Electron Device Lett. **25**, 191 (2004).

[106] Y. Sun, S. E. Thompson, and T. Nishida, J. Appl. Phys. **101**, 104503 (2007).

[107] P. Löwdin, J. Chem. Phys. **19**, 1396 (1951).

[108] J. P. Loehr, *Physics of Strained Quantum Well Lasers*, Springer Series in Solid-State Science 110 (Springer US, 1998).

[109] E. Bernardes, J. Schliemann, M. Lee, J. C. Egues, and D. Loss, Phys. Rev. Lett. **99**, 76603 (2007).

[110] J. Xia, W. Ge, and K. Chang, *Semiconductor Spintronics* (World Scientific Publishing Company, 2012).

[111] F. Bloch, Phys. Rev. **70**, 460 (1946).

[112] H. C. Torrey, Phys. Rev. **104**, 563 (1956).

[113] M. I. D'yakonov, ed., *Spin Physics in Semiconductors* (Springer, 2017).

[114] M. A. Brand, A. Malinowski, O. Z. Karimov, P. A. Marsden, R. T. Harley, A. J. Shields, D. Sanvitto, D. A. Ritchie, and M. Y. Simmons, Phys. Rev. Lett. **89**, 236601 (2002).

[115] C. Grimaldi, Phys. Rev. B **72**, 075307 (2005).

[116] P. Wenk, *Itinerant Spin Dynamics in Structures of Reduced Dimensionality*, Ph.D. thesis, Jacobs University Bremen (2011).

[117] M. I. Dyakonov and V. I. Perel, Sov. Phys. JETP **33**, 1053 (1971), [Zh. Eksp.. Teor. Fiz. **60**, 1954 (1971)].

[118] G. E. Pikus and A. N. Titkov, in *Optical Orientation*, Modern Problems in Condensed Matter Sciences, Vol. 8, edited by F. Meier and B. P. Zakharchenya (North-Holland, Amsterdam, 1984) Chap. 3.

[119] A. G. Mal'shukov, L. Y. Wang, C. S. Chu, and K. A. Chao, Phys. Rev. Lett. **95**, 146601 (2005).

[120] V. A. Froltsov, Phys. Rev. B **64**, 045311 (2001).

[121] M. Trushin and J. Schliemann, New J. Phys. **9**, 346 (2007).

[122] F. Dettwiler, J. Fu, S. Mack, P. J. Weigele, J. C. Egues, D. D. Awschalom, and D. M. Zumbühl, Phys. Rev. X **7**, 031010 (2017).

[123] S. M. Badalyan, A. Matos-Abiague, G. Vignale, and J. Fabian, Phys. Rev. B **79**, 205305 (2009).

[124] Z. Li, F. Marsiglio, and J. P. Carbotte, Sci. Rep. **3**, 2828 (2013), article.

[125] J. Schliemann, D. Loss, and R. M. Westervelt, Phys. Rev. B **73**, 085323 (2006).

[126] J. Fabian and M. W. Wu, *Handbook of Spin Transport and Magnetism* (Chapman and Hall/CRC, New York, 2011) p. 303.

[127] A. Kiss, L. Szolnoki, and F. Simon, Sci. Rep. **6**, 22706 (2016).

[128] R. J. Elliott, Phys. Rev. **96**, 266 (1954).

[129] Y. Yafet, in *Solid State Physics*, Vol. 14, edited by F. Seitz and D. Turnbull (Academic, New York, 1963).

[130] J. N. Chazalviel, Phys. Rev. B **11**, 1555 (1975).

[131] G. L. Bir, A. G. Aronov, and G. E. Pikus, Sov. Phys. JETP **42**, 705 (1976), [Zh. Eksp. Teor. Fiz. **69**, 1382 (1975)].

[132] A. W. Overhauser, Phys. Rev. **89**, 689 (1953).

[133] W. Nolting, *Viel-Teilchen Theorie* (Springer, 2015).

[134] G. Czycholl, *Theoretische Festkörperphysik Band 2* (Springer, 2017).

[135] A. Crépieux and P. Bruno, Phys. Rev. B **64**, 014416 (2001).

[136] E. Akkermans and G. Montambaux, *Mesoscopic Physics of Electrons and Photons* (Cambridge University Press, 2017).

[137] D. A. Greenwood, Proc. Phys. Soc. **71**, 585 (1958).

[138] H. Bruus and K. Flensberg, *Many-Body Quantum Theory in Condensed Matter Physics: An Introduction* (Oxford Graduate Texts, 2002).

[139] J. Rammer, *Quantum Transport Theory* (Westview Press, 2004).

[140] P. Drude, Ann. Phys. **306**, 566 (1900).

[141] P. Drude, Ann. Phys. **308**, 369 (1900).

[142] S. Kettemann and R. Mazzarello, Phys. Rev. B **65**, 085318 (2002).

[143] S. Hikami, A. I. Larkin, and Y. Nagaoka, Prog. Theor. Phys. **63**, 707 (1980).

[144] S. V. Iordanskii, Yu. B. Lyanda-Geller, and G. E. Pikus, JETP Lett. **60**, 206 (1994), [Pis'ma Zh. Eksp. Teor. Fiz. **60**, 199 (1994)].

[145] F. G. Pikus and G. E. Pikus, Phys. Rev. B **51**, 16928 (1995).

[146] W. Knap, C. Skierbiszewski, A. Zduniak, E. Litwin-Staszewska, D. Bertho, F. Kobbi, J. L. Robert, G. E. Pikus, F. G. Pikus, S. V. Iordanskii, V. Mosser, K. Zekentes, and Yu. B. Lyanda-Geller, Phys. Rev. B **53**, 3912 (1996).

[147] C. Beenakker and H. van Houten, in *Semiconductor Heterostructures and Nanostructures*, Solid State Physics, Vol. 44, edited by H. Ehrenreich and D. Turnbull (Academic Press, 1991) pp. 1 – 228.

[148] A. G. Malshukov, K. A. Chao, and M. Willander, Phys. Rev. B **56**, 6436 (1997).

[149] K. Yoshizumi, A. Sasaki, M. Kohda, and J. Nitta, Appl. Phys. Lett. **108**, 132402 (2016).

[150] S. D. Ganichev, S. N. Danilov, V. V. Bel'kov, E. L. Ivchenko, M. Bichler, W. Wegscheider, D. Weiss, and W. Prettl, Phys. Rev. Lett. **88**, 057401 (2002).

[151] D. G. Seiler, B. D. Bajaj, and A. E. Stephens, Phys. Rev. B **16**, 2822 (1977).

[152] T. Korn, M. Kugler, M. Griesbeck, R. Schulz, A. Wagner, M. Hirmer, C. Gerl, D. Schuh, W. Wegscheider, and C. Schüller, New J. Phys. **12**, 043003 (2010).

[153] M. Kugler, T. Andlauer, T. Korn, A. Wagner, S. Fehringer, R. Schulz, M. Kubová, C. Gerl, D. Schuh, W. Wegscheider, P. Vogl, and C. Schüller, Phys. Rev. B **80**, 035325 (2009).

[154] M. Hirmer, M. Hirmer, D. Schuh, W. Wegscheider, T. Korn, R. Winkler, and C. Schüller, Phys. Rev. Lett. **107**, 216805 (2011).

[155] B. Grbić, R. Leturcq, T. Ihn, K. Ensslin, D. Reuter, and A. Wieck, Phys. Rev. B **77**, 125312 (2008).

[156] I. Vurgaftman, J. R. Meyer, and L. R. Ram-Mohan, J. Appl. Phys. **89**, 5815 (2001).

[157] M. Willatzen, M. Cardona, and N. E. Christensen, Phys. Rev. B **50**, 18054 (1994).

[158] E. Ivchenko and P. Pikus, *Superlattices and Other Heterostructures: Symmetry and Optical Phenomena*, Springer Series in Solid-State Science 110 (Springer, 1995).

[159] E. L. Ivchenko, A. Y. Kaminski, and U. Rössler, Phys. Rev. B **54**, 5852 (1996).

[160] R. Magri and A. Zunger, Phys. Rev. B **62**, 10364 (2000).

[161] B. Habib, J. Shabani, E. P. De Poortere, M. Shayegan, and R. Winkler, Phys. Rev. B **75**, 153304 (2007).

[162] G. E. Pikus, V. A. Maruschak, and A. N. Titkov, Sov. Phys. Semicond. **22**, 185 (1988).

[163] A. G. Aronov and Yu. B. Lyanda-Geller, Phys. Rev. Lett. **70**, 343 (1993).

[164] F. E. Meijer, A. F. Morpurgo, and T. M. Klapwijk, Phys. Rev. B **66**, 033107 (2002).

[165] J. S. Sheng and K. Chang, Phys. Rev. B **74**, 235315 (2006).

[166] B. Berche, C. Chatelain, and E. Medina, Eur. J. Phys. **31**, 1267 (2010).

[167] P. Wojcik, J. Adamowski, M. Woloszyn, and B. Spisak, Phys. E **59**, 19 (2014).

[168] I. Kokurin, Phys. E **74**, 264 (2015).

[169] A. Bringer and Th. Schäpers, Phys. Rev. B **83**, 115305 (2011).

[170] M. P. Trushin and A. L. Chudnovskiy, JETP Lett. **83**, 318 (2006).

[171] L. Magarill, D. Romanov, and A. Chaplik, J. Exp. Theor. Phys. **86**, 771 (1998).

[172] A. Manolescu, T. Rosdahl, S. Erlingsson, L. Serra, and V. Gudmundsson, EPJ B **86**, 445 (2013).

[173] P. Wenk and S. Kettemann, Phys. Rev. B **83**, 115301 (2011).

[174] P. Wenk and S. Kettemann, in *Handbook on Nanophysics*, edited by K. Sattler (Francis & Taylor, 2010) p. 49.

[175] J. S. Meyer, V. I. Fal'ko, and B. L. Altshuler, in *Nato Science Series II*, Vol. 72, edited by I. V. Lerner, B. L. Altshuler, V. I. Fal'ko, and T. Giamarchi (Kluwer Academic Publishers, Dordrecht, 2002) p. 117.

[176] R. Mazzarello, *Localization and density of states of disordered low-dimensional systems in a magnetic field*, Ph.D. thesis, Universität Hamburg (2004).

[177] C. Blömers, *Electronic transport in narrow-gap semiconductor nanowires*, Ph.D. thesis, RWTH Aachen (2012).

[178] K. Storm, G. Nylund, L. Samuelson, and A. P. Micolich, Nano Lett. **12**, 1 (2012).

[179] O. Karlström, A. Wacker, K. Nilsson, G. Astromskas, S. Roddaro, L. Samuelson, and L. E. Wernersson, Nanotechnology **19**, 435201 (2008).

[180] D. Rainis and D. Loss, Phys. Rev. B **90**, 235415 (2014).

[181] M. Akabori, K. Sladek, H. Hardtdegen, Th. Schäpers, and D. Grützmacher, J. Cryst. Growth **311**, 3813 (2009).

[182] L. E. Golub, Phys. Rev. B **71**, 235310 (2005).

[183] M. M. Glazov and L. E. Golub, Semicond. Sci. Tech. **24**, 064007 (2009).

[184] Y. Araki, G. Khalsa, and A. H. MacDonald, Phys. Rev. B **90**, 125309 (2014).

[185] B. L. Al'tshuler and A. G. Aronov, JETP Lett. **33**, 499 (1981), [Pis'ma Zh. Eskp. Teor. Fiz. **33**, No. 10, 515 (1981)].

[186] I. L. Aleiner and V. I. Fal'ko, Phys. Rev. Lett. **87**, 256801 (2001).

[187] F. Wang, S. Yip, N. Han, K. Fok, H. Lin, J. J. Hou, G. Dong, T. Hung, K. S. Chan, and J. C. Ho, Nanotechnology **24**, 375202 (2013).

[188] E. Khalaf and P. M. Ostrovsky, Phys. Rev. B **94**, 165431 (2016).

[189] S. Furthmeier, F. Dirnberger, M. Gmitra, A. Bayer, M. Forsch, J. Hubmann, C. Schüller, E. Reiger, J. Fabian, T. Korn, and D. Bougeard, Nat. Commun. **7**, 12413 (2016).

[190] P. E. Faria Junior, G. Xu, Y.-F. Chen, G. M. Sipahi, and I. Žutić, Phys. Rev. B **95**, 115301 (2017).

[191] G. E. Pikus and A. N. Titkov, in *Optical Orientation*, Modern Problems in Condensed Matter Sciences, Vol. 8, edited by F. Meier and B. P. Zakharchenya (North-Holland, Amsterdam, 1984).

[192] C. W. J. Beenakker and H. van Houten, Phys. Rev. B **38**, 3232 (1988).

[193] Ç. Kurdak, A. M. Chang, A. Chin, and T. Y. Chang, Phys. Rev. B **46**, 6846 (1992).

[194] J. J. Lin and J. P. Bird, J. Phys.: Condens. Matter **14**, R501 (2002).

[195] K. K. Choi, D. C. Tsui, and K. Alavi, Phys. Rev. B **36**, 7751 (1987).

[196] K. Hiruma, M. Yazawa, T. Katsuyama, K. Ogawa, K. Haraguchi, M. Koguchi, and H. Kakibayashi, J. Appl. Phys. **77**, 447 (1995).

[197] S. Chakravarty and A. Schmid, Phys. Rep. **140**, 193 (1986).

[198] F. Glas, J.-C. Harmand, and G. Patriarche, Phys. Rev. Lett. **99**, 146101 (2007).

[199] G. Patriarche, F. Glas, M. Tchernycheva, C. Sartel, L. Largeau, J.-C. Harmand, and G. E. Cirlin, Nano Lett. **8**, 1638 (2008).

[200] L. Zhang, J.-W. Luo, A. Zunger, N. Akopian, V. Zwiller, and J.-C. Harmand, Nano Lett. **10**, 4055 (2010).

[201] P. Krogstrup, S. Curiotto, E. Johnson, M. Aagesen, J. Nygård, and D. Chatain, Phys. Rev. Lett. **106**, 125505 (2011).

[202] T. Rieger, M. I. Lepsa, Th. Schäpers, and D. Grützmacher, J. Cryst. Growth **378**, 506 (2013).

[203] P. Schroth, M. Köhl, J.-W. Hornung, E. Dimakis, C. Somaschini, L. Geelhaar, A. Biermanns, S. Bauer, S. Lazarev, U. Pietsch, and T. Baumbach, Phys. Rev. Lett. **114**, 055504 (2015).

[204] A. Fontcuberta i Morral, Nature **531**, 308 (2016).

[205] D. Jacobsson, F. Panciera, J. Tersoff, M. C. Reuter, S. Lehmann, S. Hofmann, K. A. Dick, and F. M. Ross, Nature **531**, 317 (2016).

[206] A. De and C. E. Pryor, Phys. Rev. B **81**, 155210 (2010).

[207] M. Gmitra and J. Fabian, Phys. Rev. B **94**, 165202 (2016).

[208] Y. V. Pershin and V. A. Slipko, Phys. Rev. B **82**, 125325 (2010).

[209] M. O. Hachiya, G. Usaj, and J. C. Egues, Phys. Rev. B **89**, 125310 (2014).

[210] P. E. Faria Junior, T. Campos, C. M. O. Bastos, M. Gmitra, J. Fabian, and G. M. Sipahi, Phys. Rev. B **93**, 235204 (2016).

[211] T. Campos, P. E. Faria Junior, M. Gmitra, G. M. Sipahi, and J. Fabian, Phys. Rev. B **97**, 245402 (2018).

[212] J. M. Kikkawa and D. D. Awschalom, Phys. Rev. Lett. **80**, 4313 (1998).

[213] R. I. Dzhioev, K. V. Kavokin, V. L. Korenev, M. V. Lazarev, B. Y. Meltser, M. N. Stepanova, B. P. Zakharchenya, D. Gammon, and D. S. Katzer, Phys. Rev. B **66**, 245204 (2002).

[214] J. H. Buß, J. Rudolph, S. Starosielec, A. Schaefer, F. Semond, Y. Cordier, A. D. Wieck, and D. Hägele, Phys. Rev. B **84**, 153202 (2011).

[215] C. Schierholz, T. Matsuyama, U. Merkt, and G. Meier, Phys. Rev. B **70**, 233311 (2004).

[216] G. M. Minkov, A. A. Sherstobitov, A. V. Germanenko, O. E. Rut, V. A. Larionova, and B. N. Zvonkov, Phys. Rev. B **71**, 165312 (2005).

[217] B. Grbić, R. Leturcq, T. Ihn, K. Ensslin, D. Reuter, and A. D. Wieck, Phys. Rev. B **77**, 125312 (2008).

[218] R. Moriya, K. Sawano, Y. Hoshi, S. Masubuchi, Y. Shiraki, A. Wild, C. Neumann, G. Abstreiter, D. Bougeard, T. Koga, and T. Machida, Phys. Rev. Lett. **113**, 086601 (2014).

[219] Y. Aharonov and D. Bohm, Phys. Rev. **115**, 485 (1959).

[220] F. Haas, T. Wenz, P. Zellekens, N. Demarina, T. Rieger, M. Lepsa, D. Grützmacher, H. Lüth, and Th. Schäpers, Sci. Rep. **6**, 24573 (2016).

[221] Y. Aharonov and A. Casher, Phys. Rev. Lett. **53**, 319 (1984).

[222] J. Nitta, T. Bergsten, Y. Kunihashi, and M. Kohda, J. Appl. Phys. **105**, 122402 (2009).

[223] B. L. Al'tshuler, A. G. Aronov, and B. Z. Spivak, JETP Lett. **33**, 94 (1981), [Pis'ma Zh. Eksp. Teor. Fiz. **33**, 101 (1981)].

[224] M. Jung, J. S. Lee, W. Song, Y. H. Kim, S. D. Lee, N. Kim, J. Park, M.-S. Choi, S. Katsumoto, H. Lee, and J. Kim, Nano Lett. **8**, 3189 (2008).

[225] M. Büttiker, Y. Imry, and R. Landauer, Phys. Lett. A **96**, 365 (1983).

[226] J. Splettstoesser, M. Governale, and U. Zülicke, Phys. Rev. B **68**, 165341 (2003).